UNIVERSITÀ DEGLI STUDI DI PADOVA

Sede Amministrativa: Università degli Studi di Padova

Dipartimento di Scienze Chimiche

SCUOLA DI DOTTORATO DI RICERCA IN

SCIENZA ED INGEGNERIA DEI MATERIALI

CICLO: XXVII

A rational approach to the optimization of efficient electrocatalysts for the next generation Fuel Cells

Direttore della Scuola: Ch.mo Prof. Gaetano Granozzi

Supervisore: Dr. Stefano Agnoli

Dottorando: Marco Favaro

CONTENTS

Acronyms

Here following are reported the principal acronyms that are used in this thesis work.

AFM	Atomic Force Microscopy
Ar-HOPG	Argon-sputtered HOPG
ARPES	Angle Resolved PES
BE	Binding Energy
BSE	Back-Scattered Electron
CE	Counter Electrode
CL	Cathode Luminescence
CMG	Chemically Modified Graphene
CQD	Carbon Quantum Dot
CV	Cyclic Voltammetry
DEFC	Direct Ethanol Fuel Cell
DET	Dissociative Electron Transfer
DFT	Density Functional Theory
DMFC	Direct Methanol Fuel Cell
DOF	Degree of Freedom
DOS	Density of States
EIS	Electrochemical Impedence Spectroscopy
ET	Electron Transfer
EDX	Energy Dispersive X-ray analysis
FC	Fuel Cell
FEG	Field Emission Gun
FWHM	Full Width at Half Maximum
FSCI	Final State Configuration Interaction
FT	Fourier Transform
G	Graphene
GO	Graphene Oxide
GC	Glassy Carbon
GOQD	Graphene Oxide Quantum Dot
GQD	Graphene Quantum Dot
HER	Hydrogen Evolution Reaction
HOPG	Highly Oriented Pyrolitic Graphite
HOR	Hydrogen Oxidation Reaction
HR-PES	High Resolution PES
IMFP	Inelastic Mean Free Path
KE	Kinetic Energy
KL fit	Koutecky-Levich fit
LDOS	Local Density Of States
LEED	Low Energy Electron Diffraction
LSV	Linear Sweep Voltammetry
MC	Mesoporous Carbon
ML	Mono Layer
MLE	Mono Layer Equivalent

NEXAFS	Near Edge X-ray Absorption Fine Structure
N-HOPG	Nitrogen-doped HOPG
NP	Nano Particle
OCP	Open Circuit Potential
OER	Oxygen Evolution Reaction
ORR	Oxygen Reduction Reaction
PBS	Phosphate Buffer Solution
PE	Photon Energy
PES	Photoelectron Spectroscopy
PEM	Proton Exchange Membrane
PRNG	Pseudo Random Number Generator
QCE	Quantum Confinement Effect
QD	Quantum Dot
QMS	Quadrupole Mass Spectrometer
RDE	Rotating Disk Electrode
RE	Reference Electrode
ResPES	Resonant PES
RGA	Residual Gas Analysis
RMS	Root Mean Square
R_p	Projected Range
SCE	Saturated Calomel Electrode
SCSE	Small Cluster Size Effect
SE	Secondary Electron
SEI	Secondary Electron Imaging
SEM	Scanning Electron Microscopy
SHE	Standard Hydrogen Electrode
SMSI	Strong Metal-Support Interaction
SOS	Spin Orbit Splitting
STM	Scanning Tunneling Microscopy
TEM	Transmission Electron Microscopy
TNT	Titania Nano-Tube
TPD	Thermal Programmed Desorption
UHV	Ultra High Vacuum
UPS	Ultraviolet Photoelectron Spectroscopy
VB	Valence Band
WE	Working Electrode
WR	Water Remediation
XPS	X-ray Photoemission Spectroscopy
XRD	X Ray Diffraction

General Data and Fundamental Constants

Here following are reported the tabulated physical constants that are used in this thesis work (taken from D. R. Lide, *Handbook of Chemistry and Physics*, CRC Press, **2000**).

Quantity	Symbol	Value	Power of ten	Units
Speed of light	c	2.997 925 58	10^{8}	m s^{-1}
Elementary charge	e	1.602 176	10^{-19}	C
Faraday constant	$F = N_A e$	9.648 53	10^{4}	C mol^{-1}
Boltzmann constant	k	1.380 65	10^{-23}	J K^{-1}
Gas constant	$R = N_A k$	8.314 47		J K^{-1} mol^{-1}
		8.314 47	10^{-2}	L bar K^{-1} mol^{-1}
		8.205 74	10^{-2}	L atm K^{-1} mol^{-1}
		6.236 37	10	L Torr K^{-1} mol^{-1}
Planck's constant	h	6.626 08	10^{-34}	J s
	$\hbar = h/2\pi$	1.054 57	10^{-34}	J s
Avogadro's constant	N_A	6.022 14	10^{23}	mol^{-1}
Atomic mass unit	u	1.660 54	10^{-27}	kg
Mass				
electron	m_e	9.109 38	10^{-31}	kg
proton	m_p	1.672 62	10^{-27}	kg
neutron	m_n	1.674 93	10^{-27}	kg
Vacuum permittivity	$\varepsilon_0 = 1/c^2 \mu_0$	8.854 19	10^{-12}	J^{-1} C^2 m^{-1}
	$4\pi\varepsilon_0$	1.112 65	10^{-10}	J^{-1} C^2 m^{-1}
Vacuum permeability	μ_0	4π	10^{-7}	J s^2 C^{-2} m^{-1} (= T^2 J^{-1} m^3)
Magneton				
Bohr	$\mu_B = e\hbar/2m_e$	9.274 01	10^{-24}	J T^{-1}
nuclear	$\mu_N = e\hbar/2m_p$	5.050 78	10^{-27}	J T^{-1}
g value	ge	2.002 32		
Bohr radius	$a_0 = 4\pi\varepsilon_0\hbar^2/m_e e^2$	5.291 77	10^{-11}	m

Abstract

The PhD project has been performed in the *Surfaces and Catalysts group* active in the Department of Chemical Sciences, within the frame of the grant "*A rational approach to the optimization of efficient electrocatalysts for the next generation Fuel Cells*", funded by CARIPARO foundation. The project has been focused on the preparation and characterization of new carbon-based materials for applications in Polymer Electrolyte Membrane Fuel Cells (**PEMFCs**), also known as *oxygen-hydrogen FCs*. The preparation of the materials has been performed using different techniques, depending on the type of the target material and on the possible applications that these materials can offer. With reference to the studied model systems (Highly Oriented Pyrolytic Graphite (HOPG) and Glassy Carbon (GC)), the introduction of doping heteroatoms has been performed by ion implantation (publications 1, 2, 5 and 7, see "List of publications" reported at the end of this chapter), while the study of new chemical functionalities has been allowed by the use of Wet Chemistry techniques, in particular derived from the electrochemical synthesis (publications 9 and 12) [1].

The deposition of thin films or nanoparticles (metal or oxides of transition metals) on the ion-modified materials has been carried out *in-situ* by using advanced techniques under Ultra High Vacuum conditions (UHV), such as Physical Vapor Deposition (PVD) (Publication 2). Within the study of the model systems, PVD was chosen because of its ability to provide an atomic scale control of the metal deposition. In a second time, conventional deposition techniques such as chemical or electrochemical reduction of suitable metal precursors (Publications 5 and 7) have been performed, in a synergistic combination between Surface Science and Electrochemistry-derived techniques (Publications 5 and 7).

[1] R. Ruoff, *J. Mater. Chem.* **21** (2011) 3272; Y. Xu, G. Shi, *J. Mater. Chem.* **21** (2011) 3311; Z. Zhang, J. Zhang, N. Chen, L. Qu, *Energy Environ. Sci.* **5** (2012), 8869; Y. Li, Y. Hu, Y. Zhao, G. Shi, L. Deng, Y. Hou, L. Qu, *Adv. Mater.* **23** (2011), 776.

The characterization of these materials has been performed using the facilities of the Surface Science group, such as the X-ray and Ultraviolet Photoelectron Spectroscopy (XPS - UPS), Scanning Tunneling and Atomic Force Microscopy (STM - AFM), Scanning Electron Microscopy (SEM), Energy Dispersive X-ray spectroscopy (EDX) and Low Energy Electron Diffraction (LEED) (see **Section 1**). To get a deeper insight in the chemistry/structure/properties of the prepared systems, synchrotron light-based techniques such as HR-XPS, NEXAFS, ARPES, ResPES and PEEM have been extensively used. The study of the electro-catalytic activity has been performed using conventional Electrochemistry techniques, in particular Cyclic and Linear Sweep Voltammetry (CV - LSV), as well as electro-dynamic techniques such as Rotating Disk Electrode (RDE). Finally, in order to support the experimental data or to bring their understanding at a deeper level, simulations using Density Functional Theory (DFT) have been performed in collaboration with the group coordinated by Prof. Cristiana Di Valentin (University of Milano Bicocca). During the course of the doctorate, several collaborations have been pursued with other research groups operating in the Department of Chemical Sciences or abroad, such as the "Interfaces and Energy Conversion E19" research unit, Technical University of Munich (TUM, Germany), coordinated by Profs. O. Schneider and J. Kunze-Liebhäuser.

During the PhD several topics have been studied; the main ones (on which this thesis work is focused) are listed below:

1. Study of the chemical reactivity of metal nanoparticles deposited on HOPG and GC substrates modified by implantation of nitrogen and sputtering with Ar (**Section 2**).

The following study, focused on the understanding of the metal-dopants interaction in model systems (HOPG, GC) doped with nitrogen, has demonstrated that the use of ion-modified substrates, characterized by good reactivity towards the *Oxygen Reduction Reaction* (ORR, cathodic side of a conventional fuel cell, publication 1) allows the obtaining of metal overlayers (in particular Pd) having poor catalytic performances and stabilities over time (publications 2 and 7) towards the ORR; on the other hand, the same systems exhibit an excellent activity towards the electrochemical reduction of halo-aromatic organic pollutants present in industrial waste water (publication 5). The deposition of the metal nanoparticles have been carried out both by means of PVD and electrochemical reduction. Interestingly, Pd nanoparticles (NPs) deposited on HOPG or GC implanted with N show a high stability to coarsening induced by high temperatures, as well-documented by Figure 1.

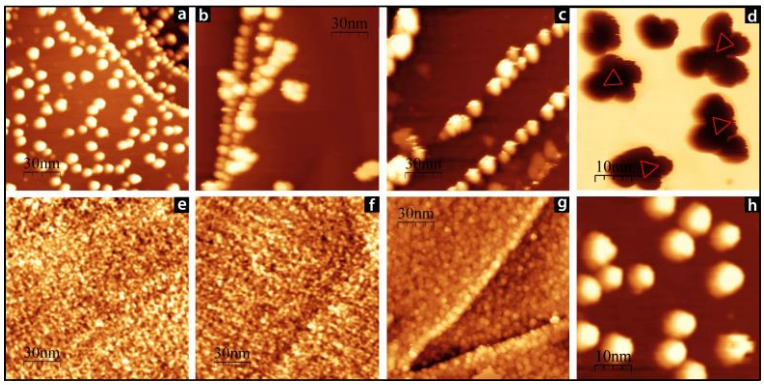

Figure 1. An example of the implantation/STM/XPS/electrochemistry work performed on Pd NPs deposited on the ion-modified systems; a, b, c, d: Pd deposited on pure HOPG; e, f, g, h: same amount of Pd deposited on N-implanted HOPG. The images (a, e), (b, f), (c, g) and (d,h) have been recorded at 25° C, 250° C, 500° C and 750°C, respectively.

2. Synthesis of Graphene Oxide (GO) via chemical oxidation of micrometric graphite powders. Preparation of GO paper-like and Foam structures (**Section 3**).

GO has been obtained using the well-known Hummers oxidation methods of commercial micrometric graphite powders. The obtained GO has been deposited by drop-casting on different polycristalline substrates, such as Cu or Ni, or GC. Thermal annealing experiments have shown that is possible to efficiently tune the type and the concentration of the typical oxygen functional groups present in the GO, making it a flexible material with a wide spectrum of potential applications (publication 3). Moreover, it has been demonstrated that the selective unzipping of GO through electrochemical etching is a powerful method for the to the preparation of GO foams (Figure 2). As reported by Figure 2, these new systems are characterized by a high surface area, which makes them suitable for applications as carbon supercapacitors (publication 9).

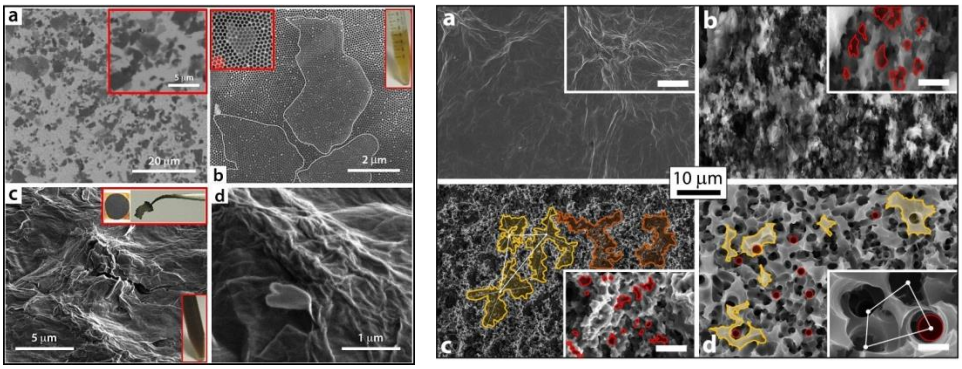

Figure 2. Left: SEM images of GO single layers deposited on Si (110) (a) and on AAO (Aluminum Anodic Oxide) (b); c, d: SEM images at different magnifications of the surface crumpled morphology of a GO paper obtained via drop-casting on a Cu substrate and consecutive mechanical exfoliation (upper inset in Figure c). Right: GO paper supported on GC (a) and GO foams prepared by electrochemical etching in acidic (b), neutral (buffer solution, c) and alkaline conditions (d), respectively.

The GO structures can be reduced to graphene not only by a thermal annealing but also by the evaporation in UHV of metal Ti (publication 3). This study, mainly performed at Elettra synchrotron (Trieste, IT, Bach beamline) has demonstrated that metal Ti, deposited by PVD on GO, promotes a redox surface reaction with the oxygen functional groups decorating the GO surface, with the final obtaining of high quality graphene supporting nanoclusters of sub-

stoichiometric titania (TiO_x) and oxy-carbide phases (TiO_xC_y) (Figure 3). These model systems have been widely studied in order to rule out the chemistry/physics of the graphene/TiO_x/TiO_2 and graphene/TiO_xC_y interface (publication 3), sheding in this way new light on the light capture and photocatalysis properties exhibited by these nano-composites.

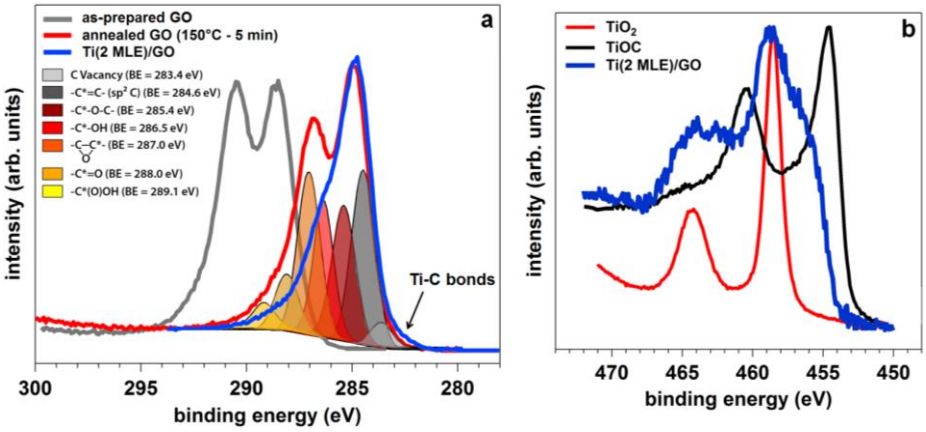

Figure 3. Redox surface reaction at the interface graphene/Ti, studied by photoemission spectroscopy; a, b: C 1s and Ti 2p photoemission lines. In Figure b, the peaks of stoichiometric titania (TiO_2) titanium oxy-carbide (TiOC) have been reported as reference.

3. Preparation and chemical, physical, structural and functional characterization of pure and doped-GO Quantum Dots (GOQDs) (**Section 4**).

Pure and different doped GOQDs systems have been prepared via electrochemical etching of GO in a molecular dopant precursor containing electrolyte. With this method, doped (B-, N- and S-GOQDs) and co-doped (B,N- and S,N-GOQDs) systems have been prepared and fully characterized using XPS, STM, TEM, NEXAFS and optical spectroscopies. These new GO nano-platelets, with a diameter of about 2 nm, exhibit excellent photoluminescence properties in the visible range. Furthermore, they have been tested towards the ORR catalized in alkaline environment, showing remarkable electro-catalytic activity. A detailed chemical/physical characterization has demonstrated that the pristine materials, whose edges are decorated by oxygen functional groups, are characterized by a high selectivity towards the 2 electron reaction pathway (with the consequent production of hydrogen peroxide). On the other hand, a mild chemical reduction treatment of the pristine GOQDs with $NaBH_4$ has shown that the decrease in the oxygen functional group amount is accompanied by a general increase in the catalytic activity and by an oxygen reduction occurring with a 4 electron mechanism (that is, with the direct reduction of oxygen to water; see the schematization reported in Figure 4). These results have been confirmed and fully supported by DFT calculations (publication 12).
The pure GOQDs have been used in many other applications, by exploiting their remarkable self-assembly properties, and in particular for the preparation of new 3D materials (publication 9). Moreover, they have been also used as source for the in-situ carbon doping of titania nanotubes, during their anodic growth (publication 13).

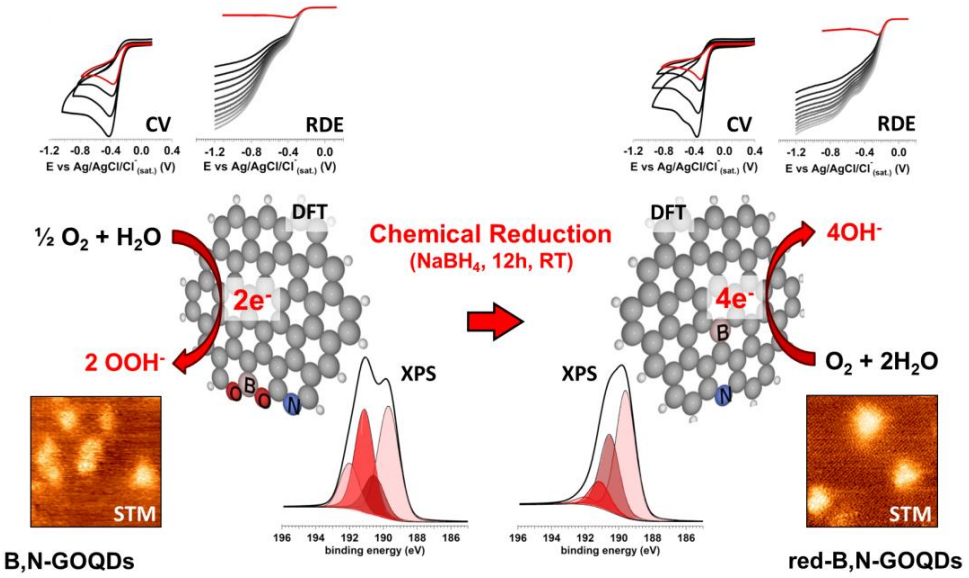

Figure 4. Schematization of the functional characterization performed on pure and doped GOQDs. The picture is in particular referred to the B,N-co-doped-GOQDs, which exhibits the higher catalytic efficiency compared to those that characterize the other doped and co-doped systems.

Il progetto di dottorato nasce all'interno del gruppo di ricerca di *Superfici e Catalizzatori* operante nel dipartimento di Scienze Chimiche, nell'ambito della borsa a titolo vincolato "*Un approccio razionale alla ottimizzazione di elettrocatalizzatori efficienti per le celle a combustibile di nuova generazione*", finanziata da fondazione CARIPARO. Le tematica è stata focalizzata sulla preparazione e caratterizzazione di nuovi materiali *a base di carbonio* utilizzabili per applicazioni in celle a combustibile di tipo **PEMFCs** (*Polymer Electrolyte Membrane Fuel Cells*) ad *ossigeno-idrogeno*. La preparazione dei materiali è avvenuta facendo uso di differenti tecniche, in relazione al tipo di materiale oggetto di studio ed alle applicazioni che tali materiali possono offrire. Con riferimento allo studio dei sistemi modello (grafite pirolitica altamente orientata, HOPG, e carbonio vetroso, GC), il drogaggio degli stessi mediante l'introduzione di eteroatomi (in particolare azoto) è avvenuto ricorrendo alla tecnica dell'impiantazione ionica (pubblicazioni 1, 2, 5 e 7 vedasi "List of publications" riportata alla fine di questo capitolo), mentre lo studio di nuove funzionalità chimiche è stato permesso dall'utilizzo di tecniche di Wet Chemistry, in particolare mutuate dalla sintesi elettrochimica (pubblicazioni 9 e 12) [1].

La deposizione di film sottili o di nanoparticelle (metalliche o a base di ossidi di metalli di transizione) su tali materiali modificati è stata effettuata facendo uso di tecniche avanzate come la deposizione fisica da fase vapore (PVD) (pubblicazione 2) in condizioni controllate di Ultra Alto Vuoto (UHV), in grado di offrire un controllo su scala atomica della deposizione di tali film. Sono state utilizzate anche tecniche di deposizione tradizionali quali la riduzione chimica o elettrochimica di opportuni precursori metallici (pubblicazioni 5 e 7): l'utilizzazione di una siffatta combinazione sinergica tra tali differenti tecniche di preparazione ha permesso di ottenere materiali caratterizzati da strutture e proprietà peculiari (pubblicazioni 5 e 7).

La caratterizzazione di tali materiali è svolta utilizzando le facilities del gruppo di Scienza delle Superfici, come la spettroscopia di fotoelettroni (XPS) o della banda di valenza (UPS), la microscopia ad effetto tunnel o a forza atomica (STM -

[1] R. Ruoff, *J. Mater. Chem.* **21** (2011) 3272; Y. Xu, G. Shi, *J. Mater. Chem.* **21** (2011) 3311; Z. Zhang, J. Zhang, N. Chen, L. Qu, *Energy Environ. Sci.* **5** (2012), 8869; Y. Li, Y. Hu, Y. Zhao, G. Shi, L. Deng, Y. Hou, L. Qu, *Adv. Mater.* **23** (2011), 776.

AFM), la microscopia elettronica e la dispersione energetica dei raggi X indotta dagli elettroni (SEM-EDX), la diffrazione di elettroni lenti (LEED) (a tal proposito si veda la sezione 1). Allo scopo di caratterizzare maggiormente in dettaglio la struttura e le proprietà chimiche dei materiali preparati sono state usate estensivamente le tecniche di indagine offerte dalla luce di sincrotrone (HR-XPS, NEXAFS, ARPES, ResPES, PEEM), mentre lo studio della reattività catalitica si basa su tecniche derivate dall'analisi elettrochimica, in particolare la voltammetria ciclica ed a scansione lineare del potenziale applicato, nonchè tecniche elettro-dinamiche come la voltammetria su elettrodo rotante. Infine, allo scopo di supportare i dati sperimentali o portare la comprensione delle proprietà dei materiali ad un livello più profondo, simulazioni mediante teoria del funzionale densità (DFT) sono state adottate per un approccio critico allo studio dei materiali preparati (in collaborazione con il gruppo coordinato dalla prof. Cristiana Di Valentin, Università di Milano Bicocca). Durante il corso del dottorato, diverse collaborazioni sono state perseguite con gruppi interni al Dipartimento di Scienze Chimiche o anche Esteri, come l'unità di ricerca "Interfaces and Energy Conversion E19", dell'università tecnica di Monaco di Baviera (TUM, Technische Universität München, Germania), coordinata dai proff. O. Schneider e J. Kunze-Liebhäuser.

Nel corso del dottorato si sono affrontate diverse tematiche, tra cui le principali (oggetto del presente lavoro di tesi) sono qui di seguito elencate:

1. Studio della reattività chimica di nanoparticelle metalliche depositate su substrati di HOPG e GC modificati mediante impianto di azoto e sputtering con Ar (**Sezione 2**).

Il seguente studio, finalizzato alla comprensione fine dell'interazione metallo-dopante in sistemi modello (HOPG, GC) dopati con azoto, ha permesso di dimostrare come l'utilizzo di substrati ion-modified, di per se stessi dotati di buona reattività verso la riduzione dell'ossigeno (comparto catodico di una convenzionale cella a combustibile, pubblicazione 1) consenta l'ottenimento di overlayer metallici (in particolare Pd) caratterizzati da prestazioni catalitiche e di stabilità nel tempo (pubblicazioni 2 e 7) non eccellenti verso l'*Oxygen Reduction Reaction* (ORR) ma ottimali per la riduzione elettrochimica di inquinanti organici alogeno-aromatici in acque industriali (*waste waters*, pubblicazione 5). La deposizione delle nanoparticelle metalliche è stata effettuata sia mediante tecniche di tipo fisico (PVD), sia mediante riduzione elettrochimica. La nanoparticelle di Pd depositate su HOPG o GC impiantato con N dimostrano una elevata stabilità al coarsening indotto da alte temperature, come riportato in Figura 1.

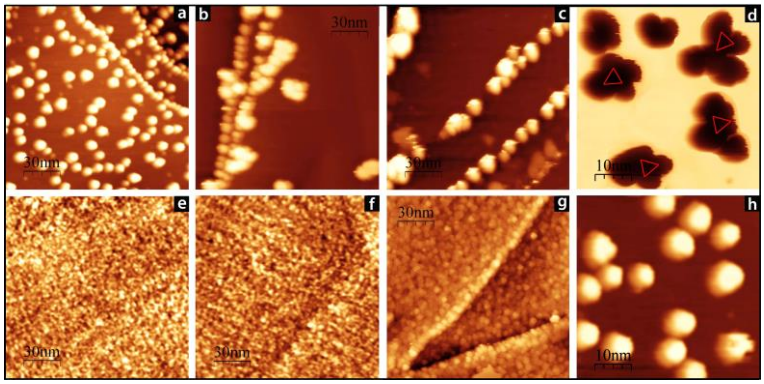

Figura 1. Un esempio del lavoro effettuato su nanoparticelle di Pd depositate HOPG pura (a, b, c, d) e dopata con azoto (e, f, g, h). Le immagini (a, e), (b, f), (c, g) e (d,h) sono relative rispettivamente a 25° C, 250° C, 500° C e 750°C.

2. Sintesi di GO (Ossido di Grafene) mediante ossidazione chimica di polveri micrometriche di grafite e relativa preparazione di strutture paper-like e schiume basate sull'ossido di grafene (sezione 3).

Si è adottata una tipologia di sintesi per la produzione di grafite e grafene ossido a partire da grafite micrometrica (commerciale), facendo uso di protocolli ben documentati in letteratura (ossidazione chimica di Hummers). Il GO così ottenuto è stato utilizzato per la realizzazione di GO paper-like depositati su differenti substrati, come rame e nichel policristallini o glassy carbon. Prove successive di annealing termici hanno dimostrato come sia possibile ottenere selettivamente differenti gruppi funzionali di ossigeno ed in differenti concentrazioni (pubblicazione 3), evidenza sperimentale che rende tale materiale particolarmente flessibile ed utilizzabile pertanto in differenti applicazioni. Previo unzipping selettivo di tali film di GO mediante tecniche di ablazione elettrochimica, è stata inoltre possibile la preparazione di "schiume" (GO foam, Figura 2) di ossido di grafene ad elevata area superficiale, dimostrandone le potenziali applicazioni come supercapacitori al carbonio (pubblicazione 9).

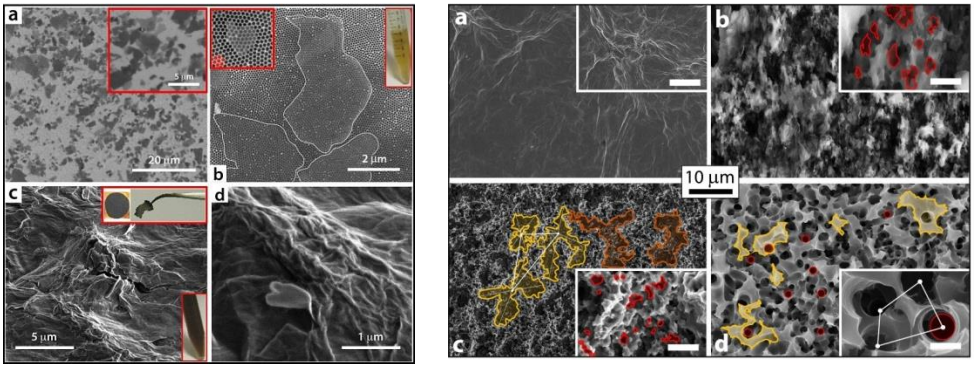

Figura 2. Sinistra: immagini SEM dei singoli layer di GO depositati su Si (110) (a) e su AAO (Aluminum Anodic Oxide) (b); c,d: immagini SEM a diversa scala di ingrandimento che mostrano la morfologia "accartocciata" di una GO paper-like ottenuta per dropcasting su rame e successiva esfoliazione meccanica (inset in Figura c). Destra: GO paper-like supportata su glassy carbon (a) e GO foams preparate mediante ablazione elettrochimica condotta rispettivamente in ambiente acido (b), neutro (soluzione tampone ai fosfati, c) ed alcalino (d).

Si è inoltre dimostrato come le strutture paper-like di grafene ossido possano essere ridotte a grafene (ovvero senza gruppi funzionali ad ossigeno) mediante la deposizione in UHV di titanio metallico. Tale studio, condotto in maggior parte presso il sincrotrone Elettra (Trieste, IT, Bach beamline), ha permesso di dimostrare come il titanio promuova una reazione redox alla superficie del GO, con l'ottenimento di grafene supportante nanoclusters di ossidi sub-stechiometrici di titania (TiO_x) ed fasi di ossi-carburo di titanio (TiO_xC_y) (Figura 3). Tali sistemi modello sono stati ampiamente indagati per la comprensione basilare che è possibile ottenere riguardo alla fisica/chimica dell'interfaccia grafene/TiO_x/TiO_2 e grafene/TiC_xO_y (pubblicazione 3), gettando così nuova luce sulle proprietà di cattura della luce e di fotocatalisi esibite da tali compositi.

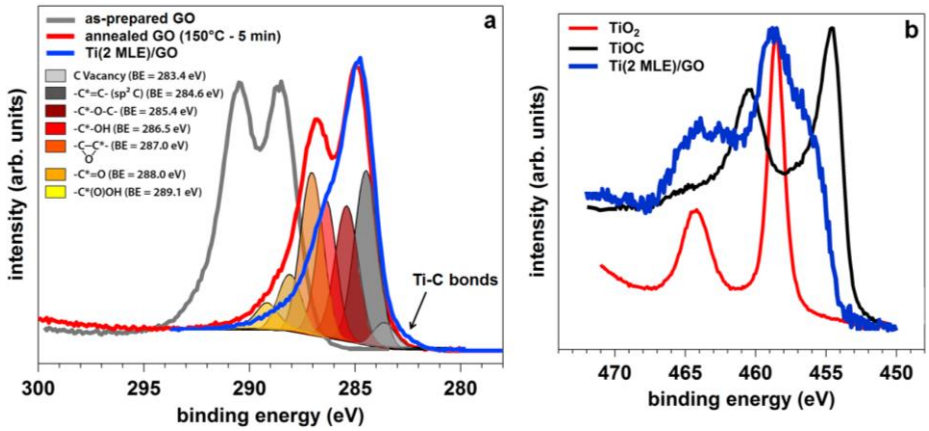

Figura 3. Reazione redox di superficie all'interfaccia grafene/titanio, studiata mediante ausilio della spettroscopia di fotoelettroni; a: picco di fotoemissione del C 1s; b: picco del Ti 2p. Gli spettri del Ti 2p relativi alla titania stechiometrica (TiO_2) ed al titanio ossi-carburo (TiOC) sono stati riportati come riferimento.

3. Preparazione e caratterizzazione chimica, fisica, strutturale e funzionale di GO quantum dots (GOQDs) puri e dopati (**Sezione 4**).

Diverse tipologie di GOQDs drogati e co-drogati sono state preparate mediante ablazione elettrochimica selettiva di un elettrodo di GO supportato su glassy carbon; l'ablazione elettrochimica è stata effettuata in un elettrolita di supporto nel quale l'inserimento di una specie molecolare contenente il drogante prescelto ha permesso la preparazione di B-, N-, S-, B,N- ed S,N-GOQDs. Tali sistemi sono stati ampiamenti caratterizzati mediante XPS, STM, TEM, NEXAFS e spettroscopie ottiche. Questi nuovi nano flakes di ossido di grafene, di circa 2 nm di diametro hanno evidenziato ottime proprietà di fotoluminescenza nel visibile. Inoltre, essi sono stati testati per la riduzione dell'ossigeno in ambiente alcalino, dimostrando spiccate proprietà catalitiche per potenziali applicazioni ai comparti catodici di celle e combustibile. Una caratterizzazione chimico-fisica fine ha permesso di dimostrare come i materiali as-prepared, i cui bordi sono funzionalizzati con gruppi funzionali ad ossigeno, siano caratterizzati da un'elevata selettività verso la reazione di riduzione dell'ossigeno bi-elettronica (con la conseguente produzione di perossido di idrogeno). E' stato effettuato un trattamento di riduzione chimica con $NaBH_4$, dimostrando che i sistemi dopati e ridotti esibiscono un miglioramento delle efficienze catalitiche rispetto ai materiali di partenza; inoltre, la rimozione dei gruppi ossigeno provoca un cambiamento del meccanismo di ORR, passando da una reazione a due elettroni ad una reazione quadrielettronica (ovvero, i sistemi ridotti promuovono la riduzione catalitica diretta dell'ossigeno ad acqua, vedasi schematizzazione riportata in Figura 4). Tali risultati sono stati confermati e pienamente supportati da calcoli DFT (publicazione 12). I GOQDs puri sono stati usati inoltre in numerose applicazioni, grazie alle loro spiccate proprietà di auto-assemblaggio, per la preparazione di nuovi materiali 3D a base grafenica (pubblicazione 9). Inoltre, essi sono stati impiegati come utile sorgente di carbonio per il drogaggio in situ di nanotubi di titania durante la loro crescita anodica (pubblicazione 13).

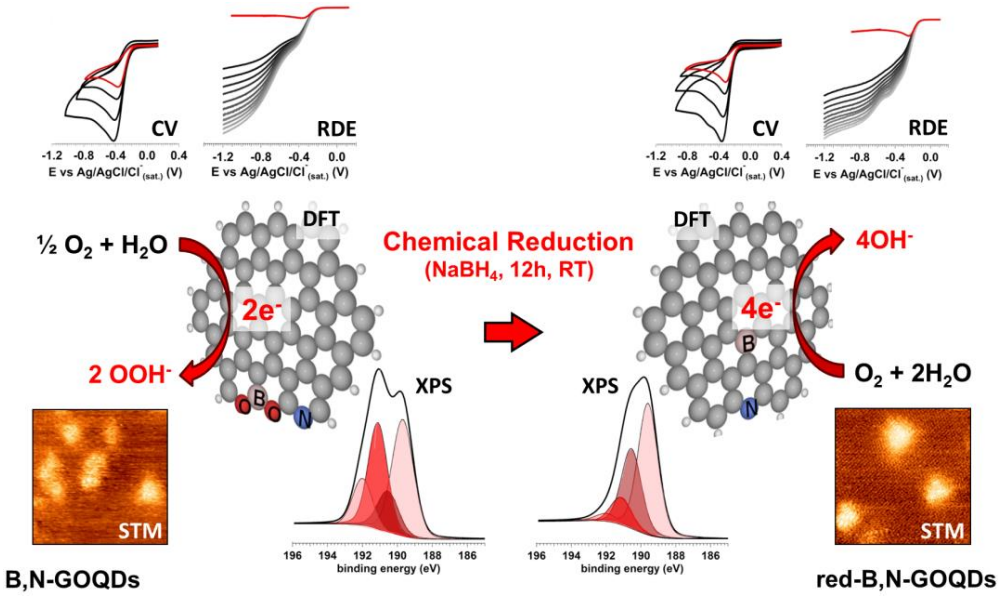

Figura 4. Schematizzazione del lavoro di caratterizzazione funzionale dei sistemi nano-grafenici dopati. Lo schema in particolare si riferisce ai GOQDs co-dopati con B ed N, dotati della più elevata efficienza catalitica tra i vari sistemi dopati preparati.

List of publications

The papers marked with ‡ have been inserted in the present thesis work.

1. **M. Favaro**, L. Perini, S. Agnoli, C. Durante, G. Granozzi, A. Gennaro*, *Electrochemical behavior of N and Ar implanted highly oriented pyrolytic graphite substrates and activity toward oxygen reduction reaction*, Electrochimica Acta 2013, 88, 477-487; ‡
2. **M. Favaro**, S. Agnoli, L. Perini, C. Durante, A. Gennaro, G. Granozzi*, *Palladium nanoparticles supported on nitrogen-doped HOPG: a surface science and electrochemical study*, Phys. Chem. Chem. Phys. 2013, 15, 2923-2931; ‡
3. M.Cattelan, S. Agnoli, **M. Favaro**, D. Garoli, F. Romanato, M. Meneghetti, A. Barinov, P. Dudin, G. Granozzi, *Microscopic View on a Chemical Vapor Deposition Route to Boron-Doped Graphene Nanostructure*, Chem. Mater. 2013, 25, 1490-1495;
4. **M. Favaro**, S. Agnoli*, C. Di Valentin, C. Mattevi, M. Cattelan, L. Artiglia, E. Magnano, F. Bondino, S. Nappini, G. Granozzi, *TiO_2/Graphene nanocomposites from the direct reduction of graphene oxide by metal evaporation*, Carbon 2014, 68, 319-329; ‡
5. L. Perini, C. Durante, **M. Favaro**, S. Agnoli, G. Granozzi, A. Gennaro*, *Electrocatalysis at palladium nanoparticles: Effect of the support nitrogen doping on the catalytic activation of carbon halogen bond*, Appl. Cat. B: Environ. 2014, 144, 300-307; ‡
6. C. Durante, V. Perazzolo, L. Perini, **M. Favaro**, G. Granozzi, A. Gennaro*, *Electrochemical activation of Carbon-Halogen Bonds: Electrocatalysis at Silver/Copper Nanoparticles*, Appl. Cat. B: Environ. 2014, 158-159, 286-295;
7. W. Ju#, **M. Favaro**#, C. Durante, S. Agnoli, O. Schneider*, U. Stimming, Gaetano Granozzi, *Pd Nanoparticles deposited on nitrogen-doped HOPG: New Insights into the Pd-catalyzed Oxygen Reduction Reaction*, Electrochimica Acta 2014, 141, 89-101; (#: these two authors have equally contributed to the work) ‡
8. C. Durante, V. Perazzolo, A. A. Isse, **M. Favaro**, G. Granozzi, A. Gennaro*, *Electrochemical Activation of Carbon-Halogen Bonds: Electrocatalysis at Palladium/Copper Nanoparticles*, Chem. Electro. Chem. 2014, 1, 1370-1381;
9. **M. Favaro**, S. Agnoli*, M. Cattelan, A. Moretto, C. Durante, S. Leonardi, J. Kunze-Liebhäuser, O. Schneider, A. Gennaro, G. Granozzi, *Shaping graphene oxide by Electrochemistry: from Foams to Self-Assembled Molecular Materials*, Carbon 2014, 77, 405-415; ‡
10. D. Mazzier, **M. Favaro**, S. Agnoli, S. Silvestrini, G. Granozzi, M. Maggini, A. Moretto*, *Synthesis of luminescent 3D microstructures formed by carbon quantum dots and their self-assembly properties*, Chem. Commun. 2014, 50, 6592-6595; ‡
11. L. Calvillo, D. Fittipaldi, C. Rüdiger, S. Agnoli, **M. Favaro**, C. Valero-Vidal, C. Di Valentin, A. Vittadini, N. Bozzolo, S. Jacomet, L. Gregoratti, J. Kunze-Liebhäuser, G. Pacchioni, G. Granozzi*, *The carbothermal transformation of TiO_2 into TiO_xC_y in UHV: tracking intrinsic chemical stabilities*, J. Phys. Chem. C 2014, 118, 22601-22610;

12. **M. Favaro**, L. Ferrighi, G. Fazio, L. Colazzo, C. Di Valentin*, C. Durante, F. Sedona, A. Gennaro, S. Agnoli*, G. Granozzi, *Single and multi-doping in graphene quantum dots: unraveling the origin of selectivity in the oxygen reduction reaction*, ACS Catalysis 2015, 5, 129-144; ‡
13. M. Cattelan, G. W. Peng, E. Cavaliere, L. Artiglia, A. Barinov, L. T. Roling, **M. Favaro**, I. Pis, S. Nappini, E. Magnano, F. Bondino, L. Gavioli, S. Agnoli*, M. Mavrikakis, G. Granozzi, *The nature of the Fe-graphene interface at the nanometric level*, Nanoscale, *accepted*;
14. F. Lamberti, L. Brigo, **M. Favaro**, C. Luni, A. Zoso, M. Cattelan, S. Agnoli, G. Granozzi, G. Brusatin, M. Giomo, N. Elvassore*, *Opto-electrochemical biorecognition by optically-transparent highly conductive graphene-modified Fluorine-doped Tin Oxide substrates*, ACS Appl. Mat. Interfaces, *accepted*;
15. **M. Favaro**, S. Leonardi, C. Valero-Vidal, S. Nappini, M. Hanzlik, S. Agnoli*, Julia Kunze-Liebhauser*, G. Granozzi, *In-situ doping of TiO_2 nanotubes via anodization in graphene oxide quantum dot containing electrolyte and carburization to TiO_xC_y nanotubes*, submitted to Adv. Mater. Interfaces (October 2014); ‡
16. L. Perini, C. Durante*, **M. Favaro**, V. Perazzolo, O. Schneider, S. Agnoli, G. Granozzi, A. Gennaro, *Effect of nitrogen doping on platinum and palladium nanoparticles supported on mesoporous carbon for oxygen reduction reaction*, submitted to ACS Appl. Mat. Interfaces (October 2014).

Introduction

At the beginning of the 20th century the efficient conversion of chemical energy into electrical energy became an important task due to the increased request in the use of electricity. During the last decade, the tendency to increase the flexibility of electricity generation, together with the increase of the world population have led to an increased interest in the development of distributed power generation [1]. It is expected that decentralized power plants will reduce both the capital cost for the installer as well as improve the overall efficiency due to the possibility of the co-generation of electricity and heat [1]. The distribution of heat is easier and more efficient in smaller systems, where production of heat and its usage are in closer proximity.

One of the major factors that influenced the development of Fuel Cells (FCs) is in the increasing concern about the *environmental consequences of fossil fuels* [2] used for the mass-scale production of electricity and for the propulsion of vehicles. The dependence of the industrialized countries on oil became apparent in the oil crises [1]. More importantly, however, there is an increasing global awareness of how human activities influence the environment and how a sustainable development can be achieved within the scenario of the tremendous increase of world population [1]. In this context, FCs *may help to reduce the dependence on fossil fuels and diminish noxious emissions into the atmosphere.* Using pure hydrogen and air as oxygen source, FCs only produce water, *thus eliminating locally all polluting emissions*.

A **fuel cell** is an *electrochemical cell* that converts chemical energy from a fuel into electric energy. Electricity is generated from the *redox reaction* between a *fuel supply* (H_2) and an *oxidizing agent* (O_2). A FC can operate continuously as long as the necessary reactant and oxidant flows are maintained and the cell efficiency is not reduced by possible poisoning.

The amount of electricity produced scales with the amount of reaction surface area or interfacial area available for the energy transfer [3]. To provide large

reaction surfaces that maximize surface-to-volume ratios, fuel cells are usually made into thin planar structures; the electrodes are highly porous to further increase the reaction surface area and ensure good gas access [3]. One side of the planar structure is provided with fuel (*the anode*), while the other side is fed with oxidant (*the cathode*). A thin electrolyte layer spatially separates cathode and anode and ensures that the two individual half reactions occur separately, virtually without crossover effects. Figure 1 reports the schematization of a typical H_2-O_2 FC.

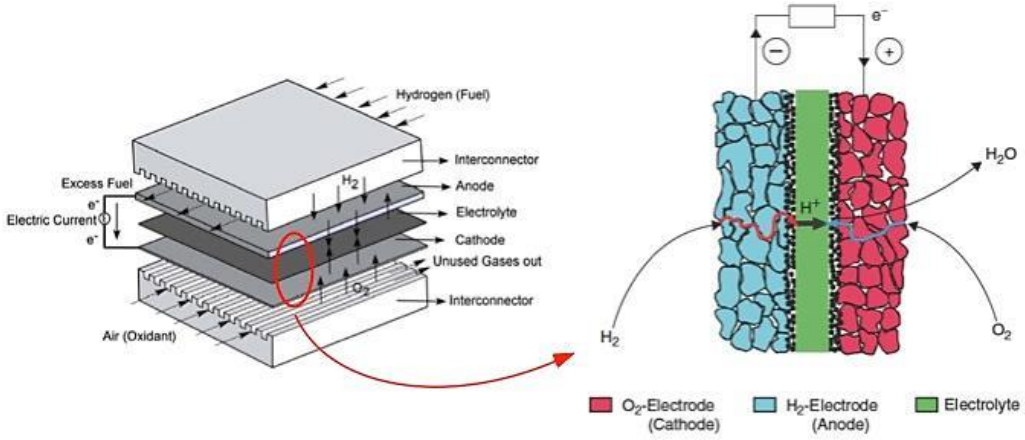

Figure 1. Schematization of a Fuel Cell.

In a FC, the electrochemical overall reaction is characterized by the thermodynamic equilibrium potential described by the *Nernst equation* [2]:

$$(1) \qquad \Delta E_{FC} = E_{cat} - E_{an} = \Delta E^{\Theta} + \frac{RT}{nF} ln\left(\frac{a_{Red}^{cat}}{a_{Ox}^{an}}\right) = \Delta E^{\Theta} - \xi,$$

where $\Delta E^{\Theta} = E_{cat}^{\Theta} - E_{an}^{\Theta}$, $\xi = -RT\, ln\left(\frac{a_{Red}^{cat}}{a_{Ox}^{an}}\right)$, n is the number of electrons exchanged during the redox reactions, F is the is the Faraday constant while $a_k = \gamma_k[k]$ is the chemical activity of the species k (since *activity coefficients* γ_k tend to unity at low concentrations, activities in the Nernst equation are frequently replaced by the concentrations). When current flows in the external circuit that connects the two electrodes (making usable work), a deviation from the open circuit voltage occurs, called *overpotential* (η). One of the reasons for the deviation of the potential from the equilibrium value is the finite rate of the reactions at the electrodes: the lower

the kinetic of the redox reaction, the higher the overpotential [2,3]. FCs are galvanic cells, in which the free energy of a chemical reaction is converted into electrical energy (via an electrical current). The Gibbs free energy change of a chemical reaction is linearly related to the cell voltage (Eq. 2):

$$(2) \qquad \Delta G = -nF\Delta E_{FC} = \Delta G^{\Theta} - RT\,ln\left(\frac{a_{Red}^{cat}}{a_{Ox}^{an}}\right) = \Delta G^{\Theta} + \xi \ ,$$

with $\Delta G^{\Theta} = -nF\Delta E^{\Theta}$.

In a *Proton Exchange Membrane Fuel Cell* (PEMFC), also known as *Polymer Electrolyte Membrane Fuel Cell* because a thin polymer membrane is employed as electrolyte (and cathode-anode separator), protons are the ionic charge carriers. The electrochemical half reactions in a H_2-O_2 PEMFC are [2,3]:

Acidic electrolytes		
Cathode	$O_2 + 4H^+ + 4e^- \rightarrow 2H_2O$	$E_{cat}^{\Theta} = 1.229$ V
Anode	$H_2 \rightarrow 2H^+ + 2e^-$	$E_{an}^{\Theta} = 0.000$ V
Total	$2H_2 + O_2 \rightarrow 2H_2O$	$\Delta E^{\Theta} = 1.229$ V
Alkaline electrolytes		
Cathode	$O_2 + 2H_2O + 4e^- \rightarrow 4OH^-$	$E_{cat}^{\Theta} = 0.401$ V
Anode	$H_2 + 2OH^- \rightarrow 2H_2O + 2e^-$	$E_{an}^{\Theta} = -0.828$ V
Total	$2H_2 + O_2 \rightarrow 2H_2O$	$\Delta E^{\Theta} = 1.229$ V

Ideally, since the standard cell potential is 1.229 V with a negative Gibbs free energy (Eq. 2), the spontaneous reaction can be utilized as an electrical energy generator. Practically, the cell potential is less than the theoretical value due to the overpotential related to the oxygen reduction reaction occurring at the cathode (ORR), which is kinetically sluggish because of the relatively large amount of energy that has to be provided to break the strong oxygen-oxygen double bond during the process [4]. This leads to a low reaction kinetic in the cathode side of the FC, which is responsible, as introduced above, of the relatively high observed overpotential.

In order to minimize this problem and to get a device that can be used under real conditions, a suitable catalyst has to be used.

The synthesis of nanoscale catalysts is a cornerstone technology to meet the current energy challenges, spanning a wide range of applications from fuel cell efficiency to pollutant degradation. On this regard, electrocatalysis is a field of particular interest and one of the most promising, owing to the ability of the combination of Surface Science and Electrochemical methods to correlate the structure and the chemistry of the electrode surface to the reaction mechanisms and electron transfer (ET) dynamics at a molecular level. Optimized nanoscale catalysts have drawn a tremendous interest in literature in the last few years [5, 6, 7, 8, 9, 10], because of the possibility to modify the kinetics of the process, reducing in this way the overpotential and hence improving the electrocatalytic performances. A key factor that has recently emerged is that the chemical modification of the substrate supporting the catalytic active phase leads to a modulation of the electronic structure of the active phase itself, with consequent improvement in the performances and stabilities of the so-prepared catalysts [5-10]. Within the FC technology, this new class of catalysts has been adopted to replace the expensive and rare platinum, which contributes to over 55% of the total cost [1-4], determining the birth of the second generation FCs [10]. Reducing the Pt loading (particularly in the cathode catalyst layer) without compromising the FC performance is an effective strategy to meet the cost requirements for its commercialization. In addition, the design of novel electrocatalysts requires not only the reduction of the amount of used Pt, but also the enhancement of the catalytic activity and durability [10].

The parameters influencing the electrocatalytic properties of metal nanoparticles [11] are: (i) particle size, (ii) particle dispersion and (iii) effect of the substrate material. In order to evaluate these parameters and possibly to singularly disentangle these effects on the overall catalytic properties, optimizing in this way the catalytic material, model systems have to be studied. In particular, this PhD work was focused on the study of graphene-related materials, due to their innovative and promising properties not only for the application in catalysis and electrocatalysis [6-10, 12, 13, 14, 15], but also for their remarkable capability of energy storage [15, 16, 17, 18, 19] and unique electrical and optical behaviour [15, 20, 21], which make them appealing multifunctional materials.

Graphene is the “mother of all graphitic forms” [22], since all of them can be formally obtained from a graphene sheet [22]. In the first part of this thesis work,

as reported in **Section 2**, 3D materials based on graphene inert supports such as Highly Oriented Pyrolytic Graphite (HOPG) and Glassy Carbon (GC) have been used in order to exploit their planar (and, regarding the HOPG, atomically flat) structure, excellent chemical stability, wide potential window and low background current [23]. In other words, these materials constitute the perfect playground to model the sp^2 carbon-based real supports commonly used in the FC field, such as carbon black and mesoporous carbons [1-3, 24, 25]. Pd was used as active catalytic phase [26], while the structure and chemical modification of these substrates has been performed using nitrogen implantation. By a careful Surface Science and Electrochemistry combined study, it has been demonstrated that the deposition of Pd on the N-modified systems is not beneficial for the promotion of low overpotentials in the oxygen reduction. However, the same systems can be used for water remediation, because of the high activity exhibited by these catalysts towards the electro-reduction of halogen-aromatic compounds.

Taking the cue from these results, new suitable graphenic materials, obtained from different state of art wet-chemistry approaches, have been prepared during the last part of the PhD. As reported in **Section 3** and **Section 4** of this thesis, Graphene Oxide (GO) has been prepared from the chemical oxidation of graphite, thus constituting the starting material for the further preparations. GO, in fact, being the oxidized form of graphene, is a flexible and easy-to-process material for the preparation of new graphene-related structures, with application-tailored properties [27, 28, 29, 30, 31]. **Section 3**, reports a detailed study of the capability of GO to undergo to a surface redox reaction mediated by Ti, recovering a high quality graphene structure.. These results have been critically compared with the data obtained using the typical GO reduction procedure, i.e. thermal annealing [32, 33], using advanced synchrotron radiation techniques and DFT calculations. Thanks to the knowledge about the surface reactivity of GO gained in our studies, it was possible to prepare new materials characterized by a high surface area and having interesting porous structures (GO Foams), with potential applications as graphene-based supercapacitors [16, 17, 18, 19, 30, 31] and high surface area catalyst supports [29, 30, 34].

Finally, in **Section 4** the same electrochemical approach adopted for the preparation of GO foams has been further developed in order to obtain nano-sized platelets of GO (known as GO Quantum Dots, GOQDs), doped by the

introduction in the sp^2 carbon lattice of heteroatoms such as B, N, S and their combinatorial assembly. These new materials have been characterized and tested towards the ORR, achieving excellent catalytic activities. Not only: by a careful combination of experimental evidences and theoretical predictions, it was possible to explore in detail the mechanism of the oxygen reduction over these materials, giving interesting and useful feedbacks for the preparation of new optimized electrocatalysts for the next generation FCs.

Moreover, by exploiting the self-assembly properties of GOQDs nano-bricks it has been possible, via different *bottom up* strategies, to prepare a new class of graphene-derived materials (from a molecular to a nano-micro scale). These new materials, whose nature is still under huge research effort, exhibit non-conventional functional properties, which elect them as potential candidate for electrochemical graphene-based supercapacitors [35, 36] and sensing applications [37, 38]. Figure 2 and 3 point out the organization of the work performed during the three years of the doctorate.

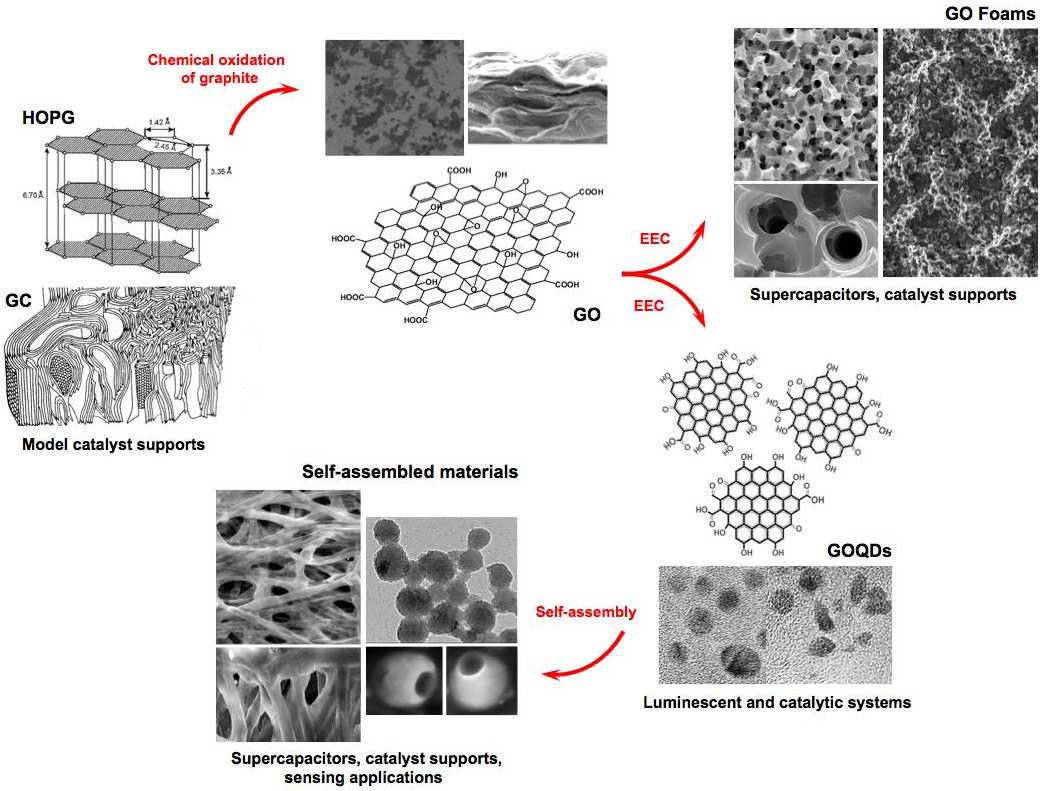

Figure 2. Different graphene-related materials studied during the PhD, starting from the model planar catalyst supports (HOPG, GC) up to nanometric platelets of GO and related 3D structures (EEC: Electrochemical Etching and selective Cutting).

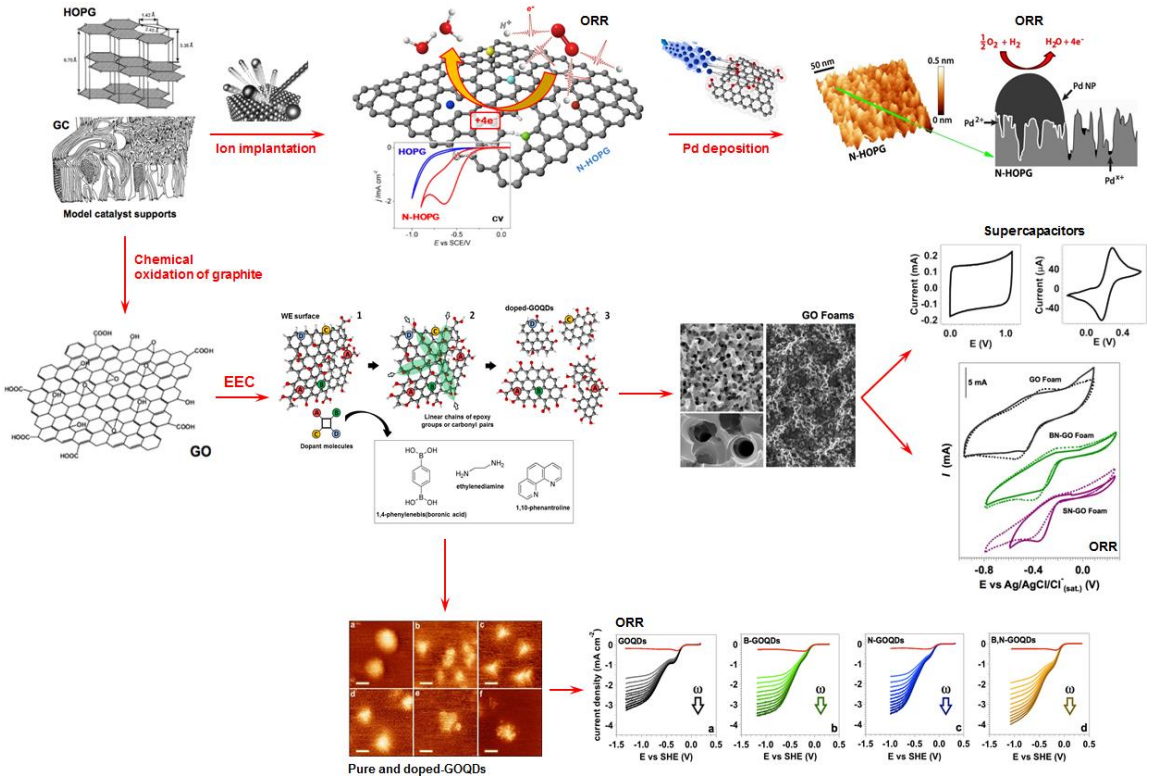

Figure 3. Electrocatalytic tests on the graphene-related materials: organization of the work during the doctorate.

As regards the already published results, the corresponding reprints have been reported as part of this thesis. On the contrary, the arguments not yet published have been discussed in details.

REFERENCES

[1] U.S. Department of Energy (DOE), *Multi-year research and development of Fuel Cells*, 2013.

[2] L. Carrette, K. A. Friedrich, U, Stimming, *Fuel Cells: Fundamentals and Applications*, *Fuel Cells* **1**, 5- (2001).

[3] R. O'Hayre, *Fuel Cell Fundamentals*, Wiley Ed., 2008.

[4] A. Wieckowski, *Fuel Cell Catalysis: a Surface Science approach*, Wiley Ed., 2009.

[5] E. Antolini, Carbon supports for low-temperature fuel cell catalysts, *Appl. Cat. B: Environ.* **88**, 1-24 (2009).

[6] Z. Yang, H. Nie, X. Chen, X. Chen, S. Huang, Recent progress in doped carbon nanomaterials as effective cathode catalysts for fuel cell oxygen reduction reaction, *J. Power Sources* **236**, 238-249 (2013).

[7] W. Y. Wong, W. R. W. Daud, A. B. Mohamad, A. A. H. Kadhum, K. S. Loh, E. H. Majlan, Recent progress in nitrogen-doped carbon and its composites as electrocatalysts for fuel cell applications, *Int. J. Hydrogen Energy* **38**, 1-17 (2013).

[8] G. Wu, P. Zelenay, Nanostructured nonprecious metal catalysts for oxygen reduction reaction, *Acc. Chem. Res.* **46**, 1878-1889 (2013).

[9] D. S. Su, S. Perathoner, G. Centi, Nanocarbons for the development of advanced catalysts, *Chem. Rev.* **113**, 5782-5816 (2013).

[10] M. Liu, R. Zhang, W. Chen, Graphene-supported nanoelectrocatalysts for fuel cells: synthesis, properties, and applications, *Chem. Rev.* **114**, 5117-5160 (2014).

[11] B. R. Cuenya, Synthesis and catalytic properties of metal nanoparticles: size, shape, support, composition and oxidation state effects, *Thin Solid Film* **518**, 3127-3150 (2010).

[12] J. P. Paraknowitsch, A. Thomas, Doping carbons beyond nitrogen: an overview of advanced heteroatom doped carbons with boron, sulphur and phosphorus for energy applications, *Energy Environ. Sci.* **6**, 2839-2855 (2013).

[13] D.-W. Wang, D. Su, Heterogeneous nanocarbon materials for oxygen reduction reaction, *Energy Environ. Sci.* **7**, 576-591 (2014).

[14] X. K. Kong, C.-L. Chen, Q.-W. Chen, Doped graphene for metal-free catalysis, *Chem. Soc. Rev.* **43**, 2841-2857 (2014).

[15] Z. Zhang, J. Zhang, N. Chen, L. Qu, Graphene quantum dots: an emerging material for energy-related applications and beyond, *Energy Environ. Sci.* **5**, 8869-8890 (2012).

[16] H.-J. Choi, S.-M. Jung, J.-M. Seo, D. W. Chang, L. Dai, J.-B. Baek, Graphene for energy conversion and storage in fuel cells and supercapacitors, *Nano Energy* **1**, 534-551 (2012).

[17] J. Hou, Y. Shao, M. W. Ellis, R. B. Moore, B. Yi, Graphene-based electrochemical energy conversion and storage: fuel cells, supercapacitors and lithium ion batteries, *Phys. Chem. Chem. Phys.* **13**, 15384-15402 (2011).

[18] Y. Zhu, S. Murali, M. D. Stoller, K. J. Ganesh, W. Cai, P. J. Ferreira, A. Pirkle, R. M. Wallace, K. A. Cychosz, M. Thommes et al., Carbon-based supercapacitors produced by activation of graphene, *Science* **332**, 1537-1541 (2011).

[19] G. Wang, L. Zhang, J. Zhang, A review of electrode materials for electrochemical supercapacitors, *Chem. Soc. Rev.* **41**, 797-828 (2012).

[20] L. Li, G. Wu, G. Yang, J. Peng, J. Zhao, J.-J. Zhu, Focusing on luminescent graphene quantum dots: current status and future perspectives, *Nanoscale* **5**, 4015-4038 (2013).

[21] S.N. Baker, G. A. Baker, Luminescent Carbon Nanodots: Emergent Nanolights, *Angew. Chem. Int. Ed.* **49**, 6726-6744 (2010).

[22] A. K. Geim, K. S. Novoselov, The rise of graphene, *Nat. Mat.* **6**, 183-191 (2007).

[23] C. E. Banks, R. G. Compton, New electrodes for old: from carbon nanotubes to edge plane pyrolytic graphite, *Analyst* **131**, 15-21 (2006).

[24] H. Chang, S. H. Joo, C. Pak, Synthesis and characterization of mesoporous carbon for fuel cell applications, *J. Mater. Chem.* **17**, 3078-3088 (2007).

[25] A. Stein, Z. Wang, M. A. Fierke, Functionalization of porous carbon materials with designed pore architecture, *Adv. Mat.* **21**, 265-293 (2009).

[26] Z. Chen, D. Higgins, A. Yu, L. Lei Zhang, J. Zhang, A review on non-precious metal electrocatalysts for PEM fuel cells, *Energy Environ. Sci.* **4**, 3167-3192 (2011).

[27] O. C. Compton, S. T. Nguyen, Graphene oxide, highly reduced graphene oxide and graphene: versatile building blocks for carbon-based materials, *Small* **6**, 711-723 (2010).

[28] Y. Zhu, S. Murali, W. Cai, Y. Li, J. W. Suk, J. R. Potts, R. S. Ruoff, Graphene and graphene oxide: synthesis, properties and applications, *Adv. Mater.* **22**, 3906-3924 (2010).

[29] H. Bai, C. Li, G. Shi, Functional composite materials based on chemically converted graphene, *Adv. Mater.* **23**, 1089-1115 (2011).

[30] Y. Sun, Q. Wu, G. Shi, Graphene based new energy materials, *Energy Environ. Sci.* **4**, 1113-1132 (2011).

[31] D. Chen, H. Feng, J. Li, Graphene oxide: preparation, functionalization, and electrochemical applications, *Chem. Rev.* **112**, 6027-6053 (2012).

[32] C. Mattevi, G. Eda, S. Agnoli, S. Miller, K. A. Mkhoyan, O. Celik, D. Mastrogiovanni, G. Granozzi, E. Garfunkel, M. Chhowalla, Evolution of Electrical, Chemical, and Structural Properties of Transparent and Conducting Chemically Derived Graphene Thin Films, *Adv. Funct. Mater.* **19**, 2577-2583 (2009).

[33] S. Pei, H.-M. Cheng, The reduction of graphene oxide, *Carbon* **50**, 3210–3228 (2012).

[34] Y. Shao, J. Liu, Y. Wang, Y. Lin, Novel catalyst support materials for PEM fuel cells: current status and future prospects, *J. Mater. Chem.* **19**, 46-59 (2009).

[35] J. Cao, Y. Wang, P. Xiao, Y. Chen, Y. Zhou, J.-H. Ouyang, D. Jia, Hollow graphene spheres self-assembled from graphene oxide sheets by a one-step hydrothermal process, *Carbon* **56**, 383-391 (2013).

[36] N. Brun, K. Sakaushi, L. Yu, L. Giebeler, J. Eckert, M. M. Titirici, Hydrothermal carbon-based nanostructured hollow spheres as electrode materials for high-power lithium–sulfur batteries, *Phys. Chem. Chem. Phys.* **15**, 6080-6087 (2013).

[37] L. Li, G. Wu, G. Yang, J. Peng, J. Zhao, J.-J. Zhu, Focusing on luminescent graphene quantum dots: current status and future perspectives, *Nanoscale* **5**, 4015-4038 (2013).

[38] W. Kwon, S. Do, J. Lee, S. Hwang, J. K. Kim, S.-W. Rhee, *Chem. Mater.* **25**, 1893-1899 (2013).

Section 1

Methods and Experimental Setup

Chapter 1.1
Surface Science Experimental Setup

The techniques used in *Surface Science* need to operate in *Ultra-High Vacuum* (UHV), to avoid *contamination of the sample* and *scattering of X-rays and electrons* with gas molecules [1,2]. Vacuum is considered ultrahigh when pressure is lower than 10^{-8} mbar [2]. Such a low pressure guarantees that the impurity level inside the vacuum chamber is sufficiently low to prepare samples with negligible contaminations. The UHV environment is obtained using high density stainless steel chambers and several pumping stages, including ion and turbomolecular pumps.

1.1.1 XPS, STM and UPS experimental equipment

The surface science experiments were performed using two different UHV systems, both owned by the *Surfaces and Catalysts Group* in Padova. The XPS-STM experiments were carried out in a multi technique UHV chamber (Figure 1.1), equipped with a 4 degree of freedom (x, y, z and polar angle θ) manipulator and the possibility to heat the sample up to 1000 K and down to 100 K, an high sensibility QMS, a four grid rear-view LEED, a double anode (Mg/Al) X ray source interfaced with a 5 channeltron electron hemispherical analyzer, two e-beam water-cooled evaporators and a cold cathode ion gun. STM experiments were performed in a second chamber connected to the first one described above. Figure 1.2 reports an inside view of the STM chamber and of the STM head-sample holder assembly.

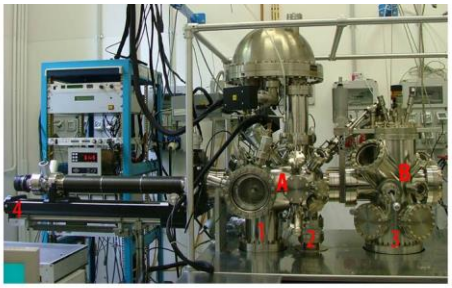

A. Preparation Chamber (UHV: 5.0 10^{-9} mbar, *RHK Technology UHV-750*)
B. STM/AFM Chamber (UHV: 6.5 10^{-11} - 1.0 10^{-10} mbar, *RHK Technology UHV-750 / SPM1000*)

1. Conductance to prep-chamber ionic pump (*VARIAN Diode Ion Pump*)
2. Conductance to prep-chamber turbomolecular pump (*PFEIFFER VACUUM TPH 180 HM*)
3. Conductance to analysis-chamber ionic pump (*VARIAN Diode Ion Pump*) / TSP (Titanium Sublimation Pump, *TiTan Gamma Vacuum*)
4. Manipulator (*VG Scienta*)
5. Ion Gun (*Omicron ISE 5 Ion Source*)
6. Photoelectron analyser (*Omicron EA 125 Energy Analyser*)
7. LEED (Low Energy Electron Diffraction, *Omicron SpectaLeed*)
8. Electron-Beam Evaporator (*Specs EBE-4*)
9. X-Ray Source (*Omicron DAR 400* double anode Al-Mg, maximum power 300W) Operating conditions: ΔV=15KV, emission current=20mA.
10. RGA QMS (Residuals Gas Analyser Quadrupole, *Extorr RGA XT100*)
11. Load Lock or Fast Entry (HV: 5.0 10^{-7} mbar)

Figure 1.1. XPS-STM equipment.

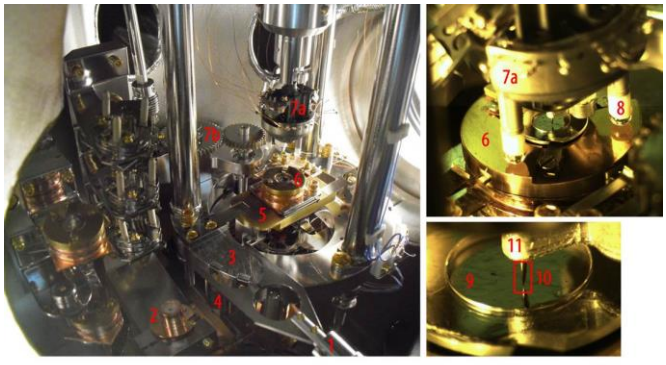

1. Wobble stick for sample handling
2. Tip conditioning (via e-beam heating) stage
3. Chassis
4. Damping magnets
5. STM/AFM stage (suspended and uncoupled from the chassis by damping magnets)
6. Sample holder
7a. STM/AFM scan head
7b. Gearing system for the STM/AFM head handling
8. Piezoelectric crystal
9. HOPG sample
10. STM Scan Tip (Pt-Ir 80:20)
11. Tip holder

Figure 1.2. Inside view of STM chamber and of the sample holder-tip assembly.

Sample heating is performed by electron-beam bombardment. As reported in Figure 1.3, the filament contacts connect the external current generator to a thoriated-tungsten coil, placed in a pocket inside the copper body of the sample holder and grounded to the earth potential; when a current (1.5-2.5 A) flows through the filament a high temperature can be reached, allowing the filament to emit electrons by the *Richardson-Hushley effect*. Such electrons are subsequently accelerated on to the sample by the high voltage applied through the bias contact (which is also used to polarize the sample during STM experiments).

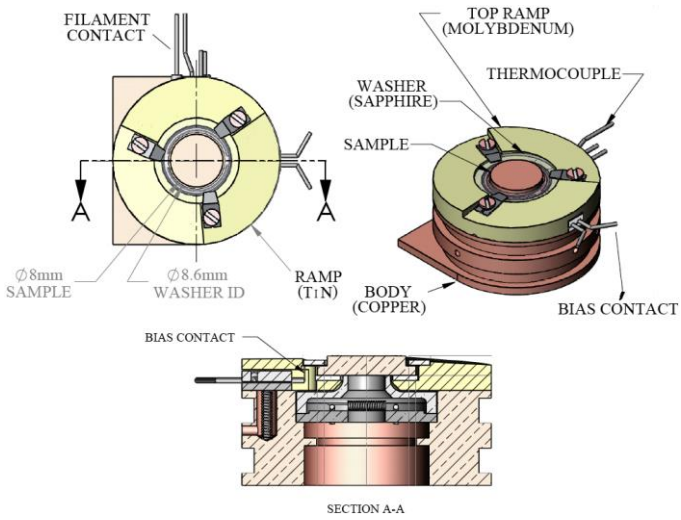

Figure 1.3. Schematic drawing of the sample holder.

The XPS and UPS experiments were performed in a second multi technique UHV chamber (Figure 1.4) equipped with a 5 degree of freedom (x, y, z, polar angle θ and azimuthal angle φ) manipulator and the possibility to heat the sample up to 1000 K, a four grid rear-LEED, a double anode (Mg/Al) X ray source interfaced with a 5 channeltron electron hemispherical analyzer, an UV radiation source (used for UPS, He I and He II photon excitation energies), two e-beam water cooled evaporators, a QMS for the residual gas analysis and a cold cathode ion gun.

1. Load lock
2. Load lock manipulator (2 DOF)
3. Main manipulator (5 DOF)
4. Preparation chamber
5. Analysis chamber
6. LEED (*Omicron SpectaLEED*)
7. Evaporators (*Tectra*)
8. Ion Gun (*Omicron ISE 5*)
9. Helium UV source (*VG MK II*)
10. X ray source (*PSP TX 400*)
11. Photoelectron analyzer (*VG MK II*)

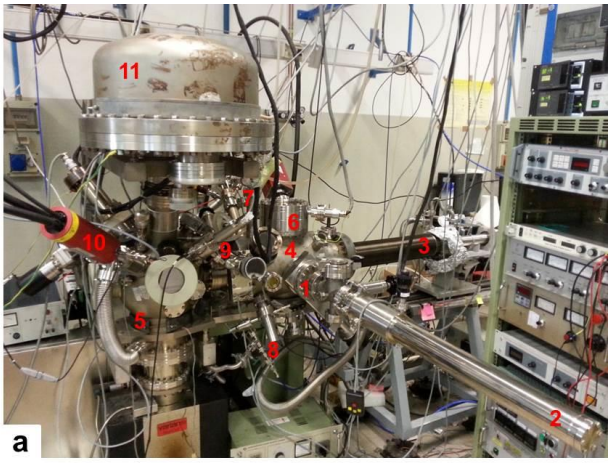

12. Azimuthal angle handling
13. Manipulator (x,y,z and θ DOF)
14. Manipulator head and filament housing
15. Sample holder

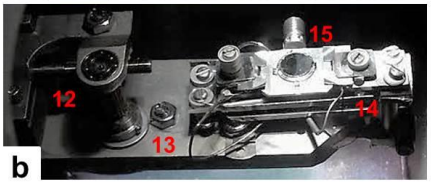

Figure 1.4. XPS-UPS equipment.

Table 1.1 reports the energies and the FWHM of the X ray and UV lines commonly used in the PES-UPS experiment.

Table 1.1. Characteristic lines used in PE and UPS.

	Energy (eV)	**FWHM (eV)**
Mg Kα	1253.601	0.711
Al Kα	1486.712	0.861
He I	21.220	0.055
He II	40.801	0.052

1.1.2 SEM experimental equipment

The SEM measurements were performed using a Zeiss Supra 35VP set up (Figure 1.2), equipped with a 4 degree of freedom (x, y, z and polar angle θ) sample stage, 5 different Everhardt-Thornley based *scintillator-photomultiplier detectors* (secondary electron detector, InLens secondary electron detector, STEM, back scattering and X-ray detectors) and a Schottky Field Emission Gun (FEG). In the Schottky type electron guns, in which thermionic emission is enhanced by barrier lowering in the presence of a high electric field, the emitters are made by coating a sharp tungsten tip with a layer of zirconium oxide, which has the peculiar property of increasing in electrical conductivity at high temperature [3].

At the usual experimental conditions[1], the spatial resolution was about 2.0 nm.

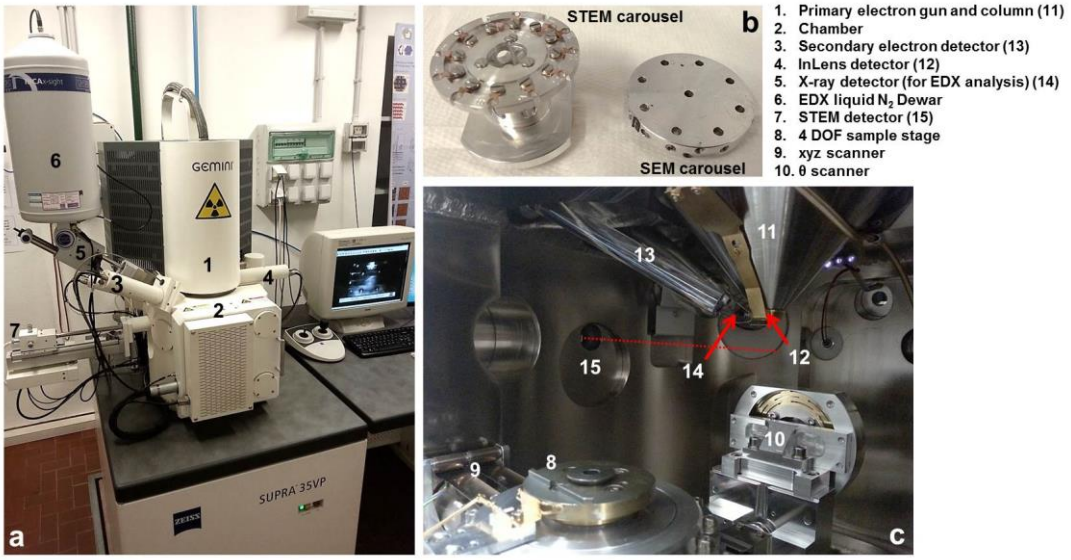

Figure 1.5. a: Zeiss Supra 35VP SEM set up used in the thesis work, equipped with EDX detector cooled at liquid nitrogen (~80K, Oxford Instruments INCA 200); b: different type of sample holders; c: inside view of the main chamber.

[1] Primary electron kinetic energy: 5÷10 keV, beam current ~ 10 nA, InLens detector, p~10^{-7} mbar.

REFERENCES

[1] J. T. Yates Jr., *Experimental Innovations in Surface Science*, Springer-Verlag, 1998.

[2] P. A. Redhead, J. P. Hobson, E. V. Kornelsen, *The Physical Basis of Ultrahigh Vacuum*, AVS Classics, 1997.

[3] W. Zhou, Z. L. Wang, *Scanning Microscopy for Nanotechnology: Techniques and Applications*, Springer, 2006.

Chapter 1.2
Surface Science Methods

1.2.1 Ion implantation

Ion implantation was carried out using an ion gun where the precursor gas (in this work Ar or N_2) was fed directly in an ionization chamber (*cold cathode ion source*). High voltage (typically 5 kV) was applied between anode and cathode to initiate and sustain the gas discharge. The longitudinal magnetic field in the source region induced a spiral path in the discharge-generated electron (at typical current about 1mA) which enables them to cause large secondary ion and electron generation. The ions are then accelerated at the anode potential, which is finally the beam energy (tunable between 100 eV and 3.5 keV) relative to the sample grounded to the earth potential. The ions are extracted from the gas cell through a circular aperture in the cathode plate into the flight tube; here, double electrostatic lenses allows the focusing of the ion beam on to the sample surface.

The interactions between charged particles and matter (electrons and nuclei) can be described through the concept of *scattering cross section* [1,2]:

$$\sigma(\theta) = -\frac{b}{\sin(\theta)}\frac{db}{d\theta} \quad , \tag{2.1}$$

which is a function of the scattering angle between the incidence direction and the scattering direction, while b is a phenomenological parameter known as *impact parameters*. The Figure 2.1 reports a schematization of the scattering geometry.

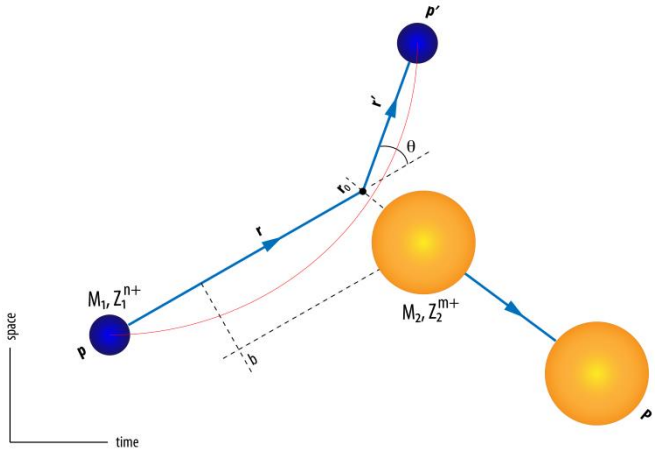

Figure 2.1. Particle trajectories and collision geometry in the center of mass reference system.

The total cross section of the collision event is given by the integration of the *differential cross section* $d\sigma/d\Omega$ over the solid angle Ω:

$$\sigma(\theta) = \int_{\Omega} \frac{d\sigma}{d\Omega} d\Omega \qquad (2.2)$$

The differential cross section defines the ratio of the *number of particles scattered into the infinitesimal solid angle to the incident flux per unit time.* In this way, the *cross section* is a quantity that is related to the *scattering event probability*.

To obtain the differential cross section for each scattering event, the Schrödinger equation must be resolved within the *adiabatic approximation* [1], which considers only the initial and final particle states. Then, the wave function of a free charged particle before the close-encounter event with electrons or nuclei of matter is simply an *eigenstate of the momentum* ($\mathbf{p} = \hbar\mathbf{k}$). The relative eigenfunction is [1]:

$$|\mathbf{k}| = \sqrt{\frac{2m_e\hbar^2}{E}} \; . \qquad (2.3)$$

With the Green's function formalism [1,2], it is possible to verify that the *state of the scattered* particle (that is after the interaction), *far from the scattering point*, is described by a superposition of the initial state (impulse eigenstate) and final state, resulting in a spherical damped wave (by the term r^{-1}) weighted by the *scattering amplitude* $f(\mathbf{k}', \mathbf{k})$ ($|\mathbf{k}'| = \sqrt{2m_e\hbar^2/E'}$, $\mathbf{p}' = \hbar\mathbf{k}'$):

$$(2.4) \qquad \psi_{SCAT}(\mathbf{k}',\mathbf{k},\mathbf{r}) = f(\mathbf{k}',\mathbf{k})\frac{e^{i\mathbf{k}\cdot\mathbf{r}}}{r}$$

Since the number of the interacting particles with the system must be conserved, it is possible to demonstrate that [1,2]:

$$(2.5) \qquad \frac{d\sigma}{d\Omega} = \left| f(\mathbf{k}',\mathbf{k}) \right|^2$$

To evaluate the scattering amplitude, this is possible to use the *Born' approximation* (first order on potential energy). In this way, the scattering amplitude is given by [1,2]

$$(2.6) \qquad f(\mathbf{k}',\mathbf{k}) = -\frac{\mu}{4\pi(2\pi\hbar)^{3/2}}\int_{\in^3} e^{i(\mathbf{k}-\mathbf{k}')\mathbf{r}'}V(\mathbf{r}')d^3r'$$

This equation has a crucial importance, because it allows the calculation of the differential cross section for each scattering event, simply by the knowledge of the interaction potential between incident particles and target. Moreover, the Born' approximation shows that *the scattering amplitude* (and then the differential cross section by equation 2.5) *can be derived simply taking the Fourier transform of the interaction potential that leads to the scattering event*.

An ion retains most of the chemical properties of the original atom. After it has been injected into the lattice, it may recombine or remain ionized. A third option, usually the most probable with chemically active ions such as B^+, N^+ or O^{2+}, is the direct chemical interaction between the ion and the matrix, with the consequent formation of new chemical bonds between the implanted ion and the surrounding target atoms [3,4]. The chemical interactions between the implanted ions and the matrix can be tuned by tuning the temperature of the subsequent thermal annealing that it is usually performed after the implantation process [3,4]; the thermal annealing step allows to induce a wide formation of chemical bonds between the target and the implanted atoms, and also the recovering of the structure of the target lattice [3,4]. Figure 2.2 shows a cross sectional view of a gold single crystal after ion implantation with Ar^+ at 1.0 keV, as-implanted and after thermal annealing at 500°C.

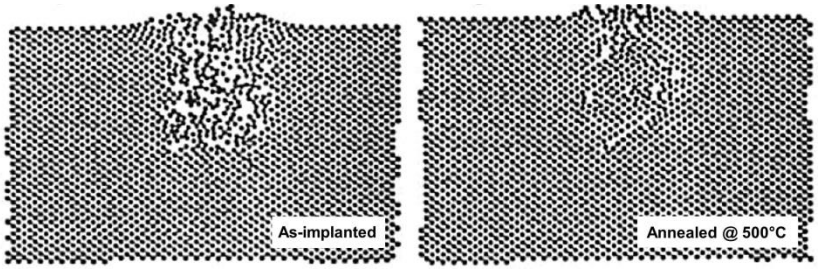

Figure 2.2. Cross sectional view of a gold single crystal after ion implantation with Ar^+ at 1.0 keV, based on a molecular dynamics calculation. Left: as-implanted. Right: after thermal annealing at 500°C (taken from ref. 3).

Since ion is electrically charged, it can be accelerated to any desired velocity and electrically deflected and focused; thus, an ion beam can be used to dope only in a tiny volume of material. Ion implantation has several advantages, the most important of which are [3,5]:

- doping levels can be precisely controlled, since the *incident ion beam can be measured accurately as an electrical current;* doping uniformity across a surface can be accurately controlled too;
- the depth profile can be finely tuned by tuning the incident ion energy;
- it is a low-temperature process. This feature is not necessarily important with HOPG as in this work, but some semiconductor compounds are unstable at high temperatures;
- extreme purity of the dopant (since their precursors usually are gas species) can guarantee chemical selective doping.

In the ion implantation process, atoms of the desired doping element are ionized, accelerated at the working implantation energy and then focused on the sample surface. Due to their momentum, the incident ions cause several secondary events in the sample; Figure 2.3a shows the principal secondary events that occurs during the ion beam-surface interaction.

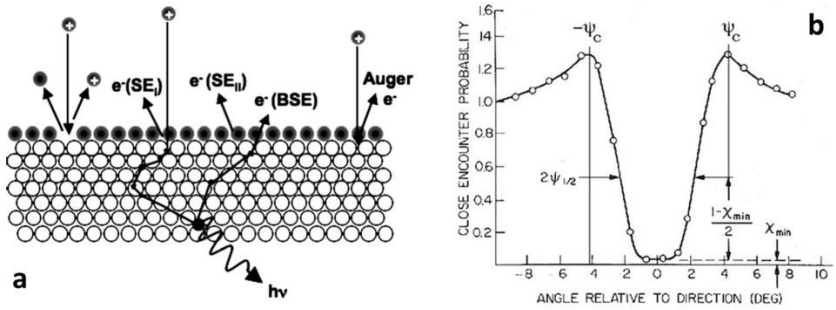

Figure 2.3. a: elastic and inelastic collision events that occur at the surface of a sample exposed to a primary ion beam (SE_I: primary electron emission; SE_{II}: secondary electron emission excited by the E_I; BSE: backscattered electron emission; hν= X-ray fluorescence induced by the primary ions or by primary-secondary electrons); b: typical channeling "dip".

The total distance that an ion travels before coming to rest is called its range (R); *the projection of this distance onto the direction of incidence is called the projected range* (R_p). The doping profile is characterized by the projected range and its *standard deviation* ΔR_p. If the target is not aligned in a major crystallographic direction with the ion beam, dopant concentration profiles resulting from implantation are nearly *Gaussian in shape*. The dopant concentration as a function of the distance from the surface is given as [5,5,5]:

$$(2.7) \qquad N(z) = N_{\max} \exp\left[-\frac{(z-R_p)^2}{\Delta R_p^2}\right], \quad N_{\max} = \frac{N_p}{2.5\Delta R_p}$$

N_p is the number of implanted atoms per unit surface (cm^{-2}).

Under certain experimental conditions, such as the use of well-collimated ion beams aligned toward a channel (crystallographic directions in which open spaces exist among the rows or planes of atoms), the incident ions are able to deeply penetrate in to the crystal lattice before coming to rest in interstitial or substitutional sites. This is a well-known phenomenon called *channelling*. The directions that allow large fraction of ion channelling are limited. When the crystal is examined from other directions than along a channel or plane, the atoms appear in a random configuration, roughly as in a dense atomic gas. This phenomenon is very pronounced when the incidence angle approaches the critical angle, as shown in Figure 2.3b. It is possible to see that in proximity of the critical angle the close encounter probability has two symmetric maxima. The minimum values of the close encounter probability between

the two maxima indicates the incidence angles that lead to ion channelling. However, even when ions are injected along a non-channelling direction, it is difficult to completely prevent some ion channelling. To conclude, the penetration depth and the final distribution of the ions in the crystal depend on the ion energy, on the atomic mass of the target atoms and on the angular alignment of the ion beam with the crystal axis.

1.2.2 X-Ray Photoelectron Spectroscopy (XPS)

X-ray photoelectron spectroscopy is a powerful surface technique to measure the binding energies (BE) of electrons in matter. This technique, based on the *photoelectric effect* explained by Einstein in 1905 [6], was developed during the 60's of the last century by K. Siegbahn and his research group (for this application of the photoelectric effect Siegbahn was awarded with the Nobel Prize in Physics in 1981). Figure 2.4 depicts a schematic representation of the XPS experimental setup usually adopted in surface science studies.

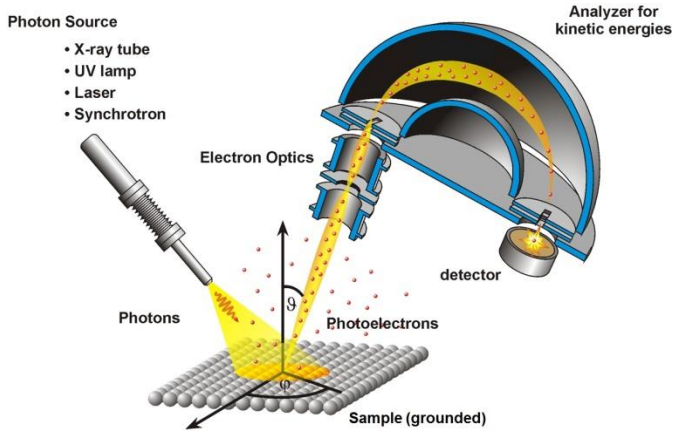

Figure 2.4. Schematic representation of the XPS setup.

When a sample is irradiated with X-rays, the photon energy is partially used to ionize the atom, while the rest is given as kinetic energy (KE) to the photoelectrons that are emitted from the sample. Since the *energy is conserved*, the KE of the photoelectrons is related with the BE and to the X-rays energy ($h\nu$) by the formula [8,7]

$$\text{KE} = h\nu - \text{BE} \qquad (2.8)$$

The electron hole that remain in the atomic level that has been ionized by the interaction with the X-ray photon is refilled with a second electron of higher energy; the energy relaxations takes place through two different processes: the first one is the re-emission of a X-ray photon (known as X-ray fluorescence), while the second is the Auger emission [7,8]. Figure 2.5 shows these two different processes. The X-ray fluorescence and the Auger emission are competitive processes; the first has a higher cross section than the second for "heavy" elements (Z>35), while the second is

favourite for "light" element (Z<35). Figure 2.5 shows a pictorial view of the possible relaxation processes.

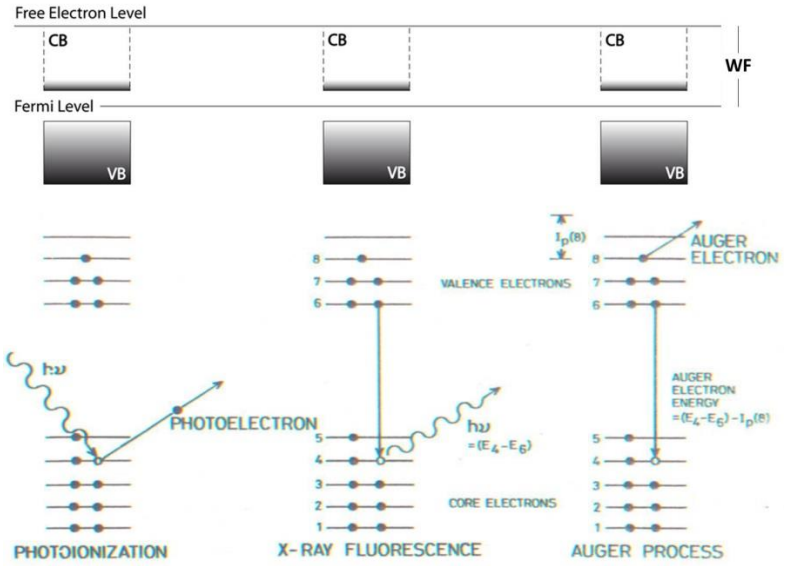

Figure 2.5. Different relaxations (X-Ray fluorescence and Auger emission) after the photoionization process (adapted from ref. 8).

Therefore, if *hv* and BE are known, it is possible to predict the KE of the emitted photoelectron. Relation (2.8) has the vacuum level as reference; on the other hand, since the sample is electrically connected with the spectrometer, it is necessary to include in (2.8) the *work function of the spectrometer* (Φ_{spect}) [7]. In this way, it becomes:

$$(2.9) \qquad KE = hv - BE - \Phi_{spect}$$

Under a Hartree-Fock representation, the system wave function can be expressed by a single Slater determinant [9], built up with one-electron orbitals, which can be represented as a linear combination in a vector space defined by an orthonormal base. The appropriate expression of that linear form can be found with the lagrangian functional under the orbital orthonormalization constraint, using the variational principle to calculate the indeterminate Lagrange coefficients λ_I [9]. Within this eigenstate representation, each discrete BE value corresponds to the ionization energy of the single one-electron level that originates the photoemission event: in other words, given a N-electron Hartree-Fock single determinant $\left|{}^{N}\Psi_0\right\rangle$ with occupied spin-orbital ζ having an energy ε_0^{ζ}, the ionization potential to produce an

(N-1)-electron single determinant $\left|{}^{N-1}\Psi_i\right\rangle$ with identical spin-orbitals system (*Sudden Approximation*), merely obtained by removing an electron from spin-orbital ζ, is just $-\varepsilon_0^{\zeta}$ (BE) (*Koopman's one-electron approximation theorem*) [8,9,10,11].

The analyzer can discriminate between the different photoelectron energies, giving a spectrum of *intensity* (counts per second) versus BE.

Initial State Effects are caused by chemical bonding, which influences the electronic configuration in and around the atom [7,11,11]. Thus, the energetic shift caused by the initial state effects is known as *chemical shift*.

Final State Effects in the PES spectra deserve a different discussion, based on many-body interaction approach [10,11].

By using Fermi's golden rule as a result of first order perturbation theory within a many-body description of the photoemission process, the total photoemission current is given by [10,11]:

$$J_k(h\nu)=\frac{2\pi}{\hbar}\sum_s\left|\left\langle {}^{N-1}\Psi_{\mathbf{K}}^s\left|\hat{H}_{PE}\right|{}^{N}\Psi_0\right\rangle\right|^2\delta(\varepsilon_{\mathbf{K}}-\varepsilon_s-h\nu) \quad , \tag{2.10}$$

with $\left|{}^{N}\Psi_0\right\rangle$ N-electron *initial state* (having an energy equal to ε_0), $\left\langle {}^{N-1}\Psi_{\mathbf{K}}^s\right|$ is the *final state* which is constituted of N-1 electron system $\left|{}^{N-1}\Psi_i^s\right\rangle$ with *s*-excitation channel (*i* stays for "ionized") and of an outgoing spherical damped wave $|\mathbf{K}\rangle$ (impulse eigenstate), that is the photoemitted electron with kinetic energy $\varepsilon_{\mathbf{K}}=\hbar^2K^2/2m_e$ (so, $\left|{}^{N-1}\Psi_{\mathbf{K}}^s\right\rangle=\left|\mathbf{K},{}^{N-1}\Psi_i^s\right\rangle$). Finally, $\varepsilon_s=\varepsilon^s(N-1)-\varepsilon_0$, with the *s* index that refers to a set of quantum numbers that contains all possible excitations of the final state, such as electron–hole pairs generation and multiple excitations). $\hat{H}_{PE}$ is the perturbation hamiltonian that describes the interaction of the radiation with the matter. The field-electron interaction Hamiltonian (perturbation Hamiltonian) is given by [11,12,13]:

$$\hat{H}_{PE}=\frac{1}{2}\left(\mathbf{A}\cdot\hat{\mathbf{p}}+\hat{\mathbf{p}}\cdot\mathbf{A}\right) \quad , \tag{2.11}$$

where $\hat{\mathbf{p}}=-i\hbar\vec{\nabla}$ is the linear momentum operator, while $\mathbf{A}$ is the vector potentials which is define, together with the scalar potentials φ *Lorentz' electromagnetic*

gauge. From Maxwell's electromagnetic field equations, since $\mathbf{E} = -\frac{\partial \mathbf{A}}{\partial t} - \vec{\nabla}\varphi$ and $\mathbf{B} = \vec{\nabla} \times \mathbf{A}$, it is possible to fixed the *Lorentz' gauge condition* [12] $\vec{\nabla} \cdot \mathbf{A} + \varepsilon_0 \mu_0 \frac{\partial \varphi}{\partial t} = 0$ (it is necessary because φ is invariant under an addition of an arbitrary constant while $\mathbf{A}$ is invariant under an addition of a vectorial field built taking the gradient of a scalar field). The perturbation Hamiltonian that describes the field-charge interaction is often simplified to $\hat{H} = \mathbf{A} \cdot \hat{\mathbf{p}}$ [11,12,13], assuming that $\hat{\mathbf{p}} \cdot \mathbf{A} \cong \vec{\nabla} \cdot \mathbf{A} \approx \mathbf{0}$: *spatial variations of the radiation field is small on the atomic scale*. While this is a plausible assumption deep in the bulk, this is not true for variations of **A** across the surface barrier due to the rapid change in the dielectric response of the solids; this causes the so-called *surface photoelectric effect*, which has been shown to play a non-negligible role in photoemission from simple metals [14]. To obtain a many-body description of the photoelectron emission process, the interaction operator must be expressed in the following form [11,13]:

$$\hat{H}_{PE} = \sum_{i=1}^{N} \mathbf{A}(\mathbf{r}_i) \cdot \hat{\mathbf{p}}_i \quad , \tag{2.12}$$

where the index *i* sums over all electrons in the solid.

By using the *second quantization formalism*, the final state $\left| {}^{N-1}\Psi_{\mathbf{K}}^{s} \right\rangle$ can be written as following [11,13]:

$$\left| {}^{N-1}\Psi_{\mathbf{K}}^{s} \right\rangle = \left| \mathbf{K}, {}^{N-1}\Psi_{i}^{s} \right\rangle = \hat{c}_{\mathbf{K},s}^{+} \left| {}^{N}\Psi_{0} \right\rangle \quad , \tag{2.13}$$

with $\hat{c}_{\mathbf{k},s}^{+}$ is the *photoelectron creation operator*.

This involves two approximations:

- it is assumed that the photoelectron decouples from the core hole immediately after the excitation (*Sudden Approximation*) and carries thus no information about the relaxation of the (*N*-1)-electron excitation. *The Sudden Approximation is increasingly accurate the faster is the photoelectron that escapes from the excitation region* [11].
- it is also neglects inelastic scattering of the photoelectron on its way from the excitation to the surface, which can lead to *extrinsic loss features in the*

spectrum (such as electron-plasmon interactions in metals, or the σ→π* transition that occurs in graphite).

Expressing the interaction operator in second quantization by $\hat{H}_{PE}\hat{c}^{+}_{\mathbf{k},s}\hat{c}_0$ and keep into account the equation (2.10), the photoemission current becomes [11,13]:

$$J_{\mathbf{K}}(h\nu)=\frac{2\pi}{\hbar}\sum_i\left|\Delta_{\mathbf{K},\mathbf{K}}\right|^2 A^{<}_{\mathbf{k_i}}\left(\varepsilon_{\mathbf{k_i}}-h\nu\right) \quad , \tag{2.14}$$

with

$$\Delta_{\mathbf{K},\mathbf{K}}=\langle\mathbf{K}|\hat{H}_{PE}|\mathbf{K}\rangle \tag{2.15}$$

matrix element for the photoemission process, while

$$A^{<}_{\mathbf{k_i}}\left(\varepsilon_{\mathbf{k}_i}-\hbar\nu\right)=\sum_s\left|\left\langle {}^{N-1}\Psi^{s}_{\mathbf{K}}\left|\hat{c}^{+}_{\mathbf{K},s}\right|{}^{N}\Psi_0\right\rangle\right|^2\delta(h\nu-\varepsilon_s) \tag{2.16}$$

is the *one-electron spectral function* [11,13].

The one-electron spectral function is related to the single-particle *Green's function*, a key quantity in the many-body theoretical description of an interacting electron system [13], by $A^{<}_{\mathbf{k_i}}\left(\varepsilon_{\mathbf{k}_i}-\hbar\nu\right)=\frac{1}{\pi}\Im m\left[G\left(\mathbf{k}_i,\varepsilon_{\mathbf{k}_i}-i0^{+}\right)f(\varepsilon_{\mathbf{k}_i},T)\right]$, with $f(\varepsilon_{\mathbf{k}_i},T)$ Fermi-Dirac function [13]. $A^{<}_{\mathbf{k_i}}\left(\varepsilon_{\mathbf{k}_i}-\hbar\nu\right)$ gives *the probability that an electron of wave-vector* $\mathbf{k}_i$ *and energy* $\varepsilon_{\mathbf{k}_i}$ *can be removed from the interacting electron system*.

The many-body effects or, with more detail, *the Final State Configuration Interaction* (FSCI, such as e^{-}-e^{-} and e^{-}-h^{+} interactions) *are taken into account in the spectral function* [15,13]. For example, the spectral function for the description of low-energy electron–hole excitations in the conduction band gives an asymmetric peak; this is the well-known *Mahan–Doniach–Šunjić (MDS) shake up lineshape* (intrinsic feature), which can be observed in metal system [11]. Other final state many-body effects are important and have a great influence on the XPS spectra. In particular, *relaxations* or *charge distribution rearrangements* have a relevant importance to shift the binding energy with respect to what is predicted by the Koopman's theorem-Sudden approximation coupling [11].

Most of the atomic relaxation results from rearrangement of outer shell electrons. Inner shell electrons of higher binding energy make a small contribution [8,11]. The

nature of a material conductivity determines the nature of extra-atomic relaxation. In conductors such as metals, valence electrons are free to move from one atom to a neighbour to screen the hole created by photoionization. In an insulator, electrons do not possess such mobility. They react by being polarized by the core hole. Hence, the magnitude of the extra-atomic relaxation in metals (as much as 5-10eV) is greater than that of insulators [11,11].

The intensity dN_K (*number of photoelectron that hit the detector per unit time and per unit energy*) of a photoelectron peak that has been generated from k levels localized in the infinitesimal volume element dt = dx dy dz, can be evaluated through the following equation [7,15]:

$$dN_k = I_0 \exp\left(-\frac{z}{\Lambda_X \sin\phi}\right)(\rho(z)dxdydz)\left(\frac{d\sigma_k}{d\Omega}\Omega(E_k,\theta,x,y)\right)\exp\left(-\frac{z}{\Lambda_e \sin\theta}\right)D_0(E_k) \quad (2.17)$$

where $I_0 \exp\left(-\frac{z}{\Lambda_X \sin\phi}\right)$ is the exponential law that describes the x-ray intensity attenuation occurring during the path from the sample surface to the volume element dx dy dz; L_X is the *inelastic x-ray attenuation length*; $\rho(z)dxdydz$ is the local material density at depth equal to z in the element volume dx dy dz, while $\frac{d\sigma_k}{d\Omega}\Omega(E_k,\theta,x,y)$ is the *probability that an electron that escapes from a plane positioned in x,y with a trajectory forming an angle q from the sample surface and generated from the k level having binding energy* E_k *can be emitted within the analyser acceptance solid angle*. The differential cross section can be finally evaluated by the following expression [7,15]:

$$\frac{d\sigma_k}{d\Omega} = \frac{\sigma_{nl}(E_k)}{4\pi}\left[1-\frac{1}{2}\beta_{nl}(E_k)\left(\frac{3}{2}\cos^2\alpha-\frac{1}{2}\right)\right] \quad (2.18)$$

The total photoionization cross section, obtainable simply by integration of the 2.18 and tightly correlated to Δ_{kk} [10,11], is defined as the *ratio between the number of the electrons emitted per unit time and the number of X-photons incident per unit time and unit surface*; finally, $\beta_{nl}(E_k)$ is the asymmetry parameter that characterizes the angular distribution of photoemitted electrons, while α is the angle formed

between the X-ray propagation direction and the direction of photoemitted electron detection.

$exp\left(-\frac{z}{\Lambda_e \sin\theta}\right)$ is the sampling depth, that depends on the electron kinetic energy, while Λ_e is the *inelastic electron attenuation length* Λ_e. The photoelectron waves are directly attenuated by inelastic scattering: the factor $-z/\sin\theta$ is the length covered by the photoelectrons. It is possible to demonstrate that, for a fixed θ, the 65%, 86% and 95% of the signal comes from a depth of about Λ_e, $2\Lambda_e$ and $3\Lambda_e$, respectively [7,15]. The trend of the inelastic mean free path for the photoelectron is reported in the Figure 2.6, as function of the kinetic energy.

Since the actual sampled depth is inversely proportional to $\sin\theta$, the surface sensitivity of XPS can be enhanced by detecting the photoelectrons at an angle far from the surface normal; in this way, they have to travel a longer path inside the material before being expelled from the surface.

Finally, $D_0(E_k)$ is the experimental detection efficiency of the detector apparatus.

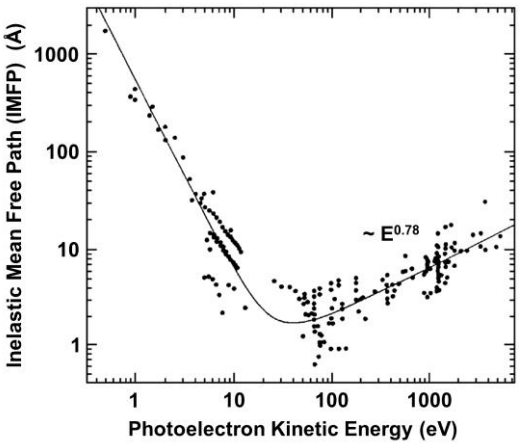

Figure 2.6. Λ_e trend for some elements as function of the photoelectron kinetic energy.

In a typical XPS spectrum, the peaks are usually labelled with the quantum number of the orbital from which the electron was emitted. A peak is identified with nl_j, where n is the *principal quantum number* and identifies the level of the orbital from which the electron has been emitted (n=1, 2,…), while l corresponds to the *secondary quantum number* (l = 0÷n-1, with 0 = s, 1 = p, 2 = d, 3=f…) that indicates the angular momentum of the orbital. Finally, j is the total quantum number ($j=|l \pm s|$, $s=\pm½$) in the $l+s$ coupling representation.

The spin-orbit interaction energy can be evaluated introducing in the hamiltonian of the system an additional term, in the following form [11,15]:

$$E_{SO} = \xi_{nl}\left(j^2 + l^2 + s^2\right) \qquad (2.19)$$
$$\xi_{nl} = \frac{e^2}{16\pi\varepsilon_0 m^2 c^2}\frac{1}{\left\langle r^3\right\rangle} \text{ (spin orbit coupling constant)}$$

So, it is possible to calculate the influence of the spin-orbit coupling on the photoemission peak shape:

l=0 : $\Delta E_{SO}\big|_{j=\pm 1/2}^{l=0,\, s=\pm 1/2} = 0$ → no splitting, *s* core level;

l=1 : $\Delta E_{SO}\big|_{j=1/2,\,3/2}^{l=1,\, s=\pm 1/2} = 2\xi_{nl}$ → *p* orbital, l = 1 is split in to two peaks, one with j = |1 + 1/2| = 3/2 and one with j = |1 – 1/2| =1/2. These two components will have an energy difference depending upon the spin-orbit coupling constant; furthermore, the relative intensity of the two components of the doublet depends on the ratio of their degeneration [15,15]:

$$R_{SO} = \frac{2j_{s=+1/2}+1}{2j_{s=-1/2}+1} \qquad (2.20)$$

It is important to highlight that this phenomenology is valid for all l values ≠ 0 (that is *p*, *d*, *f* … orbitals). Finally, the width of photoemission peak is determined to a large extent by the lifetime of the excited hole (*homogenous broadening*) and instrumental resolution. The instrumental resolution is determined not only by the energy analyser resolution ($\Delta E_{analyser} \cong 0.25 \div 0.30 eV$), but also by the linewidth of the incident X-rays (for a non-monochromatized source, $\Delta E_{X-source} \cong 0.70 \div 0.85 eV$). Then, the FWHM of a typical XPS signal is given by the following three-components convolution (for a non-monochromatized source) [7,15]:

$$\Delta E_{peak} = \sqrt{\Delta E_{X-source}{}^2 + \Delta E_{analyser}{}^2 + \Gamma^2} \qquad (2.21)$$

Through the Heisenberg uncertainty relation, the *intrinsic peak width* Γ is inversely related to the *hole lifetime* τ [15,15]:

$$\Gamma = \frac{h}{\tau} \qquad (2.22)$$

The lifetime generally decreases the deeper is the core hole, due to the filling by higher lying electrons; then, the deeper the core hole, the more de-excitation channels are available [10,11]. Analogously, for a given energy level the lifetime decreases (the linewidth increases) as the atomic number increases. Intrinsic lifetime broadening is an example of homogenous broadening and it is characterized by a Lorentzian shape [11]. The XPS technique allows to quantify the chemical elements present in the sample; the atomic concentration of the identified element *i* is :

$$C_i^{\%} = \frac{A_i}{S_i} \frac{1}{\sum_{j \neq i}^{n} \frac{A_j}{S_j}} \cdot 100 \ , \qquad (2.23)$$

where A_i is the area below the element peak (which has been previously subjected to the subtraction of the inelastic background due to the bremsstrahlung effect), while S_i is the *sensitivity factor* which is given by [7,15]:

$$S_i = K \frac{d\sigma_k}{d\Omega} \Lambda_e \ . \qquad (2.24)$$

K is the analyzer transmittance which is a KE dipendent factor. With good approximation, its value can be taken as 1 in a BE range between 0 and 600 eV.

1.2.3 Scanning Tunneling Microscopy (STM)

Since the first successful experiments by Gerd Binnig, Heinrich Rohrer and co-workers at the IBM Zürich Research Laboratory in 1981, scanning tunnelling microscopy (STM) has developed into an invaluable and powerful surface and interface technique [16]. As a confirm of this, only five years after the first operations of STM, Binnig and Rohrer received the Nobel Prize in Physics for 1986 (together with the german physicist E. A. F. Ruska for his contributions to the development of electron microscopy). The scanning tunnelling microscopy has two main important characteristics [16]:

- It is a local probe, due to the fact that the probe is an extremely (atomically) sharp tip;
- STM is a proximal probe because of the close proximity of the probe tip and the sample surface, required for obtaining the high spatial resolution.

STM allows the probing of the surface properties of a material at high spatial resolution. Moreover, the tip can be positioned with atomic accuracy above a preselected surface site and a local experiment can be performed. This ability to perform local experiments, together with the ability to characterize non-periodic surface structures can be regarded as the main advantage of STM compared with other surface analysis techniques [16,17].

According to classical mechanics, a particle of total energy E in the region $x<0$, which is incident upon the barrier in the direction of increasing x, will have probability one of being *reflected* if $E<V_0$, and probability one of being *transmitted* into the region $x>a$ if $E>V_0$. Neither of these statements describes accurately the *quantum mechanical* results. In fact, if E is not much smaller than V_0, quantum mechanics predicts that there is a non-zero probability that the particle will be transmitted through the barrier into the region $x>a$.

The Schrödinger equation breaks up into the three separate equations for the three regions:

1. $x<0$ (left of the barrier);
2. $x>a$ (right of the barrier);

3. 0<x<a (within the barrier).

In the regions to the left and to the right of the barrier the equations are those for a free particle of total energy E. In the region within the barrier, indeed, the form of the equation, and of its general solution, depends on whether $E<V_0$ or $E>V_0$. So:

$$\text{(2.25)} \quad \begin{aligned} &\text{a.} \quad \psi(x) = Ae^{ik_I x} + Be^{-ik_I x} && x<0 \\ &\text{b.} \quad \psi(x) = Ce^{ik_I x} + De^{-ik_I x} && x>a \end{aligned} \qquad k_I = \sqrt{\frac{2m_e E}{\hbar}}$$

$$\text{(2.26)} \quad \begin{aligned} &a. \quad \psi(x) = Fe^{k_{II} x} + Ge^{-k_{II} x} && k_{II} = \sqrt{\frac{2m_e(V_0 - E)}{\hbar}}, \quad E < V_o \\ &b. \quad \psi(x) = Fe^{ik_{III} x} + Ge^{-ik_{III} x} && k_{III} = \sqrt{\frac{2m_e(E - V_0)}{\hbar}}, \quad E > V_o \end{aligned} \qquad 0 < x < a$$

In the region to the right of the barrier there can be only a transmitted wave as there is nothing in that region to produce a reflection. Thus it is possible to set D=0. However, it is not possible to set G=0, since $\psi(x)$ for $E<V_0$ cannot become infinitely large even if the increasing exponential is present. Nor it can be possible to set G=0 in the case of $E>V_0$, since $\psi(x)$ will have a reflected component in the barrier region that arises from the potential discontinuity at x=a. In matching $\psi(x)$ and $d\psi(x)/dx$ at the points x=0 and x=a, four equations in the arbitrary constants A, B, C, G and F will be obtained, with A that determines the amplitude of the wave function incident upon the barrier potential in the x<0 region. The solution of the wave equation for the barrier propagation problem is reported in the Figure 2.7.

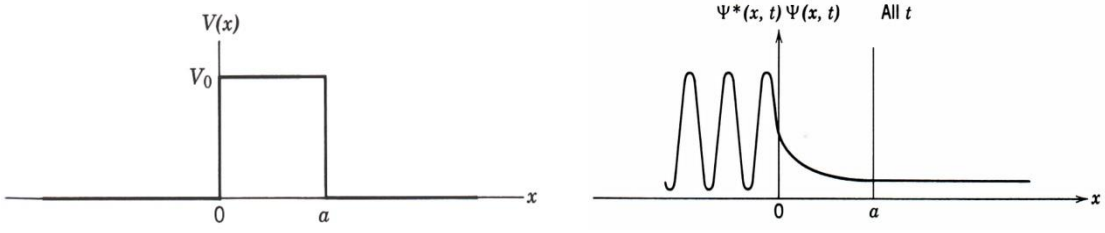

Figure 2.7. Left: schematization of the barrier potential used to model quantum tunnelling. Right: probability density function for a typical barrier penetration phenomenon (for $E<V_0$).

It is possible to demonstrate that a particle of mass m_e and total energy E, incident on a potential barrier of height $V_0>E$ and finite thickness a, has a certain probability T of penetrate the barrier and appear on the other side. This phenomenon is called *barrier*

penetration, and the particle is said to *tunnel* through the barrier. Figure 2.8a reports the reflection and the transmission coefficients.

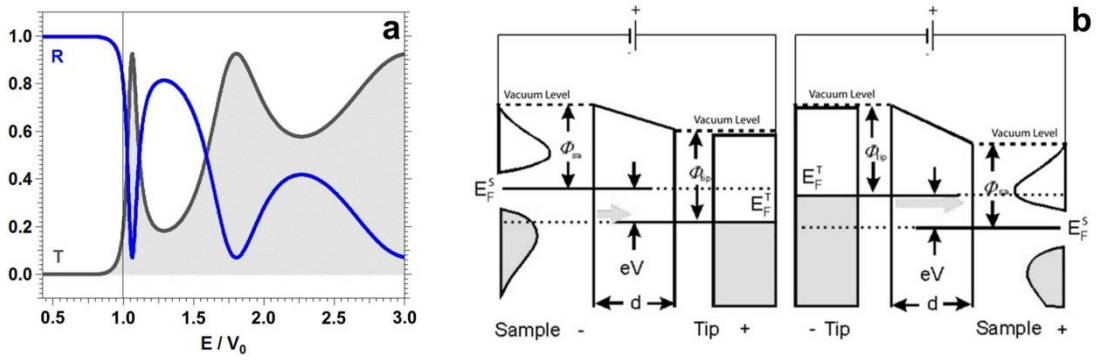

Figure 2.8. a: reflection and transmission coefficients R and T for a particle incident upon a potential barrier of height V_0 and thickness a. The abscissa E/V_0 is the ratio of the total energy of the particle to the height of the barrier; b: changes in tip-sample system energy and tunneling conditions as function of the bias polarity.

Experimental procedure consists in applying a voltage bias between sample and tip, which is brought close to the sample by some coarse sample-to-tip control, which is turned off when the tip and sample are sufficiently close. At close range, fine control of the tip in all three dimensions is typically piezoelectric, keeping a tip-sample separation W typically of about 10 Å. In this situation, the voltage bias will cause electron tunnelling between the tip and the sample, creating a current that can be measured. The influence of the bias potential on the tunnelling conditions is reported in Figure 2.8b.

The most common used mode of operation, first introduced for the STM by Binnig, Rohrer and co-workers, is the *constant current mode*. In this mode, a feedback loop system forces the tip via a piezoelectric driver to be always at a distance to the sample surface that the tunnelling current, flowing between these two electrodes, remains constant. By recording the voltage which has to be applied to the piezoelectric driver in order to keep the tunnelling current constant, i.e. recording the height of the tip z(x,y) as a function of position, a topographical image can be obtained. In the case of electron tunnelling from tip to sample states, using Bardeen's many-body approach [18] it is possible to obtain the *tunnelling probability* (in the first order of perturbation):

$$(2.27) \qquad P_{\mu\nu}^{ST} = \frac{2\pi}{\hbar}\left|M_{\mu\nu}^{ST}\right|^2 \delta\left(E_\nu - E_\mu\right) \ ,$$

which is a Fermi's golden rule for *elastic tunnelling* from a sample state with energy E_μ into a tip state with energy E_ν. $M_{\mu\nu}^{ST}$ is the tunnelling matrix element between the ψ_μ state of the sample surface and the ψ_ν state of probing tip; Bardeen [18] has shown that

$$M_{\mu\nu}^{ST} = \frac{\hbar^2}{2m_e}\int_\Omega d\mathbf{S}\cdot\left(\psi_\mu^*\vec{\nabla}\psi_\nu - \psi_\nu\vec{\nabla}\psi_\mu^*\right) \quad (2.28)$$

where the integral is over any surface Ω lying entirely within the vacuum (barrier potential) region separating the sample and the tip. The quantity in parentheses is the *current operator*.

By applying a bias V and treating the Fermi distribution as a step function [18]:

$$I = \frac{2\pi e}{\hbar}\sum_{\mu,\nu} f\left(E_\mu\right)\left[1 - f\left(E_\nu + eV\right)\right]\left|M_{\mu\nu}^{ST}\right|^2 \delta\left(E_\mu - E_\nu\right) \quad (2.29)$$

where $f(E)$ is the Fermi-Dirac distribution function and V is the applied bias voltage[1]. In the limit of small bias voltage, the tunnelling current I is given by [19]:

$$I = \frac{2\pi}{\hbar}e^2 V\sum_{\mu,\nu}\left|M_{\mu\nu}^{ST}\right|^2 \delta\left(E_\nu - E_F^S\right)\delta\left(E_\mu - E_F^T\right) \quad (2.30)$$

To evaluate $M_{\mu\nu}^{ST}$, Tersoff and Hamann [19] demonstrated that is possible to *expand the surface wave function over a* **G** *series* (surface reciprocal-lattice vector); moreover, since the microscopic structure of the tip is not yet known, the tip wave function can be modelled as locally spherical. So, Tersoff and Hamann [19] introduced the approximation in which the tip wave function is taken as an *asymptotic spherical form*:

1. Note that the previous equation, even if it resembles the ordinary first-order perturbation theory, is formally different from the usual quantum mechanics formalisms; in fact, ψ_μ and ψ_ν are non-orthogonal eigenstates of different Hamiltonians (and then, belonging to different Hilbert' spaces).

$$\psi_\nu = \frac{1}{\sqrt{\Omega_S}} \sum_{\mathbf{G}} a_{\mathbf{G}} e^{z\sqrt{\lambda^2+|\mathbf{k_G}|^2}} e^{i\mathbf{k_G}\cdot\mathbf{x}}$$
$$\psi_\mu = \frac{1}{\sqrt{\Omega_T}} \lambda R e^{\lambda R} \frac{e^{-\lambda|\mathbf{r}-\mathbf{R}_0|}}{\lambda|\mathbf{r}-\mathbf{R}_0|} \quad (2.31)$$

Ω_S and Ω_T are the sample and tip volume, $\lambda = \frac{1}{\hbar}\sqrt{2m_e\phi}$ (ϕ is the work function, assumed the same for the tip and the surface), $\mathbf{k_G} = \mathbf{k}_{||} + \mathbf{G}$, where $\mathbf{k}_{||}$ is the surface Bloch wave vector of the state, R is the local curvature radius of the tip. Finally, d is the distance of nearest approach of the tip to the sample surface. The tip-surface close-encounter during a STM measurements is showed in the Figure 2.9.

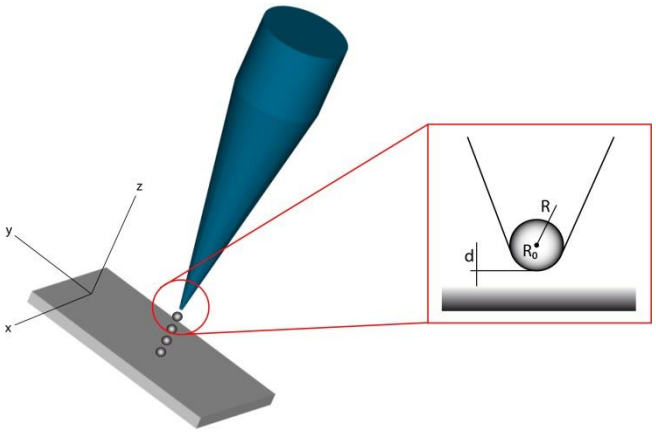

Figure 2.9. Schematization of the tip-surface close-encounter.

In this way, the tunnelling matrix element $M_{\mu\nu}^{ST}$ is

$$M_{\mu\nu}^{ST} = \frac{\hbar^2}{m_e} \frac{2\pi R}{\sqrt{\Omega_T}} e^{\lambda R} \psi_\nu(\mathbf{R}_0) \quad . \quad (2.32)$$

Consequently, the tunnelling current is given by the substitution of equation 2.32 in 2.30 [19]:

$$I = \frac{32\pi^3}{\hbar} e^2 V \phi^2 \frac{R^2 e^{2\lambda R}}{\lambda^4} D_T(E_F) \sum_\nu |\psi_\nu(\mathbf{R}_0)|^2 \delta(E_\nu - E_F^S) \quad , \quad (2.33)$$

where $D_T(E_F)$ is the density of state per unit volume of the probe tip.

Note that $\rho(\mathbf{R}_0, E_F^S) = \sum_\nu |\psi_\nu(\mathbf{R}_0)|^2 \delta(E_\nu - E_F^S)$ is the sample *surface local density of states* (S-LDOS) at the point $\mathbf{R}_0$ or, equivalently, the charge per unit energy from surface states at the Fermi level. In this way, *at constant current the tip follows a contour of constant* $\rho(\mathbf{R}_0, E_F^S)$ [19]. The comparison between the STM tunneling data and the LDOS obtained from DFT calculations is reported in the Figure 2.10.

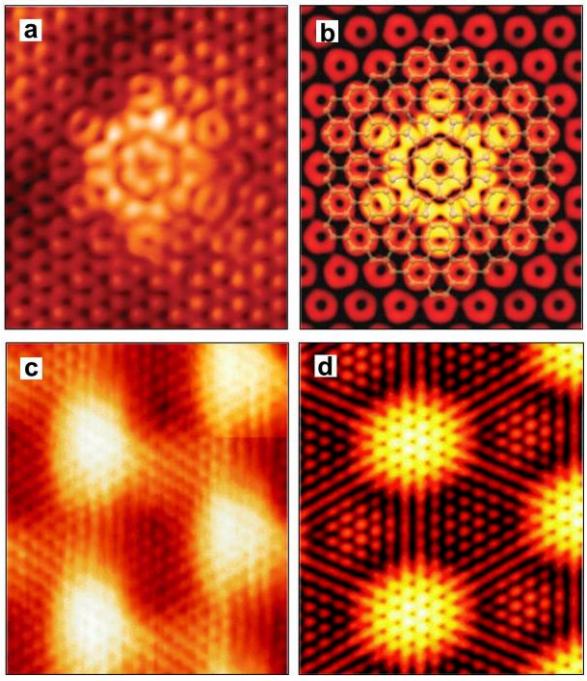

Figure 2.10. STM-calculated LDOS correlation; a. experimental STM image of a punctual defect in graphite and (b) the relative calculated LDOS of the defect site (taken from E. Cockayne, *Phys. Rev. B* **83**, 195425, 2011); c: Moirè pattern of single layer graphene on Ru(0001) and (d) the relative calculated LDOS (taken from B. Wang, M.-L. Bocquet, S. Marchini, S. Günther, J. Wintterlin, *Phys. Chem. Chem. Phys.* **10**, 3530-3534, 2008). Both of the LDOS were calculated with a Hamann-Tersoff based-calculation.

1.2.4 Low Energy Electron Diffraction (LEED)

The Low Energy Electron Diffraction (LEED) is based on the oscillation behavior of a primary electron beam at low energy (20-500 eV), whose corresponding wavelengths variation is between 0.5 and 2.0 Å [17]. If this beam interacts with a crystal lattice having comparable inter-atomic distances, then the electrons are diffracted and the images obtained are diffraction spots matching the reciprocal lattice ones [17]. Analyzing these spots it is possible to trace back to the real lattice and then to the surface geometry.

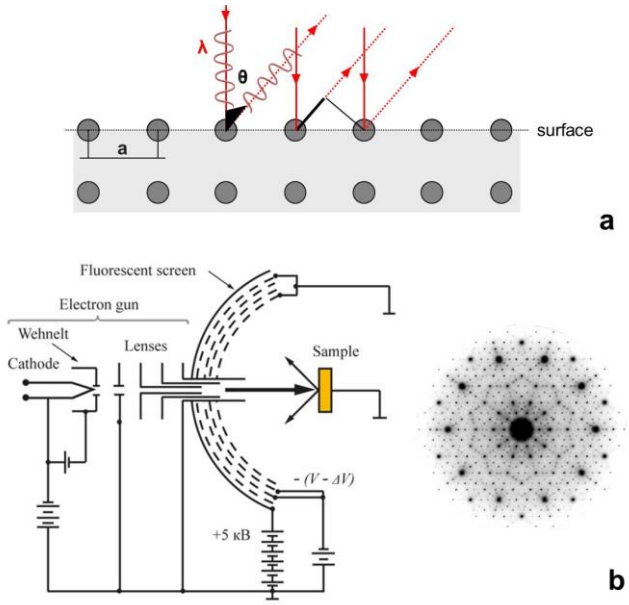

Figure 2.11. a: Schematic representation of the diffraction process from surface atoms separated by a periodic distance a; b: Example of a rear-view LEED configuration.

The electrons mean escape depth values are low (as reported previously for XPS), usually less than 10 Å, so that electrons are used to analyze the surface atoms layers. In the usual experimental setup (Figure 2.11) the sample is illuminated with an electron beam, produced through thermoionic effect from a filament placed in the back screen side (electron gun). The electrons are then accelerated up to the desired energy through a potential gap and collide on the sample. The diffracted electrons are emitted back in precise directions (with respect to the primary beam), until they collide with a suppressor made by a series of grids kept at a variable potential, in order to select their energy.

The selected electrons, emerging from the last grid, are then able to hit the hemispheric fluorescent screen where the diffraction spots are revealed.

The diffraction spots are typical of the sample crystal lattice and are also used to obtain important information on the degree of surface order. If they are small, intense and well defined (with respect to the screen background), they indicate large and ordered domains. On the contrary, an high spots background indicates an electron diffusion in many directions and then the presence of a disordered lattice [17]. The diffraction spots correspond to the positive interference of the waves. If we consider the example reported in Figure 2.11a, where an electron beam with λ wavelength colliding with a mono-dimensional chain of atoms separated by a distance (a) is reported, the positive interference condition is given by the Bragg's law:

$$n\lambda = a\,sin(\theta) \quad , \tag{2.34}$$

where $n\lambda$ is an entire number of waves (n is the diffraction order) and $asin(\theta)$ is the inter-atomic distance projection along the propagation direction [17]. The first diffraction order is then obtained when $sin(\theta) = \lambda a^{-1}$. Hence, if the value of θ is known, it's easy to get the inter-atomic distance a. The simplest way to measure θ is to put the sample at the centre of the LEED screen, so that the distance between the zero order spot (covered by the electron gun) and the first diffraction order a can be easily measured. Therefore, knowing the values of both the distance between the screen and the sample (R) and the one between the zero and first order diffraction spots (a^*) the following relation can be obtained: $sin(\theta) = a^*/R$, thus allowing us the calculation the a value [17]:

$$a = \frac{R \cdot \lambda}{a^*} \quad . \tag{2.35}$$

1.2.5 Scanning Electron Microscopy (SEM)

The birth of the electron microscopy and, in particular, of the electron optics is a direct consequence of the discover of the dual nature of electrons (and, in general, of any particle) by C. J. Davisson, L. H. Germer and J. J. Thomson in 1927, inspired by the theoretical work of the French physicist L. De Broglie. De Broglie, in 1924, adopting an approach similar to the one developed by A. Einstein for the electromagnetic radiation, postulated that particles such as electrons, protons etc. are characterized by the same properties held by waves. For a particle of mass m in motion with a velocity v, the wave-particle duality is expressed by the well-known De Broglie equation:

$$\lambda = \frac{h}{mv} \quad , \tag{2.36}$$

where h is the Planck constant.

A more general expression for λ is obtainable including the relativistic effects [20]:

$$\lambda = \frac{h}{\sqrt{2m_0 eV\left(1+\frac{eV}{2m_0c^2}\right)}} \quad , \tag{2.37}$$

where m_0 is the electron rest mass, V is the acceleration potential and c the speed of light. Taking into account the equation 2.37, the electron wavelength at 10 kV is equal to 0.012 nm, still appreciably less than the interatomic distances in solids. Then, at the typical energies of the SEM measurements, electrons can be considered as particle [20].

The electron beam, which typically has an energy ranging from 1 keV to 30 keV, is focused by one or two condenser lenses to a spot having a diameter between 0.4 nm and 5 nm [20,21]. The beam passes through pairs of scanning coils or pairs of deflector plates in the electron column, which deflect the beam in the x and y axes so that it can raster the desired area of the sample surface. A schematic structure of an electron microscope is reported in Figure 2.12a. When the primary electron beam interacts with the sample, the electrons lose energy by repeated random scattering and absorption within a teardrop-shaped volume of the specimen known as the interaction volume [20,21], which extends from less than 100 nm to approximately 5

μm into the surface, as schematically reported in Figure 2.12b. The size of the interaction volume depends on the electron kinetic energy, the atomic number of the specimen elements and the specimen density [21]. The energy exchange between the electron beam and the sample results in the reflection of high-energy electrons by elastic scattering, emission of secondary electrons by inelastic scattering and the emission of electromagnetic radiation, each of which can be detected by dedicated detectors, usually based on scintillator-photomultiplier systems (Everhardt-Thornley detectors) [20,21]. Electronic amplifiers of various types are used to amplify the signals, which are displayed in a 2D map as variations in brightness on a grey-scale. Each pixel of the map is synchronized with the position of the beam on the specimen in the microscope, and the resulting image is therefore a distribution map of the intensity of the signal emitted from the scanned area of the specimen.

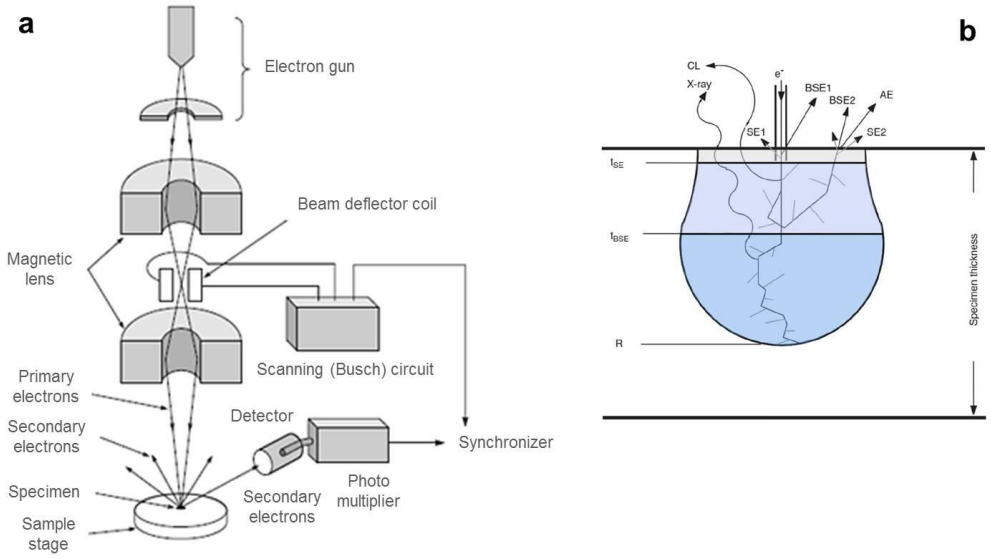

Figure 2.12. a: Schematic structure of a scanning electron microscope; b: pictorial view of the interaction volume.

As introduced above, the types of signals produced during a SEM measurement include Secondary Electrons (SE), back-scattered electrons (BSE), characteristic X-rays, UV-Vis light (Cathode Luminescence, CL) and specimen current. In the most common or standard detection mode, Secondary Electron Imaging or SEI, the SEM can produce very high-resolution images of a sample surface, revealing details nominally up to 1 nm in size [20,21]. Due to the very narrow electron beam, SEM micrographs have a large depth of field yielding a characteristic three-dimensional

appearance, useful for the understanding of the surface structure of the materials [20,21]. An example of SEM analysis of graphene-based materials is reported in Figure 2.13.

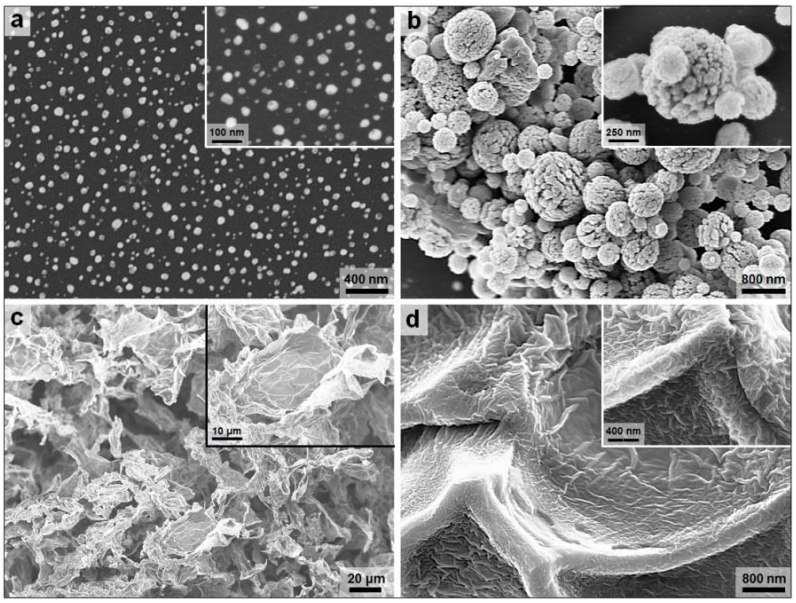

Figure 2.13. Carbon-based material imaging by SEM: Pd nanoparticles on GC (a), MoS_2/GO nanohybrids on HOPG (b), GO 3D foam obtained by freeze-pump-thaw process (c) and highly-crumpled GO film (d).

Depending on the different type of set-up, a wide range of magnifications is possible, from about 100 times up to 10^6 times. Back-scattered electrons (BSE) are beam electrons that are reflected from the sample by elastic scattering. BSE are often used in analytical SEM along with the spectra collected from the characteristic X-rays (by the Energy Dispersive X-ray spectroscopy, or EDX), since the intensity of the BSE signal is strongly related to the atomic number of the specimen [21]. For this reason, BSE images can provide information about the distribution of different elements in the sample [21]. Characteristic X-rays are emitted when the electron beam removes an inner shell electron from the sample (typically from a K-shell) [21], causing an internal decay of a higher-energy electron to fill the shell and the consequent release of a X-photon (X-ray fluorescence). These characteristic X-rays are used to identify the composition and measure the abundance of elements in the sample [21].

REFERENCES

[1] G. Pisent, *Teoria dello Scattering e delle reazioni nucleari*, Nuclear Physics lecture notes, department of Physics G. Galilei, 2001.

[2] G. Nardulli, *Meccanica Quantistica*, vol I-II, Franco Angeli Editore, 2007.

[3] H. Bernas, Materials Science with Ion Beams, *Topics Appl. Physics* **116**, 1-28 (2010).

[4] A. Meldrum, R. F. Haglund, L. A. Boatner, C. W. White, Nanocomposite Materials formed by Ion Implantation, *Adv. Mater.* **13**, 1431-1444 (2001).

[5] I. Brodie, J. J. Muray, *The physics of micro/nano-Fabrications*, Plenum Press, 1992.

[6] A. Einstein, Über einen die Erzeugung und Verwandlung des Lichtes betreffenden heuristichen Gesichtspunkt, *Annalen der Physik* **17**, 132–148 (1905).

[7] S. Hofmann, Auger and X-ray *Photoelectron Spectroscopy in Materials Science*, Springer, 2013.

[8] J. H. D. Eland, *Photoelectron Spectroscopy*, Butterworths & Co. Publishers, 1984.

[9] A. Szabò, N. S. Ostlund, *Modern quantum chemistry: introduction to advanced electronic structure theory*, Courier Dover Pubblications, 1996.

[10] D. A. Shirley, *Many-Electron and Final-State effects*, in *Photoemission in Solids I. General Principles*, Springer-Verlag, 1978.

[11] S. Hüfner, R. Claessen, F. Reinert, T. Straub, V. N. Strocov, P. Steiner, Photoemission spectroscopy in metals: band structure-Fermi surface-spectral function, *J. Elect. Spectr. Rel. Phenomen.* **100**, 191-213 (1999).

[12] S. Weinberg, *Field Theory: Quantum Electrodynamics*, Wiley Ed., 1998.

[13] A. L. Fetter, J. D. Walecka, Quantum Theory of Many-Particle Systems, Dover Books on Physics, 2003

[14] T. Miller, W.E. McMahon, T.C. Chiang, Interference between bulk and surface photoemission transitions in Ag(111), *Phys. Rev. Lett.* **77**, 1167-1170 (1996).

[15] C. S. Fadley, *Electron Spectroscopy: Theory, Thechniques and Applications*, Pergamon Press 1978.

[16] H. J. Güntherodt, R. Wiesendanger, *Scanning Tunneling Microscopy I*, Springer-Verlag, 1992.

[17] R. Eisberg, R. Resnick, *Quantum Physics*, Wiley Ed., 1985.

[18] J. Bardeen, Tunnelling from a many-particle point of view, Phys. Rev. Lett. **6**, 57-59 (1961).

[19] J. Tersoff, D. R. Hamann, Theory of the scanning tunnelling microscope, *Phys. Rev. B* **31**, 805-814 (1985).

[20] B. Kaplan, *Microstructure Characterization of Materials*, Wiley Ed., 1999.

[21] W. Zhou, Z. L. Wang, *Scanning Microscopy for Nanotechnology: Techniques and Applications*, Springer, 2006.

Chapter 1.3
Electrochemical Methods

1.3.1 Linear and Cyclic Voltammetry (LSV-CV)

The voltammetric experiments have been performed in an *electrochemical cell* equipped with a *three electrode system*: a *working electrode* (WE) where the redox process takes place, a *reference electrode* (RE) for the potential application and a *counter electrode* (CE) in order to close the circuit.

During the experiments, the potential of the WE referred to the RE is monitored using a potentiostat; thus, it is crucial that the RE potential remain constant during the experiment, in order to assign every variation of the potential difference to the potential of WE. With the three electrode configuration, the cell current flows from WE to CE, while RE is inserted within an *electric circuit* having an *high impedence*; in this way, the current that flows through this electrode is negligible. Thus, the RE potential remains constant and substantially equal to its open circuit value (that is, no Ohmic falls occur at the RE).

The linear sweep voltammetry (LSV) technique consists in applying a potential ramp between WE and CE. The potential linear scan starts from E_i (usually the open circuit potential of the cell, OCP) toward positive or negative values; in correspondence to the E_π potential, the potential linear scan is alternatively stopped or the direction of the scan is inverted. In this case, this measurement represent a cyclic voltammetry (CV) and the E_π is called *inversion potential.*

In this way, $E_i=E_f$:

$$(3.1) \quad \begin{cases} E = E_i - \mathrm{v}t & 0 < \mathrm{t} \le \pi \\ E = E_i - 2\mathrm{v}\pi + \mathrm{v}t & \mathrm{t} > \pi \end{cases},$$

where *v* is the *potential scan rate* and π is the *time instant when the potential is inverted* during the CV.

If a redox couple is present in solution with the equilibrium Ox + $n\,e^-$ ⇄ Red , the concentration of the redox species close to the WE surface (x=0) are given by the Nernst equation [1]:

$$(3.2) \qquad E = E^{\Theta} + \frac{RT}{nF}\ln\left(\frac{a_{\mathrm{Ox}}^{\mathrm{An}}}{a_{\mathrm{Red}}^{\mathrm{Cat}}}\right) = E^{\Theta} + \frac{RT}{nF}\ln\left(\frac{C_{\mathrm{OX}}(x=0,t)}{C_{\mathrm{Red}}(x=0,t)}\right),$$

where n is the number of electrons exchanged during the redox reactions, R is the gas universal constant (8.314 J mol^{-1} K), F is the *Faraday constant* (number of coulombs per mole of electrons: $F \approx 9.65\times10^4$ C mol^{-1}), while $a_k = \gamma_k[k]$ is the chemical activity of the species k (since *activity coefficients* γ_k tends to unity at low concentrations, activities in the Nernst equation are frequently replaced by the simple concentrations $C_k(x,t)$ [2]). Figure 3.1a shows the potential program applied between WE and CE during a voltammetry measurement (see Figure 3.1b).

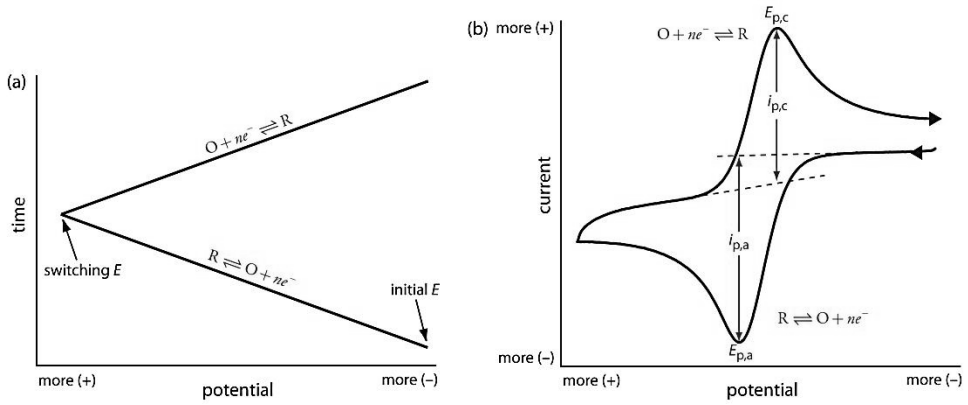

Figure 3.1. a: potential program applied between WE and CE; b: voltammetric response of a redox couple present in the electrolyte (Fe^{2+}/Fe^{3+}), over a glassy carbon (GC) WE.

The potential scan starts from a value E_i more positive than E^{Θ} of the redox process; thus, a small *capacitive current* flows in this potential region. When the applied potential E approximates E^{Θ}, the reduction of the species Ox starts and a *faradic current* flows between WE and CE [3]. As the potential increase towards negative values the concentration of the reduced species at the electrode increase; when $E^{\Theta} << |E|$ the surface concentration of Ox close to the WE becomes negligible [2,3]. Under this conditions, the current that flows between the WE and CE depends only on the *Ox diffusion rate* from the "bulk" of the solution towards the WE surface [2,3]. On the other hand, as the time increase the *diffusion layer thickness* Δ increase

(see pictures 6.46); thus, the *concentration gradient* that exists between the bulk of the solution and the electrode surface (x=0), $\left[\partial C_{Ox}(x,t)/\partial x\right]_{x=0}$, decreases [2,3]. Similarly, the current decrease with the concentration gradient because it is proportional to this latter, as it is showed by *Cottrell equation* [2]:

$$(3.3) \qquad i = nFA_{WE}D_{Ox}\left[\frac{\partial C_{Ox}(x,t)}{\partial x}\right]_{x=0} = \frac{nFA_{WE}C^{*}_{Ox}}{\sqrt{\pi t}}\sqrt{D_{Ox}} \ ,$$

where A_{WE} is the surface area of the WE exposed in the solution (cm^2), while D_{Ox} and C^{*}_{Ox} are the diffusion coefficient ($cm^2\ s^{-1}$) and the analytical concentration (mol cm^{-3}) of the Ox species in solution, respectively. Thus, the superposition of these two effects, that is the increase of the current caused by the progressive growth of the reduction rate (as the potential E increases) and the time decay of the current caused by the increase of the diffusion layer, generates a *cathodic peak*. If the system is *completely reversible*, when the potential E is inverted in proximity of E_{π} will occurs the inverse process (Red ⇄ Ox + $n\,e^-$); in this way, it will be possible to observe the *anodic peak*. The quantity $E_{1/2}$ is directly correlated to the *standard potential* of the redox process [2,3]:

$$(3.4) \qquad E_{1/2} = \frac{E_{p,c} + E_{p,a}}{2} = E^{\Theta} + \frac{RT}{2nF}\ln\left(\frac{D_{Ox}}{D_{Red}}\right) \ ,$$

where $E_{p,c}$ and $E_{p,a}$ are the potentials where the cathodic and anodic peak are centered. The peak current, i_p, is given by the *Randles-Sevcik equation*, which is related to the square root of the *scan rate v* (V s^{-1}) of the voltammetric experiment [2,3]:

$$(3.5) \qquad i_p = 0.4463nFA_{WE}C^{*}_{Ox}\left(\frac{nF}{RT}\right)^{1/2}\sqrt{D_{Ox}v} \ .$$

To characterize quantitatively the *electronic transfer process* (ET) that occurs at the surface of the WE, it is possible to compute from the experimental data the *electron transfer constant*, k°, which is defined through the application of the *transition state theory* and the *Butler-Volmer model* to the equilibrium Ox + $n\,e^-$ ↔ Red [2]:

$$(3.6) \qquad \begin{aligned} k_c &= k^\circ e^{-\alpha n_\alpha F\left(E-E^\Theta\right)/RT} \\ k_a &= k^\circ e^{(1-\alpha) n_\alpha F\left(E-E^\Theta\right)/RT} \end{aligned} ,$$

where *kinetic constants* k_c^{red} and k_a^{ox} for the reduction and oxidation reaction are related to α and k°, which are respectively the *electronic transfer coefficient and standard rate constant*, that is the common value of k_c and k_a when $E = E^\Theta$.
Within the theoretical treatment developed by *Nicholson* and *Shain* (which assumes D_{Ox} and D_{red} to be equal), an empirical model relates $\Delta E_p = \left|E_{cp} - E_{ap}\right|$ to the Ψ function [2,4]:

$$(3.7) \qquad \Delta E_p(\Psi) = E_0 + g e^{R_0 \log(\Psi)} ,$$

where E_0, g and R_0 are adjustable parameters for fitting experimental data. Ψ is defined, within this model, as [2,4]:

$$(3.8) \qquad \Psi = k^\circ \frac{1}{\sqrt{\nu \frac{n\pi FD}{RT}}} .$$

Using the logarithm properties, it is possible to get an effectiveness equation by which it is possible to get k° from experimental data simply fitting ΔE_p obtained for different scan rate *v* against $\log\left(\nu^{-1/2}\right)$ [2,4]:

$$(3.9) \qquad \Delta E_p(\Psi) = E_0 + g e^{R_0\left[\log(k^\circ)+\log\left(\nu^{-1/2}\right)+\log\left[\left(\frac{n\pi FD}{RT}\right)^{-1/2}\right]\right]} .$$

1.3.2 Rotating Disk Electrode (RDE)

The rotating disc electrode (RDE) is the classical hydrodynamic electroanalytical technique used to limit the diffusion layer thickness. The electrode rotates during experiments inducing a flux of analyte to the electrode. These working electrodes are used in electrochemical studies when investigating reaction mechanisms related to redox chemistry, among other chemical phenomena.

Compared to transient methods such as stationary electrode voltammetry, hydrodynamic methods have several advantages including a rapid establishment of a high rate of steady-state mass transport and an easily and reproducibly controlled convection over a wide range of mass transfer coefficients [2,3].

The RDE consists of a disk (made in metal, glassy carbon or graphite) embedded in an inert non-conductive polymer or resin (usually PTFE or PEEK) that can be connected to an electric motor characterized by a fine control of the electrode rotation rate. As the disk turns (typically between 400 and 10000 rpm), the solution close to the electrode surface (described as the *hydrodynamic boundary layer)* is dragged by the spinning disk and the resulting centrifugal force flings the solution away from the center of the electrode. Once the equilibrium is established, a positive flux of solution from the bulk electrolyte is induced by the electrode rotation perpendicularly to the electrode itself, continuously replacing in this way the *boundary layer* [2]. The sum result is a laminar flow of solution towards and across the electrode, as it is depicted in Figure 3.2a.

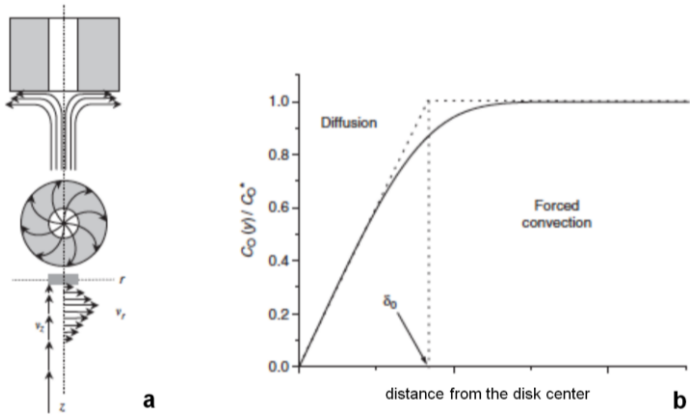

Figure 3.2. a: Flow streamlines and vector representation of the fluid velocities close to a RDE; b: steady-state concentration profile at the RDE surface, as a function of the distance from the disk center. Between 400 and 10000 rpm, the critical distance (δ_0) is between 20 μm and 100 μm [2].

The rate of the solution flow can be controlled by the electrode angular velocity and modeled mathematically. This flow can quickly achieve conditions in which the steady-state current is controlled by the solution flow rather than diffusion. This is a contrast to stationary experiments such as cyclic voltammetry where the steady-state current is limited by the diffusion of species in solution. By running linear sweep voltammetry at various rotation rates, different electrochemical phenomena can be investigated, including *multi-electron transfers*, *kinetics of slow electron transfers*, *adsorption/desorption steps* and *electrochemical reaction mechanisms* [2]. Potential sweep reversals as used in cyclic voltammetry are different for a RDE system, since the products of the potential sweep are continually swept away from the electrode. A reversal would produce a similar *i-E* curve, which would closely match the forward scan, except for capacitive charging current. A RDE cannot be used to observe the behavior of the electrode reaction products, since they are continually swept away from the electrode. However, the rotating ring-disk electrode is well suited to investigate this further reactivity. The peak current in a cyclic voltammogram for a RDE is a plateau like region, governed by the Levich equation. The limiting current is typically much higher than the peak current of a stationary electrode, being that the mass transport of reactants is actively stimulated by the rotating disk, and not just governed by diffusion, as is the case for a stationary electrode.

Considering the concentration profile shown in Figure 3.2b, the limiting current is defined by the Levich equation [2,5]:

$$j_l = 0.620 n F A_{WE} C D^{2/3} \upsilon^{-1/6} \omega^{1/2} \quad , \tag{3.10}$$

where υ is the kinematic viscosity, ω (rad/s) is the angular velocity of the electrode, while C and D are the concentration and the diffusion coefficient of the redox species in the electrolyte [2,3,5]. The limiting current is achieved by recording a linear sweep voltammogram at a low scan rate (1÷10 mV/s) from an initial potential where no reaction occurs to a final potential in the region where the process becomes under diffusion control. The classical RDE experiment consists in recording a series of linear sweep voltammograms at a low scan rate for different values of ω.

The Levich equation predicts that a plot of the limiting current vs. the square root of ω should be a straight line passing through the origin with a slope determined by the number of electrons, the geometric area of the electrode, the diffusion coefficient, the

bulk concentration of the redox species and the kinematic viscosity of the solution [2,5]. If the redox process is reversible, the shape of the wave does not depend on ω. Then, at any potential the current should be proportional to $\omega^{1/2}$, like the limiting current [2,5]. More in general, if the shape of the curve depends instead on ω (irreversible redox processes), the redox process is kinetically limited by the electron transfer. In this case, one can measure the current at fixed potentials along the linear sweep voltammograms, plotting for each potential the inverse of the current vs. $\omega^{1/2}$. This is known as a Koutecky–Levich plot, described by the related equation [2,3,6]:

$$\frac{1}{j} = \frac{1}{j_k} + \frac{1}{j_d} = \frac{1}{j_k} + \frac{1}{B\sqrt{\omega}} \quad , \tag{3.11}$$

where j_k is the kinetic current and B is the Levich slope given by the equation 3.12:

$$B = 0.2\, n\, F \sqrt[3]{D^2}\, \frac{C}{\sqrt[6]{\upsilon}} = 0.0355 \cdot n \quad . \tag{3.12}$$

n is the number of exchanged electrons during the studied redox process while the constant 0.2 is adopted when the angular rotation speed is expressed in rpm [2].

Figure 3.3 reports a typical electrochemical equipment used for the study of the electrocatalytic properties of the materials.

Figure 3.3. Experimental equipment for electrochemical tests; a: whole equipment (1: potentiostat); b: electrochemical cell with thermostatic bath (2: stirrer, 3: four cones cell, 4: RDE-WE, 5: Pt-CE, 6: RE, 7: Ar inlet for the outgas of the electrolyte).

REFERENCES

[1] J. O'M. Bockris, R. E. White, B. E. Conway, *Modern Aspects of Electrochemistry*, Springer-Verlag, 1996.

[2] A. J. Bard, L. R. Faulkner, *Electrochemical Methods: Fundamentals and Applications*, Wiley & Co., 2000.

[3] B. W. Rossiter, J. F. Hamilton, *Physical Methods in Chemistry: Electrochemical Methods*, vol. 2, Wiley, 1986.

[4] R. S. Nicholson, Theory and application of cyclic voltammetry for measurement of electrode reaction kinetics, *Anal. Chem.* **37**, 1351-1355 (1965).

[5] V. G. Levich, *Physicochemical Hydrodynamics*, Englewood Cliffs Prentice-Hall, 1962.

[6] J. Koutecky, B.G. Levich, *Zhurnal Fizicheskoi Khimii USSR*, **32**, 1565 (1958).

Chapter 1.4
Optical Spectroscopies

1.4.1 Raman-Scattering Microscopy

Raman spectroscopy (named after C. V. Raman) is a spectroscopic technique used to study vibrational, rotational, and other low-frequency modes in a system [1,2]. It relies on inelastic scattering, or Raman scattering, of monochromatic light, usually from a laser in the visible, near infrared, or near ultraviolet range (typically, lasers working at 514 nm and 633 nm are widely used). The laser light interacts with molecular vibrations, phonons or other excitations in the studied system, resulting in an upward or downward energy shift of the laser. The shift in energy gives information about the vibrational modes in the system. Infrared spectroscopy yields similar, but complementary, information.

Although the inelastic scattering of light was predicted by Adolf Smekal in 1923, only in the 1928 the Indian scientist Sir C. V. Raman observed for the first time this effect by using sunlight (together with K. S. Krishnan and independently by Grigory Landsberg and Leonid Mandelstam) [1]. For his discovery, Raman was awarded with the Nobel Prize in Physics in 1930. Systematic pioneering theory of the Raman effect was then developed by Czechoslovak physicist George Placzek between 1930 and 1934.

Typically, a sample is illuminated with a laser beam. Light from the illuminated spot is collected with a lens and sent through a monochromator. Wavelengths close to the laser line, due to *elastic Rayleigh scattering*, are filtered out while the rest of the collected light is dispersed by a detector.

Spontaneous Raman scattering is typically very weak, thus the main difficulty of Raman spectroscopy is the correct separation of the weak inelastically scattered light from the intense Rayleigh scattered laser light. Historically, Raman spectrometers used holographic gratings and multiple dispersion stages to achieve a high degree of laser rejection. In the past, photomultipliers were the typical detectors for dispersive

Raman setups, which resulted in long acquisition times. However, modern instrumentations almost universally employ notch or edge filters for laser rejection, spectrographs based on Czerny-Turner (CT) monochromators and CCD detectors.
In the Raman scattering process that occurs in solids, the sequence of events can be described as follows:

1) the first electronic transition to an intermediate *electron-hole pair state* takes place with the annihilation of the incident photon. Using second quantization formalism, the process can be described as follows [3,4]:

$$\hat{a}^{-}_{\mathrm{s},\mathbf{k}} \left| n^{\mathrm{s}}_{\mathbf{k}} \right\rangle = \sqrt{n^{\mathrm{s}}_{\mathbf{k}} - 1} \left| n^{\mathrm{s}}_{\mathbf{k}} - 1 \right\rangle \quad , \tag{4.1}$$

where $\hat{a}^{-}_{\mathrm{s},\mathbf{k}}$ is the annihilation operator for photons (which is defined in a Fock space); with the creation operator, $\hat{a}^{+}_{\mathrm{s},\mathbf{k}}$, it is possible to write the following properties (*canonical quantization*), which are valid for *each field quantization* (such as the electromagnetic field and the elastic deformation field in periodical lattice, that carries to the phonon definition as the vibrational energy quantum) [3,4]:

$$\begin{aligned} &a. \quad \hat{a}^{-}_{\mathrm{s},\mathbf{k}} \hat{a}^{+}_{\mathrm{s},\mathbf{k}} = n^{\mathbf{s}}_{\mathbf{k}} \\ &b. \quad \left[\hat{a}^{-}_{\mathrm{s},\mathbf{k}}, \hat{a}^{+}_{\mathrm{s},\mathbf{k}} \right] = 1 \end{aligned} \tag{4.2}$$

$n^{\mathrm{s}}_{\mathbf{k}}$ is the total number of photons (or, in general, field bosons) characterized by wave vector **k** and polarization s. If the thermal equilibrium is established, $\left\langle n^{\mathrm{s}}_{\mathbf{k}} \right\rangle$ (average number of photons at thermal equilibrium with wave vector **k** and polarization s) coincides with the *Bose-Einstein statistical distribution for identical indistinguishable bosons with energy* $\varepsilon_{\mathbf{k}}$:

$$\left\langle n^{\mathrm{s}}_{\mathbf{k}} \right\rangle = \left\langle \hat{a}^{-}_{\mathrm{s},\mathbf{k}} \hat{a}^{+}_{\mathrm{s},\mathbf{k}} \right\rangle = \frac{1}{e^{(\varepsilon_{\mathbf{k}} - \mu)/\mathrm{K_B T}} - 1} \quad . \tag{4.3}$$

The *electron-photon interaction Hamiltonian*, derived in detail by Heitler (1954), is given by [2,3]:

$$(4.4) \qquad \hat{H}_{ER} = \frac{e}{m_e}\sum_j\sum_{\mathbf{k},\mathrm{s}}\sqrt{\frac{2\pi\hbar}{\eta V\omega_{\mathbf{k},\mathrm{s}}}}\left(\hat{a}^-_{\mathrm{s},\mathbf{k}}e^{i\mathbf{k}\cdot\mathbf{r_j}} + \hat{a}^+_{\mathrm{s},\mathbf{k}}e^{-i\mathbf{k}\cdot\mathbf{r_j}}\right)\mathbf{s_k}\cdot\mathbf{p_j} \quad ,$$

where $\omega_{\mathbf{k},s}$ is the angular pulsation of the incident radiation with polarization s, $\mathbf{p_j}$ and $\mathbf{r_j}$ are the momentum and position of electron *j*, η is the optical dielectric constant, *V* the crystal volume and $\mathbf{s_k}$ is the unit polarization vector of the photon **k**.

2) The second electronic transition to another electron-hole pair state occurs with the creation ($\hat{c}^+_{\mathrm{b},\mathbf{q}}$) or annihilation ($\hat{c}^-_{\mathrm{b},\mathbf{q}}$) of a phonon with wave vector **q** and polarization *b* (respectively the *Stokes* and *anti-Stokes process*):

$$(4.5) \qquad \begin{array}{ll} \text{a.} & \hat{c}^+_{\mathrm{b},\mathbf{q}}\left|n^{\mathrm{b}}_{\mathbf{q}}\right\rangle = \sqrt{n^{\mathrm{b}}_{\mathbf{q}}+1}\left|n^{\mathrm{b}}_{\mathbf{q}}+1\right\rangle \\ \text{b.} & \hat{c}^-_{\mathrm{b},\mathbf{q}}\left|n^{\mathrm{b}}_{\mathbf{q}}\right\rangle = \sqrt{n^{\mathrm{b}}_{\mathbf{q}}-1}\left|n^{\mathrm{b}}_{\mathbf{q}}-1\right\rangle \end{array}$$

through the electron-lattice interaction described by the electron-phonon interaction Hamiltonian [4]:

$$(4.6) \qquad \hat{H}_{EL} = \frac{ze^2}{c}\sqrt{\frac{n_0}{m_e}}\sum_{\mathbf{k},\mathrm{s}}\sum_{\mathbf{q},\mathrm{b}}\sqrt{\frac{\hbar\omega_{\mathbf{q},\mathrm{b}}}{2V}}\frac{4\pi}{\mathbf{q}^2}\Theta\left(\omega_D-\omega_{\mathbf{q},\mathrm{b}}\right)\left(\hat{a}^+_{\mathrm{s},\mathbf{k}+\mathbf{q}}\hat{a}^-_{\mathrm{s},\mathbf{k}}\hat{c}^-_{\mathrm{b},\mathbf{q}} + \hat{a}^+_{\mathrm{s},\mathbf{k}}\hat{a}^-_{\mathrm{s},\mathbf{k}+\mathbf{q}}\hat{c}^+_{\mathrm{b},\mathbf{q}}\right)$$

z is the valence of ions, c the speed of elastic waves in solids, n_0 the number of atoms per unit volume, $\omega_{\mathbf{q},\mathrm{b}} = \Omega$ is the frequency of the normal oscillation mode for the phonon with wave vector **q** and polarization *b*, Θ and ω_D are respectively the *Debye characteristic temperature* ($\Theta = \frac{\hbar\omega_D}{\mathrm{K_B}}$) and the *Debye frequency* ($\omega_D = \frac{c}{2\pi}\sqrt[3]{\frac{9n_0}{4\pi}}$).

The intensity ratio of the Stokes and the anti-Stokes component of a Raman spectrum is:

$$(4.7) \qquad \frac{I_{anti-Stokes}}{I_{Stokes}} = \frac{\left(\omega_{\mathbf{k},\mathrm{s}}+\Omega_b\right)^4}{\left(\omega_{\mathbf{k},\mathrm{s}}-\Omega_b\right)^4}e^{-\frac{\hbar\Omega_b}{K_BT}}$$

3) The third transition to the electronic ground state takes place with the creation of the scattered photon with wave vector $\mathbf{k}'$ and frequency $\omega'_{\mathbf{k}',s}$:

$$\hat{a}^{+}_{s,\mathbf{k}'}\left|0^{s}_{\mathbf{k}'}\right\rangle = \left|1^{s}_{\mathbf{k}'}\right\rangle \qquad (4.8)$$

In this way, it is simple to verify that the photon inelastic scattering is a *phonon mediated process*; furthermore, *energy is conserved only in the total process, whereas the wave vector is conserved in each step*.
The total process can be described with three particles – first order Feynman diagrams, as reported in Figure 4.1:

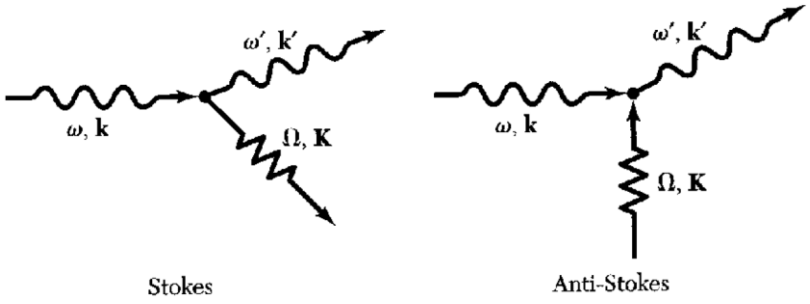

Figure 4.1. Left: Feynman first order diagrams for Stokes (left) and anti-Stokes (right) processes that occur in solids as result of the interaction with a laser radiation.

The two conservation equations relatively to the Feynman processes reported in Figure 4.1 are given by:

$$\hbar\omega_{s,\mathbf{k}} = \hbar\omega'_{s,\mathbf{k}'} \pm \hbar\Omega \quad \text{energy conservation} \qquad (4.9)$$

$$\hbar\mathbf{k}_{s} = \hbar\mathbf{k}'_{s} \pm \hbar\mathbf{q}_{b} \quad \text{momentum conservation} \qquad (4.10)$$

Since $|\mathbf{k}| = 2\pi/\lambda$, for the condition on the momentum conservation, the maximum value for the phonon momentum is given in a backscattering process:

$$|\mathbf{q}_{b}|_{max} \cong 2|\mathbf{k}_{s}| \approx 10^{5} cm^{-1}\ , \qquad (4.11)$$

for a visible photon. On the other hand, the extension limit of the *first Brillouin zone* is equal to $2\pi/a \approx 10^{8} cm^{-1}$ ($a \cong 1$ Å). In this way, *only the normal mode with momentum close to the centre of the Brillouin zone* ($\mathbf{q}_{s} \to 0$) *will be Raman active* [2]. Finally, using *first–order* perturbation theory, selection rules for the optical

phonon branches close to the the centre of the Brillouin zone can be obtained verifying which normal modes fulfill the condition

$$\langle e|\chi_{\mu\sigma}|g\rangle \neq 0 \ , \tag{4.12}$$

where $\chi_{\mu\sigma}$ is the Raman tensor, that is the *transition susceptibility* of the solid at the *first order*, while $\langle e|$ and $\langle g|$ is the *initial* and *final states* which correspond to a sum over the *Bloch states* [2].

1.4.2 Infrared Reflection Absorption Spectroscopy (IRAS)

The Schrödinger equation for a vibrational motion along the z-direction, describing a one-dimensional harmonic quantum oscillator can be written as (supposed that the potential energy can be expressed with a quadratic 1-form or, alternatively, under slight displacement from the equilibrium points on the system surface potential energy) [5]:

$$(4.13) \qquad \left[-\frac{\hbar}{2\Omega}\frac{\partial^2}{\partial z^2}+\frac{1}{2}k(z-r_e)^2\right]\psi_v(z)=\varepsilon_v\psi_v(z) \ ,$$

$$(4.14) \qquad \psi_v(z)=N_v\,H_v(z)\,e^{-z^2\sqrt{a}/2}$$

H_v(z) are the Hermite polynomials, which constitutes a succession of orthogonal polynomials on the whole real number field respectively to the gaussian function $e^{-z^2\sqrt{a}/2}$; in the Rodrigues representation [5] they are given by (see Figure 4.2 for the first four harmonic oscillator):

$$(4.15) \qquad H_v(z)=(-1)^v\,e^{z^2\sqrt{a}}\,\frac{\partial^v}{\partial z^v}\left[e^{-z^2\sqrt{a}}\right]$$

N_v is a normalization factor that ensures the unitary norm of the eigenstate, v is the *vibrational quantum number* (that assumes only integer values from 1 to infinite) and $a=\Omega\omega_0/\hbar$ (Ω is the reduced mass of the one-dimensional system, referred to the mass reference system).

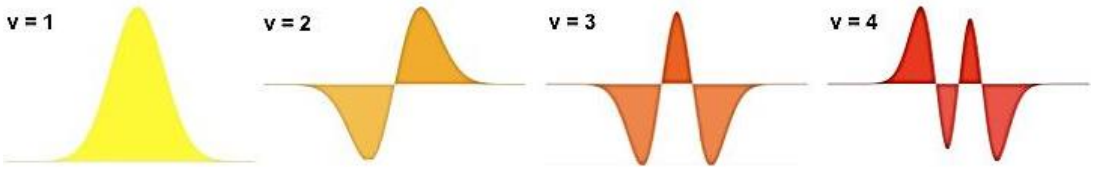

Figure 4.2. The first four vibrational eigenfunctions.

Using the mechanical resonance frequency of the system (with k bond constant),

$$(4.16) \qquad \omega_0=\sqrt{\frac{k}{\Omega}}$$

it can be possible to give the following form for the eigenvalue that appears in the equation 4.13, which is the energy of the vibrational state *v*:

$$\varepsilon_v = \hbar\omega_0\left(v+\frac{1}{2}\right) \qquad (4.17)$$

The application of IR spectroscopy to the study of surface chemistry owes much of its early development to the work of Eischens [6], Sheppard [7] and Greenler [8]. The absorption of infrared radiation by adsorbed species on the surface or by decorating functional groups depends on the *transition dipole moment*, which is given by

$$M_{vv'} = \langle v'|\hat{\mu}|v\rangle = \int_{-\infty}^{+\infty} dz\, \psi_v(z)\,\hat{\mu}(z)\,\psi_{v'}(z) \quad , \qquad (4.18)$$

where $\psi_v(z)$ e $\psi_{v'}(z)$ are the initial and final state vibrational wavefunctions, while $\hat{\mu}(z)$ is the dipole molecular moment hermitian operator (defined, as the vibrational eigenstate of the system, in an Hilbert space having an infinite-dimensional orthonormal base [5]. To have a nonzero probability of a particular vibrational transition, the transition integral must be nonzero (at least one of its x, y or z components). Then, expanding the dipole moment operator $\hat{\mu}$ in first order Taylor series (and calculating the derivatives on the equilibrium point of the oscillator), $M_{vv'}$ assumes the following form:

$$\begin{aligned} M_{vv'} &= \langle v'|\hat{\mu}|v\rangle = \langle v'|\mu_0 + \sum_{k=1,2,3}\left(\frac{\partial\hat{\mu}}{\partial x_k}\right)_{x_k=0}\hat{x}_k|v\rangle = \\ &= \mu_0\langle v'|v\rangle + \sum_{k=1,2,3}\left(\frac{\partial\hat{\mu}}{\partial x_k}\right)_{x_k=0}\langle v'|\hat{x}_k|v\rangle = \\ &= \sum_{k=1,2,3}\left(\frac{\partial\hat{\mu}}{\partial x_k}\right)_{x_k=0}\langle v'|\hat{x}_k|v\rangle \end{aligned} \qquad (4.19)$$

with $\langle v'|v\rangle = \delta_{v'v} = 0$ due to the orthonormality that characterize the vibrational eigenstate. So, two selection rules can be attained from the previous equation:

- *General Selection Rule*: the dipole moment $\hat{\mu}$ must be variable with variation of the normal coordinate (at least one of its components must be variable);

- *Specific Selection Rule*: due to the Hermite polynomials properties, the transition dipole moment will be nonzero only for $\Delta v = \pm 1$.

Group theory and symmetry considerations can be used to determine which *modes are IR active* [9]: that is, those normal modes that make $\psi_v(z)\hat{\mu}(z)\psi_{v'}(z)$ totalsymmetric [5]:

$$\left(\frac{\partial \hat{\mu}}{\partial x_k}\right)_{x_k=0} \neq 0 \quad \text{(4.20)}$$, in accord with the general selection rule.

In an IRAS experiment, the strength of an adsorption feature depends not only on the transition dipole moment (as IR absorption by gases and liquids), but also on the strength of the electric field associated with the infrared light incident on the sample and on the *polarization of the electric field vector with respect to the transition dipole moment* [9]. Semiconductors and insulators can support the electric fields both perpendicular and parallel to their surface; metals, however, can only support a perpendicular electric field, because only in this way the molecular dipole moment will leads the normal mode vibration due to the interaction with IR radiation. Unlike this, if the dipole moment lies with his axis parallel to the sample surface, the image dipole moment which is created inside the metal by the *quasi-free electron Fermi gas* will crosses the molecular induced dipole, giving no energy exchange between field and adsorbates. Thus, on a metal only vibrations with a component along the surface normal (out of plane) will be observed in IR absorption spectra. Figure 4.3 reports a schematic vision of the image charge and dipole moment that take place when an electromagnetic field interacts with a metal surface.

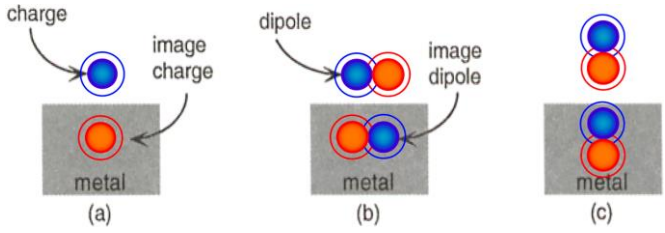

Figure 4.3. Image charge and dipole moment generated in metals by the quasi-free electron Fermi gas excited by an orthogonal electromagnetic radiation.

In a typical IRAS experiment, the reflection spectrum is measured for the clean substrate, $R_0(v)$, and the adsorbate-covered substrate, $R(v)$.

The absorption spectrum is usually expressed in terms of the relative change in reflectivity:

$$(4.21) \qquad \frac{\Delta R(\nu)}{R_0(\nu)} = \frac{R_0(\nu) - R(\nu)}{R_0(\nu)}$$

The relative change in reflectivity is related to the absolute coverage σ (molecules per unit area) and to the adsorbate polarizability $\alpha(iv)$, according to equation 4.22 [10]:

$$(4.22) \qquad \frac{\Delta R(\nu)}{R_0(\nu)} = \frac{8\pi^2 \nu}{c} F(\vartheta)\, \sigma\, \Im m[\alpha(i\nu)] \quad ,$$

where ϑ is the angle of incidence (5°÷7°) and $F(\vartheta)$ contains the dielectric response of the system [10]. Since the adsorbate polarizability $\alpha(v)$ is given by (with $\omega_{0,k}$ resonance frequency for the transition $v_0 \rightarrow v_k$) [10]:

$$(4.23) \qquad \alpha(i\omega) = \frac{2}{\hbar} \sum_k \frac{\omega_{0,k} \left| \langle v_k | \hat{\mu} | v_0 \rangle \right|^2}{\omega_{0,k}^2 - \omega^2 - i\frac{\omega}{\tau}} \quad ,$$

$F(\vartheta)$ for reflection at a metal surface becomes [10]:

$$(4.24) \qquad F(\vartheta) = \frac{sin^2 \vartheta}{cos \vartheta} \frac{4}{|\alpha(i\omega)|^2} \quad .$$

1.4.3 UV-Vis Absorption and photoluminescence spectroscopy

Ultraviolet–visible spectroscopy (UV-Vis) refers to absorption spectroscopy performed in the ultraviolet-visible spectral region. In this region of the electromagnetic spectrum, molecules undergo to electronic transitions. This technique is complementary to the fluorescence spectroscopy, which deals with transitions from excited states to the ground state, while absorption measures transitions from the ground state to excited state [11].

In the *absorption spectroscopy*, the system is excited from its ground electronic state (S_0) to one of the various vibrational states in the excited singlet (S_1) electronic state, by an absorption of a photon. The process is schematically depicted in Figure 4.4. By making the comparison between the detected radiation after the interaction with the sample and a blank measurement, as reported in Figure 4.5a for a double-ray absorption spectrophotometer, it is possible to detect which wavelengths are in resonance with the system [11].

In fluorescence spectroscopy, the species is first excited, by absorbing a photon, from its ground electronic state to one of the various vibrational states in the excited electronic state. Collisions with other molecules cause the excited molecule to lose vibrational energy until it reaches the lowest vibrational state of the excited electronic state. This process can be visualized with a Jablonski diagram [11], as reported in Figure 4.4.

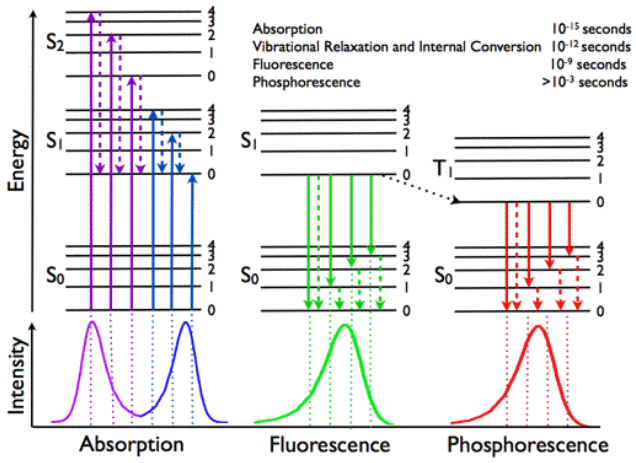

Figure 4.4. Jablonski diagram for a molecular excitation and de-excitation process, involving also intersystem crossing between the excitated singlet (S_1) and triplet (T_1) states.

The excited system then drops down to one of the various vibrational levels of the ground electronic state again, emitting a photon in the process. As molecules may drop down into any of several vibrational levels in the ground state, the emitted photons will have different energies, and thus frequencies. Therefore, by analyzing the different frequencies of light emitted in fluorescent spectroscopy, along with their relative intensities, the structure of the different vibrational levels can be determined. Figure 4.5b reports the typical 90° geometry used in fluorimeters for the detection of the induced fluorescence [11].

In a typical fluorescence (emission) measurement, the excitation wavelength is fixed and the detection wavelength varies, while in a fluorescence excitation measurement the detection wavelength is fixed and the excitation wavelength is varied across a region of interest.

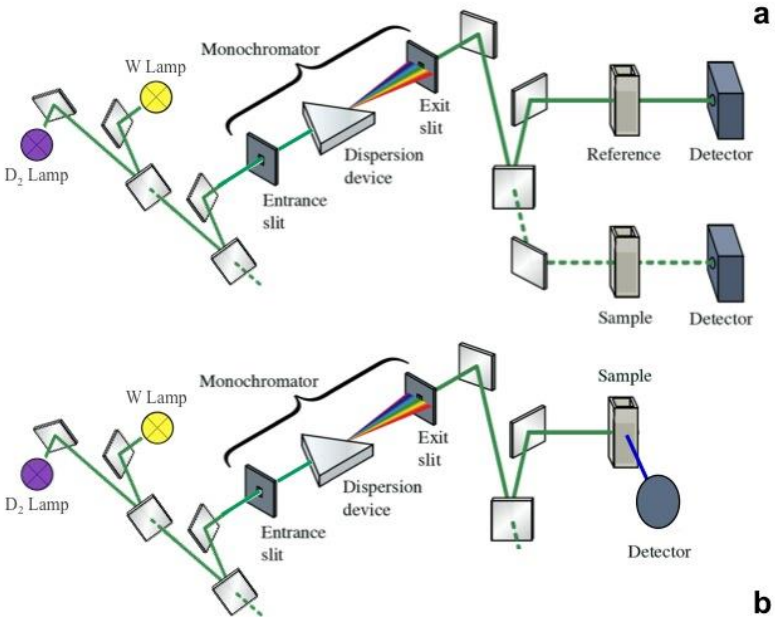

Figure 4.5. Schematic structures of a double-ray spectrophotometer (a) for absorption measurements and of a fluorimeter (b) for fluorescence spectroscopy.

In general, both absorption and fluorescence phenomena can be modeled using the probability of transitions [12]. The efficiency of light absorption at a wavelength λ by an absorbing medium is characterized by the *absorbance* A(λ) or by the *transmittance* T(λ), defined as

$$A(\lambda) = \log \frac{I_\lambda^0}{I_\lambda} = -\log T(\lambda) \qquad T(\lambda) = \frac{I_\lambda^0}{I_\lambda} \tag{4.25}$$

where I_λ^0 and I_λ are the light intensities of the beams entering and leaving the absorbing medium, respectively. In many cases, the absorbance of a sample follows the Lambert-Beer Law

$$A(\lambda) = \log \frac{I_\lambda^0}{I_\lambda} = \varepsilon(\lambda)\ell C \tag{4.26}$$

where $\varepsilon(\lambda)$ is the *molar absorption coefficient* (commonly expressed in L mol^{-1} cm^{-1}), C is the concentration (in mol L^{-1}) of absorbing species and ℓ is the absorption path length (thickness of the absorbing medium) (in cm) [11,12].

Failure to obey the linear dependence of the absorbance on concentration, according to the Lambert-Beer Law, may be due to aggregate formation at high concentrations or to the presence of other absorbing species [11,12].

The molar absorption coefficient, $\varepsilon(\lambda)$, expresses the ability of a molecule to absorb light in a given solvent [12]. In the classical theory, molecular absorption of light can be described by considering the molecule as an oscillating dipole. Then, the transition that occurs as result of the absorption of a "resonant" photon can be characterized by a quantity called the *oscillator strength*, *f*, which is directly related to the integral of the absorption band as follows:

$$f = \frac{mc^2}{N_a \pi e^2 n} \int \varepsilon(\bar{\nu}) d\bar{\nu} \tag{4.27}$$

where m and e are the mass and the charge of the electron, respectively, c is the speed of light, N_a is the Avogadro number and n is the index of refraction. In the definition of the oscillator strength, the absorption coefficient is usually expressed as a function of the wavenumber (in cm^{-1}). *f* is a dimensionless quantity and it is normalized so that its maximum value is 1. The oscillator strength is related to the square of the transition moment integral through the *Fermi golden rule*, in an equation that bridges the gap between the classical and quantum mechanical

approaches. Then, equation 4.28 states that the oscillator strength is given by the transition probability between the molecular initial and final states [12]:

$$f = \frac{mc^2}{N_a \pi e^2 n} \int \varepsilon(\bar{\nu}) d\bar{\nu} = \frac{8\pi^2 m\nu}{3he^2} \left| \langle \Psi_{ex} | \hat{M} | \Psi_{gr} \rangle \right|^2 , \tag{4.28}$$

where ν is the frequency of the incident radiation, h the Planck's constant, $\hat{M}$ the perturbation hamiltonian, while Ψ_{gr} and Ψ_{ex} are the ground state and the excited state wavefunctions, respectively.

REFERENCES

[1] D. J. Gardiner, *Practical Raman spectroscopy*, Springer-Verlag, 1989.

[2] R. Loudon, Theory of the first order Raman effect in crystals, *Proc. Royal Soc. A*, **275**, 218-232 (1963).

[3] W. H. Heitler, *The quantum theory of radiation*, Dover Publication, 1954.

[4] A. L. Fetter, J. D. Walecka, *Quantum Theory of Many-Particle Systems*, McGraw-Hill, 2000.

[5] G. B. Arfken, H. J. Weber, *Mathematical Methods for Physicist*, Academic Press, 2006.

[6] R. P. Eischens, S. A. Francis, W. A. Pliskin, The effect of surface coverage on the spectra of chemisorbed CO, *J. Phys. Chem.* **60**, 194-201 (1956).

[7] N. Sheppard, D. J. C. Yates, Changes in the infra-red spectra of molecules due to physical adsorption, *Proc. R. Soc. London A* **238**, 269-275 (1956).

[8] R. Greenler, Infrared study of adsorbed molecules on metal surfaces by reflection techniques, *J. Phys. Chem.* **44**, 310-315 (1966).

[9] K. W. Kolasinski, *Surface Science*, Wiley ed., 2008.

[10] Y. J. Chabal, Surface infrared spectroscopy, *Surf. Sci. Rep.* **8**, 211-357 (1988).

[11] D. A. Skoog, J. J. Leary, *Principles of instrumental analysis*, Saunders College Pub., 1992.

[12] B. Valeur, *Molecular Fluorescence: Principles and Applications*, Wiley-VCH Verlag, 2001.

Section 2

Ion-Modified Highly Oriented Pyrolytic Graphite (HOPG)

Chapter 2.1
Pd-catalyzed Oxygen Reduction Reaction and Water Remediation

This chapter reports the work performed on the ion-modified HOPG-based model catalysts during the first two years of the PhD.

As already discussed in the introduction, the best way to reach the goal of stable, efficient and cost effective electrodic materials for FCs is to use a rational design of the catalyst NPs/support assembly. In this respect, the approach is mainly based on rigorous studies of model electrodes, whose outcomes are capitalized to implement efficient real electrodes to be properly tested in real working conditions. In particular, HOPG (Highly Oriented Pyrolytic Graphite) is the most suitable sp^2-carbon model substrate, and it represents a simplified playground where the interaction between the catalyst NPs and the support can be easily studied.

HOPG is a carbon-based material made by high-temperature decomposition of gaseous hydrocarbons, often acetylene, followed by hot pressing at high pressure and temperature [1]. Pyrolytic carbon usually has a single cleavage plane because the graphene sheets crystallize in a planar order, as opposed to graphite, which forms microscopic randomly-oriented zones. Because of this peculiar structure, pyrolytic carbon exhibits several unusual anisotropic properties [1]. It is for example more thermally conductive along the cleavage plane than graphite, making it one of the best planar thermal conductors available. Moreover, pyrolytic graphite forms *mosaic crystals* with controlled mosaicities up to a few degrees [1].

Concerning the morphology, pure HOPG shows microcracks with varied length and width [2]. The existence of these cracks in crystallites of polycrystalline graphite was proposed firstly by Mrozowski [3]; for this reason, these features are usually known as *Mrozowski cracks*. In situ observations shows that these cracks tend to close up heating the sample at high temperature [2], as it is reported in Figure 2.1a.

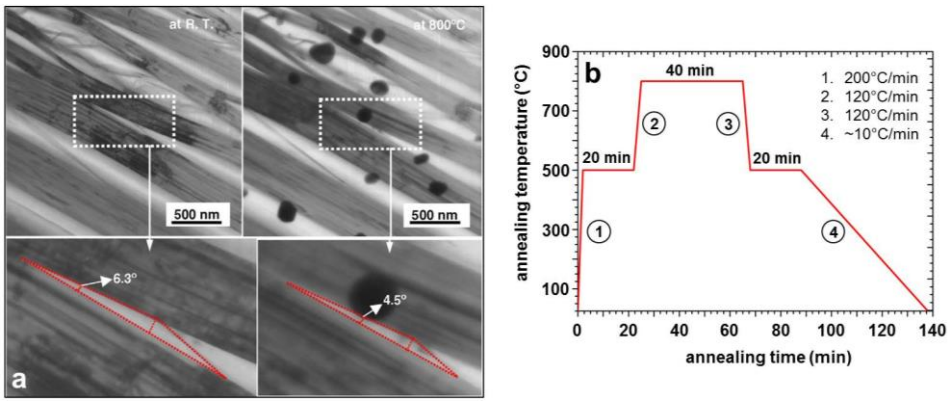

Figure 2.1. a: Comparison of the images of a feature (triangle) at room temperature (RT) and at 800°C (insets). Heating caused the contraction of the triangle and the cracks tend to close upon heating (taken from ref. [2]); b: Thermal annealing cycle carried out on the HOPG sample after the introduction in UHV chamber.

The walls of these cracks can expose dangling bonds that represent active sites for adsorbates (in particular molecular oxygen and water), disturbing therefore the subsequently surface analysis.

For this reason, in order to obtain a clean and flat sample surface, annealing in UHV has been performed after the peeling (by scotch tape) of HOPG in air, according to the procedure depicted in Figure 2.1b.

Following this recipe, it was possible to obtain a clean and atomically flat HOPG surface, as highlighted in Figure 2.2, which reports STM images taken after peeling and thermal annealing (in UHV) HOPG samples.

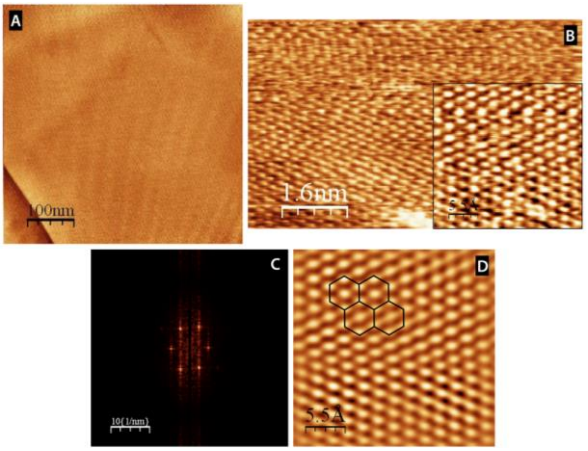

Figure 2.2. STM images taken on pure, peeled and annealed HOPG. a: large range image (500x500nm); b: high resolution image (with 2.5x2.5nm inset); c: Fourier transform of the inset in figure b; c: filtered image of atomic resolution of the (0001) basal plane of HOPG. All the images have been taken at positive bias (0.2 V) and with a set-point current equal to 0.2nA.

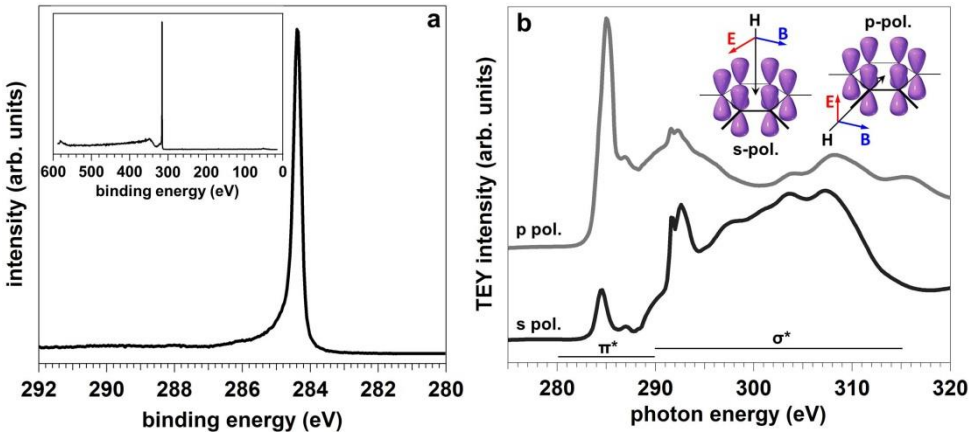

Figure 2.3. a: C 1s spectral region of annealed HOPG, acquired at 595 eV (the inset reports a wide survey scan); b: NEXAFS measurements of annealed HOPG acquired in s polarization (in plane) and p polarization (out of plane).

Figure 2.3 reports X-ray spectroscopy data obtained on annealed HOPG, at Bach beamline. Figure 2.3a reports the C 1s peak of HOPG, acquired with a photon energy of 595 eV. The peak shows a Doniach-Sunjic shape, with a FHWM of 0.35 eV. The high cleanliness of the surface and the low presence of defects is also highlighted by the survey scan reported in inset in Figure 2.3a and by the Near Edge X ray Absorption Fine structure Spectroscopy (NEXAFS) measurements reported in Figure 2.3b. For the NEXAFS measurement acquired in p polarization mode (*out of plane*) it is possible to observe the typical 1s-π* sharp transition at 285.0 eV [4], whereas the 1s-σ* transitions (between 290 and 315 eV) can be measured in s polarization mode (*in plane*) [4].

A viable strategy to enhance the catalyst NPs/support interaction is associated with the introduction of substrate defects that can act as trapping sites for anchoring highly dispersed catalyst NPs. In general, any morphological defect introduced by a carbon atom re-hybridization (sp^2 to sp^3) and amorphization of the substrate is beneficial to increase the substrate/NPs interaction [5]. In addition, if extrinsic chemical defects (such as boron, nitrogen and sulfur) are introduced by means of doping, specific interactions, possibly modulating the electronic charge of the catalyst NPs, can be produced. Therefore the modification of the support allows tailoring of the electronic properties of the catalyst

In the last few years, the chemical doping of sp^2–carbon materials by nitrogen has been studied [5,6,7,8], and excellent stability and high performances over time of the NPs/support assembly have been obtained [5,7,9]. Moreover, specific chemical interactions can trigger an enhanced chemical reactivity so that even normally inert

materials become highly reactive. Even more interestingly, it has been fully demonstrated that a properly doped support can become catalytically active itself [6,7,8].

Recent studies have demonstrated that the presence of distinct chemical defects in N-doped HOPG (hereafter N-HOPG) determines very interesting catalytic performance [6,7,8].

In the studies reported in § 2.1.1, § 2.1.2 and § 2.1.3 following a surface science approach, HOPG was used as a model system for mimicking sp^2 hybridized carbon based supports and ion implantation as doping technique. This route has been chosen because, being a kinetic driven technique, it allows obtaining of a wide set of N-based species.

The ion implantation by nitrogen and argon[1], has been performed under the same plasma conditions: i.e. at room temperature and with a pressure of the precursor gas (nitrogen or argon) equal to $2.2\ 10^{-6}$ mbar. In order to obtain a low projected range of ions into the target (to have chemical defect localized close the surface, in the case of N-implantation) and, at the same time, to study the influence of the surface morphology and chemistry of the surface after the implantation, the energy of the incident ions was set to 100 and 500 eV. The effect of the different implantation energies can be visualized by the LEED patterns reported in Figure 2.4. The LEED pattern of the pure support (Figure 2.4b) is a superposition of the diffraction patterns of the single orientational domains present in HOPG [10]; because ZYB grade HOPG has little distortion angles between adjacent mosaic tessellation (≈0.4°), the pattern is not characterized by single spots, but it assumes a circular geometry [10] due to the overlap of all the single domain diffraction spots (such as the *Debye-Scherrer* phenomenon that occurs in X-ray diffraction of powders, see Figure 2.4a). Figure 2.4c shows that the implantation at 100 eV leads to a weaker and more diffuse LEED pattern, because of the partial surface amorphization with the consequent loss of the crystalline order. On the other hand, the ion implantation performed at 500 eV generates a heavily amorphous surface, which eventually gives no diffraction. Thus, the surface does not show a LEED pattern, as evident in Figure 2.4d.

---

[1] In order to disentangle the effects on the material connected to the presence of new functional groups from those deriving from the morphological defects introduced by ion implantation, the Ar^+ implanted HOPG (Ar-HOPG) was also studied and used as an internal reference to gauge the results.

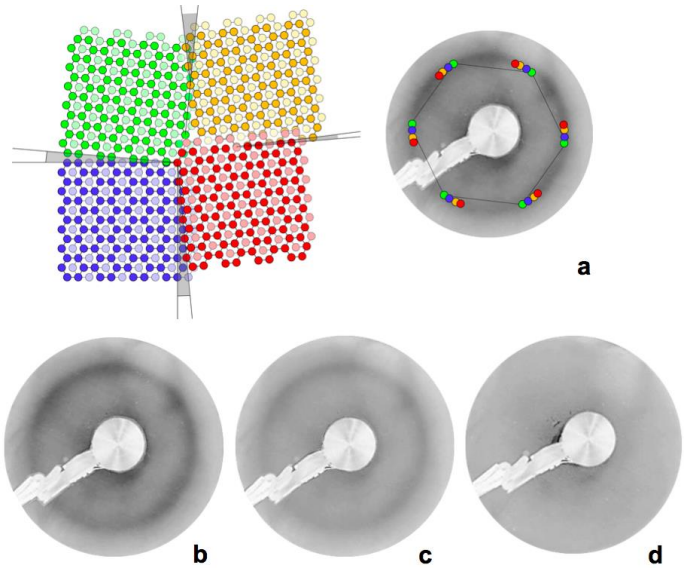

Figure 2.4. a: Mechanism at the base of the formation of the "Debye-Scherrer" rings in the LEED pattern of HOPG; b, c, d: LEED patterns (acquired at 170 eV) of pure HOPG and after nitrogen implantation at 100 eV and 500 eV, respectively.

In order to have a deeper physical insight on the ion implantation procedure, Monte Carlo simulations of the N-implantation in HOPG have been carried out assuming the Kinchin-Pease modelling [11] of the ion-target atom interaction.

Under the experimental conditions of the N-implantation, performed by using common ion guns, the nitrogen plasma contains both N^+ and N_2^+ ionic species. By simulating the interaction of both the species with the carbon support and taking the average, Monte Carlo simulations give a *projected range*, R_p, and a *full width at half maximum,* **(**FWHM) of the distribution, ΔR_p, equal to 7.9 Å and 10.3 Å for the 100 eV implantation, and to 18.6 Å and 17.3 Å for the implantation at 500 eV. Thus, using the combination of Surface Science techniques and Monte Carlo simulations, it has been demonstrated that it is possible to tune the projected range of the implanted atoms. At the same time, for the studied energies, it has been observed that no change occurs in the type or in the relative concentration of the chemical functionalities introduced by the N implantation (see § 2.1.1 and 2.1.3).

The ion implantation process can be interpreted by assuming the so-called *three step model* [12] where:

1. The interaction of the ion beam with the first layer of the target does not change significantly the energy of the ion beam itself if the energy is much higher than the displacement energy $\Delta E_{Frenkel}$ necessary to produce a Frenkel couple

($\Delta E_{Frenkel}$ = 47.3 eV for graphite [13]). Then, the energy loss of the ions due to the interaction with the first layers of the target is negligible. As a direct consequence of the high kinetic energy, an amorphous region (localized within the first layers of the target) is expected;

2. During the ion penetration and propagation into the target, thermal spikes can occur along the ion trajectories due to the energy exchange between ions and target. The consequent *high energy collision cascades* can be at the origin of *non-equilibrium* or *non-thermodynamic defects* production (due to the high local temperature generated in these thermal spikes the reactions taking place within this scenario are obviously under *kinetic control*);
3. Finally, for spatial regions close to the R_p, the ions are considered in thermal equilibrium with the target and the chemical reactions are under *thermodynamic control*. In this way, *equilibrium* or *thermodynamic defects* are generally localized close to the R_p.

Figures 2.5a and b report the multipeak analysis of the C 1s and N 1s signals of the as-implanted N-HOPG, acquired in normal emission (NE) and grazing emission (GE) at Bach beamline (using a photon at 595 eV). The implantation was performed in situ at using 100 eV ions. In the case of the C 1s de-convolution, four components at 283.7, 284.4, 285.5 and 286.5 eV, can be resolved. According to literature, they can be assigned to carbon vacancy (dangling bonds) [14,15], to sp^2 hybridized carbon forming the pure graphitic lattice, to sp^3 hybridized carbon from the partial surface amorphization induced by the ion implantation [16 ,17] and finally to C-N bonds [7,8,18], respectively. A fifth minor component, centered at about 288.1 eV can be associated with C bound to N and O (formally described as C-N(O)), due to low oxygen contamination of the preparation chamber or of the gas line providing the N_2 to the ion gun.

N-doping induces many different chemical defects in HOPG (the C-N signal counts for the 12.3% of the total C 1s photoemission line), whose characterization has been carried out by analysing the N 1s XPS signal for the as-implanted HOPG, as reported in Figure 2.5b. Five different components have been identified, whose FWHM and BE values are perfectly in agreement with the literature data on related systems. The components centered at 398.1 eV, 400.2 eV and 401.4 eV correspond to sp^2 C-N defects, which can be described as *pyridinic* [7,8,19,20], *pyrrolic* [7,8,19] and *N*

graphitic defects [7,8,19,20], respectively. The component centered at 399.0 eV matches with –CN terminal groups [20,20]. Finally, the component centered at 402.8 eV can be attributed to a N^+ or N_2^+ ion species trapped into a carbon vacancy [14].

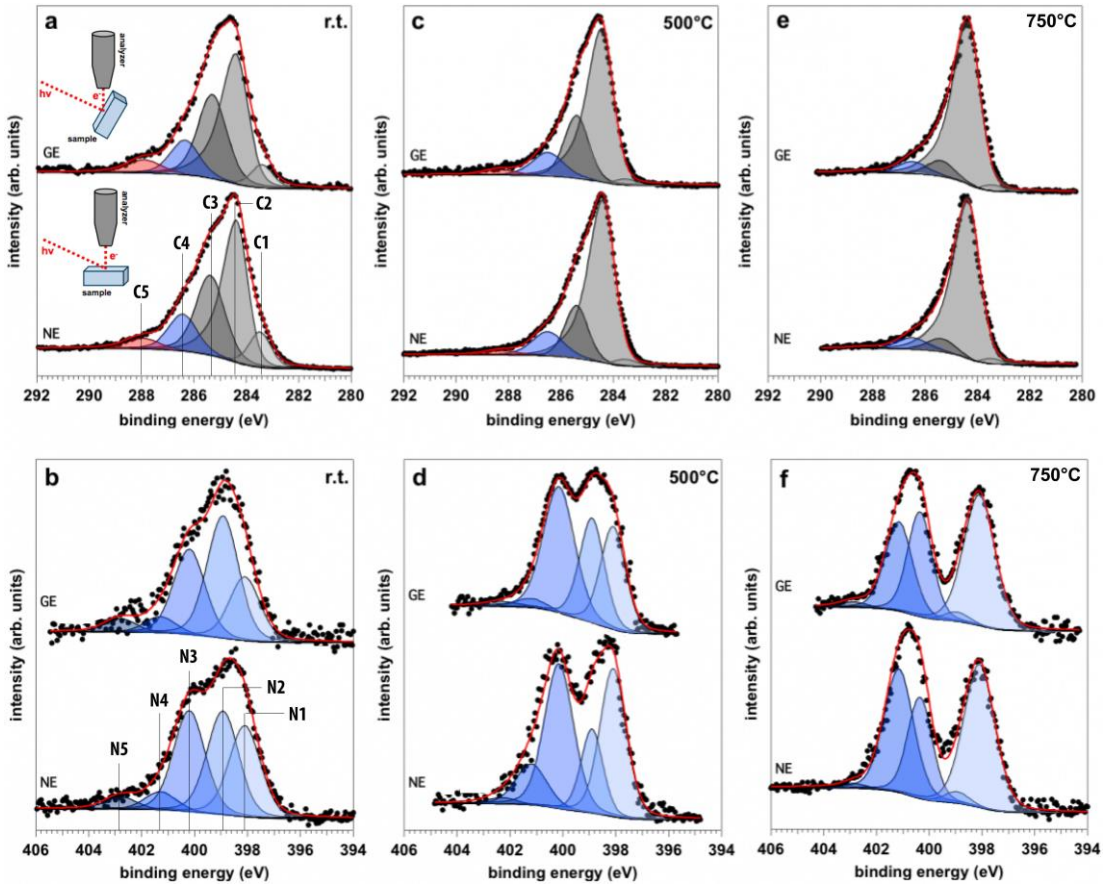

Figure 2.5. Multi peak analysis of C 1s and N 1s core levels, for as-implanted (a, b) and annealed N-HOPG, at 500°C (c, d) and 700°C (e, f).

In order to observe the temperature evolution of these defects, C 1s and N 1s photoemission measurements at different annealing temperatures (at 500°C and 750°C) have been carried out. Every thermal cycle was 30 minutes long. The ratio of the area of each chemically shifted peak over the total core level signal area is shown in Figure 2.6 and reported in Table 2.1. The most striking feature is the removal –CN groups as the annealing temperature increases (see also the change in the shape of the N 1s signal obtained after annealing at 500°C and 750°C, reported in Figure 2.5d and f, which is due to the decrease of the –CN related peak). This result is in agreement with previous works [21,22], where the authors report TPD measurements indicating that the desorption of CN species (as HCN by H uptake from the residual H_2 in the UHV chamber) starts from 140°C. Another important consequence of the thermal

annealing is the increase of the intensity of the *N substitutional* defects with the increase in the annealing temperature. This phenomenon has been observed also in the case of the thermal treatment of N-doped graphene layers obtained by chemical vapor deposition [18], and seems to point to a higher thermodynamic stability of this kind of defects as it can be easily inferred considering that in this case the N atoms can exploit the highest coordination with other C atoms.

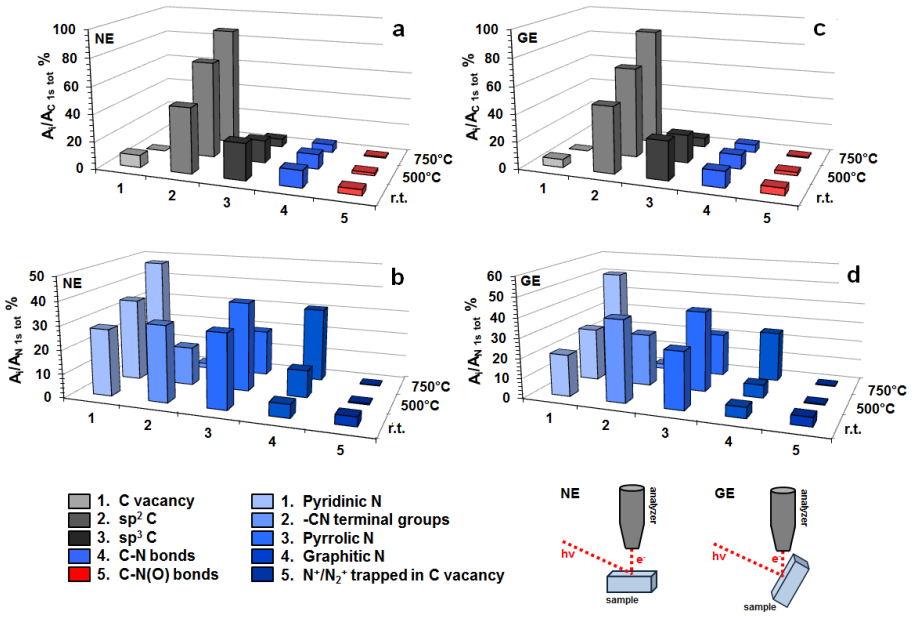

Figure 2.6. Trend of the normalized intensities of the single chemically shifted components for C 1s (a, c) and N 1s (b, d) photoemission peaks, as function of the annealing temperature. Figures a, b and c, d report the results obtained in case of NE and GE, respectively.

As a general comment, it is interesting to highlight that the pyrrolic defect can be efficiently converted in graphitic defects upon thermal annealing at temperature higher than 500°C [8,18]. As it possible to observe from Figure 2.6 and Table 2.1, the pyridinic defect concentration (together with the concentration of the other sp^2 C-N defects) undergoes an initial increase at 500°C, as result of the general decrease in the overall N 1s signal due to the desorption of HCN and healing of the carbon vacancies with the consequent release of N_2. For temperature above 500°C, the concentration of graphitic N increases as a product of the conversion of the pyrrolic defect, whose concentration undergoes an important decrease. Moreover, the thermal annealing cycles are accompanied by an important decrease in the surface amorphization (as it is observable from the decrease in the sp^3 C component), appreciable in particular at 750°C. All these results consistently delineate a picture

where HOPG modified surfaces can be used as model system where to investigate the impact of different C-N functional groups on specific electrochemical processes.

Table 2.1. Trend of the normalized intensities of the single chemically shifted components for C 1s and N 1s photoemission peaks, as function of the annealing temperature and for the two emission geometry.

	r.t.		**500°C**		**750°C**	
	NE	**GE**	**NE**	**GE**	**NE**	**GE**
C vacancy	9.04	5.96	0.40	0.35	0.21	0.16
sp^2 C	47.79	48.73	70.82	66.47	87.21	86.62
sp^3 C	26.71	28.43	16.16	20.40	5.95	6.69
C-N	12.33	11.74	10.73	10.40	5.89	5.76
C-N(O)	4.13	5.14	1.89	2.38	0.74	0.77
Pyridinic N	27.92	20.86	34.71	26.41	47.31	50.49
-CN terminal groups	31.77	40.86	16.17	26.23	2.00	2.36
Pyrrolic N	30.97	28.47	37.32	40.41	19.36	21.65
Graphitic N	5.51	5.33	11.37	6.56	31.10	25.18
N^+ / N_2^+ trapped C vacancy	3.83	4.48	0.43	0.39	0.23	0.32

Moreover, this ability to control the surface functionality and to study in detail its atomic structure represents an important methodological achievement. Another important observation can be discussed about the spatial localization of the N-based defects, from the angle resolved XPS (AR-XPS) measurements performed on the as-implanted and annealed N-HOPG. As it can be observed from Figure 2.6 and Table 2.1, in the as-implanted sample the –CN defects are localized mainly in the first atomic layers constituting the HOPG surface, since the relative intensity of the –CN defect component is higher when the take-off angle approximates the GE condition (high surface sensitivity). On the other hand, with the exception of the pyridinic defect, whose concentration is higher close the R_p (Table 2.1), the other defects are homogeneously distributed in the sample. At high annealing temperature (i.e. 750°C), Figure 2.6 and Table 2.1 show that the N-defects distribution is quite uniform in the sample, with the exception of the graphitic N, whose concentration is higher close to the top most layer. Furthermore, as introduced above, the pyrrolic N is unstable above 500°C and it converts to graphitic N. From Table 2.1 it is possible to observe that the concentration trend of pyrrolic N is closely related to the one observed for the graphitic defect: for both NE and GE, upon decrease of about 18 % of the pyrrolic N concentration which passes from 500°C to 750°C, the graphitic N concentration accordingly increases by the same amount.

To gain further insight into the site- and symmetry- specific electronic properties of the N-HOPG, NEXAFS measurements have been performed on the as-prepared and on the annealed (at 750°C) samples. It is well-known that NEXAFS can be successfully applied to explore the orientation and bond length of planar π-conjugated molecules adsorbed on a surface. Moreover, it was widely used to study the polarization dependence of the π- and σ-resonances for graphene- and graphite-functionalized systems. Figure 2.7 reports the polarization dependence of the NEXAFS spectra of C and N K edges. By the analysis of the N K edges, it is possible to observe a triplet centered between 399 eV and 402 eV, related to the N 1s – π* transition of different chemical states of N. The first feature, centered at 399.0 eV is associated with pyridinic nitrogen [19,23], while the third one (at 401.8 eV) represents the graphitic N defects [19,23]. The second absorption peak is ascribed to the terminal –CN groups, as reported in literature [23], supporting the XPS analysis discussed above. It is interesting to highlight that the graphitic N component results to be the most intense feature on the NEXAFS spectrum (acquired in p polarization) after the annealing at 750°C.

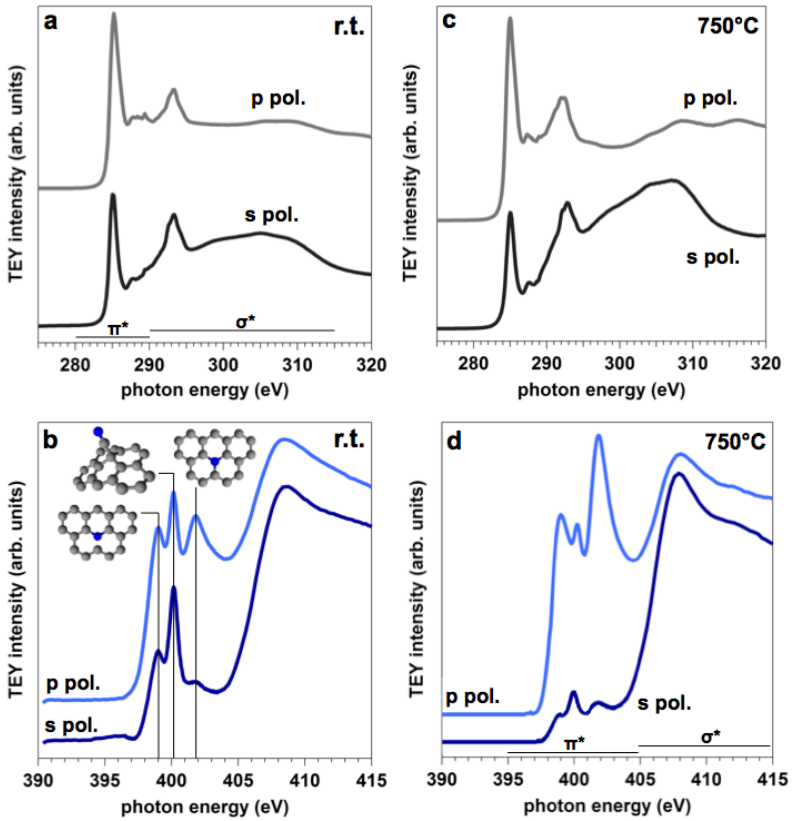

Figure 2.7. NEXAFS measurements of C (a, c) and N K edge (b, d) on N-HOPG at different polarizations, for the as-implanted (a, b) and the annealed (750°C) system (c, d).

In the first reported paper (§ 2.1.1), nitrogen and argon implanted (HOPG) electrodes (at 500 eV) have been studied, to the end of distinguishing whether the electrocatalytic activity towards the ORR of the modified electrodes is preferentially driven by chemical or morphological defects.

To understand the influence of nitrogen implantation in ORR, freshly cleaved HOPG and both Ar-HOPG and N-HOPG electrodes have been tested in an O_2 saturated 100 mM H_2SO_4 solution: the results are shown in Figure 2.8a and compared with the electrolyte background (indexed numbers). A remarkable difference can be seen between the implanted and pristine HOPG. The N-HOPG electrode shows a well-defined diffusion peak at −0.64 V vs. SCE, while Ar-HOPG shows a less defined peak, which is indicative of a more sluggish kinetics.

The observed peak current for O_2 reduction over the N-HOPG is proportional to the square root of the scan rate, indicating a diffusion-controlled process (inset Figure 2.8b). The oxygen reduction reaction mechanism at N-HOPG was studied combining RDE method at different electrode rotation rates with Koutecky-Levich analysis (Figures 2.8b and c). In this way, it was possible to determine the number of the transferred electrons and therefore the predominant reaction pathway for the ORR (by the value of the straight line slope reported in the inset of Figure 2.8c, derived at a potential equal to -0.64 vs. SCE). A value of 3.95 ± 0.12 was reproducibly found, indicating that O_2 is directly reduced to H_2O (with no side production of hydrogen peroxide) accordingly with the following reaction (for an acidic medium):

$$O_2 + 4H^+ + 4e^- \rightarrow 2H_2O \quad (2.1)$$

The results obtained clearly state that the activity of the N-HOPG toward ORR is the result of nitrogen doping since both Ar-HOPG and N-HOPG possess similar surface morphology and surface area, but different chemical surface functionalization. The enhanced catalytic activity of N-HOPG with respect to Ar-HOPG arises from the chemical interaction between O_2 and nitrogen functional groups, possibly through preferential adsorption and reactions at these sites. Then, the results indicate that the chemical defects are important factors in ORR kinetics, playing a pivotal role in the electrocatalytic activity [7,8].

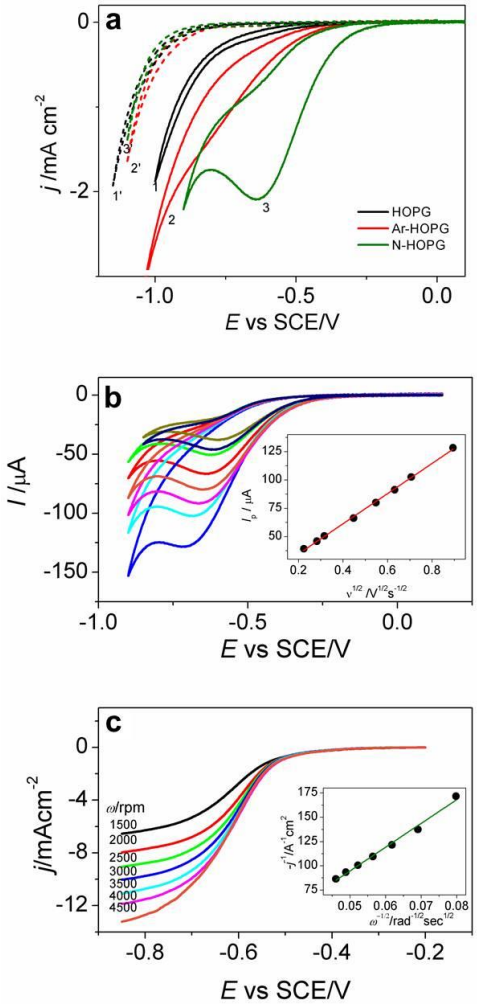

Figure 2.8. a: CV response of HOPG (1), Ar-HOPG (2) and N-HOPG (3) in a O_2-saturated 100 mM H_2SO_4 recorded at a scan rate of 30 mV/s. The indexed numbers are the corresponding CV responses in absence of O_2; b: CV response of N-HOPG electrode as a function of scan rate in the O_2-saturated electrolyte. The inset shows the cathodic peak currents versus the square root of the scan rate; c: RDE voltammetry curves for the ORR at N-HOPG electrode at different rotation speeds. The inset shows the corresponding Koutecky–Levich plot (scan rate, 5 mV/s) (adapted from § 2.1.1).

In the second reported paper (§ 2.1.2), the growth and the thermal stability of palladium nanoparticles, deposited in situ by physical vapour deposition (PVD), have been studied on pure and on nitrogen-doped HOPG (after implantation at 500 eV). Since most of the nitrogen-derived defects are buried below the surface (for an implantation energy of 500 eV the projected range is about 18 Å), they can not chemically interact with the Pd nanoparticles (Pd NPs). The amorphization induced by the ion beam in the outermost layers of the substrate however, beneficially affects the metal morphology, limiting the size of the NPs and improving their thermal stability, as well-documented by Figures 2.9a-d. The supported nanoparticles have been then tested towards the oxygen reduction reaction, indicating that the

electrochemical activity does not depend significantly on the ion implantation, but mostly on the amount of palladium, as reported in Figure 2.9e. This is in good agreement with the observation that there is no direct interaction between Pd and the N-based defects.

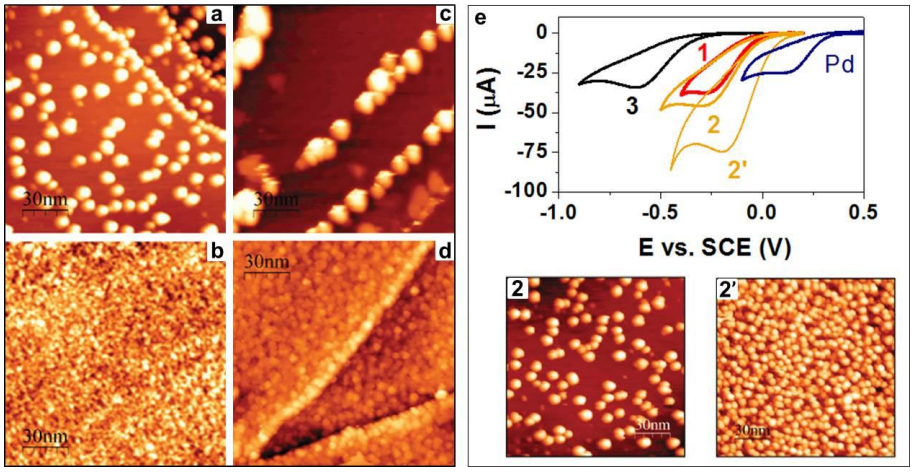

Figure 2.9. STM images taken at r.t. of 1.4 ML of Pd deposited onto pure (a, c) and N-HOPG (b, d). The (a, b) and (c, d), images are relative to the as-deposited and to the annealed systems (500°C – 15 min), respectively. Figure e report the CVs of bulk Pd, Pd(1.4 ML)/HOPG (1), Pd(1.4 ML)/N-HOPG (2), Pd(3.0 ML)/N-HOPG (2') and N-HOPG (3) in O_2 saturated 100 mM H_2SO_4 (adapted from § 2.1.2).

Then, in order to unravel the real role of the nitrogen-based defects on the electrocatalytic activity of the deposited metal (in particular, of Pd), in the third work here reported (§ 2.1.3) nitrogen functional groups have been introduced into the outermost layers of HOPG by soft ion implantation at 100 eV. Pd NPs have been then deposited onto both pure and nitrogen-doped HOPG. Interestingly, the Pd 3d photoemission peak for the Pd/N-HOPG sample taken under NE conditions (Figure 2.10a) shows an additional component compared to the deposition on pure HOPG, centered between 337 and 338 eV, which is partially attenuated when the take-off angle approximates the grazing emission (see § 2.1.3). For this reason, this component cannot be present at the surface of the Pd NPs but rather be attributed to very small Pd nanoclusters decorating surface defect sites (the lateral size of these small clusters have to be not more than 2-3 nm, since the photoelectron mean free path for the photoelectrons coming from the Pd 3d core level, in the condition of the measurements reported in this work, is equal to 1.2 nm). In these clusters, hosted in sub-nanometric pits induced by the ion implantation, the coordination by the nitrogen

functional groups leads to the formation of Pd^{x+} species with x = 2 – 4 at the interface with the substrate.

The same phenomenology is observed also in the case of the Pd deposition on the N-HOPG system annealed at 750°C, as well-documented by Figure 2.10a.

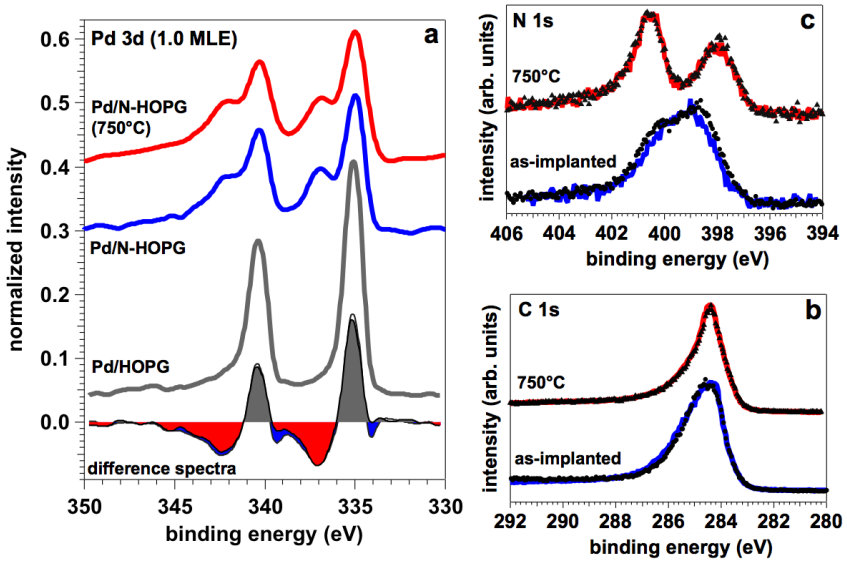

Figure 2.10. a: Pd 3d spectra acquired at 595 eV on 1.0 MLE of Pd deposited on pure, as-implanted and annealed N-HOPG. The reported difference spectra have been obtained by the subtraction of red and blue curves from the grey curve; b, c: C 1s and N 1s photoemission lines acquired after the deposition of 1.0 MLE of Pd on the as-implanted (blue curves) and annealed N-HOPG (red curves), respectively (the symbols represent the same photoemission signal acquired on the same systems before to the Pd deposition).

In order to observe the formation of highly oxidized Pd^{x+} ions, it is necessary that the Pd atoms trapped in the surface defect sites interact with a large number of electron withdrawing groups. As a proof of that, in the previous study on Pd deposited on N-HOPG implanted at 500eV (with a Rp=18.2Å), the same photoemission feature in the Pd 3d spectra was not observed; due to the higher implantation energy, the interface between the Pd NPs and the substrate was in that case constituted by an amorphous carbon layer, with a lower amount of nitrogen groups. Hence, in order to observe the high binding energy component in the Pd 3d spectrum (that means the presence of Pd^{x+} species), it is necessary to have a surface whose topmost layer is rich in strong electron withdrawing groups. It is interesting to highlight that no counterpart features in the C or N 1s peaks have been detected, as result of the Pd-N interaction (see Figures 2.10 b and c). The lack of these features, which are

reproducible and observable also in case of other Pd deposition techniques[2], is controversial and still under investigation. However, The presence of highly oxidixed pd species is in agreement by findings reported in literature; in particular, Seo et al observed the same component at high BE after the Pd deposition on graphene sheets functionalized by surface epoxy, hydroxyl and carboxyl groups [24]. This is in line with literature reports on Pt on N-HOPG, where oxidized Pt species due to charge transfer to the support were observed as well [5].

Interestingly, even if in this case Pd is directly interacting with the N centers, the supported Pd NPs on N-HOPG show the same electrocatalytic activity for ORR as the ones supported on pure HOPG (see § 2.1.3), similarly to what has been observed in the work reported in § 2.1.2. Moreover, the stability of Pd NPs on N-HOPG towards potential cycling decreased strongly due to the existence of Pd^{2+} at the interface, which can accelerate the dissolution of Pd atoms. This scenario is quite different from most literature works dealing with Pt NPs supported on nitrogen doped graphite [5,25]. Holme et al. [26] investigated theoretically that pyramidal Pt_4 clusters supported on pyridinic and pyrrolic nitrogen defects of N-HOPG had a weaker binding to oxygen atoms than that on pristine HOPG because of larger electron transfer from Pt NPs deposited over N-based defects. As the Pt-O binding energy is a little stronger than the optimal value [27], the slightly weakened binding of Pt to oxygen atoms points to a more active catalyst for ORR and methanol oxidation reaction (MOR). As a member of Pt group, Pd was expected to present the same behaviour of Pt, when supported on nitrogenous defects.

Since Pd on N-HOPG exhibited a low catalytic activity towards the ORR, a second reduction reaction, with enormous impact on the society of nowadays, has been considered: the electrochemical reduction of halogenated aromatic compounds, in particular benzyl chloride. Halogenated organic compounds represent one of the most important classes of molecules employed in organic synthesis both as reagents and solvents. This is particularly true in the case of organic chlorides since they are rather inexpensive. The efficient formation of carbon-carbon bonds is the most challenging aspect of the organic synthesis and innumerable examples can be found in literature, where organic chlorides or bromides are employed in coupling [28,29],

---

[2] In the work reported in § 2.1.3 the Pd nanoparticles were deposited in 100 mM H_2SO_4 via electrochemical reduction of $Pd(NO_3)_2$.

carboxylation [30] cyclization [31] and polymerization reactions [32]. These are just few examples for emphasizing the huge quantity of chemicals that every passing minute is processed for manufacturing useful drugs, material or products for the everyday life. The other side of the coin is that a variegated range of waste with stable chemical properties and toxicity is produced. In fact, organic chlorides cannot undergo an easy and fast natural degradation and this put some concern on their disposal and treatment. The degradation or conversion of organic chlorides is usually based on the reductive hydrodehalogenation reaction. However, because of the relatively high dissociation energy of C−Cl bond, catalysts are needed: the hydro-dehalogenation process is usually mediated by a transition-metal catalyst, such as Pd or Fe under hydrogen pressure [33] or by microbial methods [34]. Besides to chemical or biological methods, the electrochemical approach is becoming a valid alternative. In fact, electrocatalysis can be successfully employed either in organic electrosyntesis [35] or in degradation or conversion of halogenated pollutants to less harmful and possibly more valuable compounds [36]. This has boosted over the last decade the research of electrode materials active toward the C−X bond breaking, and, so far, Ag [37], Cu [38] and in particular Pd [39] were found to possess interesting electrocatalytic properties.

To investigate the benefits of ion implantation as doping technique of carbon materials in general, glassy carbon (GC) was used as substrate. The choice of GC was driven by the fact that it is a well-known and widely used standard material for electrodes and for many electrochemical applications [40].

GC is made by heat-treating various polymers, like polyacrylonitrile or phenolic resins [41,42,43,44]. By heating the polymer under pressure in an inert atmosphere up to 1000÷2000 °C, the heteroatoms evaporate until only carbon remains; the C-C bonds in the polymer backbone do not break at these temperatures, so the carbon atoms can form graphitic planes of limited size [43,44]. GC is constituted by carbon ribbons where nanometric graphene layers (trigonal carbon, sp^2 hybridization) having a lateral size (L_π) between 30÷70 Å [43,44,45] are assembled in graphitic stacking with L_z in the range of 50÷100 Å [43,44,45] (Figure 2.11). Tetrahedral carbons (sp^3 hybridization) form the main part of the cross linkages that connect together the different carbon nanoribbons in a random way [44,45].

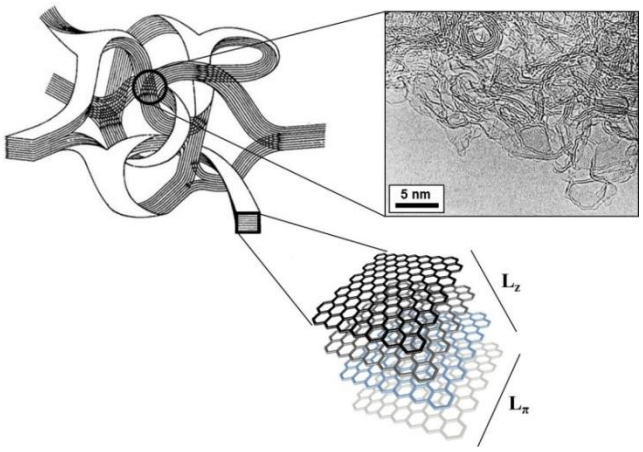

Figure 2.11. Structure of GC; the nanoribbon-based structure is evident in the reported TEM image (right).

Moreover, the usual surface treatments performed in order to obtain a clean system with a low surface roughness, such as the mechanical polishing of the GC surface with abrasive diamond or SiC pastes, have the effect of introduce a higher amount of sp^3 C and oxygen functional groups like alcohols (–OH), carbonyls (=O) and carboxyls (–COOH) [46], as reported in Figure 2.12, that can act as efficient traps for the extended nucleation of metal nanoparticles.

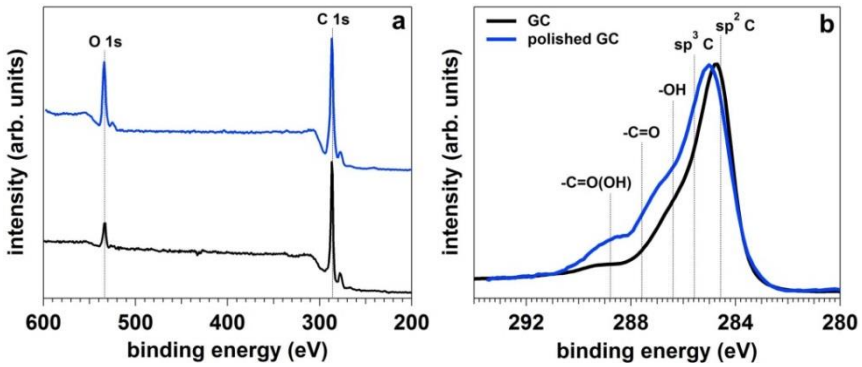

Figure 2.12. XPS analysis on GC and polished GC; a: survey scans; b: C 1s photoemission lines [46].

Then, in the last reported work (§ 2.1.4) Pd nanoparticles (NPs) were electrochemically deposited on three differently modified glassy carbon (GC) supports: pristine GC, nitrogen modified GC and Ar modified GC (N-GC and Ar-GC, respectively), both implanted at 500 eV.

The aim of this approach was to discriminate whether the electrocatalytic activity of Pd NPs toward the activation of carbon halogen bond is preferentially driven by chemical or morphological defects. Pd NPs morphology, dimension and distribution

were investigated by scanning electron microscopy. The outcomes indicated that the electrodeposition of Pd NPs on nitrogen-implanted GC results in smaller catalyst particle sizes and higher particle dispersion with respect to pristine GC, as demonstrated by Figure 2.13.

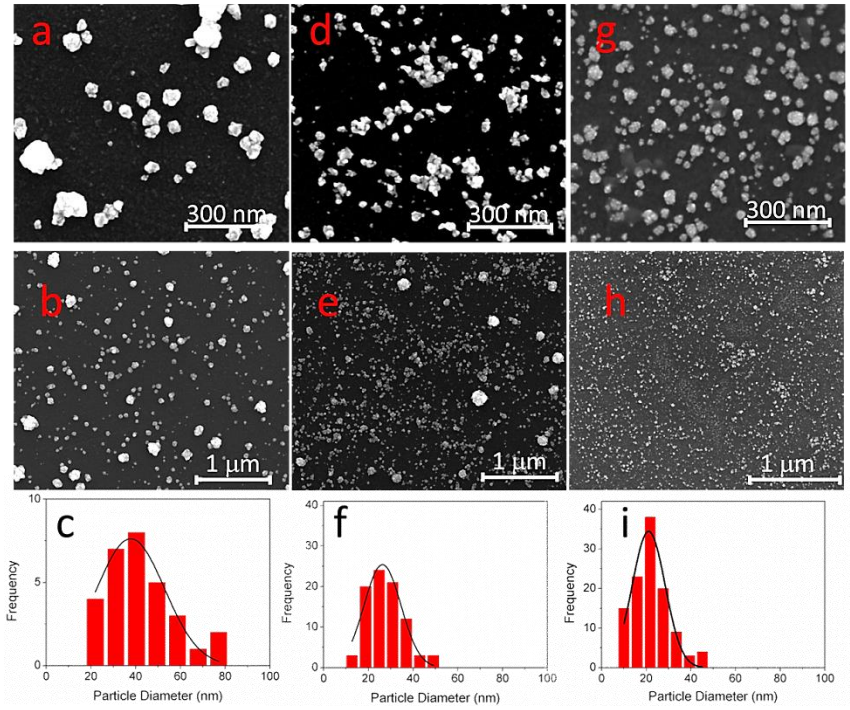

Figure 2.13. SEM images at two different magnifications and particle size distributions for: a-c) Pd/GC; d-f) Pd/Ar-GC and g-i) Pd/N-GC, obtained at the same Pd loading (taken from § 2.1.4).

The electrochemical behaviour of Pd on pure, Ar- and N-GC towards the reduction of the benzyl chloride ($PhCH_2Cl$)[3] is reported in Figure 2.14. As previously discussed, Pd NPs on Ar-GC are smaller and more uniformly dispersed than on pristine GC; however, besides a little difference of peak current, which may be associated with a different active surface area, Pd/Ar-GC shows similar catalytic activity and reduction mechanism with respect to Pd/GC (see § 2.1.4). These results assert that, even though Ar-GC has an increased number of defects with respect to pristine GC and the Pd NPs size is sensibly different between the two samples, the catalytic activity is not influenced by the morphology of the substrate surface. Furthermore, it must be stressed that both Pd/GC and Pd/Ar-GC do not show better

[3] If an efficient proton donor is not present in the elctrolyte, the charge consumption is very close to $1e^-$/molecule of $PhCH_2Cl$. When the applied potential is negative enough to ensure the reduction of the intermediate and stable benzyl radical, together with the presence of a proton source in the medium (e. g. water or a mineral acid), toluene is formed as principal reduction product.

performance in terms of catalytic activity with respect to bulk Pd, and this, also considering the benefit of employing a small amount of catalyst, puts a limit on the practical advantage of using a nanostructured electrode with respect to a bulk one.

As shown in Figure 2.14, Pd@N-GC is more active in terms of overpotential, mass catalytic activity (peak current/grams of Pd) and specific catalytic activity (peak current/surface area) not only with respect to Pd/GC or Pd/Ar-GC, but also to bulk Pd. The integrated current for the deposition process indicates that the Pd amount loaded on N-GC is comparable to that on Ar-GC; thus, the improved catalytic activity is not the result of different Pd loading or particle size on the three supports. This represents a clear example where the electrodic support exerts a synergistic action, promoting the catalytic activity of metal NPs toward a catalytic process. The nature of this increased catalytic activity derives from the interaction between nitrogen functional groups and Pd NPs during the reduction process since the Pd free N-GC was found to be not active by itself. Actually, both N-GC and Ar-GC supports result to be even less active than pristine GC by several mV. Then, it has been demonstrated that the modulation of the electronic properties of the metal overlayer by the interaction with support chemical or morphological defects may increase the catalytic activity and selectivity of the overall catalyst. Furthermore, thanks to the high surface-to-volume ratio it is possible to obtain high current density than the use of bulk Pd. DMoreover, the low loading of active phase enhances the efficiency while decreasing the reaction time and the process costs.

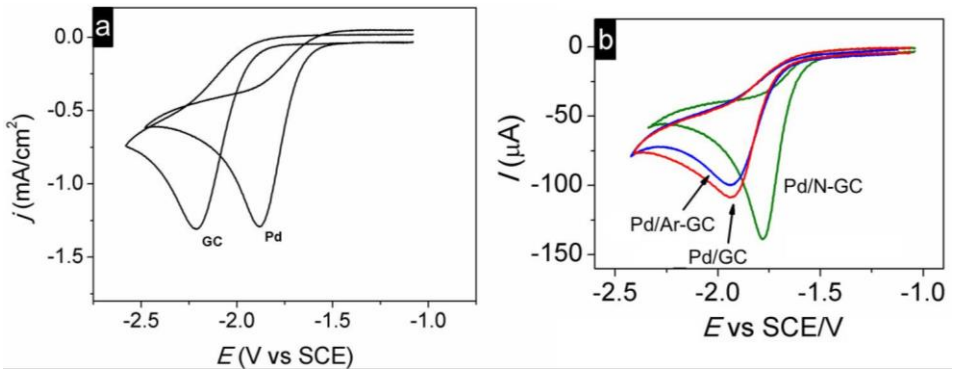

Figure 2.14. CVs of 2 mM benzyl chloride recorded in CH_3CN + 0.1 M tetrabutylammonium tetrafluoroborate ($TBABF_4$) at different electrodes: on pristine GC and bulk Pd (a) and on Pd/GC, Pd/Ar-GC and Pd/N-GC (b) (adapted from § 2.1.4).

2.1.1 Reprint of the paper: Electrochemical behavior of N and Ar implanted highly oriented pyrolytic graphite substrates and activity toward oxygen reduction reaction.

Electrochimica Acta 88 (2013) 477–487

Contents lists available at SciVerse ScienceDirect

Electrochimica Acta

journal homepage: www.elsevier.com/locate/electacta

Electrochemical behavior of N and Ar implanted highly oriented pyrolytic graphite substrates and activity toward oxygen reduction reaction

Marco Favaro, Lorenzo Perini, Stefano Agnoli, Christian Durante, Gaetano Granozzi, Armando Gennaro*

Dipartimento di Scienze Chimiche, Università degli Studi di Padova, Via Marzolo 1, 35131 Padova, Italy

ARTICLE INFO

Article history:
Received 13 July 2012
Received in revised form 15 October 2012
Accepted 15 October 2012
Available online 1 November 2012

Keywords:
Doped HOPG
Oxygen reduction reaction
Electrocatalysis
Ferrocyanide
Nitrogen functional groups

ABSTRACT

In this paper nitrogen and argon implanted highly oriented pyrolytic graphite (HOPG) electrodes have been studied, with the aim of distinguishing whether the electrocatalytic activity of the modified electrodes is preferentially driven by chemical defects or by morphological defects. Modified HOPG electrodes have been prepared by ion implantation and fully characterized by photoemission spectroscopy and scanning tunneling microscopy. Several different N-based defects have been identified and characterized in terms of their thermal stability. The modified electrodes were electrochemically characterized considering the electron-transfer kinetics of two redox probes $Ru(III)(NH_3)_6Cl_3$ and $K_4Fe(II)(CN)_6$: both types of electrodes show an increased performance in terms of standard rate constant k^0 with respect to pristine HOPG for the oxidation of $Fe(CN)_6^{4-}$ and this effect has been exclusively related to a morphological effect. N-implanted HOPG electrodes show an increased reactivity toward oxygen reduction reaction (ORR), the onset potential being more positive with respect to both Ar-implanted HOPG and pristine HOPG (0.09 and 0.28 V, respectively) and follow a four electrons reduction pathway to H_2O. The results indicate that morphological as well as chemical defects are important factors for influencing the ORR kinetics. However, the enhanced ORR activity at N-HOPG suggests a pivotal role played by the N-based chemical defects.
© 2012 Elsevier Ltd. All rights reserved.

1. Introduction

Carbon based materials are unquestionably the most common supports used in electrochemistry due to both their relative low cost and the predisposition to be chemically modified [1]. However, they generally exhibit poor inherent catalytic activity for many technologically relevant reactions, particularly for the oxygen reduction reaction (ORR), which is a topic of tremendous interest in the field of electrocatalysis, primarily in fuel cells [2] and metal-air batteries [3].

An ideal electrocatalyst support, besides being stable itself, should be specifically tailored to improve the catalytic activity and durability of the catalyst, which is mainly present as nanoparticles (NPs). A viable strategy for enhancing the durability of the catalyst/support assembly is to strengthen the catalyst NPs/support interaction by the introduction into the substrate of defects that can act as trapping sites for anchoring the catalyst NPs. In addition, if extrinsic chemical defects are introduced, specific interactions, possibly modulating the electronic charge of the catalyst NPs, can be produced, so that a modification of the electronic properties of the catalyst can be obtained by operating on the support.

Actually, in the last period the chemical doping of sp^2–carbon materials with nitrogen has gained attention [4–6], since excellent stability and high performances over time of the NPs/support assembly have been obtained [4,6]. Moreover, the specific NPs/support interactions trigger an enhanced chemical reactivity so that even normally inert cheap materials become active toward ORR [6]. Even more interestingly, it has been suggested that a properly doped support can become catalytically active itself [7]. However, the broad range of methodologies and materials employed to produce nitrogen doped catalysts make it extremely complicated to discern controlling parameters such as porosity, surface area, crystallinity and to understand the correlation between surface functionalities and their respective roles in the electrocatalytic activity. Actually, rigorous studies of model electrodes in terms of surface characterization and electrochemical behavior for the rationalization of the effects deriving from the doping of the supports is still missing. In this respect, Highly Oriented Pyrolytic Graphite (HOPG) is the most suitable sp^2-carbon *model* substrate and it is of particular interest because the electrochemical behavior of carbon nanotubes or graphene are commonly interpreted with reference to the graphite surface [8,9]. Therefore the outcomes of adopting HOPG as benchmark electrodes can be capitalized to implement efficient real electrodes based on the most innovative carbon based materials to be properly tested under working conditions. Recent studies have demonstrated

* Corresponding author. Tel.: +39 0498275132; fax: +39 0498275829.
E-mail address: armando.gennaro@unipd.it (A. Gennaro).

0013-4686/$ – see front matter © 2012 Elsevier Ltd. All rights reserved.
http://dx.doi.org/10.1016/j.electacta.2012.10.100

Link to the full paper: http://www.sciencedirect.com/science/article/pii/S0013468612017148

2.1.2 Reprint of the paper: Palladium nanoparticles supported on nitrogen-doped HOPG: a surface science and electrochemical study.

PCCP

RSC Publishing

PAPER

View Article Online
View Journal | View Issue

Palladium nanoparticles supported on nitrogen-doped HOPG: a surface science and electrochemical study

Cite this: *Phys. Chem. Chem. Phys.*, 2013, **15**, 2923

Marco Favaro, Stefano Agnoli, Lorenzo Perini, Christian Durante, Armando Gennaro and Gaetano Granozzi*

We have investigated by photoemission spectroscopy and scanning tunnelling microscopy what are the chemical and structural changes induced by nitrogen ion implantation (500 eV) on highly oriented pyrolytic graphite and how the defects induced by this process modify the growth and thermal stability of palladium nanoparticles, deposited *in situ* by physical vapour deposition. Since nitrogen derived defects are mostly buried below the surface, they are not accessible for a chemical interaction with metal nanoparticles; however, the amorphization induced by the ion beam in the outermost layers of the substrate beneficially affects the metal morphology, limiting the size of the nanoparticles and improving their thermal stability. The supported nanoparticles have been tested towards the oxygen reduction reaction indicating that the electrochemical activity does not depend significantly on the ion implantation, but mostly on the amount of palladium.

Received 21st November 2012,
Accepted 17th December 2012

DOI: 10.1039/c2cp44154c

www.rsc.org/pccp

1. Introduction

Metal nanoparticles (NPs) supported onto carbon based materials or oxides are unquestionably the most common and important heterogeneous catalysts and electrocatalysts. The great impact of supported NPs on the chemical production and refining explains the large efforts devoted to optimizing their efficiency and durability. However, these goals can be accessible only if a detailed knowledge of the whole set of parameters involved in the catalytic processes is achieved, *i.e.* understanding of structure, energy, nature and thermal evolution of the catalytic active sites. This includes also the support itself, which, besides being stable, should be specifically tailored to avoid degradation of the chemically active NPs. Therefore, a Surface Science (SS) characterization of the catalyst/support assembly at the atomic scale is a fundamental step for a knowledge based design of better catalytic systems.

In general, a strong NP/support interaction is beneficial to improve both the activity and durability of the (electro)catalyst. As to the activity, charge-transfer phenomena and interfacial reactive sites can be of relevance. Concerning the durability, an enhanced anchoring of catalyst NPs may prevent their agglomeration.

A viable strategy to improve the (electro)catalyst NP/support interaction involves the introduction in the substrate of tailored defects (morphological or chemical) that can act as trapping sites for highly dispersed NPs. When extrinsic chemical defects are introduced by means of doping, new specific interactions can be exploited to modulate the electronic structure of the catalyst itself.[1–3] Actually, enhanced stability and performances of NP/support assemblies have been reported adopting N-doped carbon supports.[4,5] In particular, some recent papers show that ion implantation (*i.e.* using an ion gun with a N_2 gas source) is an efficient technique to prepare N-doped carbon supports: M/N-doped (M = Pt, Pd, Fe, Co, Ru) assemblies were tested with respect to prototypical electrochemical (EC) reactions of relevance for fuel cell technology, batteries or in O_2 or H_2O_2 sensors, showing exceptional performances.[6–11] However, the morphological defects induced by the implantation process have been somewhat overlooked, and there is not yet a clear picture of the role of the different implantation parameters in the actual performances of the relative (electro)catalysts.

Very recently, we have reported a combined SS/EC study where Highly Oriented Pyrolytic Graphite (HOPG) substrates were compared after Ar- and N-implantation in order to discriminate between morphological and chemical effects:[12] several chemical defects were identified by an accurate X-ray photoemission spectroscopy (XPS) analysis, *i.e.* N^+ ions trapped into a carbon vacancy, –C=N terminal groups and C sp^2-N defects, which can be described as *pyridinic*, *pyrrolic* and *N substitutional* (or N graphitic).[13] The results indicate that morphological as well as chemical defects are important factors for influencing the oxygen reduction reaction (ORR) kinetics. However, the enhanced ORR activity at metal-free N-HOPG suggests a pivotal role played by the N-based chemical defects.

Dipartimento di Scienze Chimiche ed Unità di Ricerca INSTM, Università degli Studi di Padova, Via Marzolo 1, 35131 Padova, Italy. E-mail: gaetano.granozzi@unipd.it

This journal is © the Owner Societies 2013

Link to the full paper:
http://pubs.rsc.org/en/content/articlelanding/2013/cp/c2cp44154c#!divAbstract

2.1.3 Reprint of the paper: Pd Nanoparticles deposited on nitrogen-doped HOPG: New Insights into the Pd-catalyzed Oxygen Reduction Reaction.

Electrochimica Acta 141 (2014) 89–101

Contents lists available at ScienceDirect

Electrochimica Acta

journal homepage: www.elsevier.com/locate/electacta

Pd Nanoparticles deposited on nitrogen-doped HOPG: New Insights into the Pd-catalyzed Oxygen Reduction Reaction

Wenbo Ju[a,2], Marco Favaro[b,2], Christian Durante[b], Lorenzo Perini[b], Stefano Agnoli[b], Oliver Schneider[a,c,*], Ulrich Stimming[a,d,e], Gaetano Granozzi[b,1]

[a] Department of Physics E19, Technische Universität München, James-Franck-Str.1, 85748, Garching, Germany
[b] Department of Chemical Science, Università degli Studi di Padova, Via Marzolo 1, 35131, Padova, Italy
[c] Institute of Informatics VI, Technische Universität München, Boltzmannstr.3, 85748, Garching, Germany
[d] Institute of Advanced Study (IAS), TechnischeUniversität München, Lichtenbergstr. 2a, 85748 Garching, Germany
[e] TUM CREATE Ltd., 1 CREATE Way, #10-02CREATE Tower, Singapore 138602, Singapore

ARTICLE INFO

Article history:
Received 18 November 2013
Received in revised form 25 June 2014
Accepted 25 June 2014
Available online 11 July 2014

Keywords:
Oxygen reduction reaction
Electrocatalysis
Substrate effect
XPS
Nitrogen doped HOPG

ABSTRACT

The combination of surface science and electrochemistry is an effective method to approach a fundamental understanding of electrocatalytic systems, especially of the catalyst/support assemblies. Extrinsic chemical defects in the support can affect the performances and this topic is much investigated in recent electrocatalyst research. In this work, nitrogen functional groups are introduced into the outermost layers of highly oriented pyrolytic graphite (HOPG) by ion implantation with a beam energy of 100 eV. Palladium nanoparticles (Pd NPs) are then electrochemically deposited onto both pure and nitrogen doped HOPG (N-HOPG). Pd^{2+} species located at the interface between the NPs and the nitrogen-rich surface were observed in the latter case. The supported Pd NPs on N-HOPG show the same electrocatalytic activity for oxygen reduction reaction (ORR) as compared with those supported on pure HOPG. However, the stability of Pd NPs on N-HOPG towards potential cycling decreases strongly due to the existence of Pd^{2+} at the interface, which can accelerate the dissolution of Pd atoms. This result is contradictory to results on supported Pt NPs from the literature where the merit of the N-doping was outlined.

© 2014 Elsevier Ltd. All rights reserved.

1. Introduction

Supported metal nanoparticles (NPs), as the most common heterogeneous catalysts and electrocatalysts, have attracted a significant amount of research. A single supported NP in contact with an electrolyte is a complex system whose general performances, such as activity, selectivity and stability, depend on many factors, i.e. surface composition, facets, lower-coordinated atoms and defects, size effects, support effects, specific properties of the electrochemical interface, electrolyte composition, and other parameters [1]. To achieve the goal of developing electrocatalysts with optimized efficiency and durability, the knowledge of the whole set of parameters included in the electrocatalytic processes is essential. Therefore, a surface science and electrochemistry (EC) approach to characterize the catalyst/support assembly at the nano-scale is fundamental to achieve a full understanding of an electrocatalytic system under investigation.

There is still an open debate on the influence of a support material on the catalytic performance of supported metal NPs [2]. Significant progress has been made in the past ten years especially in theoretical description of the elementary steps of electrocatalytic reactions. Both geometrical and electronic effects have been reported and been explained theoretically [3–5]. The introduction of tailored defects onto the support surface can improve the dispersion of metal NPs so as to reduce the amount of catalyst without compromising the electrochemical performance [2]. The defects can act as trapping sites for anchoring the metal NPs in order to prevent the decrease in the surface area caused by the agglomeration of metal NPs [6,7]. A charge transfer and electronic interactions between support and catalyst can modify the electronic structure of supported metal NPs, and thus can influence their activity for some specific reactions such as CO oxidation and O_2 reduction [8–10]. A lattice strain introduced into supported metal NPs by adjusting to the lattice structure of the support material can lead to a change

* Corresponding author. Tel.: +498928918105; fax: +498928918107.
E-mail addresses: oliver_m.schneider@tum.de (O. Schneider), gaetano.granozzi@unipd.it (G. Granozzi).
[1] 1Tel: +390498275158, Fax: +390498275161
[2] [2]W. Ju and M. Favaro contributed equally to this work and should be considered first authors

http://dx.doi.org/10.1016/j.electacta.2014.06.141
0013-4686/© 2014 Elsevier Ltd. All rights reserved.

Link to the full paper: http://www.sciencedirect.com/science/article/pii/S0013468614013577

2.1.4 Reprint of the paper: Electrocatalysis at palladium nanoparticles: Effect of the support nitrogen doping on the catalytic activation of carbon halogen bond.

Applied Catalysis B: Environmental 144 (2014) 300–307

Contents lists available at ScienceDirect

Applied Catalysis B: Environmental

journal homepage: www.elsevier.com/locate/apcatb

Electrocatalysis at palladium nanoparticles: Effect of the support nitrogen doping on the catalytic activation of carbon—halogen bond

Lorenzo Perini, Christian Durante, Marco Favaro, Stefano Agnoli, Gaetano Granozzi, Armando Gennaro*

Department of Chemical Sciences, University of Padova, Via Marzolo, 1, 35131 Padova, Italy

ARTICLE INFO

Article history:
Received 20 May 2013
Received in revised form 2 July 2013
Accepted 8 July 2013
Available online 17 July 2013

Keywords:
Doped glassy carbon
Electrocatalysis
Palladium
Nitrogen doping
Benzyl chloride

ABSTRACT

Pd nanoparticles (NPs) were deposited electrochemically on three differently modified glassy carbon (GC) supports: pristine GC, nitrogen implanted GC and Ar implanted GC. The aim of such an approach is to discriminate whether the electrocatalytic activity of Pd NPs toward the activation of carbon—halogen bond is preferentially driven by chemical or morphological defects. Modified GC electrodes were prepared by ion implantation whereas Pd was deposited according to a double-step potential deposition in a 1 mM $PdSO_4$ + 0.1 M H_2SO_4 solution.

The electrodes were fully characterized by X-ray photoemission spectroscopy, which allowed the identification of several different N-based defects. Pd NPs morphology, dimension and distribution were investigated by scanning electron microscopy. The outcomes indicate that the electrodeposition of Pd NPs on nitrogen-implanted GC results in smaller catalyst particle sizes and higher particle dispersion with respect to pristine GC. The palladium nitrogen-implanted electrode was tested in the electrochemical reduction of benzyl chloride, showing that Pd NPs result in a much higher catalytic activity than bulk Pd and Pd NPs loaded on the pristine GC electrode.

© 2013 Elsevier B.V. All rights reserved.

1. Introduction

Activation of the carbon—halogen (C—X) bond is a highly explored field in organic electrochemistry since it finds huge application in organic synthesis [1,2], in the control over radical polymerization [3,4], in pollutant degradation [5–7] and in mechanistic investigation on dissociative electron transfer (DET) [8–11]. The main drawback associated with the electrochemical activation of C—X is the very negative potentials required, and this is particularly true in the case of organic chlorides, which represent the most investigated ensemble among organic molecules containing a nucleofuge group. This has boosted over the last decade the research of electrode materials active toward the C—X bond breaking, and, so far, Ag, Cu and Pd were found to possess extraordinary electrocatalytic properties [12–16]. However, attempts to improve catalytic activity by changing from bulk electrode to nanoparticles (NPs) dispersed on a support, or by introducing a second or a third metal have not yet led to the desired improvements [17,18].

In principle, the catalytic activity can be increased either by a fine dispersion of the NPs or by modulating the electronic properties of the catalyst NPs by interaction with support chemical or morphological defects; as an example, a way to enhance the durability of the catalyst support assembly in the case of oxygen reduction is to strengthen the catalyst NPs support interaction by introducing into the substrate defects that can act as trapping sites for anchoring the catalyst NPs [19,20]. In this regard, Minguzzi et al. have recently observed that the electrochemical activation of a carbon surface in acidic media introduces oxygen functional groups which enhances the stability and the electrocatalytic activity of Ag NPs toward the C—X bond activation [21].

Among various forms of carbon, glassy carbon (GC) is the most important for use as an electrode in electrochemistry, since it shows very low electrical resistivity, it is non-porous and impermeable to gases, it has high chemical resistance and the widest potential range observed for graphitic carbon electrodes and, last but not least, it can be easily polished and managed [22]. This renders GC an optimal material for a basic investigation on how the chemical modifications of the support can affect the activity of the loaded catalyst. The chemical modification (hereafter referred to as doping) of a GC surface is generally performed by the adsorption or by the covalent bonding (grafting) of molecular catalyst or electronic mediators. Another option is to synthetize a doped GC by thermolysis of suitable carbon precursors (usually polymers) containing the desired heteroatoms [22,23] or by the mixture of resins and an inorganic source of heteroatoms, such as boric acid and ammonia [24]. In the present case, following a different approach, nitrogen

* Corresponding author. Tel.: +39 049 8275132; fax: +39 049 8275829.
E-mail address: armando.gennaro@unipd.it (A. Gennaro).

0926-3373/$ – see front matter © 2013 Elsevier B.V. All rights reserved.
http://dx.doi.org/10.1016/j.apcatb.2013.07.023

Link to the full paper: http://www.sciencedirect.com/science/article/pii/S0926337313004426

REFERENCES

[1] W. D. Callister, D. G. Rethiwisch, *Materials Science and Engineering: an Introduction*, Wiley & Co., 2010.

[2] K. Wen, J. Marrow, B. Marsden, Microcracks in nuclear graphite and Highly oriented pyrolytic graphite (HOPG), *J. Nucl. Mat.* **381**, 199-203 (2008).

[3] S. Mrozowski, Semiconductivity and diamagnetism of polycrystalline graphite and condensed ring systems, *Phys. Rev.* **85**, 609-620 (1952).

[4] R. A. Rosenberg, P. J. Love, V. Rehn, Polarization-dependent C(K) near-edge x-ray-absorption fine structure of graphite, *Phys. Rev. B* **33**, 4034-4037 (1986).

[5] Y. Zhou, R. Pasquarelli, T. Holme, J. Berry, D. Ginley, R. O'Hayre, Improving PEM fuel cell catalyst activity and durability using nitrogen-doped carbon supports: observations from model Pt/HOPG systems, *J. Mater. Chem.* **19**, 7830-7838 (2009).

[6] X. Wang, X. Li, L. Zhang, Y. Yoon, P. K. Weber, H. Wang, J. Guo, H. Dai, N-doping of graphene through electrothermal reactions with ammonia, *Science* **324**, 768-771 (2009).

[7] L. Qu, Y. Liu, J. B. Baek, L. Dai, Nitrogen doped graphene as efficient metal-free electrocatalyst for oxygen reduction in fuel cells, *ACS Nano* **4**, 1321-1326 (2010); L. Feng, L. Yang, Z. Huang, J. Luo, M. Li, D. Wang, Y. Chen, Enhancing electrocatalytic oxygen reduction on nitrogen-doped graphene by active sites implantation, *Sci. Rep.* **3**, 3306 (2013).

[8] Z. H. Sheng, L. Shao, J. J. Chen, W. J. Bao, F. B. Wang, X. H. Xia, Catalyst-free synthesis of nitrogen-doped graphene via thermal annealing graphite oxide with melamine and its excellent electrocatalysis, *ACS Nano* **5**, 4350-4358 (2011).

[9] T. Kondo, T. Suzuki, J. Nakamura, Nitrogen doping of graphite for enhancement of durability of supported platinum clusters, *J. Phys. Chem. Lett.* **2**, 577-580 (2011).

[10] A. Güttler, T. Zecho, J. Küppers, A LEED and STM study of H (D) adsorption of C (0001) surfaces, *Chem. Phys. Lett.* **395**, 171-176 (2004).

[11] G. H. Kinchin, R. S. Pease, The displacement of atoms in solids by radiation, *Rep. Prog. Phys.* **18**, 1-51 (1995).

[12] R. Bertoncello, A. Glisenti, G. Granozzi, G. Battaglin, F. Caccavale, E. Cattaruzza, P. Mazzoldi, Chemical interactions in titanium- and tungsten-implanted fused silica, *Journal of Non-Crystalline Solids* **162**, 205-216 (1993).

[13] D. Marton, K. J. Boyd, T. Lytle, J. W. Rabelais, Near-threshold ion-induced defect production in graphite, *Phys. Rev. B* **48**, 6757-6766 (1993).

[14] a: D. Q. Yang, E. Sacher, A spectroscopic study of CN_x formation by the keV N_2^+ irradiation of highly oriented pyrolytic graphite surfaces, *Surf. Sci.* **531**, 185-198 (2003); b: D. Brete, D. Przyrembel, C. Eickhoff, R.Carley, W. Freyer, K. Reuter, C. Gahl, M. Weinelt, Mixed self-assembled monolayers of azobenzene photoswitches with trifluoromethyl and cyano end groups, J. Phys.: Condens. Matter **24**, 394015 (2012).

[15] J.-A. Yan, M. Y. Chou, Oxidation functional groups on graphene: Structural and electronic properties, *Phys. Rev. B* **82**, 125403 (2010).

[16] R. A. P. Smith, G. C. Smith, P. Weightman, Effects of low energy argon ion irradiation on the carbon 1s photoelectron line of highly oriented pyrolytic graphite. *J. Electron Spectrosc. Relat. Phenom.* **152**, 152-157 (2006).

[17] T. S. Wang, J. J. Ding, R. Cheng, H. B. Peng, X. Lu, Y. T. Zhao, Diamond-Like Carbon produced by highly charged ions impact on highly oriented pyrolytic graphite, *Nuclear Instruments and Methods in Physics Research B* **272**, 15-17 (2012).

[18] C. Zhang, L. Fu, N. Liu, M. Liu, Y. Wang, Z. Liu, Synthesis of nitrogen-doped graphene using embedded carbon and nitrogen sources, *Adv. Mater.* **23**, 1020-1024 (2011).

[19] D. Usachov, O. Vilkov, A. Grüneis, D. Haberer, A. Fedorov, V. K. Adamchuk, A. B. Preobrajenski, P. Dudin, A. Barinov, M. Oehzelt, C. Laubschat, D. V. Vyalikh, Nitrogen doped graphene: efficient growth, structure, and electronic properties, *Nano Lett.* **11**, 5401-5407 (2011).

[20] N. Hellgren, J. Guo, Y. Luo, C. Såthe, A. Agui, S. Kashtanov, J. Nordgren, H. Ågren, J. E. Sundgren, Electronic structure of carbon nitride thin films studied by X-ray spectroscopy techniques, *Thin Solid Films* **471**, 19-34 (2005).

[21] I. Kusunoki, M. Sakai, Y. Igari, S. Ishidzuka, T. Takami, T. Takaoka, M. Nishitani-Gamo, T. Ando, XPS study of nitridation of diamond and graphite with a nitrogen ion beam, *Surf. Sci.* **492**, 315-328 (2001).

[22] J. A. Taylor, G. M. Lancaster, J. W. Rabalais, Interactions of nitrogen (N_2^+) and nitrosyl (NO^+) ions with surfaces of graphite, diamond, teflon and graphite monofluoride, *J. Am. Chem. Soc.* **100**, 4441-4447 (1978).

[23] X. Wang, Z. Hou, T. Ikeda, M. Oshima, M. Kakimoto, K. Terakura, Theoretical characterization of X‑ray absorption, emission, and photoelectron spectra of nitrogen doped along graphene edges, *J. Phys. Chem. A* **117**, 579-589 (2013).

[24] M.H. Seo, S.M. Choi, J.K. Seo, S.H. Noh, W.B. Kim, B. Han, The graphene-supported palladium and palladium–yttrium nanoparticles for the oxygen reduction and ethanol oxidation reactions: Experimental measurement and computational validation, *Appl. Cat. B: Environ.* **129**, 163-171 (2013).

[25] R. I. Jafri, N. Rajalakshmi, S. Ramaprabhu, Nitrogen doped graphene nanoplatelets as catalyst support for oxygen reduction reaction in proton exchange membrane fuel cell, *J. Mater. Chem.* **20**, 7114-7117 (2010).

[26] T. Holme, Y. Zhou, R. Pasquarelli, R. O'Hayre, First principles study of doped carbon supports for enhanced platinum catalysts, *Phys. Chem. Chem. Phys.* **12**, 9461-9468 (2010).

[27] J. K. Norskov, J. Rossmeisl, A. Logadottir, L. Lindqvist, J. R. Kitchin, T. Bligaard, H. Jónsson, Origin of the overpotential for oxygen reduction at a fuel-cell cathode, *J. Phys. Chem. B* **108**, 17886-17892 (2004).

[28] X. F. Wu, P. Anbarasan, H. Neumann, M. Beller, From Noble Metal to Nobel Prize: Palladium-Catalyzed Coupling Reactions as Key Methods in Organic Synthesis, *Angew. Chem. Int. Ed.* **49**, 9047-9050 (2010).

[29] R. N. Dhital, C. Kamonsatikul, E. Somsook, K. Bobuatong, M. Ehara, S. Karanjit, H. Sakurai, Low-Temperature Carbon–Chlorine Bond Activation by Bimetallic Gold/Palladium Alloy Nanoclusters: An Application to Ullmann Coupling, *J. Am. Chem. Soc.* **134**, 20250-20253 (2012).

[30] A. A. Isse, C. Durante, A. Gennaro, One-pot synthesis of benzoic acid by electrocatalytic reduction of bromobenzene in the presence of CO_2, *Electrochem. Commun.* **13**, 810-813 (2011).

[31] F. Bellesia, A. J. Clark, F. Felluga, A. Gennaro, A.A. Isse, F. Roncaglia, F. Ghelfi, Efficient and green route to γ-lactams by copper-catalysed reversed atom transfer radical cyclisation of α-polychloro-N-allylamides, using a Low Load of Metal (0.5 mol%), *Adv. Synth. Catal.* **355**, 1649-1660 (2013).

[32] A. J. D. Magenau, N. C. Strandwitz, A. Gennaro, K. Matyjaszewski, Electrochemically mediated atom transfer radical polymerization, *Science* **332**, 81-84 (2011).

[33] Y. Xie, D. M. Cwiertny, Chlorinated solvent transformation by palladized zerovalent iron: mechanistic insights from reductant loading studies and solvent kinetic isotope effects, *Environ. Sci. Technol.* **47**, 7940-7948 (2013).

[34] C. Scheutz, N. D. Durant, M. H. Hansen, P. L. Bjerg, Natural and enhanced anaerobic degradation of 1,1,1-trichloroethane and its degradation products in the subsurface – A critical review, *Water Res.* **45**, 2701-2723 (2011).

[35] M. J. Medeiros, C. S. S. Neves, A. R. Pereira, E. Dunãch, Electroreductive intramolecular cyclisation of bromoalkoxylated derivatives catalysed by nickel(I) tetramethylcyclam in "green" media, *Electrochim. Acta* **56**, 4498-4503 (2011).

[36] B. Huang, A. A. Isse, C. Durante, C. Wei, A. Gennaro, Electrocatalytic properties of transition metals toward reductive dechlorination of polychloroethanes, *Electrochim. Acta* **70** 50-61 (2012).

[37] A. A. Peverly, J. A. Karty, D. G. Peters, Electrochemical reduction of (1R,2r,3S,4R,5r,6S)-hexachlorocyclohexane (Lindane) at silver cathodes in organic and aqueous–organic media, *J. Electroanal. Chem.* **692**, 66-71 (2013).

[38] J. Simonet, Reactivity of α,ω-dibromoalkanes at copper and silver cathodes: (I) Behaviour of 1,3-dibromopropane, *J. Electroanal. Chem.* **632**, 30-38 (2009).

[39] A. A. Isse, S. Gottardello, C. Durante, A. Gennaro, Dissociative electron transfer to organic chlorides: Electrocatalysis at metal cathodes, *Phys. Chem. Chem. Phys.* **10**, 2409-2416 (2008).

[40] J. O'M. Bockris, R. E. White, B. E. Conway, *Modern Aspects of Electrochemistry*, Springer-Verlag, 1996; A. J. Bard, L. R. Faulkner, *Electrochemical Methods: Fundamentals and Applications*, Wiley & Co., 2000.

[41] J. C. Lewis, B. Redfern, F. C. Cowlard, Vitreous carbon as a crucible material for semiconductors, *Solid-State Electronics* **6**, 251-254 (1963).

[42] T. Noda, M. Inagaki, The structure of Glassy Carbon, *Bull. Chem. Soc. Jpn.* **37**, 1534-1538 (1964).

[43] F. C. Cowlard, J. C. Lewis, Vitreous carbon. A new form of carbon, *J. Mater. Sci.* **2**, 507-512 (1967).

[44] G. M. Jenkins, K. Kawamura, Structure of Glassy Carbon, *Nature* **231**, 175-176 (1971).

[45] A. F. Craievich, On the structure of Glassy Carbon, *Mater. Res. Bull.* **11**, 1249-1255 (1976).

[46] M. Favaro, L. Perini, C. Durante, S. Agnoli, G. Granozzi, A. Gennaro, *unpublished work*.

Section 3

Graphene Oxide (GO)

Chapter 3.1
Novel Approaches to GO Nanostructures

One specific branch of the research on graphene and graphene-related materials, which have made a profound impact in many areas of science and technology due to their remarkable physicochemical properties, deals with Graphene Oxide (GO). This can be considered as the most important wet chemistry-derived precursor for graphene synthesis by either chemical or thermal reduction processes [1,2,3,4]. GO consists of a single-layer of graphite oxide and is usually produced by the chemical treatment of graphite through oxidation, with subsequent dispersion and exfoliation in water or suitable organic solvents.

GO contains a wide range of reactive oxygen functional groups, which can be exploited in many applications. Principally, it is widely used as an easily obtainable wet-chemistry precursor of graphene [1,2,3,4].

Despite the relative novelty of graphene as a material of broad interest and potentialities [1,4], since its "discovery" in 2004, GO has a history that extends back for many decades to some of the earliest studies involving the chemistry of graphite [1]. The first attempt to obtain an oxidized form of graphite was performed in 1859 by the British chemist B. C. Brodie. He carried out the partial oxidation of graphite flakes by adding potassium chlorate ($KClO_3$) to a slurry of graphite in fuming nitric acid (HNO_3) [1,3,4,5]. Brodie determined that the resulting material was composed of carbon, hydrogen and oxygen, resulting in an increase in the overall mass of the graphite flakes [5].

Nearly 40 years after Brodie's seminal discovery, the German chemist L. Staudenmaier improved Brodie's $KClO_3$-fuming HNO_3 preparation by adding the chlorate in multiple aliquots over the course of the reaction (also, with the addition of concentrated sulfuric acid to increase the acidity of the mixture), rather than in a single addition as Brodie had done [1-4]. This slight change in the procedure resulted in an overall extent of oxidation similar to Brodie's multiple oxidation approach (C:O~2:1). This method is still used for obtaining partially reduced graphenes

(PRGs) [6,7]. Nearly 60 years after Staudenmaier, Hummers and Offeman developed an alternative oxidation method by reacting finely minced graphite with a mixture of potassium permanganate ($KMnO_4$) and concentrated sulfuric acid (H_2SO_4) [8]. This is still the primarily used graphite oxidation method, that allows obtaining in high yield high quality graphite oxide, the final precursor of GO [1-4].

Though others have developed slightly modified versions, these three methods comprise the primary routes for GO production, and little about them has changed. The GO synthesis that has been used in this doctorate thesis is reported in Appendix, and it is known as *modified Hummers' oxidation method* [9].

Importantly, it has been demonstrated that the products of these reactions are sensibly depending not only on the particular oxidants used, but also on the graphite source and reaction conditions [1-4].

Though permanganate is a commonly used oxidant (e.g. dihydroxylations), the active species is, in this case, the *diamanganese (VII) heptoxide* [1-4,10]. This dark red oil is formed by the reaction of potassium permanganate with sulfuric acid, through the following mechanism that leads to the dimerization of the MnO_4^- tetraoxide units [1,10]:

$$KMnO_4 + 3\,H_2SO_4 \rightarrow K^+ + MnO_3^+ + H_3O^+ + 3\,HSO_4^- \quad (3.1)$$

$$MnO_3^+ + MnO_4^- \rightarrow Mn_2O_7 \quad (3.2)$$

The Mn_2O_7 consists of a pair of tetrahedra that share a common vertex. The vertices are occupied by oxygen atoms and with the the Mn(VII) ion at the center of the tetrahedron . The connectivity is indicated by the formula $O_3Mn\text{-}O\text{-}MnO_3$, where the Mn-O-Mn angle is 120.7° [10]. The bimetallic heptoxide is by far more reactive than its monometallic tetraoxide counterpart [11]; moreover, Trömel and Russ demonstrated the ability of Mn_2O_7 to selectively oxidize unsaturated aliphatic double bonds over aromatic double bonds (such as styrene) [12]. Then, the presence of localized defects in the graphite π-structure may serve as seeds for the oxidation process.

Aside from the operative oxidative mechanisms, the precise chemical structure of GO has been the subject of considerable debate over the years, and even to this day no clear model exists. There are many reasons for this, such as the instrinsic complexity of the material (including sample-to-sample variability) due to its

amorphous, *berthollide character* (i.e. nonstoichiometric atomic composition) and the lack of analytical techniques for characterizing such materials (or mixtures of materials).

Despite these problems, considerable effort in research has been directed toward understanding the intimate structure of GO [1-4]. The earliest structural models of GO proposed regular lattices composed of discrete repeat units, in a way that is possible to describe as the "2D polymer" approach. The most well-known early models of GO are reported in Figure 3.1a.

The most recent models of GO have rejected the 2D polymer based model and have focused on a nonstoichiometric, amorphous alternative. The most well-known model is the one developed by *Lerf and Klinowski* (Figure 3.1b) [13,14]. By using several characterization techniques (NMR, cross polarization/magic angle spinning and FTIR) Lerf and Klinowski pointed out that the dominant structural features present on the surface of GO are tertiary alcohols and ethers, most likely 1,2-ethers (i.e. epoxides) [1,13,14]. A detailed chemical and structural characterization based on XPS, FTIR, UV-Vis absorption and Raman spectroscopies of the produced GO is reported in the appendix.

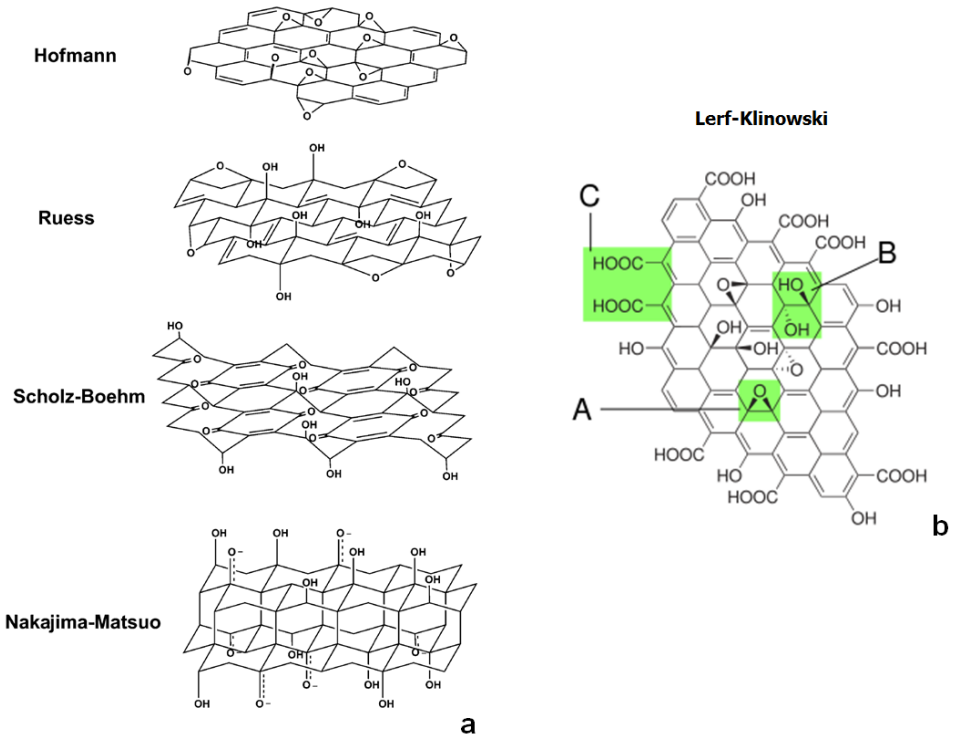

Figure 3.1. a: Old GO structures based on the 2D polymer model (taken from ref. 1); b: Lerf- Klinowski model of the GO structure (A: epoxy groups; B: hydroxyl groups; C: carboxyl groups).

GO and graphite oxide are semiconductor materials due to their disrupted sp^2 bonding networks. Because electrical conductivity can be recovered by restoring the π-network, one of the most important reactions of graphene oxide is its reduction [1,4,6]. Both experimental and computational studies show that the higher the oxidation grade of the GO, the higher is the energy gap between HOMO and LUMO [1-4,15]. Interestingly, it has been demonstrated that the *ratio of epoxides to alcohols increases with increasing the GO oxidation grade* [15]. Then, it is possible to control the charge transport properties of GO by changing the relative amount of epoxide groups with respect to the other oxygen functional groups. Epoxides are highly reactive [16], and can be easily reduced (recovering the π-structure of the graphitic plane) via several procedures, the most common of which are thermal treatments and chemical reductions [1-4,6,7,17].

An example of the reactivity of the epoxides on GO is reported in Figure 3.2: the evaporation of 2.0 MLE of metal Ti (by means the use of UHV-assisted PVD) on a GO free-standing paper (see appendix for the preparation details) leads to the loss of the initial charging effect (which caused a positive shift towards higher BE of the C 1s peak) by the reduction of the epoxides, recovering in this way the π-conjugation of the graphitic surface with the consequent decrease in the energy band gap of the material. As Figure 3.2a shows, the chemical reduction of GO via the surface redox reaction with metallic titanium is more efficient, in reducing GO, than a thermal annealing at 150°C for 5 min (in UHV environment).

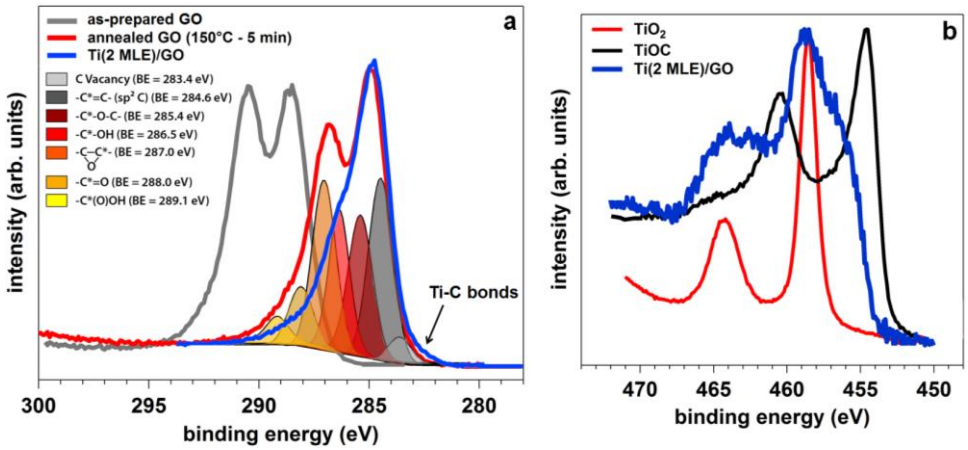

Figure 3.2. Surface redox reaction between metal Ti and GO studied by conventional XPS; a: C 1s photoemission lines for as-prepared GO, annealed GO (with decomposition into single chemical shifted components) and Ti(2MLE)/GO; b: Ti 2p peak of the Ti(2MLE)/GO. The Ti 2p signals for fully stoichiometric titania and for titanium oxy-carbide (TiOC) are reported for comparison.

Moreover, Figure 3.2b shows that Ti, which undergoes an oxidation to sub-stoichiometric titania (TiO_x) and to TiO_2 (upon the reduction of the GO), is also involved in the formation of C-Ti bonds. This constitutes an interesting result: titanium is rather selective in the interaction with the GO substrate: firstly Ti atoms undergo a redox reaction with oxygenated carbon groups, and only afterwards they react with carbon to form carbides. In particular, it has been found out that this reaction starts only at a nominal coverage between 1.5 and 2.0 MLE. This phenomenology has been studied in the paper reported in §3.1.1. A detailed description of the surface redox reaction between metallic Ti and GO is provided by combining in situ synchrotron radiation-based photoemission spectroscopy measurements and DFT calculations: the titanium atoms readily react with the oxygenated groups of graphene oxide, disrupting the C–O bonds, with the consequent formation of titania and the recovery of the sp^2 hybridized carbon atoms. When all surface oxygen is consumed, titanium can react with the carbon substrate and form carbidic species. As schematically illustrated in Figure 3.3c, the surface comprises small patches where GO has not been reduced (probably because of morphologically hidden areas) and large areas where the pristine GO has been converted into TiO_2/RGO or TiO_xC_y/RGO nano-clusters. The consistency of this model was proved by acquiring the C 1s signal with different photon energies (Figure 3.3a and b, at 596.5 and at 400.0 eV, respectively). This allows tuning the photoelectron inelastic mean free path (IMFP) and then the surface sensitivity of the PES measurements. Thanks to this analysis, it turns out that the peaks connected to oxidized carbon are very superficial, while the reduced and, especially, the carbidic ones are several layers deep, buried below multilayer islands of titanium oxides or oxy-carbides.

This clear sequence of possible redox reactions indicates that in oxidative conditions (i.e. in presence of external oxygen) the nucleation of titania takes place without the formation of direct Ti–C bonds, and this latter structural configuration is possible only when all the available oxygen is consumed. This is an important information for understanding the superior photocatalytic properties of TiO_2/G nano-clusters, since very recently the presence of direct Ti–C bonds has been claimed to be at the origin of the observed enhanced performances [18,19]. Resonant photoemission spectroscopy measurements allow identifying the presence and exact energy position in the valence band of the Ti–C and Ti–O–C states, which are supposed to control

the electron and energy transfer across the TiO_2/graphene interface. This study provides therefore a versatile method and the rationale for controlling, at the atomic level, the nature of the interface of graphene/metal oxide nanocomposites.

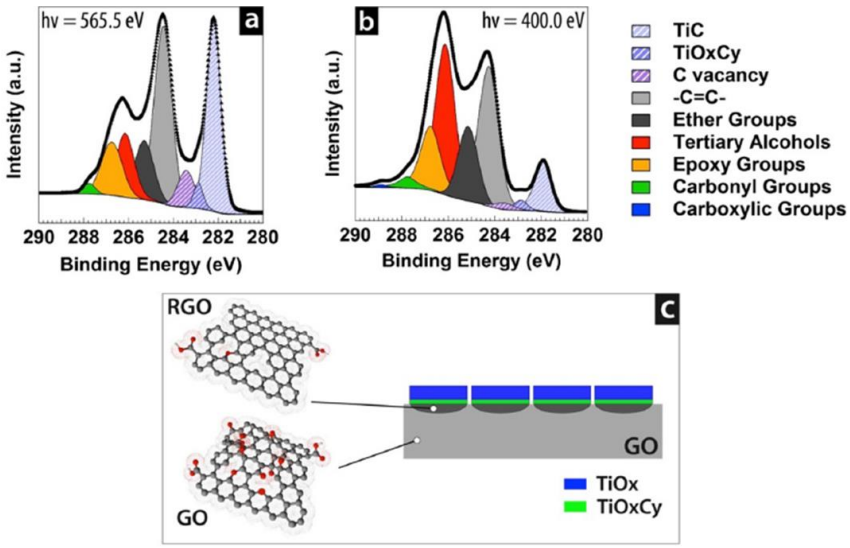

Figure 3.3. a,b: C 1s PE spectra taken at different energies of the photon beam (565.5 and 400 eV) demonstrating the different depth distribution of the C 1s components (with the support of the pictorial model reported in the figure c). The spectra have been acquired for a nominal coverage of 3.5 MLE (adapted from § 3.1.1).

The reactivity of the epoxides that decorate the GO surface can be exploited to produce new GO nanostructures. In the paper reported in § 3.1.2, it has been demonstrated that a GO paper can be nano-shaped by electrochemically cycling the GO paper itself used as a WE in a conventional three-electrode cell. As well reported in literature, during the electrochemical cycling the formation of linear chains of epoxy groups leads to the formation of carbonyl pairs that determine the unzipping of GO through the breaking of C-C bonds, with the consequent release in solution of GO nano-platelets with oxygen functionalities decorating the edges [20,21,22]. These new GO-based nano-objects, known as Graphene Oxide Quantum Dots (GOQDs), will be discussed in details in the Chapter 4.1. In the work reported in § 3.1.2, it has been demonstrated that the electrochemical etching can be used as a surgical tool to tailor the morphology of graphene electrodes and to impart special features, like micrometric channels and controlled mesoporosity (foams). The final materials, thanks to the high surface area (see the electrochemical responses reported in Figure 3.3), can represent a promising class of carbon-based supercapacitors, with potential application in energy storage [23,24,25,26].

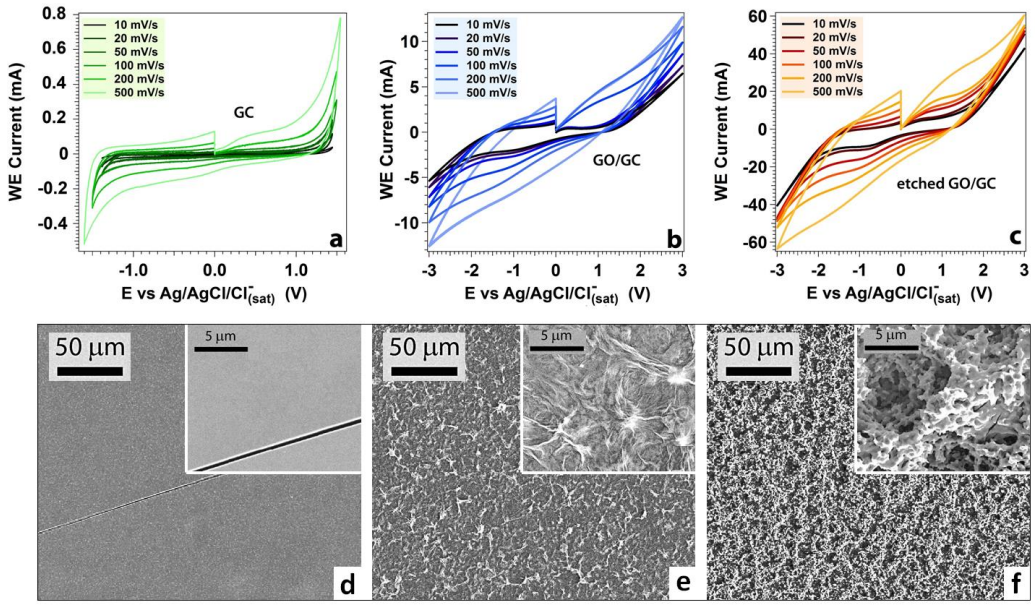

Figure 3.3. CVs at different potential scan rate (0.1 M PBS solution, pH=6.9) and SEM measurements, for (a,d) polished GC (reported as reference), (b,e) as-prepared GO/GC and (c,f) GO/GC after 2000 CV cycles (in the same electrolyte), respectively. All the three samples exposed an area of 2.5 cm^2 to the electrolyte.

Interestingly, by a suitable choice of the process parameters (i.e. pH and electrolyte concentration), different morphologies can be shaped. In particular, the GO WE has been etched within the same potential window (± 3.0 V vs. $Ag/AgCl/Cl^-_{(sat.)}$) in 0.1 M KOH, 0.1 M phosphate buffer solution (PBS) and 0.1 M H_2SO_4 in order to investigate the effect of pH (i.e. a pH of 13.0, 6.9 and 1.0, respectively) and of the intercalation of electrolyte ions. According to the literature [27], the kinetics of the etching is expected to be faster in alkaline, rather than acidic conditions because of the high concentration of oxygen-based radicals (i.e. the etching species) from the anodic electrolysis of water.

The SEM images of the *foams* obtained in the three different electrolytes are compared in Figure 3.4 with the one from the pristine GO/GC electrode. The GO/GC electrode prior to the electrochemical treatment (Figure 3.4a) presents a rather flat surface, made up by a parallel staking of the GO sheets that occasionally form wrinkles and ripples. As already discussed above, the electrochemical treatment in KOH (characterized by a faster etching kinetics) leads to a morphology of the GO/GC WE (Figure 3.4d) that consists of a sponge-like structure constituted by holes with circular shape (average diameter 1.2 ± 0.2 µm, average spacing 1.7 µm) expanding perpendicularly to the surface. These types of features have been observed in other studies [27,

28, 29] where graphite was etched in molten KOH at high temperature. The origin of the holes has been imputed to a *chemical drilling* operated by •OH [27,28], suggesting that a similar phenomenon takes place during our electrochemical treatment, but without the need of harsh conditions and with a better control of the final morphology.

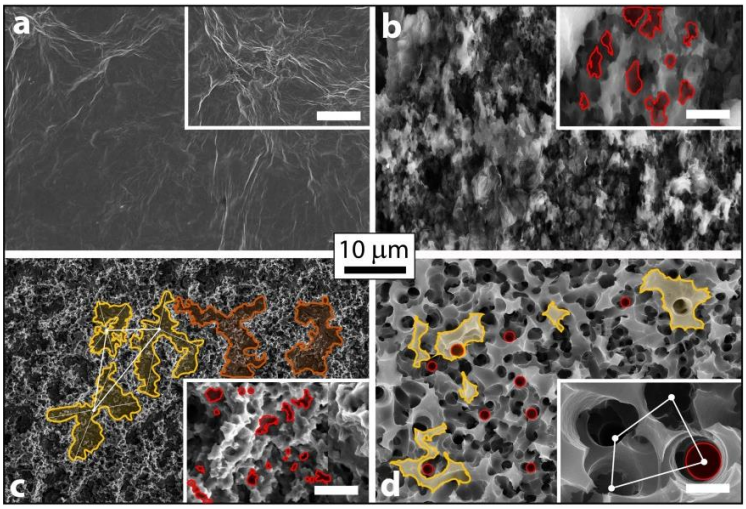

Figure 3.4. SEM micrographs of the pristine GO/GC electrode (a) and of the GO/GC WEs after the electrochemical etching in 0.1 M solution of H_2SO_4 (pH = 1.0) (b), PBS (pH = 6.9) (c) and KOH (pH = 13.0) (d). The scale bar reported in the insets is equal to 1 µm (taken from § 3.1.2).

Moreover, high-resolution SEM images indicate that the surface of these materials is decorated by *mesopores* with an average dimension between 10 and 20 nm, as shown in Figure 3.5.

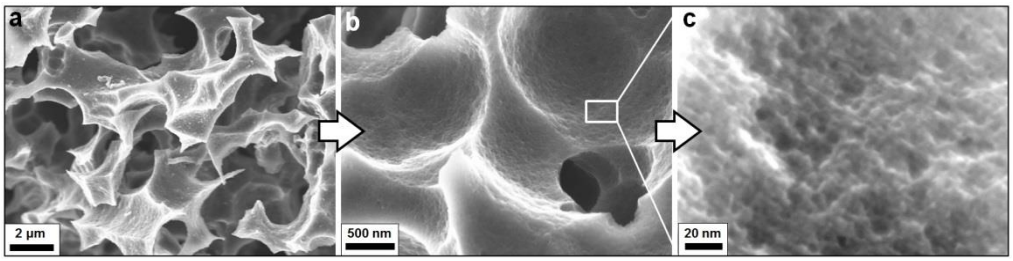

Figure 3.5. SEM micrograph of the KOH-derived GO *foams*; the high magnification SEM image (c) was taken on the white window reported in figure b (taken from § 3.1.2).

Thence, the electrochemical approach that has been explored in this work allows tailoring the morphology of the GO/GC WE and shaping the pores, providing a quite versatile method for the preparation of 3D structures for different potential applications, in particular for carbon-based electrochemical

capacitors [30,31]. With respect to the last mentioned application, specific capacitive currents were determined by means of CV on the three different *foams* in a 6.0 M KOH solution (as reported in Figure 3.6). The material obtained in KOH shows the highest specific capacitive current (calculated at 100 mV/s) of ~1 A/g, corresponding to a specific capacitance of 30 F/g, measured as reported in ref. 30 and obtaining the charge *q* by integrating the CV carried out at a scan rate of 100 mV/s [30,31]. This value is close to the best specific capacitance reached for carbon materials and aqueous electrolytes in real supercapacitors [30,32].

On the other hand, the different surface morphology exhibited by the PBS- and H_2SO_4-obtained foams leads to lower capacities compared to the previous one (24 F/g and 15 F/g, respectively).

As reported in literature [27,28,29,30] the special combination of *micro* and *mesoscopic* features of the KOH-treated sample makes it a promising candidate for potential applications in carbon-based supercapacitors and in Li^+ batteries. In fact, the vertical pores network caused by the EC etching coupled with the horizontal stacking of GO sheets constituting the electrode, may provide a quite efficient and rational grid for the mass transport of ions during the intercalation [26,31].

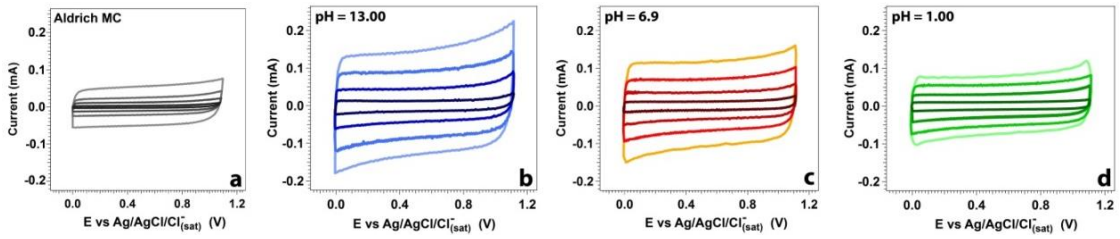

Figure 3.6. Capacitive current measurements (carried out in 6.0 M KOH electrolyte) at different scan rates (10, 20, 50, 100 mV/s) for (a) commercial *mesoporous* carbon (Aldrich, surface area in the range 150-250 m^2/g) and GO foams synthesized in 0.1 M KOH (b), phosphate buffer (c) and 0.1 M sulphuric acid (d). The CVs have been acquired with the same disk area exposed to the electrolytic solution ($1.25\ 10^{-1}\ cm^2$) (adapted from § 3.1.2).

As reported in the next chapter, it is possible to obtain also doped GOQDs simply by the introduction of dopant-bearing molecules in the electrolyte. Similarly to what has been described above for the preparation of pure GOQDs, it is possible to obtain also doped-GO foams. This highlights the potentiality of the electrochemical etching method: the introduction of an appropriate molecular precursor in the electrolyte allows to obtain, at the same time, doped-GOQDs in solution and doped-GO foams at the WE, which couple together the benefits of a high surface area with the unique catalytic properties provided by the chemical doping of the carbon lattice. Here it has been reported the ORR catalytic tests that have been performed on the co-doped systems, since the corresponding GOQDs are characterized by the higher activity between all the other prepared systems (see next chapter). The surface morphology of pure, B,N- and S,N-co-doped GO foams (hereafter GO, B,N- and S,N-GO foams, respectively) are reported in Figure 3.7.

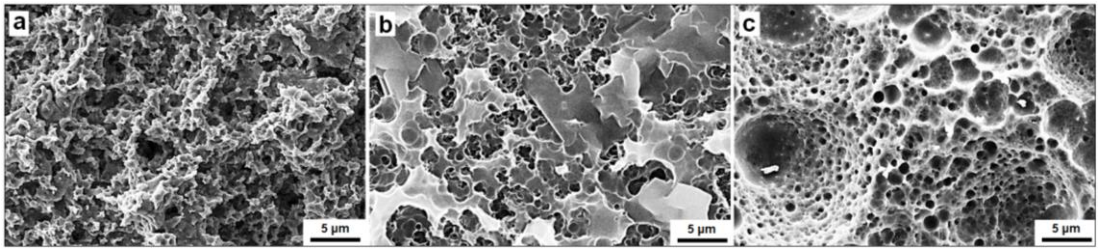

Figure 3.7. SEM topographies of pure (a, reported as reference), B,N- (b) and S,N-co-doped GO foams (c).

Figure 3.8 reports the voltammetric responses for the O_2 reduction on pure- (a-d), B,N- (e-d) and S,N-GO foams (i-n) acquired in O_2-saturated KOH 0.1 M solution; every system shows a well-defined cathodic peak for the irreversible reduction of O_2. As reported in Table 3.1, the doped systems display a positive shift of the onset and of the peak potential with respect to pure GO foam, indicating that the introduction of the heteroatoms promotes the catalytic activity towards the ORR (as it will be discussed in detail in the next chapter).

Similarly to what has been performed on the doped-GOQDs (see next chapter), ORR tests have been performed on the chemically reduced materials[1] to study the catalytic role played by the oxygen functional groups naturally present on the surface of the as-prepared systems.

[1] The chemical reduction have been performed using an excess of $NaBH_4$ under mild conditions (r.t.) for 12 hours.

From Figure 3.8 and Table 3.1 it is possible to observe that the chemical reduction treatment is beneficial for the enhancement of the electrocatalytic activity of the studied foams, with a net gain of almost 30 mV in the O_2 reduction peak potentials passing from the as-prepared to the chemically reduced systems.

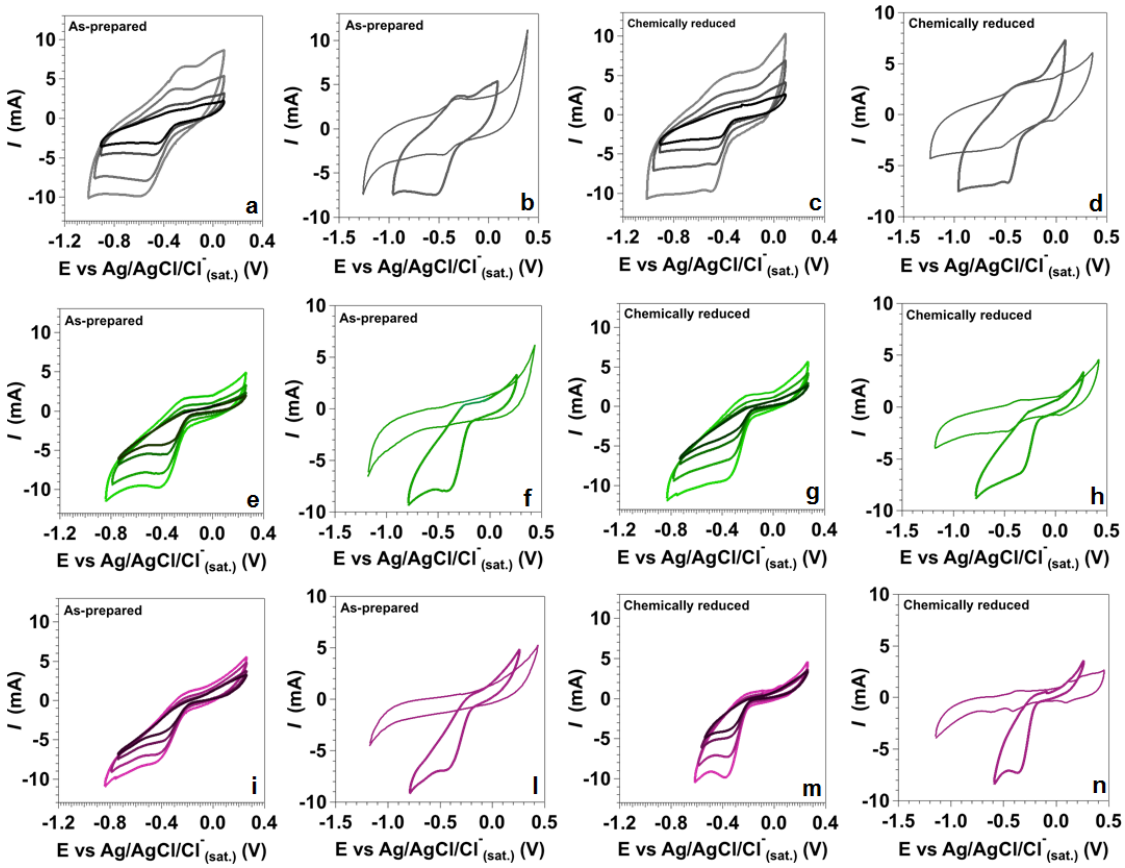

Figure 3.8. CV curves at different potentials scan rate (10, 20, 50 and 100 mV/s) recorded in O_2-saturated 0.1 M KOH solution for the as-prepared and chemically reduced pure (a, c), B,N- (e, g) and S,N-GO foams (i, m), respectively. Figures b-d, f-h and l-n reports the CVs (scan rate 50 mV/s) acquired in Ar- (thin curves) and in O_2-saturated 0.1 M KOH solution (thick curves), for the as-prepared and chemically reduced pure, B,N- and S,N-GO foams, respectively.

Table 3.1. Potential onsets (derived by the tangent method) and peak potentials for the as-prepared systems and after chemical reduction.

	Onset (V) [a]	**E_p (V)** [a]
GO Foam	-0.300	-0.470
B,N-GO Foam	-0.178	-0.340
S,N-GO Foam	-0.185	-0.356
red-GO Foam	-0.310	-0.448
red-B,N-GO Foam	-0.158	-0.312
red-S,N-GO Foam	-0.170	-0.328

[a] The values are calculated for a potential scan rate of 10 mV/s. The potentials are reported vs. the $Ag/AgCl/Cl^-_{(sat.)}$ reference electrode.

Interestingly, as also observed for the corresponding doped-GOQDs, in both cases (as-prepared and chemically reduced systems) it is observable a clear decrease of the ORR overpotential as a function of the dopant, according to the sequence pure > S,N > B,N (see also Figure 3.9).

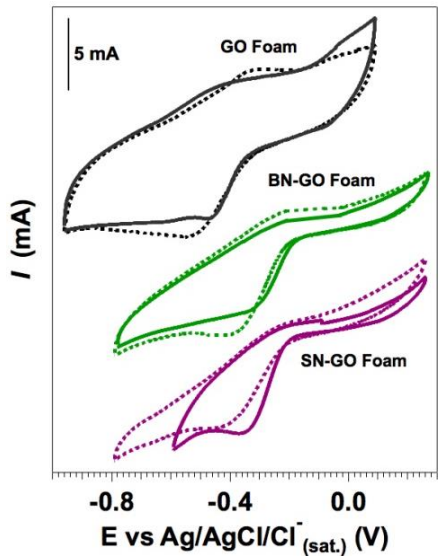

Figure 3.9. CVs recorded at 50 mV/s in O_2-saturated 0.1 M KOH solution for the as-prepared (dashed curves) and chemically reduced (solid curves) pure, B,N- and S,N-GO foams.

3.1.1 Reprint of the paper: TiO_2/Graphene nanocomposites from the direct reduction of graphene oxide by metal evaporation.

CARBON 68 (2014) 319–329

Available at www.sciencedirect.com

ScienceDirect

journal homepage: www.elsevier.com/locate/carbon

TiO_2/graphene nanocomposites from the direct reduction of graphene oxide by metal evaporation

Marco Favaro [a], *Stefano Agnoli* [a,*], *Cristiana Di Valentin* [b], *Cecilia Mattevi* [c], *Mattia Cattelan* [a], *Luca Artiglia* [a], *Elena Magnano* [d], *Federica Bondino* [d], *Silvia Nappini* [d], *Gaetano Granozzi* [a]

[a] *Department of Chemical Sciences, University of Padua, I-35131 Padova, Italy*
[b] *Dipartimento di Scienza dei Materiali, Università di Milano-Bicocca, Via Cozzi 53, 20125 Milano, Italy*
[c] *Materials Science Department, Imperial College, London, UK*
[d] *Istituto Officina dei Materiali (IOM)-CNR, Laboratorio TASC, Area Science Park-Basovizza, Strada Statale 14, Km.163.5, I-34149 Trieste, Italy*

ARTICLE INFO

Article history:
Received 24 July 2013
Accepted 1 November 2013
Available online 11 November 2013

ABSTRACT

We demonstrate that graphene oxide can be efficiently reduced by evaporating metal Titanium in high vacuum. A detailed description of this reaction is provided by combining *in situ* photoemission spectroscopy measurements and DFT calculations: the titanium atoms readily react with the oxygenated groups of graphene oxide, disrupting the C–O bonds, with the consequent formation of titania and the recovery of the sp^2 hybridized carbon atoms. When all surface oxygen is consumed, titanium can react with the carbon substrate and form carbidic species. Resonant photoemission spectroscopy measurements allow identifying the presence and exact energy position in the valence band of the Ti–C and Ti–O–C states, which are supposed to control the electron and energy transfer across the TiO_2/graphene interface. Therefore with this study we provide a versatile method and the rationale for controlling, at the atomic level, the nature of the interface of graphene/metal oxide nanocomposites.

© 2013 Elsevier Ltd. All rights reserved.

1. Introduction

Graphene oxide (GO) has emerged as one of the most effective platform for the development of carbon based nanotechnology [1,2]. GO can be produced by cheap and sustainable sources on a large scale [3,4] and can be easily manipulated by different wet chemistry methods [5] for assembling more complex nanostructures [6]. Very often, GO is used as a convenient tool for the ultimate delivery of graphene (G), and therefore of its exceptional properties, on a specific functional target. Within this scheme, the final step, where GO is reduced to disclose G (often referenced as RGO), is of the utmost importance [7].

So far, several methods have been employed for preparing RGO, such as chemical, electrochemical, thermal reduction, or UV assisted methods [7]. Chemical reduction is considered one of the mostly versatile routes, since it can be easily implemented in wet chemistry processes [8]. Most used reactants are hydrazine [9], $NaBH_4$ [10,11], $LiAlH_4$ [12] and hydroquinone [13], but also more environmentally friendly such as L-ascorbic acid [14,15] or metal powders can be used [16]. Despite the considerable number of reported works, the efficacy of these procedures is quite diverse and even contradictory.

From a perusal of the literature, some critical issues can be clearly identified:

* *Corresponding author.*
E-mail address: stefano.agnoli@unipd.it (S. Agnoli).
0008-6223/$ - see front matter © 2013 Elsevier Ltd. All rights reserved.
http://dx.doi.org/10.1016/j.carbon.2013.11.008

Link to the full paper: http://www.sciencedirect.com/science/article/pii/S0008622313010567

3.1.2 Reprint of the paper: Shaping graphene oxide by Electrochemistry: from Foams to Self-Assembled Molecular Materials.

CARBON 77 (2014) 405–415

Available at www.sciencedirect.com

ScienceDirect

journal homepage: www.elsevier.com/locate/carbon

Shaping graphene oxide by electrochemistry: From foams to self-assembled molecular materials

M. Favaro [a], *S. Agnoli* [a,*], *M. Cattelan* [a], *A. Moretto* [a], *C. Durante* [a], *S. Leonardi* [b], *J. Kunze-Liebhäuser* [b], *O. Schneider* [c], *A. Gennaro* [a], *G. Granozzi* [a]

[a] *University of Padova, Department of Chemical Sciences, Via Marzolo 1, 35131 Padova, Italy*
[b] *Technische Universität München, Physics Department E19, James-Franck-Str. 1, 85748 Garching, Germany*
[c] *Technische Universität München, Institut für Informatik VI, Boltzmannstraße 3, 85748 Garching, Germany*

ARTICLE INFO

Article history:
Received 12 March 2014
Accepted 17 May 2014
Available online 28 May 2014

ABSTRACT

The ability to control the three-dimensional architecture of graphene-based materials following a rational design is essential for technological applications. Here we demonstrate that the electrochemical etching can be used as a surgical tool to tailor the morphology of graphene electrodes and to impart special features, like micrometric channels and controlled mesoporosity (*foams*). The final materials, thanks to the high surface area, can represent a promising class of carbon-based supercapacitors. Otherwise, new materials can be prepared using a bottom-up strategy that exploits the self-assembly of the graphene oxide quantum dots produced during the electrochemical erosion. The advantages of this second approach reside not only in the possibility to downscale the control over the spatial organization as compared to the use of conventional micrometric graphene sheets, but also in the introduction of the intrinsic luminescent properties of the quantum dots in the final material. As a proof of concept we report the preparation of luminescent *nanospheres* by exploiting the self-organization of the graphene oxide quantum dots around frozen water nuclei.

© 2014 Elsevier Ltd. All rights reserved.

1. Introduction

Graphene is currently one of the brightest stars in Materials Science. This success derives not only from its intrinsic exceptional properties [1] like perfect two-dimensional nature, high electrical conductivity, outstanding mechanical strength etc., but also from the possibility to easily manipulate its size, morphology [2], chemical nature [3] and electronic properties to obtain highly specific functional properties [4–9]. This unprecedented versatility allowed a wide usage of graphene-based materials in almost any technological field. Since the early rise of graphene, a constant spotlight followed its oxidized form, called graphene oxide (GO) [10], which has already found numerous applications in catalysis [11], solar cells [12,13] and battery technology [14]. This material is soluble in a variety of solvents and can be easily produced in high yields [10]. These factors make GO the most suitable candidate for the preparation of complex carbon nanoarchitectures and for the synthesis of new composite materials by means of wet chemistry methods [5–8,15,16]. In this context, the biggest challenge is the organisation of the single 2D units into rationally designed 3D functional materials [8,17,6].

So far, several routes were undertaken, e.g. self-assembly [16,18], chemical functionalization [5] and intrinsic

* *Corresponding author.*
E-mail address: stefano.agnoli@unipd.it (S. Agnoli).
http://dx.doi.org/10.1016/j.carbon.2014.05.044
0008-6223/© 2014 Elsevier Ltd. All rights reserved.

Link to the full paper: http://www.sciencedirect.com/science/article/pii/S0008622314004849

Appendix A3.1: Synthesis of Graphene Oxide

The chemicals were used as received without further operations. 1 g of ultra-pure graphite micrometric powder (d < 150 μm, Aldrich) was slowly added to 25 mL of a 9:1 mixture of concentrated H_2SO_4/H_3PO_4 (96% and 65% respectively, Aldrich), in ice-water bath [9]. Then, operating in the ice-water bath (T ~ -15 °C), 3 g of $KMnO_4$ (Aldrich) were gradually added into the mixture under vigorous stirring. After 10 hours of stirring at r.t. (in order to increase the intercalation of sulfate ions into the graphite layered structure), the mixture was heated up to 35° C for 1 hour in ultrasonic bath. After that, the slow addition of 50 mL of deionized water causes an increase in temperature to about 98° C. The mixture was maintained at this temperature for 15-20 min. The oxidation reaction was terminated firstly diluting the mixture by adding 140 mL of milli Q water at 60° C, followed secondly by 1.5 mL of 30% H_2O_2 solution (Fluka). This leads to the reduction of the strongly oxidant permanganate ion (Mn VII) to Mn^{2+}, accordingly to the following redox reaction:

$$2MnO_4^- + 5H_2O_2 + 6H^+ \rightarrow 2Mn^{2+} + 5O_2 + 8H_2O \qquad (A3.1)$$

The mixture was cooled down to r.t. by stirring for 30 min, followed by 30 min of sonication to maximize the exfoliation of the graphite oxide into the single GO layers. The yellow-brownish product was then collected after several cycles of centrifugation-milli Q water washing, until obtaining a dispersion of GO in water with a pH of 5.5. This weak acid environment is suitable to achieve an optimum time stability of the GO dispersions. Prior to each use, few mL of a GO dispersion (15 mg/mL) were dialyzed over five days with osmotic membranes (Spectra/Por, Molecular Weight Cut-Off (MWCO) of 7 kD) in MilliQ water (ρ=18.2 MΩ·cm), to remove eventual residual contaminations.

The obtained GO dispersion was characterized by XPS, FT-IRAS and UV-VIS absorption spectroscopy, as reported in Figure A.1. The Z-potential of the obtained GO dispersions in water (measured by a Zetasizer (Nano-ZS) from Malvern Instruments) is equal to -44.8 mV.

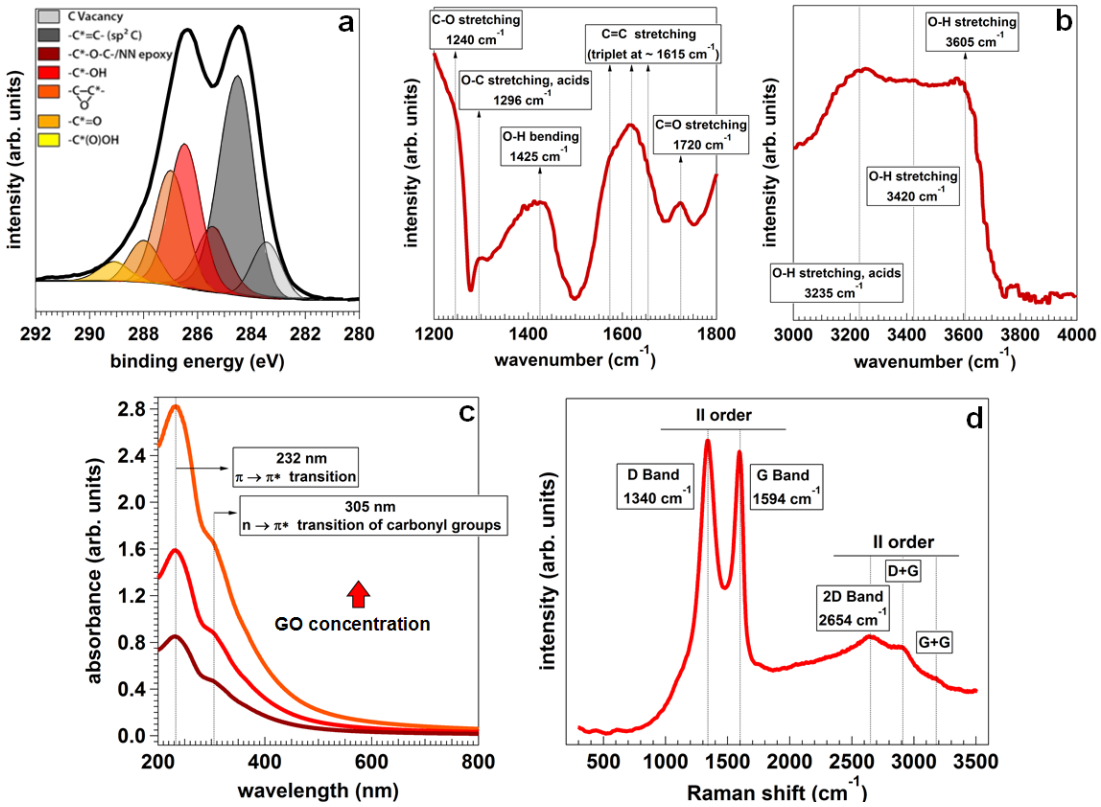

Figure A.1. Spectroscopic characterization of the pristine GO obtained by the modified-Hummers' synthesis; a: multi-component fitting of the C 1s photoemission line of a GO free-standing paper; b: FT-IRAS measurements on a GO thin film deposited by drop-casting on Cu foil; c: UV-Visible absorption spectroscopy of GO aqueous dispersions at different GO concentrations; d: Raman spectroscopy on a GO free-standing paper.

In order to characterize the lateral dimensions of the GO sheets, SEM measurements were performed on different samples, prepared using Electrophoretic Deposition (EPD) of few layers of GO on different substrates, such as P:Si (100) single crystal and AAO (Anodic Aluminum Oxide) membrane (as reported in Figure A.2a and A.2b). The deposition of GO on AAO membrane allowed to prove that the GO flakes (highlighted by a white continuous line in Figure A.2b) are mainly single layers. The top right inset in Figure A.2b shows a digital image of the yellow dispersion of GO in water (with a concentration of 1.5 mg of GO/mL), used for the few-layer depositions.

In order to obtain free-standing GO papers, 250 μL of a concentrated dispersion of GO in water (1.5 mg of GO/mL, bottom-right inset in Figure A.2) were drop casted on an electro-polished copper substrate. A first slow drying process was performed at RT for a few days, while the residual solvent was removed by vacuum pumping (10^{-2} mbar) for few hours. At the end of this procedure, a self-standing GO paper-like

substrate (about 10-20 μm) was easily obtainable by peeling off the dried film from the copper substrate.

Figure A.2c and A.2d show SEM images at two different magnifications obtained on a free-standing GO paper, while the top-right inset reported in Figure A.2c shows the digital images of the GO film deposited on the copper substrate and the free standing paper, respectively. The SEM images highlight how the surface morphology is characterized by the crumpling of the GO film; this phenomenology is due both to the high concentration of the colloidal GO dispersion used for the deposition and to the huge dispersion of the lateral size of the flakes.

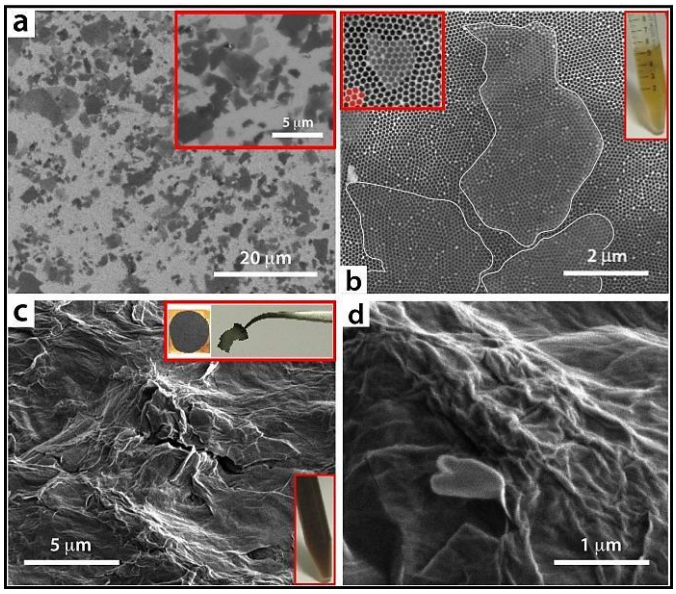

Figure A.2. a,b: SEM images of the GO flakes deposited on a Si(100) single crystal and on an AAO membrane by EPD, respectively; c,d: SEM images at different magnifications of the GO free standing paper like: the morphology is strongly characterized by the crumpling of the film driven by the huge GO flake lateral size distribution.

For the preparation of the copper substrate, Cu foils (Goodfellow, 99.9%, 0.125 mm thickness) were firstly cleaned in an ultrasonic bath of isopropyl alcohol for 10 min and then dipped in the electropolishing solution (composed of distilled water and orthophosphoric acid 85% (1:4 volume ratio)). The counter electrode was a stainless steel cylinder surrounding the sample. The voltage was set to the plateau after rapidly checking the current trend as a function of the voltage (usually set to 2.4 V). The electro-polishing was 5 min long. After the electro-polishing procedure, the foils were thoroughly rinsed in MilliQ water and sonicated in isopropyl alcohol for 10

min. Figure A.3 reports the STM and XPS measurements performed on the so-prepared Cu substrate.

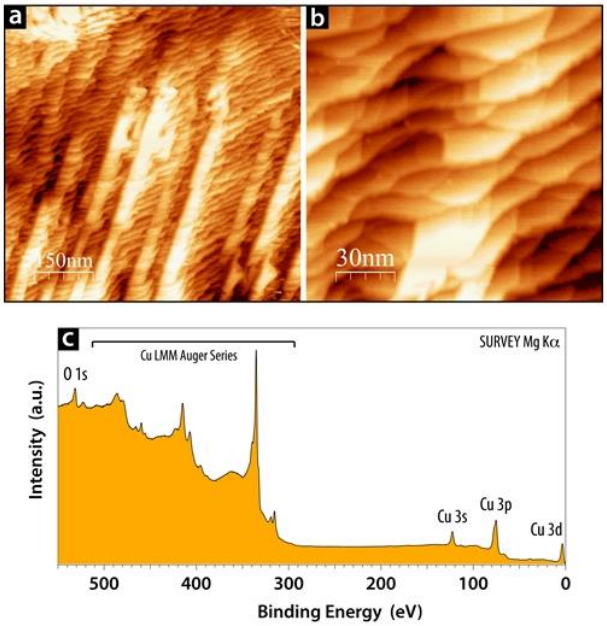

Figure A.3. STM images (a, b) at different magnification ($I_{tunnelling}$=0.8nA, ΔV=0.25V). and XPS survey scan (c) performed on the Cu electro-polished substrate.

REFERENCES

[1] D. R. Dreyer, S. Park, C. W. Bielawski, R. S. Ruoff, The chemistry of graphene oxide, *Chem. Soc. Rev.* **39**, 228–240 (2010).

[2] S. Park, R. S. Ruoff, Chemical methods for the production of graphenes, *Nat. Nanotechnol.* **4**, 217–224 (2009).

[3] O.C. Compton, S.T. Nguyen, Graphene Oxide, Highly Reduced Graphene Oxide, and Graphene: Versatile Building Blocks for Carbon-Based Materials, *Small* **6**, 711-723 (2010).

[4] Y. Zhu, S. Murali, W. Cai, X. Li, J. W. Suk, J. R. Potts, R. S. Ruoff, Graphene and Graphene Oxide: Synthesis, Properties, and Applications, *Adv. Mater.* **22**, 3906-3924 (2010).

[5] B. C. Brodie, On the atomic weight of graphite, *Philos. Trans. R. Soc. London*, 149, 249–259 (1859).

[6] S. Pei, H.-M. Cheng, The reduction of graphene oxide, *Carbon* **50**, 3210–3228 (2012).

[7] G. Eda, J. Ball, C. Mattevi, M. Acik, L. Artiglia, G. Granozzi, Y. J. Chabal, T. D. Anthopoulos, M. Chhowalla, Partially oxidized graphene as a precursor to graphene, *J. Mater. Chem.* **21**, 11217-11223 (2011).

[8] W. S. Hummers, R. E. Offeman, Preparation of graphitic oxide, *J. Am. Chem. Soc.* **80**, 1339 (1958).

[9] D. Marcano, D. V. Kosynkin, J. M. Berlin, A. Sinitskii, Z Sun, A. Slasarev, L. B. Alemany, W. Lu, J. M. Tour, Improved synthesis of graphene oxide, *ACS Nano* **4**, 4806-4814 (2010).

[10] A. Simon, R. Dronskowski, B. Krebs, B. Hettich, The crystal structure of Mn_2O_7, *Angew. Chem. Int. Ed. Engl.* **26**, 139–140 (1987).

[11] M. Wissler, Graphite and carbon powders for electrochemical applications, *J. Power Sources* **156**, 142–150 (2006).

[12] M. Trömel, M. Russ, Dimanganheptoxid zur selektiven Oxidation organischer Substrate, *Angew. Chem.* **99**, 1037–1038 (1987).

[13] H. He, T. Riedl, A. Lerf, J. Klinowski, Solid-state NMR studies of the structure of graphite oxide, J. Phys. Chem. **100**, 19954–19958 (1996).

[14] A. Lerf, H. He, M. Forster, J. Klinowski, Structure of graphene oxide revisited, J. Phys. Chem. B **102**, 4477–4482 (1998).

[15] D. W. Boukhvalov, M. I. Katsnelson, Modeling of graphene oxide, *J. Am. Chem. Soc.* **130**, 10697–10701 (2008).

[16] S. Zhou, A. Bongiorno, Origin of the Chemical and Kinetic Stability of Graphene Oxide, *Sci. Rep.* **3**, article number 2484 (2013).

[17] C. Mattevi, G. Eda, S. Agnoli, S. Miller, K. A. Mkhoyan, O. Celik, D. Mastrogiovanni, G. Granozzi, E. Garfunkel, M. Chhowalla, Evolution of Electrical, Chemical, and Structural Properties of Transparent and Conducting Chemically Derived Graphene Thin Films, *Adv. Funct. Mater.* **19**, 2577-2583 (2009).

[18] N. Yang, Y. Liu, H. Wen, Z. Tang, H. Zhao, Y. Li, et al., Photocatalytic properties of graphdiyne and graphene modified TiO2: from theory to experiment, *ACS Nano* **7**, 1504-1512 (2013).

[19] R. Leary, A. Westwood, Carbonaceous nanomaterials for the enhancement of TiO_2 photocatalysis, Carbon **49**, 741-772 (2011).

[20] T. Sun, S. Fabris, Mechanisms for Oxidative Unzipping and Cutting of Graphene, *Nano Lett.* **12,** 17-21 (2012).

[21] Z. Li, W. Zhang, Y. Juo, J. Yang, J. G. Hou, How Graphene is Cut upon Oxidation? *J. Am. Chem. Soc.* **131**, 6320-6321 (2009).

[22] L. Li, G. Wu, G. Yang, J. Peng, J. Zhao, J.-J. Zhu, Focusing on luminescent graphene quantum dots: current status and future perspectives, *Nanoscale* **5**, 4015-4038 (2013).

[23] Y. Zhu, S. Murali, M. D. Stoller, K. J. Ganesh, W. Cai, P. J. Ferreira, A. Pirkle, R. M. Wallace, K. A. Cychosz, M. Thommes, D. Su, E. A. Stach, R. S. Ruoff, Carbon-based supercapacitors produced by activation of graphene, *Science* **332**, 1537-1541 (2011).

[24] H.-J. Choi, S.-M. Jung, J.-M. Seo, D. W. Chang, L. Dai, J.-B. Baek, Graphene for energy conversion and storage in fuel cells and supercapacitors, *Nano Energy* **1**, 534-551 (2012).

[25] C. Su, M. Agik, K. Takai, J. Lu, S.-J. Hao, Y. Zheng, P. Wu, Q. Bao, T. Enoki, Y. J. Chabal, K. P. Loh, Probing the catalytic activity of porous graphene oxide and the origin of this behavior, *Nat. Comm.* **3**, 1298 (2012).

[26] J. Zhang, F. Zhao, Z. Zhang, N. Chen, L. Qu, Dimension-tailored functional graphene structures for energy conversion and storage, *Nanoscale* **5**, 3112-3126 (2013).

[27] Y. J. Kim, C. M. Yang, K. C. Park, K. Kaneko, Y. A. Kim, M. Noguchi, T. Fujino, S. Oyama, M. Endo, Edge-enriched, porous carbon-based, high energy density supercapacitors for hybrid electric vehicles, *Chem. Sus. Chem.* **5**, 535-541 (2012).

[28] a: Y. H. Lee, A. Ghosh, Carbon-based electrochemical capacitors, *Chem. Sus. Chem.* **5**, 480-499 (2012); b: B. G. Choi, M. Yang, W. H. Hong, J. W. Choi, Y. S. Huh, 3D macroporous graphene frameworks for supercapacitors with high energy and power densities, *ACS Nano* **6**, 4020-4028 (2012).

[29] Y. Zhu, S. Murali, M. D. Stoller, K. J. Ganesh, W. Cai, P. J. Ferreira, A. Pirkle, R. M. Wallace, K. A. Cychosz, M. Thommes et al., Carbon-based supercapacitors produced by activation of graphene, *Science* **332**, 1537-1541 (2011).

[30] G. Wang, L. Zhang, J. Zhang, A review of electrode materials for electrochemical supercapacitors, *Chem. Soc. Rev.* **41**, 797-828 (2012).

[31] L. Hao, X. Li, L. Zhi, Carbonaceous electrode materials for supercapacitors, *Adv. Mater.* **25**, 3899-3904 (2013).

[32] A. J. Bard, L. R. Faulkner, *Electrochemical Methods*, 2nd ed., Wiley & Co., 2001.

Section 4

Graphene-based Quantum Dots

Chapter 4.1
Graphene Quantum Dots as efficient luminescent, catalytic systems and flexible nano-bricks

Graphene exhibits an infinite exciton Bohr radius, so that quantum confinement could take place in graphenes of any finite size and is expected to result in many interesting phenomena that cannot be obtained in other semiconductors [1]. As a matter of fact, the energy bandgap between the HOMO and LUMO of a sp^2 carbon honeycomb lattice can be tuned from 0 eV, in the case of a flat and micrometric size monolayer graphene, to 4.4 eV of benzene [2], simply by varying the lateral size [3,4]. Consequently, Graphene Quantum Dots (GQDs), as a new kind of quantum dots, have emerged in the last few years and have focused a huge research interest.

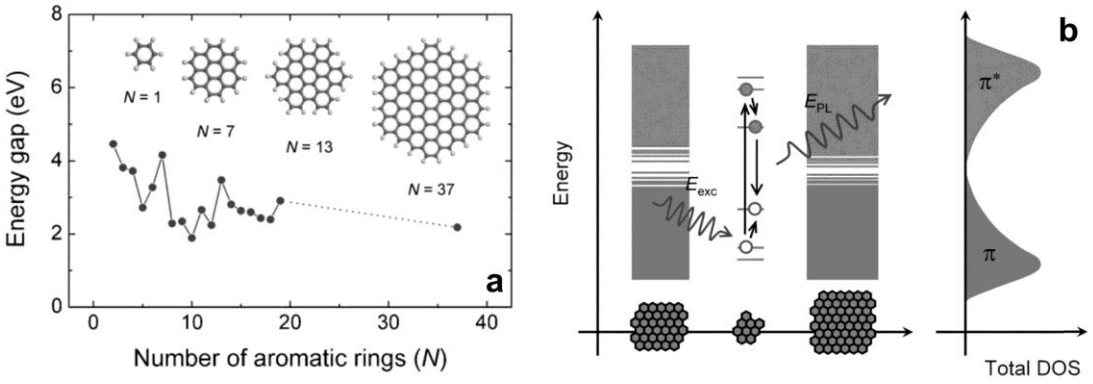

Figure 4.1. a: Energy gap of π-π* transitions calculated based on DFT as a function of the number of fused aromatic rings. The inset shows the structures of the graphene molecules used for calculation; b: Representative band structure of GO. The energy levels are quantized with large energy gap for small fragments due to confinement. A photo-generated e–h pair recombining radiatively is depicted (adapted from ref. 3).

Due to the pronounced quantum confinement and edge effects, GQDs assume numerous novel chemical/physical properties which are promising for different and heterogeneous applications such as electro and photocatalysis, sensing and bio-recognition [5,6].

Huge attention has been drawn to develop synthetic methods for the preparation of GQDs, which can be classified into two main groups: *top-down* and *bottom-up* methods.

Though the GQDs are considered as a kind of Carbon QDs (CDs), some differences must be pointed out: GQDs are generally prepared from graphene-based starting materials (like G or GO), and are defined as G or GO sheets with lateral dimensions less than 100 nm in single-, double- and few- (3÷5) layers [6,7,8]. The CDs can be either in an amorphous or crystalline state, constituted by quasi-spherical carbon nanoparticles with sizes ranging between 5 and 100 nm [6,8,9].

Table 4.1 reports the principal state of art methods for the preparation of GQDs and CDs, together with the morphological and the optical properties of the so-obtained nano-objects.

Table 4.1. Principal preparation methods for the GQDs (adapted from ref. 6).

Methods	Subclassification	Starting materials	Size (nm)	Height (nm)	Color
Top-down	Acidic oxidation	GO	5-19		Blue
		GO	5-25		Blue
		Carbon black	15	0.5	Green
			18	1-3	Yellow
	Hydrothermal	GO	5-13	1-2	Blue
		GO	1.5-5	1.5-1.9	Green
		RGO	2-5		Blue
	Amino-hydrothermal	GO	2.5	1.13	Blue to yellow
	Solvothermal	GO	5.3	1.2	Green
		GO	3-5	0.95	Blue to Green
	Microwave	GO	2-7	0.5-2	Green, blue
	Microwave-hydrothermal	GO	3	<0.7	Blue
	Ultrasonic chemistry	Graphene	3-5		Blue
	Electrochemistry	Graphene	3-5	1-2	Green
		Graphite rods	5-10	<0.5	Yellow
		MWCNTs	3±0.3	1-2	Green
			5±0.3	3	Green
			8.2±0.3	5	Green
			23±2		Green
	Photo-Fenton Reaction	GO	40	1.2	Blue
	Oxygen plasma etching	Graphene	11±4.3	4.5	
	K intercalation	MWCNTs	~20	<1	Blue
		Graphite flakes	~20	0.9	Blue
Bottom-up	Stepwise solution chemistry	Organic precursors	~2.5-5		Red
	Precursor pyrolysis	Glucose	1.65-21	3.2	DUV, blue
		Citric acid	~15	0.5-2	Blue
	Catalyzed cage-opening	C_{60}	2.7-10		
	Pyrolysis and exfoliation	Unsubstituted HBC	~60	2-3	Blue

Moreover, the GQDs can be further discriminated accordingly to their oxidation degree. If the QDs are obtained from GO (where the presence of oxygen functional groups in the system is important), they are usually known as GOQDs [10].

Finally, a fourth type of nanocarbons is constituted by nanodiamonds, in which the C atoms are present with a sp^3 hydridization in a tetragonal arrangement.

Figure 4.2 should be explicative about the classification of the different C-based QDs.

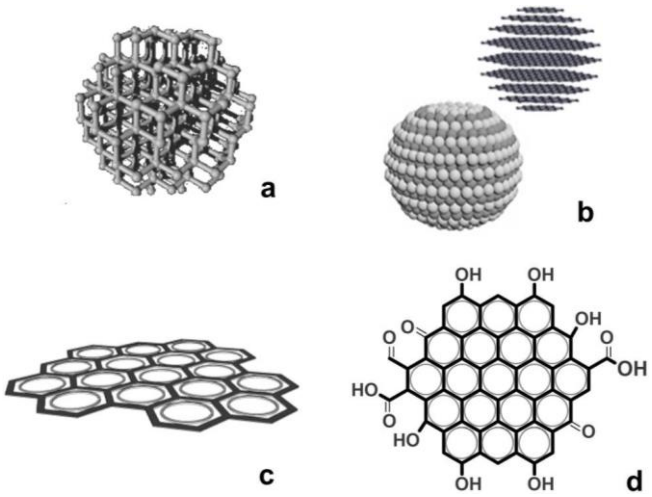

Figure 4.2. Classification of nanocarbons: nanodiamonds (a), carbon dots (b), GQDs (c) and GOQDs (d).

In this thesis work, the research was focused on the preparation and on the chemical, structural and functional characterization of pure and doped-GOQDs, because of their chemical flexibility (see § 4.1.1 and 4.1.2) and interesting optical and catalytic properties. In particular, B-, N-, B,N- and S- and S,N-doped GOQDs have been prepared (see § 4.1.1 and 4.1.2, respectively, for the detailed characterization).
The synthesis of these nano-objects has been performed by using two different approaches, whose principal characteristics are listed as follows:

1. *Electrochemical etching of GO WEs*: this method consists of cycling the GO WE in a standard three electrode electrochemical cell, using high redox potentials (ranging from ± 1.5 V to ± 3 V vs. $Ag/AgCl/Cl^-_{(sat.)}$) [11,12], which are sufficient to oxidize the C−C bonds and to induce water electrolysis. This leads to a huge production of hydroxyl and oxygen radicals that play the role of an electrochemical "scissors" in the oxidative cleavage reaction of C=C bonds. Moreover, the potential cycling can drive the intercalation of the supporting electrolyte into the carbon anode during the cathodic branch, helping in this way the dis-aggregation of the Van der Waals stacking. During the electrochemical cycling the formation of linear chains of epoxy groups and carbonyl pairs determines the unzipping of GO through the breaking of C-C bonds, with the consequent release in solution of GOQDs decorated at the edges by oxygen groups (such as hydroxylic, carbonylic and carboxylic groups). More details are reported in Appendix A4.1.

The molecular mechanism involved in the electrochemical preparation of graphene (G) and GOQDs represents is still moot [11]; nevertheless the most credited explanation is based on a radical-mediated process [12]. In order to prove the central role played by water electrolysis, the potential window during the electrochemical cycling of the GO WE was reduced, so that water dissociation and the consequent gas evolution (oxygen evolution and hydrogen evolution reactions during the anodic and cathodic branch of the CV, respectively) are suppressed (Figure 4.3a,b). In this experiment, two different GO WEs were cycled 2000 times at 500 mV/s in PBS electrolyte (see A4.1) within two different potential windows: the first one was cycled between +3.00 V and -3.00 V vs Ag/AgCl/$Cl^-_{(sat.)}$ (as performed in § 3.1.2), while the second one was cycled in the range ±0.90 V vs Ag/AgCl/$Cl^-_{(sat.)}$. As Figure 4.3c shows, the solutions produced at low potential are transparent and do not show photoluminescence, indicating that the electrodes were not etched and no GOQDS were produced. Therefore the mechanism at the basis of the formation of GOQDs must imply the participation of radical species coming from water electrolysis, which can either react with the doping molecules creating other radicals or with the GO electrode surface forming active species that later can react with the molecules bearing the dopants (as reported in §4.1.1 and 4.1.2).

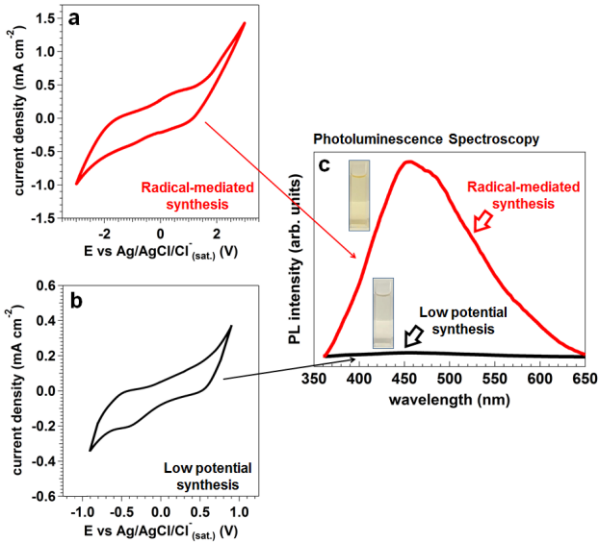

Figure 4.3. CV curves (recorded at a scan rate of 500 mV/s) during the synthesis of GOQDs within different potential ranges; a: -3.0 ÷ +3.0 V; b: -0.9 ÷ +0.9 V; c: photoluminescence spectra of the solutions obtained by the two different methods. The photoluminescence was induced by an excitation wavelength of 340 nm.

This synthetic method was used in the last chapter (§ 3.1.2) to obtain, at the same time, the GOQDs and the GO surface modification, with the consequent preparation of GO foams. Moreover, it has been exploited for the preparation of various doped-GOQDs, as reported in § 4.1.1 and 4.1.2.

2. *Microwave-assisted preparation method*: Microwave (MW)-assisted technique (performed in acidic conditions) has been widely applied to materials synthesis. As a convenient and rapid heating source, microwave assisted exfoliation and reduction of GO has been reported in several works in literature [13,14]. Initiated by the acid oxidation of epoxy groups, the rapid heating caused by the MW irradiation leads to the formation of linear defects on the carbon lattice composed of epoxy groups and, in particular, of carbonyl pairs, which make the graphitic domains fragile and readily attacked [11]. The MW-assisted method has been used for the preparation of nitrogen-doped GOQDs, as reported in § 4.1.3.

GOQDs typically show strong optical absorption in the UV region, with a tail extending into the visible range. In a typical UV-Vis absorption spectrum of a GO sample, reported in Figure 4.4a, two peaks can be observed: a peak at ~230 nm due to π–π* transition of aromatic C=C bonds [15] and a shoulder at ~300 nm assigned to n–π* transition of C=O bonds [14]. These peaks can also be observed in the UV-Vis absorption spectra of GOQDs, with the π–π* transition peak centered at a wavelength between 200 and 270 nm and the n–π* transition peak at wavelength longer than 260 nm [16], as well-documented by Figure 4.4b.

As already introduced above, GOQDs have emerged in the literature as promising materials for their strong photoluminescence (PL) properties. The exact knowledge of the origin of their PL properties is a matter of current debates. In any case, one unifying and well-known feature of the PL of GOQDs is the excitation dependence of the emission wavelength and intensity. However, whether this occurs because of the optical selection of differently sized nanoplatelets (quantum confinement effect, QCE) and/or different emissive traps on the QDs surface [10,17], is currently unresolved and not well-understood yet [5,18]. Since GOQDs are characterized by edges decorated with oxygen functional groups such as hydroxyl, carbonyl and carboxylic acid groups (Figure 4.3), the presence of isolated small (1–3 nm) sp^2 clusters within the C–O matrix leads to the localization of electron-hole pairs, facilitating the consequent radiative recombination (intrinsic state emission) [3,19].

Moreover, these functional groups can lead to the formation of the so-called "surface states" on GOQDs, which are the energy levels between the energy band gap of π and π* states of the aromatic C=C bonds. These energy levels may result in a series of emissive traps; when a certain excitation wavelength illuminates the GOQDs, a surface state emissive trap can dominate the emission [20]. In general, PL of GOQDs is attributed to either combining effect or competition between intrinsic state emission and defect state emission [5,11]. Figure 4.4 show the comparison between the PL induced in GO and in GOQDs: GO exhibits only a weak blue-luminescence [3,21], whereas GOQDs are characterized by a strong green photoluminescence [10,11].

Figure 4.4 reports the comparison between the C 1s photoemission peaks of GO and GOQDs. GOQDs are characterized by lower oxidation with respect to the pristine graphene, because of the "consumption" of epoxide and carbonyl groups during the electrochemical (or MW) assisted unzipping of the GO layer. This observation is in agreement with the Raman measurements: for the GOQDs, in fact, the D/G ratio is lower than the one that characterizes the pristine GO, meaning that GOQDs exhibit a more ordered structure with less oxygen functional groups [11,22].

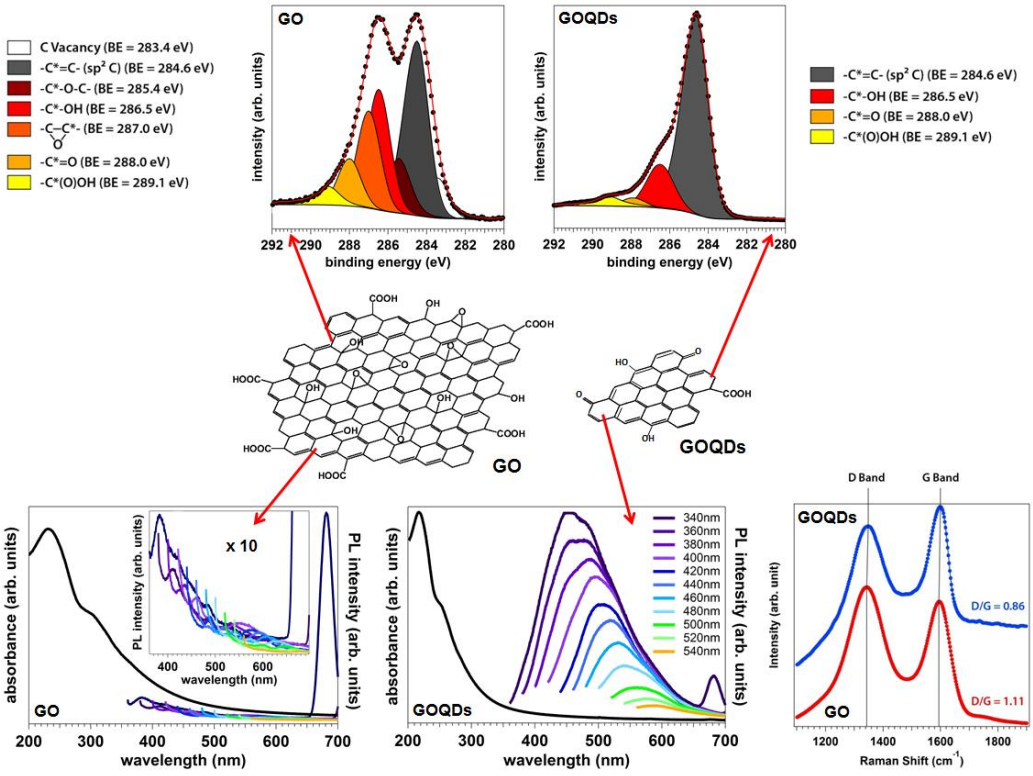

Figure 4.4. Comparison between GO and GOQDs. Top: C 1s photoemission lines; bottom: PL and Raman spectroscopy.

In the last period, chemically modified graphenes (CMGs) have drawn tremendous interest in the scientific community because of their excellent catalytic performances towards the reduction of oxygen [23]. Despite the huge amount of works appeared in literature in the last three years [23], there is still no clear understanding of the exact role played by the interaction of multiple functional groups on the catalytic activity of nano-shaped graphene materials. Actually, the presence of oxygen functional groups decorating graphitic nano-platelets influences the catalytic activity and, in particular, the O_2 reduction pathway: oxygen moieties such as quinones, anthraquinones and hydroquinones on graphitic-based material (highly oriented pyrolytic graphite, HOPG, and glassy carbon, GC) leads to a $2e^-$ reaction pathway, with the consequent production of hydrogen peroxide [24]. On the contrary, chemically modified graphitic materials with low concentration of oxygen groups such as N-doped HOPG show a selective pathway reduction of oxygen to water [25, see also § 2.1.1]. However, these studies were performed on micrometric sized materials, with a poor or absent direct interaction between the dopants and the oxygen moieties. In this context, the doped-GOQDs (prepared in this thesis work accordingly to the synthesis protocol reported in § 4.1.1 and, more in detail, in Appendix A4.1) constitute a suitable work bench, where the spatial confinement of dopants (decorating the sp^2 carbon core) and the oxygen functional groups decorating the edges of the GOQDs takes place on a nanometric scale. By combining the chemical information derived from XPS (which state that the dopants, in the as-prepared systems, strongly interact with oxygen) and the structural information from STM (which shows that the doped-GOQDs are characterized by an average lateral size of about 2.0 nm), it is possible to figure out a possible model for the doped-GOQDs, as reported in Figure 4.5.

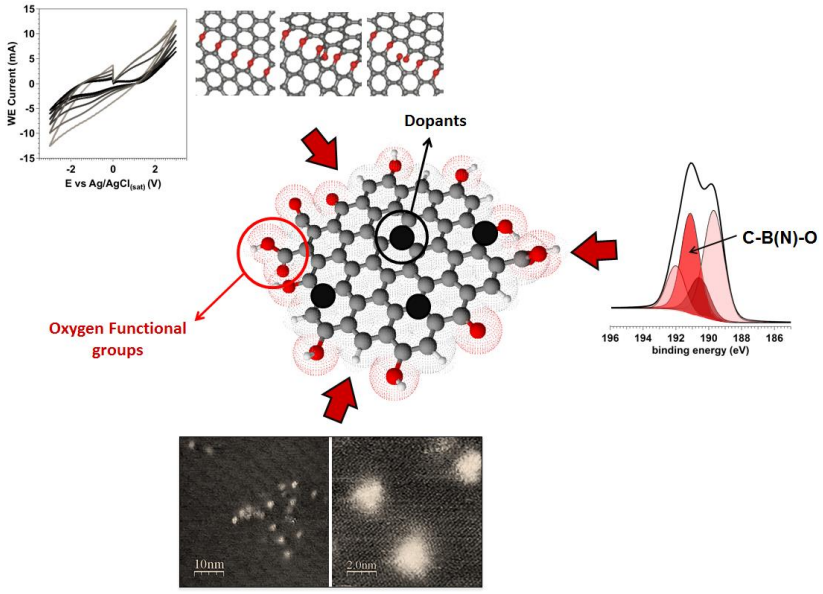

Figure 4.5. Doped-GOQD model derived from the synthesis mechanism and the surface science characterization techniques used in this thesis work.

The electrochemical activity towards the oxygen reduction reaction of the doped GOQDs has been investigated by cyclic voltammetry and rotating disk electrode measurements, observing a clear decrease of the overpotential as a function of the type of dopant according to the sequence N ~ B > B,N. Moreover, assisted by density functional calculations of the Gibbs free energy associated to every electron transfer, it has been demonstrated that the selectivity of the reaction is controlled by the interaction of the dopants with the oxygen functional groups: as-prepared GOQDs follow a two-electron reduction path that leads to the formation of hydrogen peroxide, whereas after the reduction with $NaBH_4$, the same materials promote a direct four-electron reduction of oxygen to water.

Figure 4.6 reports a schematic vision of the work performed in § 4.1.1, in particular for the B,N-co-doped-GOQDs and B,N-co-doped-chemically reduced GOQDs, which is the system that shows the best catalytic performance towards the reduction of oxygen.

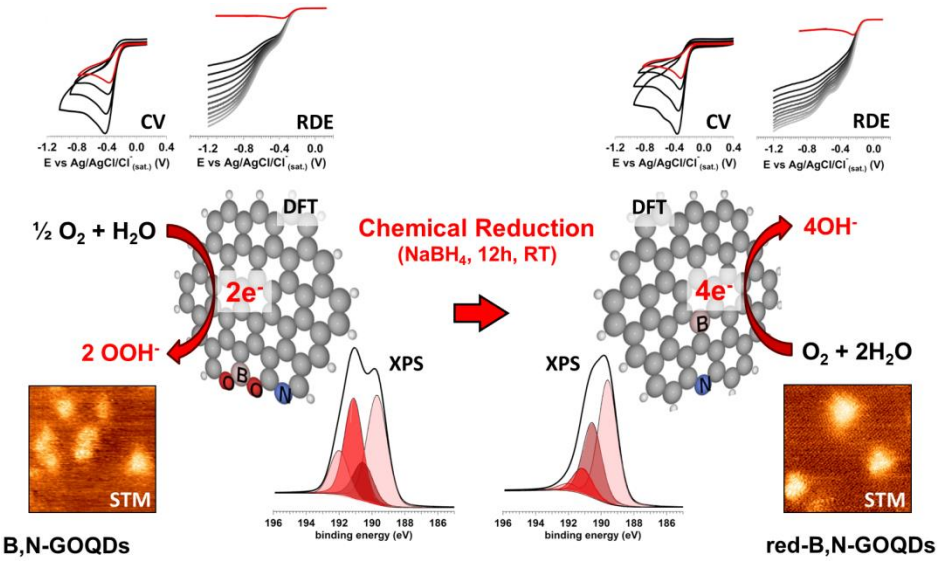

Figure 4.6. Schematic vision of the work reported in § 4.1.1 (for the B,N-co-doped-GOQDs and reduced-GOQDs).

Due to their small dimension and versatile chemistry, G and GOQDs can be easily interfaced to other nano-objects in order to build more complex systems.

Moreover, GOQDs (pure and doped) are characterized by remarkable self-assembly properties, due to the polar oxygen functional groups decorating the edges that lead to the formation of a huge number of hydrogen bonds. By exploiting the self-assembly properties of these innovative nano-bricks, it is possible to prepare new 3D materials with potential applications in catalysis, optics and batteries technologies [23a,b, 26].

The first example of a "superstructure" prepared from GOQDs is reported in § 3.1.2. Following a bottom-up approach that exploits the strong tendency of GOQDs to interacts via intermolecular hydrogen bonds (between a carboxylic or an alcoholic group and a carbonyl group residing at sheet edges) and the use of a template to guide the self-organisation it has been possible to obtain GOQD-based nanospheres. in this case spherical nuclei of frozen water (acting as a template during the freeze-pump-thaw process) were used as a hard template that drives the aggregation of the GOQDs into thin spherical shells. The synthesis mechanism is schematically reported in Figure 4.7, together with the SEM and TEM results. Interestingly, as reported in § 3.1.2, the GOQD-based nanospheres retain the same photoluminescence properties that characterized the single GOQDs. This opens the way to new potential applications in sensing and photocatalysis.

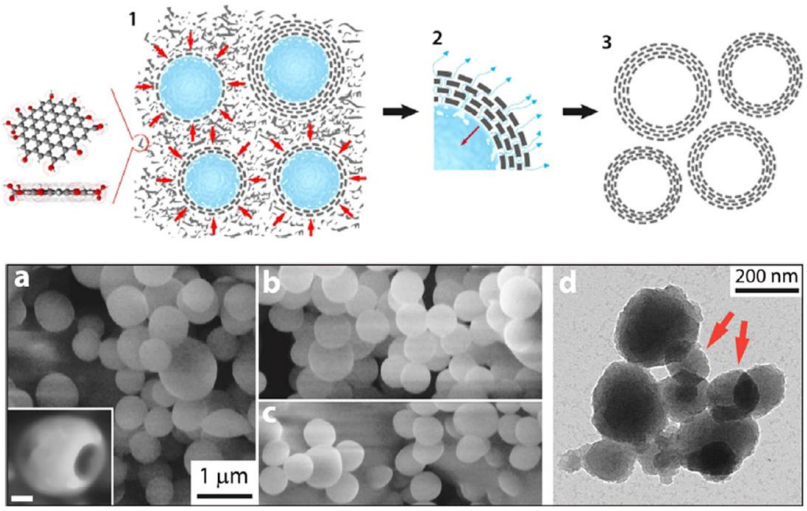

Figure 4.7. Top: schematic representation of the synthesis mechanism of the GOQD-based nanospheres. The arrows in the step 1 describe the tendency (via hydrogen and Van der Waals bonds) of the GOQDs to build a spherical multilayer shell that surrounds the ice crystals. In the step 2, the red arrow indicates that the sublimation of the ice proceeds from the surface to the core of the ice crystals; bottom: SEM (a, b, c) and TEM (d) measurements. The scale bar reported in the inset in Figure a is 90 nm (adapted from § 3.1.2).

A second example of a 3D material prepared starting from N-doped GOQDs (N-GOQDs) is reported in § 4.1.3. The N-GOQDs used in this work have been obtained via MW-assisted preparation. The N-GOQDs were used either as an initiator to give a daisy-like peptide-polymer structure or as capping agents towards more elaborated hybrid nanostructures. In particular, the synthesis of star-shaped GOQDs-(poly-c-benzyl-L-glutamate) conjugates (GOQDs-PBLG) was performed. Primary amines can be used to promote controlled N-carboxyanhydride ring opening polymerization (NCA-ROP) processes. Thus, γ-benzyl-L-glutamate carboxyanhydrides (BLG-NCA) was polymerized using N-GOQDs as the amino-group-bearing initiator. Then, the self-aggregationproperties of PBLG were exploited to generate self-assembled microstructures from hybrids **1** and **2** reported in Figure 4.9. To this end, **1** or **2** have been solubilized in a THF:DMF mixture and dialyzed against water for 48 h. In both cases, as reported in Figure 4.8, spherical aggregates with diameters ranging from 100 to 300 nm were observed. Interestingly, as already observed for the GOQD-based nanospheres, the prepared 3D systems preserve the characteristic emission properties of the native dots.

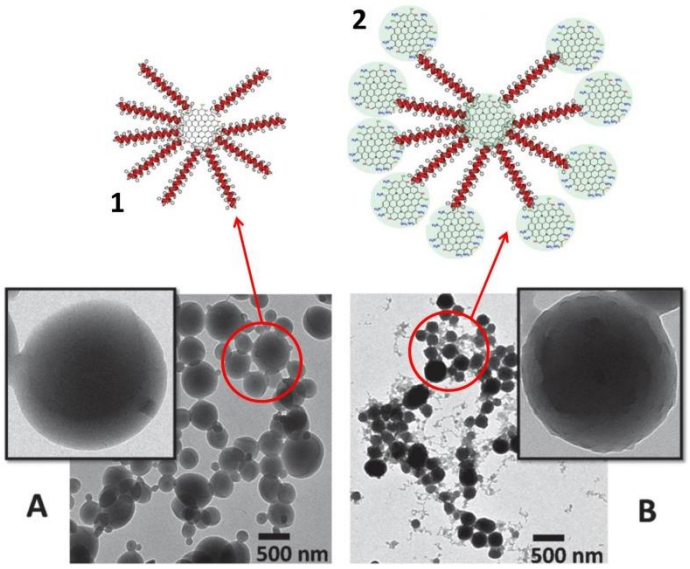

Figure 4.8. SEM and TEM measurements of the obtained GOQDs-PBLG conjugates (adapted from § 4.1.2).

GOQDs can also be used for the preparation of organic-inorganic hybrid materials, via coupling with transition metal oxides.

GOQDs can be self-assembled in solution using inorganic salts as soft templates, in order to obtain materials with a variety of morphology [27]. As a matter of fact, it is possible to induce the growth of GOQD-based microwires (GOMWs) from aqueous solutions of GOQDs by using inorganic scaffolds constituted by infinite linear chains of polyanions [28,29]. In this case 10 mg of dialyzed GOQDs (1.5 mg/mL) were added either to a 0.1 M solution of dihydrogen phosphate monohydrate ($NaH_2PO_4 \cdot H_2O$) or of anhydrous ammonium metavanadate (NH_4VO_3), while properly tuning the pH (4.5-4.8 and 6.4-6.6, respectively). The choice of these oxides, well known for their applications as lithium-ion battery cathodes [30,33,35], was also motivated by the increasing interest toward composite materials formed by their combination with graphene [31,32,33,34,35]. According to the Pourbaix diagram [28,29,36], in the adopted pH range, these salts are constituted by polyoxidic species spatially organized in infinite linear chains. In the case of phosphates, the linear chains are arranged into corner shared orthophosphates (PO_4^{3-}) tetrahedra surrounded by Na^+ ions [29,36]. The hydrate metavanadate chains, formed in solution by the hydration of the infinite chains of corner linked VO_4^{3-} tetrahedra, are constituted by edge-shared trigonal bipyramidal VO_5 units [28]. The structures are reported in Appendix A4.2. In both cases, after a few hours, it was possible to observe the formation of macroscopic aggregates with size ranging from 1 and 5 mm

that precipitate from the solution and are stable even after strong stirring or sonication. Figures 4.9a and 4.9c show the SEM micrographs of the obtained materials: they are constituted by fibres characterized by similar diameter (equal to 360±49 nm and to 375±64 nm, for the GOMWs prepared from phosphates and vanadates, respectively), intersecting each other by forming *cross* or *Y* shaped junctions. The fibres have very similar morphologies in the two cases, and result weakly branched and isotropically entangled. The combination of EDX and XPS measurements (the last reported in Appendix A4.2) indicate that the GOMWs are constituted by an inorganic core (that is the oxide scaffold) surrounded by a carbon shell derived from the progressive assembly of the GOQDs. In fact, as reported by Table 4.2, the elemental composition of the two different GOMWs obtained from EDX measurements show a higher concentration of the inorganic elements (P, Na and V) than those measured by XPS. In this case, since the inorganic scaffold is the core of the *microwire*, the inelastic attenuation due to the interaction of the escaping electrons from the core with the shell material, causes an apparent decrease of the relative concentration of the elements that constitute the inorganic core.

Thence, after the initial seeding provided by the template, the growth in diameter of the GOMWs could be driven by van der Waals interactions between the GOQDs present in solution and the GOQDs in the growing GOMWs.

Table 4.2. EDX and XPS Elemental composition of the GOMWs obtained from poly-phosphates (top) and metavanadates (bottom).

EDX	Atomic composition (%a)
P	3.5
Na	4.0
C	74.2
O	18.3

XPS	Atomic composition (%a)
P	1.5
Na	1.8
C	67.8
O	28.9

EDX	Atomic composition (%a)
V	4.5
C	76.8
O	18.7

XPS	Atomic composition (%a)
V	1.1
C	66.6
O	32.3

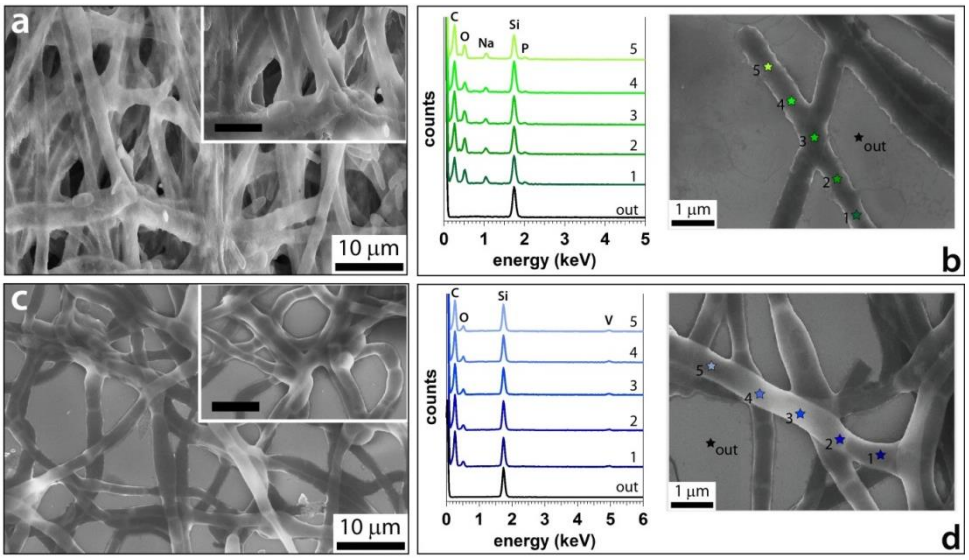

Figure 4.9. SEM micrographs (a,c) and EDX analysis (b,d) of the GOMWs deriving from orthophosphates (a,b) and metavanadates (c,d), respectively (the scale bar reported in the insets in panels a and c is 1 µm long). The energy dispersive spectra were acquired with an acceleration potential of 10 keV.

A second example of the preparation and characterization of an organic-inorganic hybrid material is reported in § 4.1.4, by coupling the GOQDs with titania nanotubes (TNT). Doping of TiO_2 has attracted considerable interest due to the possibility to extend its optical absorption to the visible spectral region [37]. To expand the utilization of TiO_2 to applications that require fast electron transport in electrolytic environments, such as electrocatalyst supports in fuel cells or Li-ion battery anode materials, the conductivity of the oxide must be enhanced while keeping the material inert towards re-oxidation [38]. § 4.1.3 reports an in-situ carburization method during the anodic production of self-organized titania nanotubes (TNTs), based on carbon uptake from an electrolyte enriched with GOQDs. The TNT-GOQD composites grown under these conditions show in-situ carbon doping, thanks to the interaction with the GOQDs, which promotes the formation of crystalline anatase TiO_2 domains (Figure 4.10a), and a slight reduction to substoichiometric oxide (TiO_x) and TiC. Surface science and electrochemical techniques have revealed that graphitic carbon is incorporated into TiO_2 upon anodic nanotube growth promoting the formation of oxygen vacancies and thus TiO_2 reduction. Upon annealing in ultrahigh vacuum, titanium oxycarbide (TiO_xC_y) is formed at temperatures ≥400°C, where the material changes from a semiconductor to a semimetal (Figure 4.10b). At the solid/liquid interface, the electron donor density increases from as-grown TNTs to as-grown TNT-GOQD composites due to the carbon doping, and the conductivity increases

further with annealing temperature due to the increasing concentration of coordinatively unsaturated C atoms, crystallinity and TiO_2 reduction.

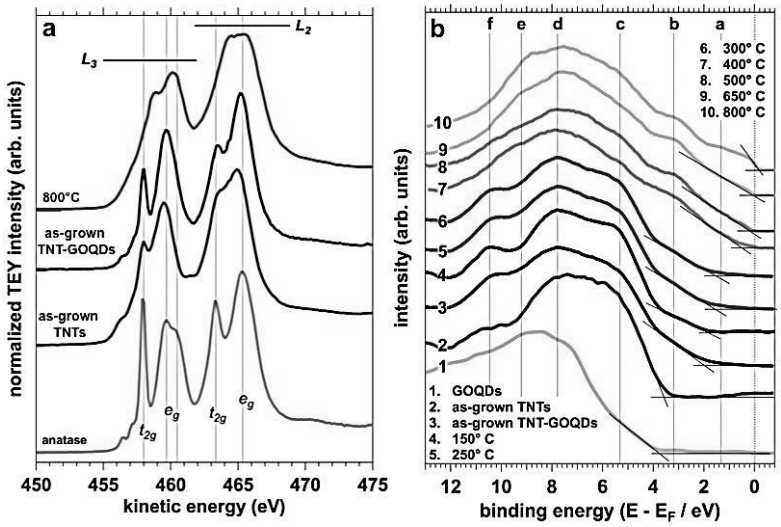

Figure 4.10. (a) Ti L edge spectra (acquired in TEY mode) for as grown TNTs, as-grown TNT-GOQDs and for TNT-GOQDs annealed at 800°C. The spectrum of anatase TiO2 is shown as reference; (b) valence band (VB) spectra acquired with 40.8 eV for GOQDs, as grown TNTs/ TNT-GOQD composites, and TNT-GOQD composites annealed between 150 and 800°C annealing temperature (adapted from § 4.1.3).

4.1.1 Reprint of the paper: Single- and Multi-Doping in Graphene Quantum Dots: Unraveling the Origin of Selectivity in the Oxygen Reduction Reaction.

ACS Catalysis

Research Article

pubs.acs.org/acscatalysis

Single and Multiple Doping in Graphene Quantum Dots: Unraveling the Origin of Selectivity in the Oxygen Reduction Reaction

Marco Favaro,[†] Lara Ferrighi,[‡] Gianluca Fazio,[‡] Luciano Colazzo,[†] Cristiana Di Valentin,*[,‡] Christian Durante,[†] Francesco Sedona,[†] Armando Gennaro,[†] Stefano Agnoli,*[,†] and Gaetano Granozzi[†]

[†]Department of Chemical Sciences, Università degli studi di Padova, Via Marzolo 1, 35131 Padova, Italy

[‡]Dipartimento di Scienza dei Materiali, Università di Milano-Bicocca, Via Cozzi 53, 20125 Milano, Italy

Supporting Information

ABSTRACT: Singly and multiply doped graphene oxide quantum dots have been synthesized by a simple electrochemical method using water as solvent. The obtained materials have been characterized by photoemission spectroscopy and scanning tunneling microscopy, in order to get a detailed picture of their chemical and structural properties. The electrochemical activity toward the oxygen reduction reaction of the doped graphene oxide quantum dots has been investigated by cyclic voltammetry and rotating disk electrode measurements, showing a clear decrease of the overpotential as a function of the dopant according to the sequence: N ~ B > B,N. Moreover, assisted by density functional calculations of the Gibbs free energy associated with every electron transfer, we demonstrate that the selectivity of the reaction is controlled by the oxidation states of the dopants: as-prepared graphene oxide quantum dots follow a two-electron reduction path that leads to the formation of hydrogen peroxide, whereas after the reduction with $NaBH_4$, the same materials favor a four-electron reduction of oxygen to water.

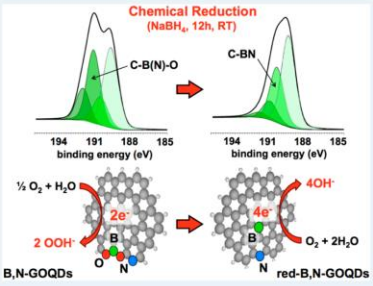

KEYWORDS: *graphene, graphene oxide quantum dots, doped-quantum dots, multidoping, electrochemical preparation, oxygen reduction reaction, density functional theory*

1. INTRODUCTION

Graphene (G) is the most fundamental archetype of carbon nanostructures, and it has gained a clear standing among materials due to its exceptional properties (superb carrier mobility, good transparency, excellent thermal conductivity, etc.). Nowadays, the forefront of research has moved from the study of the basic properties of pure G to the investigation of chemically modified G (CMG) systems,[1] i.e. doped or functionalized G, and of their composites with other nano-objects, such as nanoparticles and complex molecules. In contrast to the chemical inertness of G, CMGs present a remarkable reactivity, which stems either from defects or from new chemical functionalities. Among CMGs, G oxide (GO)[2] has gained a central role in G technology because it exhibits a tunable electric conductivity[3] and it can be easily obtained by the oxidation/exfoliation of graphite and processed to obtain wafer scaled devices.[4] Moreover, its solubility in water and facile functionalization make it a workhorse for wet chemistry applications.[3]

Together with GO, N-doped G is the other main player in the CMG arena. To prepare this material, several preparation methods were developed:[5] e.g., electrochemical reaction with NH_3,[6] exposure to nitrogen plasma,[7] chemical vapor deposition on metals (Cu and Ni) using a mixture of hydrocarbons, hydrogen, and nitrogen-containing molecules (NH_3,[8] pyridine,[9] triazine[10]), pyrolysis of polymers,[11] solvothermal synthesis,[12] and the chemical reaction between GO and melamine.[13] N-doped G immediately aroused a great deal of attention because, differently from pure G, it shows promising activity as a metal-free electrocatalyst in the oxygen reduction reaction (ORR).[5,8,14]

Recently, other doped G sheets were prepared by different routes:[15,16]

(i) S-doped G by reaction of GO with benzyl disulfide[17] or by thermal exfoliation in sulfur-containing gases[18]
(ii) B-doped G by arc discharge of graphite electrodes in the presence of a H_2 and B_2H_6 mixture[19] or by annealing GO with B_2O_3[20] or even other methods[21,22]
(iii) F-doped G by CF_4 plasma treatment of pure G[23] or by arc discharge of graphite fluoride[24]

Lately, most advanced synthetic strategies have focused on the introduction of a combination of heteroatoms in G, leading to the preparation of B−N,[25−27] S−N,[28,29] and P−N[14] dually doped materials. These doped G systems exhibit quite interesting properties in terms of electroactivity, in particular

Received: August 18, 2014
Revised: November 12, 2014

 © XXXX American Chemical Society dx.doi.org/10.1021/cs501211h | ACS Catal. 2015, 5, 129−144

Link to the full paper: http://pubs.acs.org/doi/abs/10.1021/cs501211h

4.1.2 Overview on different doped-GOQDs. Further preparations and characterizations.

Chemical and structural characterization

For the B-, N- and B,N-GOQDs the data have been already reported in § 4.1.1, and they will be not further discussed here.

The S-doped GOQDs (hereafter S-GOQDs) have been obtained using α-lipoic acid as molecular precursor (see Appendix A.4.1): the S doping is confirmed by the presence of the –CS component in the C 1s photoemission spectrum, reported in Figure 4.11.a, centered at 285.5 eV [42]. The de-convolution of the S 2p photoemission line (reported in Figure 4.11.c) highlights that the main component (**2**, 164.1 eV), which represents the 85% of the whole S 2p peak, is constituted by –C–S–C– thiophenic like units [39,40,41,42]. A weak component, associated to –SH [40,41], is also present at lower BE, centered at 162.5 eV (**1**). Finally, two weak components (contributing to the S 2p photoemission line for the 4% of the total integrated area) are localized in the tail at high BE, at 168.2 eV (**3**) and at 169.3 eV (**4**), corresponding to –C–SO_2–C– and to –C–SO_3–C– groups, respectively [39,42].

As already observed in the case of the other doped systems, the synthesis mechanism provided by the electrochemical etching of a GO WE in presence of a molecular dopant allows the introduction of *susbstitutional* chemical defects, which are well-known in literature as the most promising defects for the modulation of the electronic properties of the graphenic structure and, consequently, for the promotion of the excellent catalytic activity of these systems towards the reduction of oxygen [23,39-43].

Then, since it has been found that synergetic effects between different heteroatoms present in the graphitic networks leads to higher catalytic reactivity towards the electrochemical reduction of oxygen [23,39-43], a simple aminoacid, such as L-cysteine, has been used in order to prepare S,N-co-doped GOQDs (hereafter S,N-GOQDs).

Regarding the S,N-GOQDs, from the C 1s fit reported in Figure 4.11a it is possible to observe the presence of both –CN and –CS components [40,41]. Since they cover the same spectral region, it is not possible to distinguish between the two different contributes, therefore it is possible to observe only one intense peak (centered at 285.7 eV). The fit of the S 2p photoemission line (Figure 4.11b, carried out with 2p doublets with fixed spin orbit splitting, equal to 1.2 eV) confirms the presence of

several chemical environments for S: at 162.3 eV, 163.9 eV, 166.5 eV, 168.1 eV and 169.1 eV, which can be assigned to –SH groups (**1**, 28 %), thiophene-like groups (**2**, 40 %), -SN groups (8 %), -C-SO_2-C (**3**, 11 %) and –SO_3 (**4**, 13 %) groups, respectively [42]. It is interesting to observe that, also in this case, as already observed for the B,N-GOQDs (§ 4.1.1), the presence of direct bonds between S and N indicates the S,N co-doping of the GOQDs. Interestingly, the N 1s fit (Figure 4.11c) shows the same de-convolution discussed for N-GOQDs and B,N-GOQDs. In the case, however, the presence of the –SN counterpart component in the N 1s spectrum is not easy to detect, since the electronegativity of sulfur is comparable to the one that characterizes carbon (in the Pauling scale, EN_C= 2.55, EN_S = 2.58 while the EN_N = 3.04). In this way, such component will overlap the same spectral region of the graphitic N-based groups (**3**) (i. e. in the range of 401.1-401.4 eV). This overlap is in good agreement with the higher intensity observed for this component in the case of S,N-GOQDs, differently from what was observed in the N-GOQDs (in fact, relatively to the total intensity of the N 1s spectrum, the content of this high BE component increases from 24 %, in the case of N-GOQDs (§ 4.1.1), to 33 % for the S,N-GOQDs). Differently from B,N-GOQDs, sulfur seems to suppress the pyridinic group (**1**) content in the N 1s spectrum, with a decrease from 25 % to 17 % passing from N- to S,N-GOQDs. Similarly, the same trend is observed for the pyrrolic group (**2**) amount (41 % in the case of N-GOQDs to 28 % in the case of S,N-GOQDs). Finally, relatively to the total intensity of the N 1s spectrum, the content of the higher BE component (**4**, assigned to pyridine oxide groups) increases from 10 %, in the case of N-GOQDs, to 22 % for the S,N-GOQDs. It is interesting to highlight that the S,N-GOQDs show a higher amount of oxidized groups (both on N 1s and S 2p photoemission lines) than the N- or S-GOQDs. This can be rationalized by taking into account the C/O ratio that characterizes the dopant molecules. In fact, it is lower for L-cysteine (1.5) than the one calculated for α-lipoic acid (4); furthermore, no C/O ratio can be defined for ethylendiammine or 1,10-phenantroline, explaining the reason of the identical doping obtained using these two N-bearing molecules (§ 4.1.1).

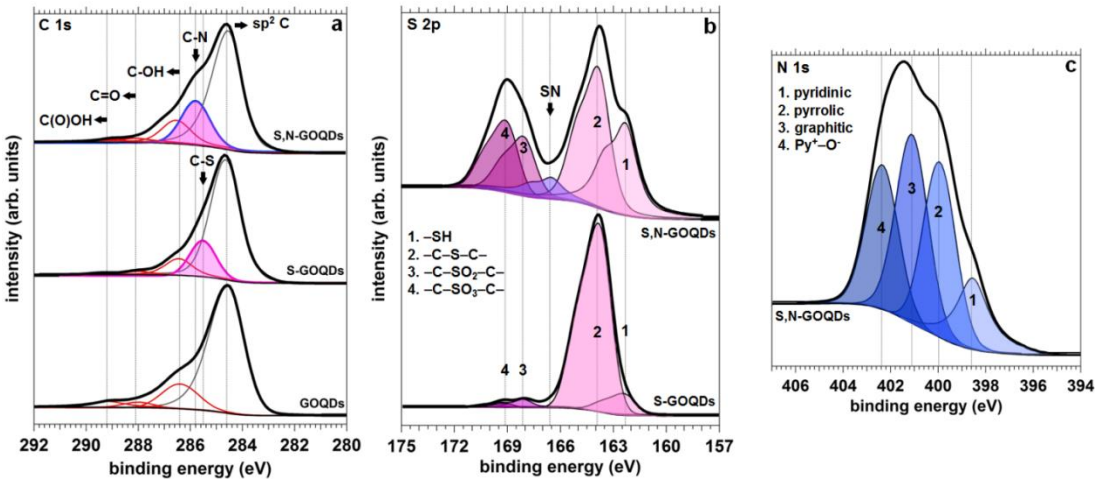

Figure 4.11. a: Multicomponent fits of the C 1s XPS peaks for pure, S- and S,N-GOQDs. Figures b and c report the relative dopant photoemission line fits, for S 2p and N 1s photoemission lines, respectively.

In order to have a deeper understanding of the chemical nature of the doped and co-doped GOQDs, NEXAFS measurements have been carried out, as reported in Figure 4.12. For all the studied systems, the C K edge spectra show the presence of the main 1s-π* transitions typical of a graphene-derived material [43]. In particular, it is possible to observe the presence of the C=C (285.0 eV, π_1), C-OH (287.2, π_2), C=O (288.2, π_3) and COOH (289.7, π_4) transitions [43]. For the B- and the B,N-GOQDs, a new component, labelled as **1**, is present in C K-edge spectra, centred at 284.2 eV. This component is attributable to the presence of boron atoms in a substitutional position in the sp^2 carbon lattice. Moreover, in the case of N-, S-, B,N- and S,N-GOQDs it is possible to observe a slight broadening of the π_1 peak, due to the presence of an additional component, centred at about 285.9 eV. This component, labelled as **2**, is attributable to the C–N or C–S bonds [44], as already observed with the conventional photoemission spectroscopy.

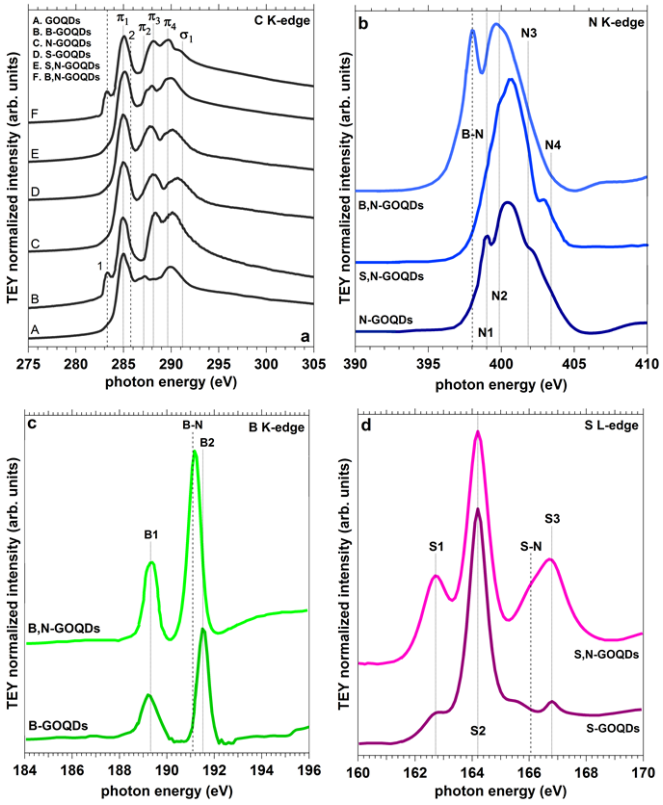

Figure 4.12. NEXAFS spectra acquired in total electron yield (TEY) mode of the carbon (a), nitrogen (b), boron (c) K-edges and sulfur L-edge (d).

As it can be observed from Table 4.3 (which reports the values of the BEs for the single chemical components derived from the fits of the XPS data and the photon energy of the relative resonances observed in the NEXAFS spectra), the detailed analysis of the absorption edges of the dopant elements basically confirm the results obtained from the XPS measurements. In particular, in the case of N- and S,N-GOQDs, the N K edge spectra show the 1s-π* transitions due to the pyridinic (N1, 399.0 eV), pyrrolic (N2, 399.8 eV) and graphitic (N3, 401.8 eV) chemical defects. [45]. The peak centered at a photon energy of 403.4 eV (N4) is attributable to the 1s-σ* transition of the N–O groups. Furthermore, regarding the B,N-GOQDs a further peak can be observed for a photon energy of 398.0 eV, which is attributable to the B-N bonds. In the case of S- and S,N-GOQDs, the S L edge spectra show the presence of –SH (S1, 162.8 eV), C–S–C (S2, 164.2 eV) and $–SO_3$ (S3, 166.8 eV) groups. In particular, for the S,N-GOQDs, a broad peak is observed for a photon energy around 165 and 168 eV, due to the concomitant presence of a relatively high amount of oxidized S-based groups and S-N groups. For the last mentioned, 1s-π* transition is centred at 166.1 eV. Similarly, the B K edge spectrum for the B-GOQDs is characterized by the presence of two distinct peaks, attributable to the 1s-π* (at 189.3

eV) and 1s-σ* (at 191.5 eV) absorption transitions of the B–sp^2 C and C-BO_2 groups, respectively. In the case of B,N-GOQDs, a further feature can be observed at 191.1 eV, due to the presence of the C–BNO bonds, in which the boron atom is bound to a nitrogen and an oxygen atom.

Table 4.3. Spectral data of the studied systems. All the values are in eV, and the ones reported between parenthesis are the energies of the resonances observed in the NEXAFS spectra. The blue and green background indicate the π* and the σ* final states of the absorption transitions, respectively.

C 1s (K-edge)		N 1s (K-edge)		S 2p (L-edge)		B 1s (K-edge)	
C=C (π_1)	284.6 (285.0)	Pyridinic (N1)	398.6 (399.0)	–SH (S1)	162.3 (162.8)	B-sp^2 C (B1)	189.6 (189.3)
C-OH (π_2)	286.4 (287.2)	Pyrrolic (N2)	400.0 (399.8)	C-S-C (S2)	163.9 (164.2)	C-BO/C-BN	190.6
C=O (π_3)	288.1 (288.2)	Graphitic (N3)	401.1 (401.8)	C-SO_2-C	168.1	C-BNO	191.1 (191.1)
COOH (π_4)	289.2 (289.7)	N-O (N4)	402.4 (403.4)	–SO_3 (S3)	169.1 (166.8)	C-BO_2 (B2)	191.5 (191.5)
B-sp^2 C (1)	283.5 (284.2)	B-N	397.5 (398.0)	S-N	166.5 (166.1)		
C-N (2)	285.8 (~285.9)						
C-S (2)	285.5 (~285.9)						

Raman microscopy has been carried out to study the local loss of symmetry in the doped-GOQDs due to the heteroatoms inserted in the graphene-like structure. Figure 4.13a compares the Raman spectra for the different obtained systems. The two bands observed at 1595 cm^{-1} and at 1325 cm^{-1} are the G band [46] (tangential vibration mode, E_{2g} symmetry group) and the D band [46], also known as disorder vibration mode (belonging to the A_{1g} symmetry group), respectively. The latter is observed only in the presence of defects that lead to a local loss of the D_{6h} symmetry of the graphitic honeycomb lattice (such as dopant atoms) [46].

In Figure 4.13b the trend of the ratio of the two bands is reported for the different prepared systems. With respect to undoped GOQDs, the doped materials are characterized by a higher D/G ratio. This is in agreement with the introduction, in the graphenic structure, of doping heteroatoms that modify the honeycomb lattice. The D/G ratio passes from 0.98 for the GOQDs to 1.08 for the S-GOQDs, with an increase of almost 10%. Moreover, the D/G ratio further increases for the co-doped systems, as a direct consequence of the presence of two heteroatoms (and, in

particular, as a consequence of the inter-dopant bonds, which strongly influences the local symmetry of graphitic or graphenic systems) [46].

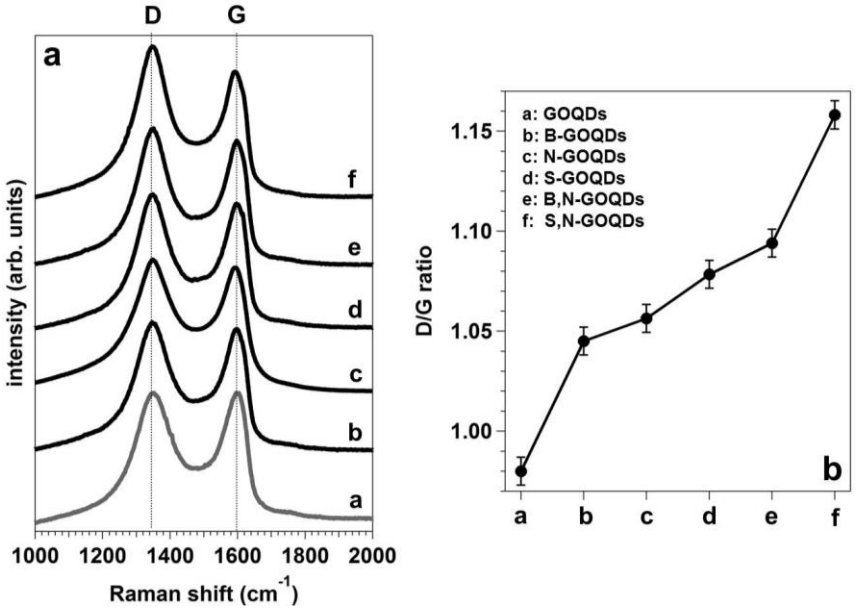

Figure 4.13. Raman spectra of pure and doped-GOQDs in the D-G band region (a) and D/G ratio for the obtained systems (b). The error bar was determined as root mean square over at least five different spectra.

Photophysical properties of pure and doped-GOQDs

The chemical doping of the GOQDs leads also to interesting photophysical properties, as reported in Figure 4.14. Since graphene and graphene oxide QDs have only recently emerged in the literature, the knowledge of the origins of their PL properties is a matter of current debates. In any case, one unifying and well-known feature of the PL of graphene-based QDs is the excitation dependence of the emission wavelength and intensity. However, whether this occurs because of the optical selection of differently sized nanoplatelets (quantum confinement effect, QCE) and/or different emissive traps on the QDs surface [10], is currently unresolved and not well-understood yet [5,18]. Moreover, it has been largely demonstrated [5] that the synthesis protocol used to produce graphene-based QDs can also tune and substantially modify the photo-physical properties of the QDs themselves, probably due to different oxidation state ("surface passivation") of this nano-sized graphene platelets. Thence, the combination of incomplete understanding in the PL mechanisms with the synthesis dependence of the photo-physical properties of these new materials, makes hard a direct comparison to and between literature data.

Regarding the UV-Visible absorption spectra of the prepared systems, it is important to highlight that the π-π* first order transition band for the doped-GOQDs is, in all the cases (and in agreement to what has been observed in previous works [5,18]), red-shifted with respect to the one that characterized the pure GOQDs (centred at 252 nm, Figure 4.14.a). In fact, the B-GOQDs are characterized by an absorption band centred at 282 nm (Figure 4.14b), with a less intense shoulder at 308 nm; the N-GOQDs (Figure 4.14c) exhibit an intense absorption band at 280 nm, with a shoulder centered at 312 nm. The S-GOQDs (Figure 4.14d) are instead characterized by an absorption band centered at 340 nm, whereas the B,N- and S,N-GOQDs (Figure 4.14e,f) show absorption features at 285 nm and 338 nm, respectively.

The GOQDs (Figure 4.14.a) show a broad excitation-dependent "near green,, emission, centered at 470 nm (for an excitation wavelength of 340 nm), as already reported in several studies appeared in literature in the last three years [5,18,47,48]. In fact, it has been reported that isolated sp^2 hybridized GOQDs platelets of nanometer size (between 1 and 10 nm) display green luminescence [22,47,48] originating from the recombination of electron-hole pairs triggered by oxygen related defects [5,18,22].

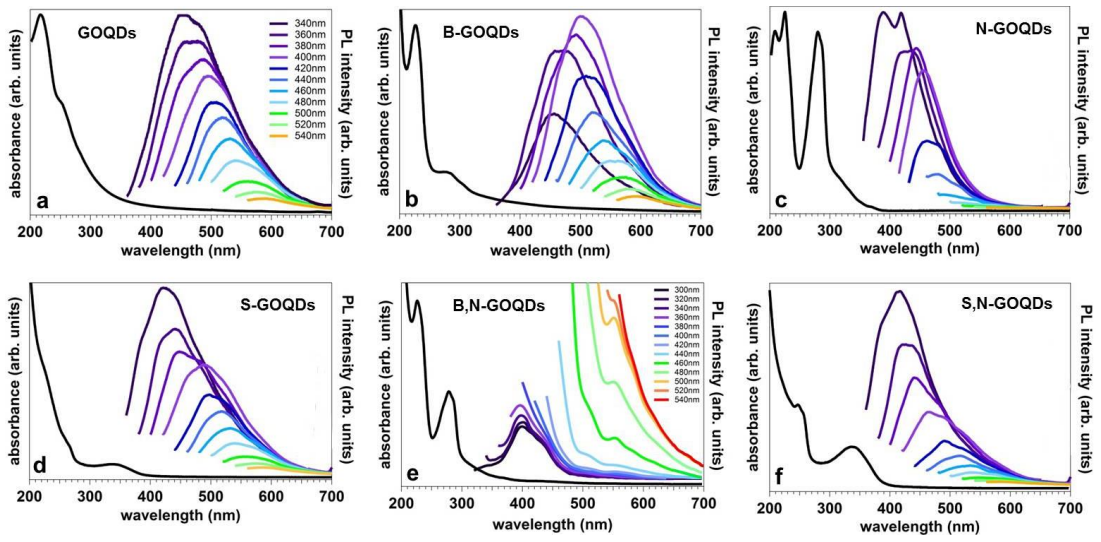

Figure 4.14. UV-Visible absorption and PL spectra acquired at different excitation wavelengths for pure (a), B- (b), N- (c), S- (d), B,N- (e) and S,N-GOQDs (f).

Interestingly, under irradiation by the same excitation wavelength, the PL spectrum of the B-GOQDs (Figure 4.14b) shows only a slight blue-shift (at 450 nm). On the contrary, the blue-shift in the PL spectra is more intense in the case of N- (Figure 4.14c), S- (Figure 4.14d) and S,N-GOQDs (Figure 4.14f), where the emission

(acquired under irradiation at 340 nm) is shifted to 410 nm, 430 nm and 415 nm, respectively. In the case of N-GOQDs, this observation in well agreement with the literature [49]; in fact, it has been reported that the relatively high electron withdrawing ability within the conjugated C plane of N atoms [50,51,52] generates a distortion in the HOMO (π)-LUMO (π^*) structure of the graphitic core of the GOQDs, [51,52,49] leading to a band gap consistent with blue emission as a result of an intraband exciton annhiliation (a π-π^* electron-hole recombination). It is also interesting to observe that N-GOQDs show a well-defined and narrower emission band than pure and B-GOQDs. Furthermore, the PL spectra of N-GOQDs exhibit a double peak structure, whose components are centered at 388 nm and at 420 nm, respectively. The detailed origin of this doublet under UV irradiation is not well understood yet [49].

Concerning the S,N-GOQDs, the only studies present in literature on the S,N co-doping of graphene-based nanoplatelets are the works of Dong et al. [53] and Qu et al. [54]; in particular, in the latter, the authors obtained S,N-graphene QDs (GQDs) via hydrothermal synthesis using thiourea as S,N molecular source. They reported a PL spectrum (under irradiation at 340 nm) centered at about 450 nm, characterized by a higher red-shift than in this work.

The optical properties that characterized the B,N-GOQDs deserve a more carefully discussion. The PL spectrum acquired at 340 nm is constituted by two peaks, centered at 400 nm and 440 nm, respectively. Then, on contrary to what is commonly observed for graphene and GO-QDs, the increase in the excitation wavelength corresponds to a drastic increase in the intensity of the PL emission, in particular for excitation wavelength beyond 450 nm. This behaviour is not already reported in other studies, and it is still under investigation.

Oxygen reduction reaction catalytic activity of pure, S and S,N-GOQDs

Figure 4.15 reports the polarization curves taken at different scan rates in a 0.1M KOH solution saturated with O_2, for pure (a), S- (b) and S,N-GOQDs (c).

Differently to the other dopants, sulfur has an electronegativity very similar to carbon (S: 2.58, C:2.55) but its atomic radius is bigger than the one of C (the atomic radius passes from 67 pm for C to 88 pm for S). Therefore the incorporation of S into the sp^2 carbon lattice can induce strain that may change the charge distribution and facilitate the oxygen chemisorption, without injecting or withdrawing charge as

result of an electronegativity-induced polarization effect.

Hence, from the values reported in Table 4.3 it is possible to observe a drastic increase in the catalytic activity of the material doped with S. In particular, the onset of the ORR is, for the S-GOQDs, shifted of 113 mV with respect the one that characterizes the GOQDs. The S,N-GOQDs also show a high catalytic activity toward the oxygen reduction. As shown by Table 4.3, the synergistic effect of the co-doping influences the reduction potential onset, which is 21 mV more positive than the one that characterizes the S-GOQDs. The net gain in the onset overpotential with respect to the pure GOQDs, taken as reference, is then equal to 134 mV.

This is in line with the previous results obtained on the other doped-GOQDs (§ 4.1.1), as reported in Table 4.3. To conclude, the graphitic basal plane is characterized by a poor catalytic reactivity (as demonstrated by the highly negative O_2 reduction potential of pure GOQDs) [55]; thus, the introduction of different heteroatoms, irrespectively of the particular mechanism that activates the oxygen adsorption, dramatically increases the activity of the basal plane, with the consequent decrease of the overpotential for the reduction of oxygen on doped-GOQDs.

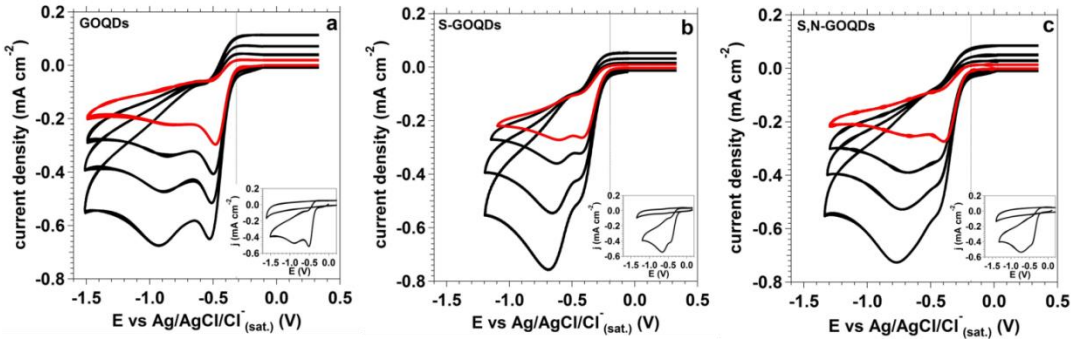

Figure 4.15. CVs of pure- (a), S- (b) and S,N-GOQDs (c) in O_2-saturated 0.1M KOH solution, at different potential scan rate (10, 20, 50 and 100 mV/s). For every each system, the inset report the CVs (at 50 mV/s) acquired in Ar- and in O_2-saturated 0.1 M KOH solutions.

In order to obtain the number of the exchanged electrons during the irreversible reduction of oxygen and, in this way, clarify the reaction mechanism on the doped-GOQDs, rotating disk electrode (RDE) measurements have been performed, in combination with Koutecky-Levich analysis.

Linear Sweep Voltammetry (LSV) curves of the ORR on the studied systems are reported in Figure 4.16a, b, and c for different electrode rotation speeds, at a scan rate of 10 mV/s. Moreover, the Koutechy-Levich analysis for pure, S- and S,N-

GOQDs are reported as well in Figure 4.16d, e and f. Table 4.4 reports the number of the exchanged electrons during the irreversible reduction of oxygen, extracted by the Koutechy-Levich linear fits reported in Figure 4.16d, e and f.

As Table 4.3 shows, all the as-prepared systems, with the only exception of the S-GOQDs, are characterized by a $2e^-$ ORR mechanism. The S-GOQDs is the only system, between those studied in this work, which shows an O_2 reduction pathway close to a $4e^-$ mechanism. This evidence can be rationalized by the fact that the S-doped system is characterized by a lower oxidation with respect to the other investigated materials and, in particular, to the S,N-GOQDs (as shown by the XPS measurements reported in Figure 4.11b). As it has been demonstrated in § 4.1.1, the presence of oxidized dopant groups on nanometric graphene patches has a negative effect on the catalytic activity and, in particular, on the $4e^-$ mechanism selectivity. Then, the high selectivity for the direct reduction of oxygen to water of the S-GOQDs is connected to the absence of oxidized C-SO_x groups.

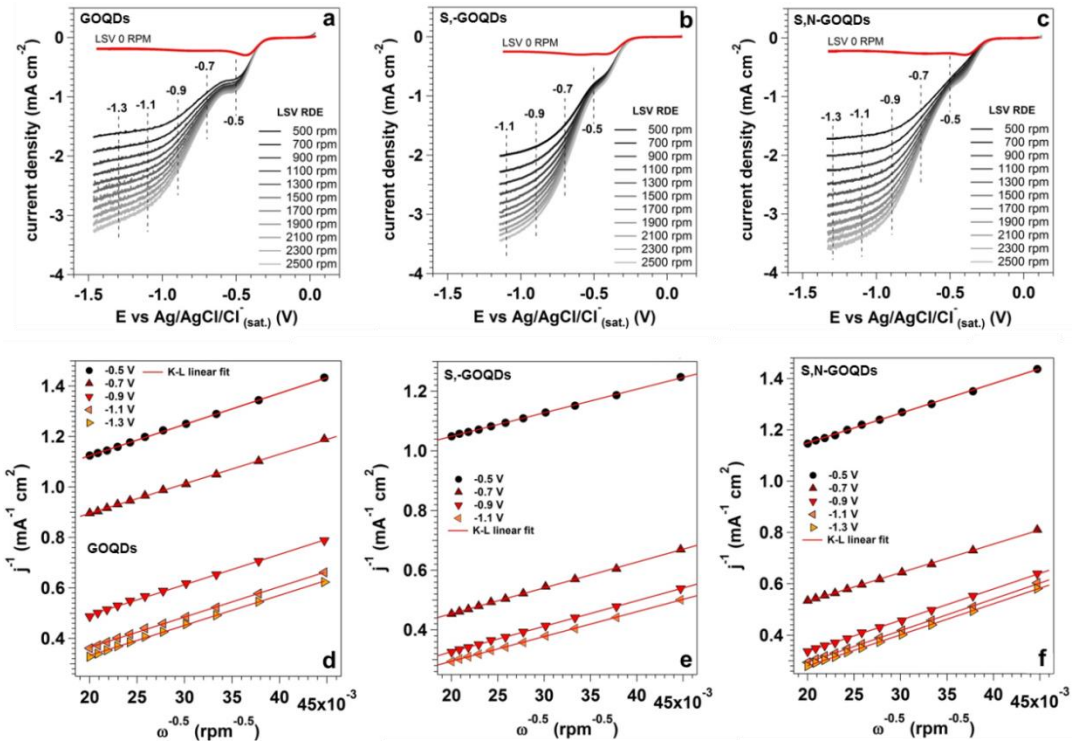

Figure 4.16. RDE linear sweeps for pure- (a), S- (b) and S,N-GOQDs (c) acquired in O_2-saturated 0.1 M KOH solution, for different rotation speeds. Koutecky-Levich plots for different potential derived from the RDE measurements, for pure- (d), S- (e) and B,N-GOQDs (f), respectively.

Taking the cue of the results obtained for the other doped-systems reported in § 4.1.1, a similar $4e^-$ reaction pathway was induced in the S,N-GOQD system performing a mild chemical reduction with $NaBH_4$ for 12 hours at room temperature. Figure 4.17a, b and c reports the S 2p and the C and N 1s photoemission lines deconvoluted into chemically shifted components, for the S,N-GOQDs after the chemical reduction (hereafter, red-S,N-GOQDs). In this case, in addition to the important decrease in the oxygen functional groups, it is possible to observe that the C-S-C component undergoes to a huge increase (from 40 % in the case of S,N-GOQDs to 62 % after reduction, relatively to the total S 2p area). This leads both to an improvement in the activity and in a $4e^-$ mediated O_2 reduction. In fact, from Figure 4.17d, it is possible to observe that the oxygen reduction potential onset falls at -0.158 V, with a positive shift of almost 20 mV with respect to the onset that characterizes the S,N-GOQDs. The Koutecky-Levich linear fits, reported in Figure 4.17f and derived from the RDE measurements reported in Figure 4.17.e, show that the *n* value is essentially constant over a potential window from -0.5 V and -1.1 V (see Table 4.4).

It is important to highlight that, in both cases, there is an important increase in the concentration of the pyridinic groups, triggered by the reduction-induced conversion of the pyridine oxide groups. In fact, concerning the red-B,N-GOQDs, the pyridinic groups pass from 39 % (for the as-prepared B,N-GOQDs) to 43 % after the reduction (with respect to the total N 1s peak area). Similarly, they pass from 17 % in the case of S,N-GOQDs to the 28 % for the red-S,N-GOQDs. As already discussed, it is well-known that the pyridinic groups are highly active towards the $4e^-$ reduction of oxygen [23,39-43,55]; this is in line to what has been discussed above: in fact, compared to the as-prepared systems, the chemical reduction treatment leads to a higher catalytic reactivity and to a direct reduction of oxygen to water.

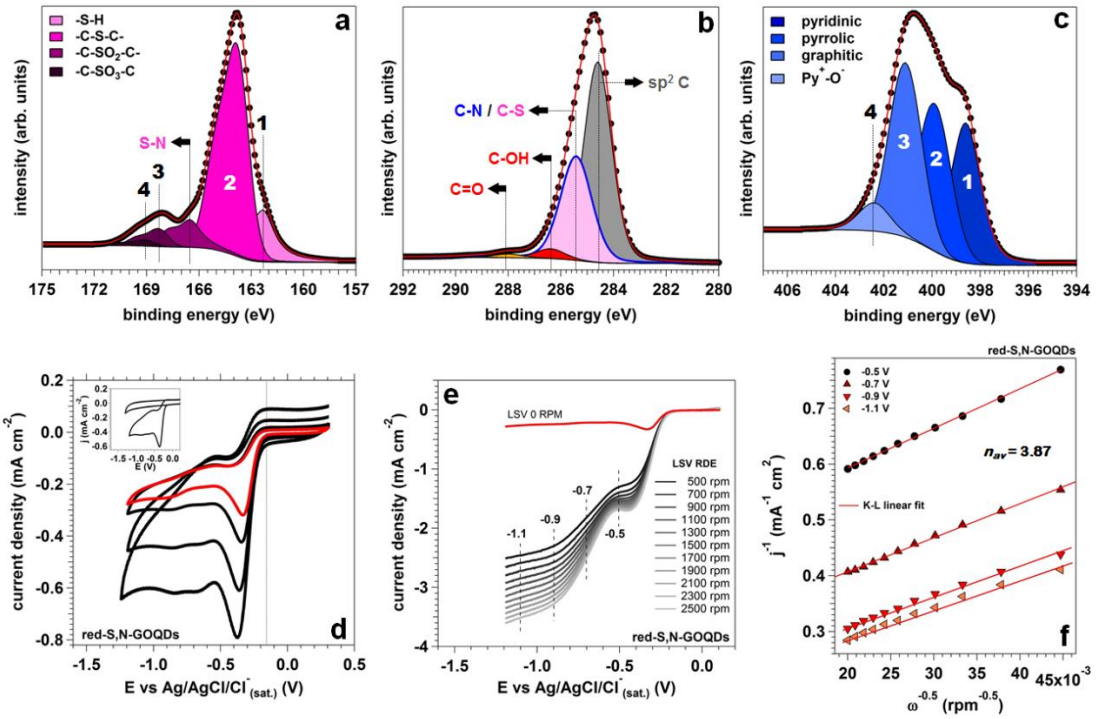

Figure 4.17. XPS analysis and catalytic tests for red-S,N-GOQDs; a, b, c: multicomponent fits on S 2p, C and N 1s photoemission lines; d: CVs in O_2-saturated 0.1 M KOH solution, at different potential scan rate (10, 20, 50 and 100 mV/s). The inset report the CVs (at 50 mV/s) acquired in Ar- and in O_2-saturated 0.1 M KOH solutions; e: RDE linear sweeps acquired in O_2-saturated 0.1 M KOH solution; f: Koutecky-Levich plots for different potential derived from the RDE measurements. The average numbers of the exchanged electrons (n_{av}) reported in the figures have been obtained as average number of the values reported in Table 4.4.

Table 4.4. Potential onsets (derived by the tangent method), peak potentials and number of electrons exchanged during the reduction of oxygen (at different potential values) for the as-prepared systems and after chemical reduction.

	Onset (V)	E_p (V) [a]	*n* (E vs. Ag/AgCl/Cl$^-_{(sat.)}$, V) [a]							
			-0.3	-0.4	-0.5	-0.6	-0.7	-0.9	-1.1	-1.3
GOQDs	-0.311	-0.497	-	-	2.21	-	2.23	2.24	2.23	2.22
S-GOQDs	-0.198	-0.443	-	-	3.31	-	3.42	3.38	3.44	-
S,N-GOQDs	-0.177	-0.392	-	-	2.44	-	2.46	2.42	2.48	2.49
B-GOQDs [b]	-0.194	-0.456	-	-	2.31	-	2.35	2.28	2.26	2.30
N-GOQDs [b]	-0.198	-0.443	-	-	2.28	-	2.27	2.24	2.23	-
B,N-GOQDs [b]	-0.162	-0.374	-	-	2.50	-	2.49	2.48	2.62	-
red-S,N-GOQDs	-0.158	-0.334	-	-	3.87	-	3.86	3.88	3.88	-
red-B-GOQDs [b]	-0.169	-0.366	-	3.47	3.61	3.69	3.82	-	-	-
red-N-GOQDs [b]	-0.179	-0.354	-	2.86	3.36	3.42	3.78	-	-	-
red-B,N-GOQDs [b]	-0.143	-0.316	-	-	3.87	-	3.91	3.92	3.94	-

[a] The values are calculated for a potential scan rate of 10 mV/s.
[b] Onset, peak potentials and number of exchanged electrons are taken from the work reported in § 4.1.1.

Water remediation over pure and S,N-GOQDs

The activity of pure and S,N-co-doped GOQDs toward the decomposition of phenol have been estimated by measuring the decomposition rate of the same chemical in an aqueous solution. 50 mL of a PBS solution (pH = 4.5), purged with O_2, have been used as electrolyte in a standard standard three-electrode EC cell, using a saturated $Ag/AgCl/Cl^-$ as RE ($E^{\Theta}_{Ag/AgCl\ (sat.)}$ = 0.197 V with respect to the standard hydrogen electrode, SHE). The WE and CE have been prepared by drop-casting 250 μL of pure or S,N-co-doped GOQDs solution (3.0 mg mL^{-1} + 5% vol. of perfluorinated Nafion alcoholic solution) onto a GC substrate (3.0 cm^{-2}), previously polished with diamond pastes at different grinding power. The cell has been enveloped with aluminium foil in order to prevent eventual decompositions of phenol by the light; the electrolyte has been kept at 25 °C during the synthesis by a thermostatic water bath. The phenol degradation tests have been performed introducing in the described system 235 mg of phenol (>99.0 %), which correspond to a concentration of 50 mM. The degradation runs have been performed under potentiostatic conditions for about 3.5 hours. The phenol degradation has been measured withdrawing small aliquots of the aqueous solution at regular time periods during the reaction (50μL, in order to avoid possible perturbation of the reaction environment). The withdrawn volumes have been diluted in 950μL of Milli-Q water in a quartz cuvette. Phenol concentration has been estimated by colorimetric method using UV–VIS spectrophotometry and the Lambert-Beer equation:

$$A = \varepsilon_M C \ell \qquad (4.1)$$

where A is the absorbance, ε_M is the molar extinction coefficient and ℓ is the optical path length. ε_M was simulated for phenol dissolved in water in presence of phosphates by PhotoChemCAD package (between 230 and 700 nm), giving a value of 2348.4 cm^{-1}/M (at 270.8 nm).

For the decomposition of organic pollutants in wastewaters, several procedures are well-known and studied in literature, such as photo-degradation over photo-active materials, the Fenton process and the decomposition over clay-based catalysts or activated carbons [56,57,58]. Most of them require the addition of H_2O_2, which serves as source for highly reactive hydroxyl radicals that are responsible for the molecular degradation of the organic pollutants. [60,61] Therefore, the main goal in

water remediation is the finding of an appropriate catalyst that can activate the hydrogen peroxide and produce free radicals during its decomposition [60,62].

Then, the as prepared-doped-GOQDs represent an ideal material for water remediation applications, since they possess a high selectivity for the $2e^-$ oxygen reduction mechanism which allows an efficient production of hydrogen peroxide. Moreover, the chemical doping (together with the presence of oxygen functional groups that decorate the QD edges) increases the intrinsic activity of these systems in converting, during anodic conditions, the H_2O_2 in efficient free OH• radicals. Then, this can be exploited for the in-situ production of H_2O_2 at a GOQD cathode and for the activation of the peroxide in OH• radicals at a same electrode used as anode, implementing in this way a closed process in which the electro-catalyst, at the same time, provides the source and the radical species that are responsible for the organic pollutants degradation.

The set-up adopted for this experiment is depicted in Figure 4.18.

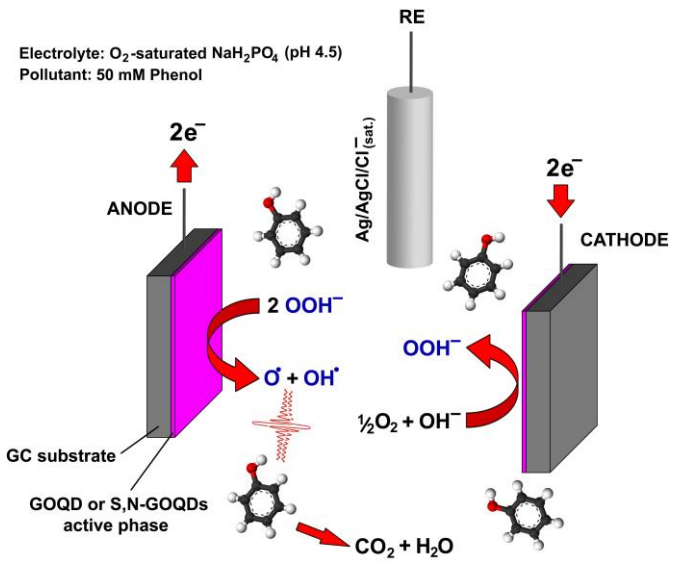

Figure 4.18. Pictorial representation of the experimental set-up adopted for this study. The figure reports the catalytic cycle that leads to the decomposition of phenol mediated by the in-situ production of hydrogen peroxide during the ORR on to as-prepared GOQD systems.

As a proof of concept, GOQDs and the S,N-GOQDs have been used as electro-catalysts for the H_2O_2-assisted decomposition of phenol.

Figure 4.19a reports the polarization curves acquired in PBS solution for both system. The reported inset shows that the two diffusion peaks, are characterized by an important difference in the ORR overpotential, with a net gain in the peak potential characterizing the S,N-GOQDs of 85 mV, with respect to the pure GOQDs.

Thence, using pure and S,N-GOQDs as both cathode and anode, two different potentiostatic experiments were performed in a solution containing 50 mM of phenol, at -845 mV and at -760 mV, respectively.

The decrease in the phenol concentration was monitored by UV-Vis absorption spectroscopy. Figure 4.19b and c report the time evolution of phenol for both experiments. The insets show the shoulder between 290 and 300 nm, attributable to phenol oxidation products. After 200 min, regarding the S,N-GOQDs system, the absorbance over the phenol spectral window is reduced by a factor 2 than that relative to the GOQDs. This observation is confirmed by the trend of the phenol concentration in the solution during the reaction, reported for both system in Figure 4.19d.

As it is possible to observe, the phenol degradation kinetic over the S,N-GOQDs is 2-fold faster than the one that characterizes the GOQDs. This evidence allows to conclude that the oxidized GOQDs are suitable systems for water remediation, and in particular for the decomposition of phenol. Moreover, thanks to their high activity toward the oxygen reduction, the S,N-GOQDs show a faster kinetic for the decomposition of phenol at a lower overpotential than the one that characterizes the pure GOQDs.

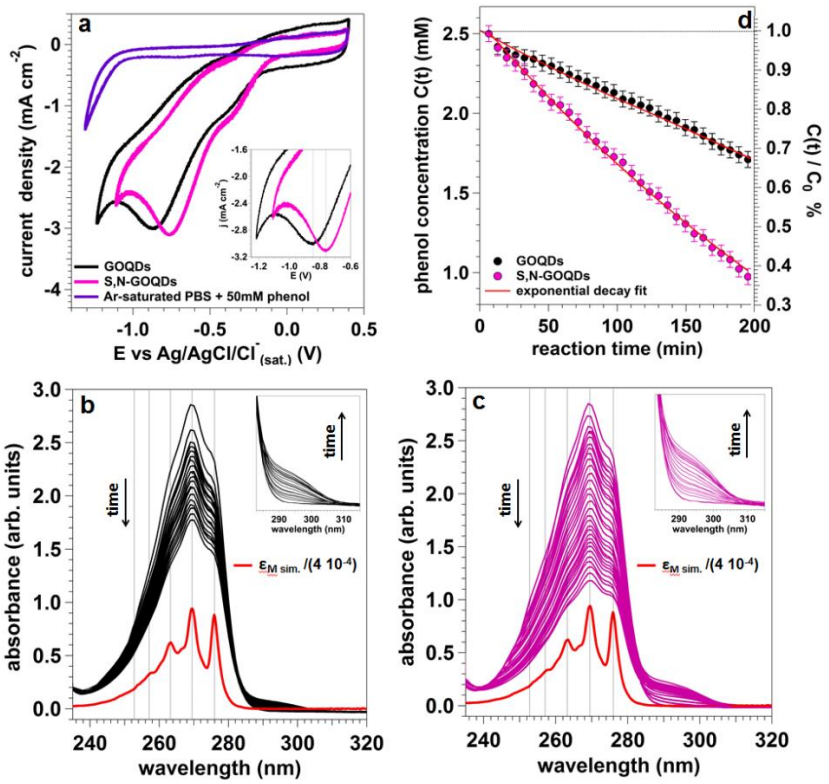

Figure 4.19. a: CVs in O_2-saturated PBS solution containing phenol, taken at 10 mV/s for pure and S,N-GOQDS (the blank measurement acquired in Ar-purged PBS solution is referred to S,N-GOQDs). The inset reports a zoom of the diffusion peaks for the two systems; b,c: time evolution of the absorbance spectrum for pure and S,N-GOQDs, respectively. The red curve represent the simulation of the ε_M for phenol in PBS solution; the insets report a zoom of the shoulder visible between 290 and 300 nm, probably due to oxidized species; d: evolution of the phenol concentration as a function of the reaction time, for both systems.

4.1.2 Reprint of the paper: Synthesis of luminescent 3D microstructures formed by carbon quantum dots and their self-assembly properties.

ChemComm

COMMUNICATION

View Article Online
View Journal | View Issue

Synthesis of luminescent 3D microstructures formed by carbon quantum dots and their self-assembly properties†

Cite this: *Chem. Commun.*, 2014, **50**, 6592

Received 4th April 2014,
Accepted 1st May 2014

DOI: 10.1039/c4cc02496f

www.rsc.org/chemcomm

D. Mazzier, M. Favaro, S. Agnoli, S. Silvestrini, G. Granozzi, M. Maggini and A. Moretto*

We report in this communication the synthesis of star-shaped carbon quantum dots–(poly-γ-benzyl-L-glutamate) conjugates that self-assemble into microstructures and retain the characteristic emission properties of the native dots. Dots were used either as an initiator to give a daisy-like peptide–polymer structure or as capping agents towards more elaborated hybrid nanostructures.

Since their discovery,[1] carbon quantum dots (CQDs) have represented a fascinating class of water-soluble carbon nanostructures, which are characterized by a discrete, quasi circular shape with diameters of up to 10 nm.[2] CQDs are non-toxic[3] carbon nanostructures that show peculiar photoluminescence (PL) properties, such as multi-colour emission that varies with the excitation wavelength.[4] They have also been proposed as interesting candidates for sensing, bioimaging and, in general, for applications where the size, cost, and biocompatibility of the label are critical issues.[5] PL properties of CQDs have been attributed to the presence of surface energy traps that become emissive upon stabilization as a result of surface passivation.[4] This requirement, in order for CQDs to become PL active, is reportedly shared by silicon nanocrystals, for which a widely accepted PL mechanism is the radiative recombination of excitons.[6] Several procedures to prepare CQDs have been reported, according to both bottom-up[7] and top-down[8] approaches. Recently, nitrogen-rich organic molecules and natural precursors (*e.g.* carbohydrates, peanut skin, soy milk) have been used to prepare highly PL active CQDs by hydrothermal treatment at high temperature for several hours, without further surface passivation.[9] Also, microwave-assisted hydrothermal transformation of amino acids has been proposed as a direct route for the production of CQDs starting from abundant and inexpensive precursors.[10] CQDs have been used either in their pristine form or blended with inorganic materials. On the other hand, they have been studied rarely in combination with organic polymers.[11] In this context, we have explored the synthesis of CQDs–polypeptide hybrids, presenting here a novel CQD–poly-γ-benzyl-L-glutamate conjugated system (CQD–PBLG) where several polymer chains are grown in a star shaped fashion over a discrete CQD core. We further modified this structure by capping the loose end of the polymer with additional CQDs, thus obtaining functional nanostructures composed by the CQD-core, PBLG-spacers and an outer CQDs-shell. In this case, the morphology of the resulting material was assayed by transmission electron microscopy (TEM) after growing silver nanoparticles (AgNPs) directly on the CQD shell. Interestingly, the CQD–PBLG and CQD–PBLG–CQDs nanosystems self-assemble in solution to give spherical aggregates that retain the peculiar emission properties of the starting CQD material. We envisioned the use of *N*-carboxyanhydride ring opening polymerization (NCA-ROP) to grow polymeric structures starting from amino groups present on the surface of CQDs.

We therefore synthesized the starting CQDs by using arginine and 1,2-ethylendiamine precursors, as schematically reported in Fig. 1A, in order to maximize the number of available amine moieties. TEM analysis of the products (Fig. 1C) revealed round particles with uniform sizes and a diameter of 1.4 ± 0.2 nm. High resolution TEM analysis (Fig. 1D) and Fast Fourier Transform (FFT) (Fig. 1D, inset) highlight an interplanar distance of 0.21 nm, compatible with the (0001) graphite basal plane. The elemental analysis yield was 71.47% for C, 5.05% for H, 17.09% for N and 5.39% for residual elements, while MALDI analysis (ESI,† Fig. S1) displayed a MW dispersion, as expected from the random combination of different atoms, centred at 1150 Da.[5c] Solid state FT-IR data (ESI,† Fig. S2) are consistent with the presence of amines. XPS measurements were carried out to provide a deeper insight into the different chemical species introduced by the synthesis. The XPS survey spectrum reported in Fig. 2a shows the C 1s, N 1s and O 1s photoemission lines to be centred at binding energies (BEs) of 284.9 eV, 399.8 eV and 531.6 eV, respectively.

The observed elemental composition (C 74.3%, N 18.8% and O 6.9%) is in good agreement with that of the previous elemental analysis. The detailed scans of C 1s and N 1s lines were deconvoluted into single chemically-shifted components, as reported in

Department of Chemical Sciences, University of Padova, Via Marzolo 1, 35131 Padova, Italy. E-mail: alessandro.moretto.1@unipd.it

† Electronic supplementary information (ESI) available: Synthetic details, SEC traces, UV-Vis absorption and emission spectra of polymers (**1** and **2**) are reported in the ESI. See DOI: 10.1039/c4cc02496f

This journal is © The Royal Society of Chemistry 2014

Link to the full paper:
http://pubs.rsc.org/en/content/articlelanding/2014/cc/c4cc02496f#!divAbstract

4.1.3 In-situ Carbon Doping of TiO_2 Nanotubes via Anodization in Graphene Oxide Quantum Dot Containing Electrolyte and Carburization to TiO_xC_y Nanotubes *(submitted work)*

Introduction

Titanium dioxide (TiO_2) has a broad field of applications that are based on its semiconducting nature. TiO_2, in its anatase or rutile form, is a wide band gap semiconductor (E_g ~ 3.0-3.2 eV) and, as such particularly suitable for applications based on UV or X-ray induced interactions. For example, this material is frequently used in photo-catalysis [1-3] and dye-sensitized solar cells.[4-6] Furthermore, it is well known for its ability to form self-organized anodic nanotube layers of highly defined morphology.[7-11]

Doping of TiO_2 has attracted considerable interest due to the possibility to extend the optical absorption of the material to the visible spectral region.[12] Doping with non-metal atoms [13,14] has been determined to be more effective than transition metal doping,[15,16] which has the drawback of yielding samples with poor photostability. Density functional theory (DFT) calculations have shown that doping TiO_2 with carbon can lead to the formation of substitutional carbon and oxygen vacancies.[17]

To expand the utilization of TiO_2 to applications that require fast electron transport in electrolytic environments, such as electrocatalyst supports in fuel cells or Li-ion battery anode materials, the conductivity of the oxide must be enhanced while keeping the material inert towards re-oxidation. TiO_2 can be made conductive via high temperature treatments in hydrogen,[18] or through carbothermal annealing. In the past, numerous approaches have been performed via both solid state synthesis [19-23] and reaction in the gas phase.[24]

Titania nanotubes (TNTs) and TiO_2 nanorods are an interesting model anode material for use in Li-ion batteries due to their excellent rate capability, cycling stability and enhanced safety compared to graphite. Compounds of TNTs and TiO_2 nanorods with carbon are known for enhanced charge transfer kinetics and superior Li intercalation properties compared to pure titania nanostructures (e.g., references [25] and [26]). In case of Li-ion battery electrodes, the carbothermal treatment is usually performed at ~400°C and aims at the production of a TiO_2 anatase phase with enhanced ionic and electronic conductivity caused by carbon coatings and by gentle carbon doping. Carbothermally treated self-organized titania nanotubes have the additional

advantage that no binder and no conductive carbon is needed for electrode preparation.[27,28] At higher temperatures, titania powders are typically reduced to a titanium oxycarbide (TiO_xC_y) which is a solid solution of titanium suboxides (TiO_x) in titanium carbide (TiC). Carbothermal reduction in the gas phase has been employed to reduce self-organized TNTs to TiO_xC_y nanotubes without destroying their nanotubular morphology.[29] Carbothermally converted planar TiO_xC_y films find use as catalyst supports.[30] The electrocatalytic activity of Pt nanoparticles supported on planar TiO_xC_y films towards the ethanol oxidation reaction correlates with the annealing temperature during support preparation, and it is enhanced for Pt on TiO_xC_y compared to Pt on Glassy Carbon.[31]

We report on an in-situ carburization method applied at room temperature (RT) in the dark, based on carbon uptake from an electrolyte enriched with graphene oxide (GO) quantum dots (GOQDs). GO, can be made from chemical exfoliation of graphite by reactions that have been known for more than 150 years,[32] a review is given in [33]. With oxygenated functional groups attached to its basal plane and edges, GO loses the electric properties of graphene and becomes an insulator, but can be readily dispersed in water and various other solvents. When self-organized TNTs are grown in certain organic electrolytes and under higher-voltage anodization, the inner nanotube layer shows an extremely high uptake of carbon from the electrolyte.[34] The presence of an inner carbon-rich contamination layer in case of TNTs formed in organic electrolytes, such as ethylene glycol, can be explained by the fact that the voltage-induced Schottky breakdown mechanism is operative for high-voltage anodization, leading to a decomposition of the organic electrolyte.[35]

In the present work, GOQDs have been dispersed in the electrolyte in which self-organized nanotubes are produced anodically at RT. The TNTs grown under these conditions show strong carbon uptake which can be referred to as in-situ doping, leading to the formation of anatase TiO_2 domains, as well as to the reduction of TiO_2 to substoichiometric oxide and TiC, which has not been observed so far. The amount of carbon introduced in the TNTs by in-situ doping is high enough to enable the conversion of TNTs to semimetallic TiO_xC_y nanotubes in the ultra high vacuum (UHV).

Results and discussion

Figure 1 depicts the morphological characteristics of TNTs and TNT-GOQD composites imaged directly after their anodic growth. The nanotubular array formed upon anodization in 0.1 M phosphate buffer solution (PBS)/NaF electrolyte is characterized by nanotube clusters forming a network of deep cracks resulting in a film with rather wavy morphology (Figure 1a). It shows traces of a capping layer partially clogging the nanotube mouths (see inset of Figure 1a). The TNTs show an average diameter of about 100 nm with a side wall thickness of ~5 nm and have an average length of 3.5 µm (Figure 1b). Self-organized TNT-GOQD composites, anodically grown in 0.1 M PBS/NaF electrolyte enriched with GOQDs, are characterized by open mouths, a uniform pore diameter of approximately 150 nm, a side wall thickness of ~5 nm (Figure 1c), and an average length of ~3.6 µm (Figure 1d). Scanning Electron Microscopy (SEM) micrographs of cross sections reveal that both TNTs and TNT-GOQD composites reach almost the same average lengths after 3 hours anodization, and their walls are characterized by the presence of ripples (Figure 1b and 1d), which is typical for self-organized TNTs grown in aqueous electrolytes.[36]

The more pronounced self-ordering effect observed for TNT-GOQD composites might be caused by a local change in pH induced by the presence of $OH^{\bullet}$ radicals formed by the strong oxidation of water at the oxide/electrolyte interface at high anodic potential.[35] Local acidification of the electrolyte solution directly influences growth rate and self-organization properties of the anodic nanotubular film.[37]

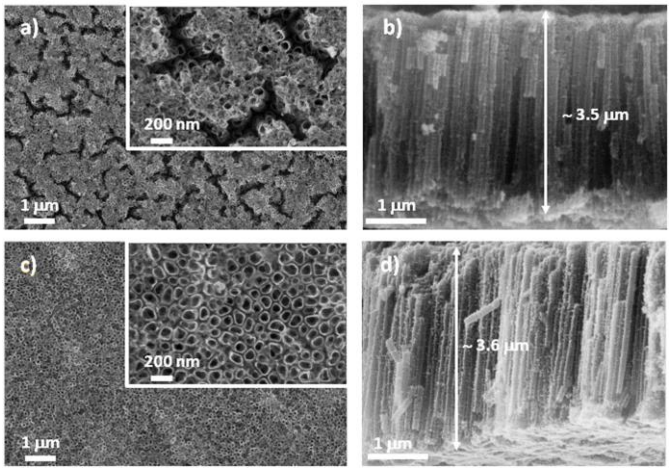

Figure 1. Morphology of TNTs and TNT-GOQD composites after anodization for 3 hours at 20 V in 0.1M PBS solution (a,b) and in PBS enriched with graphene oxide quantum dots (GOQDs) (c,d).

After anodic growth in GOQDs enriched solution, TNT-GOQD composites are annealed at different temperatures ranging from 150°C to 800°C in UHV. Top view and cross-section micrographs of nanotubular arrays after annealing at 300°C, 650°C and 800°C are shown in Figure 2. It is noteworthy that the nanotubular morphology is completely retained even after the thermal treatment at the highest temperature of 800°C (Figure 2d) with no visible increase of the side wall thickness compared to the as-anodized nanotubes (Figure 2a). Cross section micrographs (see insets of Figure 2) depict an average nanotube length of 3.6 μm, thus no change in length occurs after the thermal treatment at different temperatures.

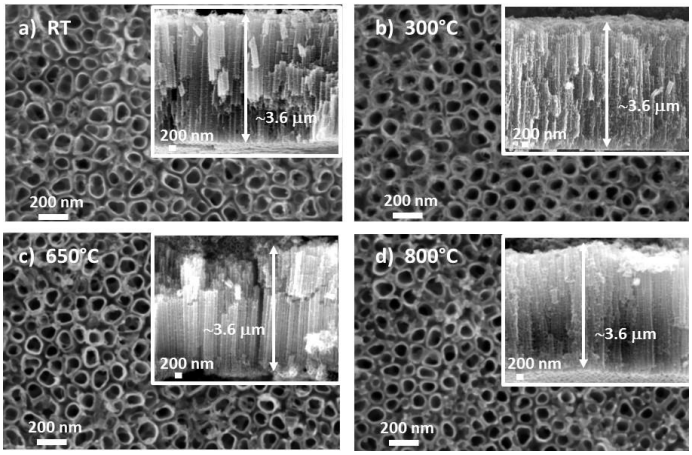

Figure 2. Morphology of TNT-GOQD composites after anodization for 3 hours at 20V in 0.1M PBS solution enriched with GOQDs (a) and after annealing at (b) 300°C ,(c) 650°C, (d) 800°C. Insets: cross sections of TNT-GOQD composited.

Core level photoelectron spectroscopy (XPS) is used to determine the chemical composition of the TNT-GOQD composites before and after annealing in UHV. The elemental composition of as-grown TNT-GOQD composites is equal to $Ti_{14.7}C_{49.1}O_{36.2}$ (at%). High-resolution spectra of the C 1s and the Ti 2p photoemission peaks are used for quantitative analysis by single component fitting. Figure 3 depicts C 1s and Ti 2p core level spectra of TNT-GOQD composites after anodic growth, and as a function of annealing temperature from 150 to 800°C. The C 1s spectrum of pure as-grown TNTs and of GOQDs (Figure 3a), and the Ti 2p spectrum of pure as-grown TNTs (Figure 3b) are shown as references. Multipeak analysis of the C 1s photoionization peak of the GOQD reference shows the presence of a graphitic sp^2 component centred at 284.6 eV (C3, Figure 3a), which is also present in the C 1s peak of the TNT-GOQD composites (Figure 3c). The identification of other components in the photoemission spectrum indicates the

presence of oxygen related defects, such as C-O (286.4 eV, C5), C=O (288.1 eV, C6) and O-C=O (289.2 eV, C7).[38-40] The peak centered at 285.4 eV (C4), visible only in the C 1s peak of the TNT-GOQD composites, but not for pristine GOQDs, can be associated with sp^3 hybridized carbon. In case of the TNT reference (see Figure 3a), carbon is also found on the surface at an impurity level, where the total carbon content is 3 at% with respect to TiO_2, which is one order of magnitude lower than in the composite system. The de-convolution of the related C 1s photoionization spectrum (Figure 3a) indicates the presence of mostly adventitious/amorphous carbon. In the C 1s signal of the TNT-GOQD composite, a peak related to TiC can also be identified, which is visible in the low binding energy (BE) region at 282.0 eV (C1).[30,40] The TiC signal in the as-grown TNT-GOQD composite constitutes 5% of the whole peak area of the C 1s signal (see Figures 3c and 4a). The Ti 2p signal shows a TiO_2 component at 458.8 eV (T3), which is the strongest peak in as-grown TNT-GOQD composites, and which decreases in intensity with increasing annealing temperature. The formation of TiC during anodic nanotube growth is confirmed by the presence of a carbide component in the Ti 2p signal of the as-grown TNT-GOQD composite at 454.6 eV (T1) [30,40] (Figure 3d). Moreover, a peak, which can be attributed to substoichiometric oxide (TiO_x) species, is detected at 456.4 eV (T2).[30,40] The presence of these reduced species can be attributed to an incipient carbon doping of TiO_2, which is known to promote the formation of oxygen vacancies and therefore Ti^{3+} ions.[17,41] Neither TiC nor TiO_x can be detected in the nanotube array grown in electrolyte without GOQDs (Figure 3b), therefore, the observed in-situ doping must be induced by the presence of GOQDs in the electrolyte solution.

The presence of sp^2 and sp^3 hybridized carbon in the TNT-GOQD composites can be explained by the presence of $OH^{\bullet}$ radicals in the electrolyte solution due to the high anodic potential applied during TNT synthesis which can cleave the covalent bonds of GOQDs, and which has been assumed to lead to carbon uptake in nanotube arrays upon anodic growth in a number of organic electrolytes.[34,35]

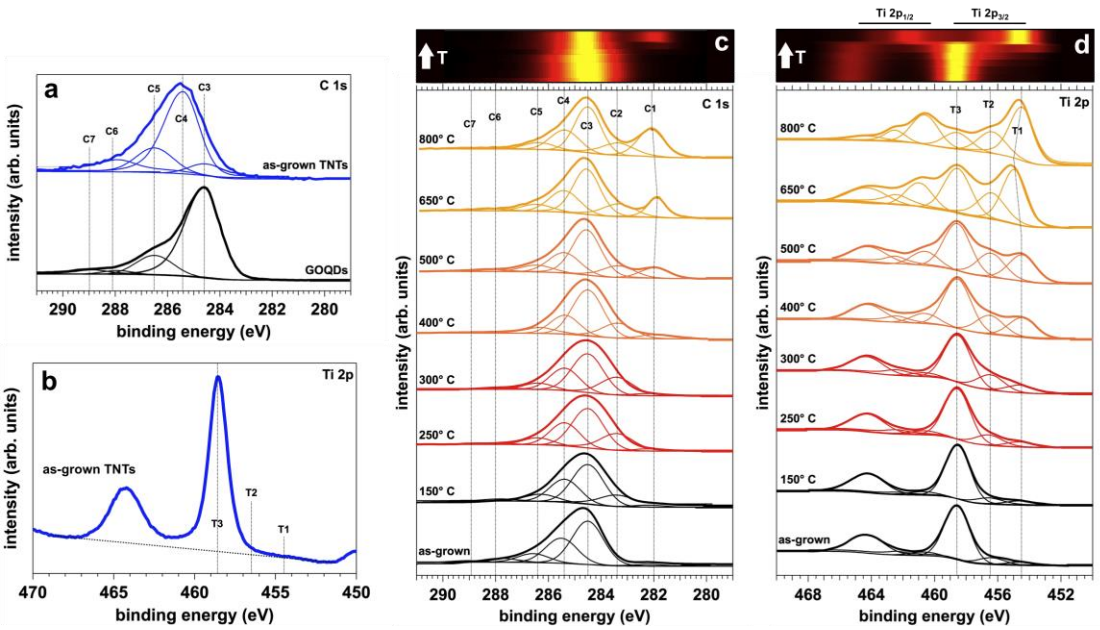

Figure 3. Photoemission spectra of as-grown TNT (C 1s, Ti 2p) and GOQD (C 1s) references (a,b). C 1s (c) and Ti 2p (d) signals of TNT-GOQD composites prior to (bottom) and after annealing at different temperatures.

The evolution of the chemical composition of the TNT-GOQD composites with increasing annealing temperature in UHV is shown in Figure 4. The amount of oxidized carbon components decreases with increasing annealing temperature due to thermal reduction, which is consistent with literature data.[40,42] Carbonyl and carboxylic groups are eliminated with the consequent evolution of CO and CO_2 [43-45], which produces C vacancies in the TNT-GOQD composite material. The presence of C vacancies is detected as a distinct component centred at 283.4 eV (C2) which is due to coordinatively unsaturated C atoms.[46] This signal can be observed between 150 and 800°C and shows a maximum at ~300°C (see Figure 4a). Above this temperature, carbon dangling bonds formed by thermal reduction can interact with Ti sub-oxide species, leading to the formation of new chemical bonds between carbon and Ti, with the consequent formation of a TiO_xC_y phase.[47] Because of this reaction, the vacancy concentration decreases between 300° and 500°C. On the other hand, the observed stabilization of both C vacancy and TiO_x concentration above 500°C (Figure 4a and 4b) might be due to a dynamical equilibrium between TiO_x/C vacancy formation and their transformation to TiO_xC_y. The temperature driven formation of TiO_xC_y seems to be triggered by the unsaturated carbon-TiO_x interaction, since the temperature onset for a continuous growth of the carbide phase is 300°C.

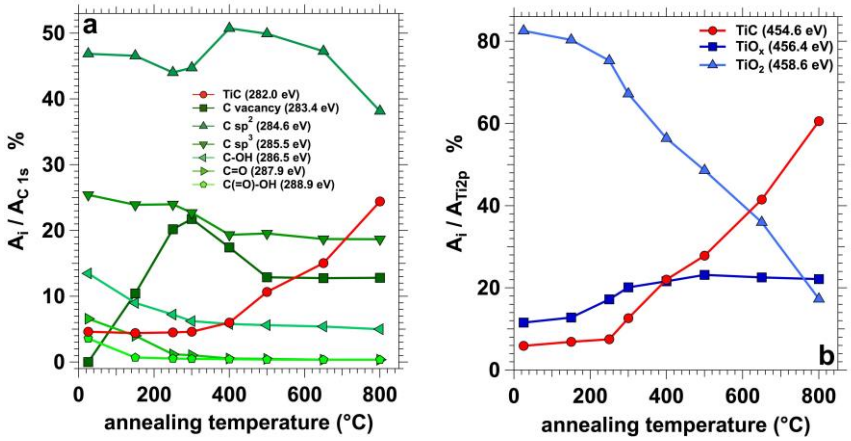

Figure 4. Atomic concentration of the components derived from the fits of C 1s (a) and of Ti 2p (b) photoemission lines as a function of the annealing temperature.

This reaction pathway is the same as that observed in previous work [48] focusing on the conversion of TiO_2 to TiO_xC_y with ethylene gas in the UHV. Also in this case, the reaction path entails the formation of an intermediate phase of reduced titania, which then reacts with the carbon source to the carbide phase.

Transmission Electron Microscopy (TEM) bright field (BF) imaging and selected area electron diffraction (SAED) are used for the structural characterization of TNTs and TNT-GOQD composites. As revealed by SAED, TiO_2 nanotubes grown in pure 0.1M PBS/ 1 wt% NaF are completely amorphous (Figure 5a), whereas nanotubes grown in GOQD containing electrolyte show a tendency to form small crystalline TiO_2 anatase domains (Figure 5b) displaying lattice fringes of 0.35 nm (Figure 5b1 and 5b2). It is very likely that the GOQDs promote the crystallization of anatase TiO_2.[49]

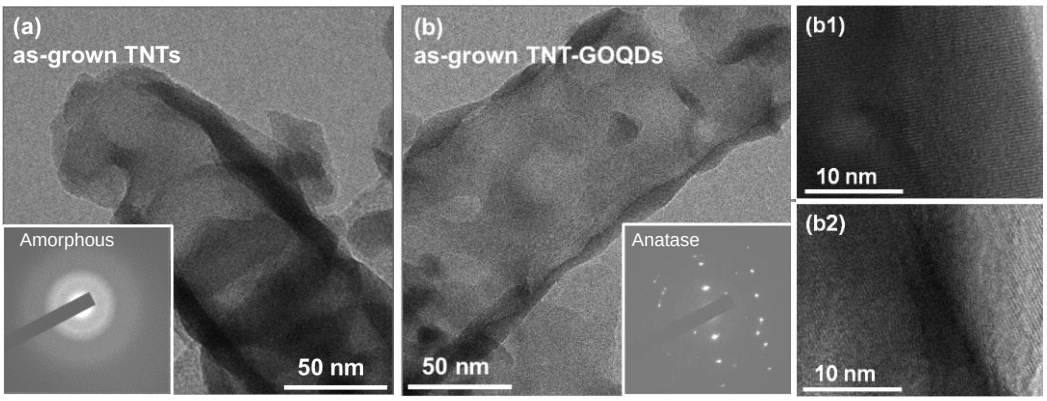

Figure 5. (a) TEM bright field images and corresponding SAED patterns of an as-grown TNT after anodization for 3 hours at 20 V in 0.1M PBS/ 1 wt%, and (b) of an as-grown TNT-GOQD composite after anodization for 3 hours at 20 V in 0.1M PBS/ 1 wt% NaF solution with GOQDs. (b1,b2) HRTEM images showing crystalline TiO_2 anatase domains with lattice fringes of 0.35nm.

Figure 6 shows TEM images of two different areas on a TNT-GOQD composite annealed at 300°C for 30 min. A remarkable increase of crystallinity is detected. The TNT is no longer composed of small crystalline domains but has transformed into one anatase single crystal. The anatase phase is identified by SAED (Figure 6a1) and by high-resolution TEM (HRTEM) micrographs showing the corresponding inter-planar lattice spacings of 0.35nm (Figure 6a2). Since carbon must be present in the material (see XPS section), we assume that TNT-GOQD composites are C-doped. In the same nanotube array, a second SAED pattern is detected (Figure 6b1) exhibiting rings consisting of sharp dots which shows the polycrystalline character of the second phase whose corresponding d-spacings can be assigned to a titanium oxycarbide (TiO_xC_y) phase. A high-resolution image of this area reveals that the oxycarbide domains are small in size compared to the anatase domains (Figure 6b2). Reflection planes of the TiO_xC_y phase and corresponding d-spacings have been calculated from angular diffraction peaks determined through X-ray Diffraction (XRD) measurements of the same material (Figure 6c). Table 1 summarizes the d-spacings and corresponding crystallographic planes for TiO_xC_y and anatase phases of Figures 5 and 6a.

TEM images and SAED patterns collected on TNT-GOQD composites annealed at 800°C confirm the coexistence of TiO_2 anatase and TiO_xC_y domains in agreement with the XRD spectra (see Figure 6c), where an intensity increase of anatase and TiO_xC_y peaks indicates the enhancement of crystallinity for TNT-GOQD composites annealed at 800°C.

The increase in size of anatase and TiO_xC_y domains with annealing temperature is in good agreement with the XPS and XRD analysis reported below. Even after annealing at 800°C, no TiO_2 rutile formation is observed, and the XRD spectra of C-containing anatase show no difference compared to pure anatase. These data confirm that carbon can be incorporated in the lattice without changing crystallographic parameters, but resulting in a stabilization of the anatase phase, and in a retardation of rutile formation.[50]

To investigate the local structure of the TNT-GOQD composites, and to confirm the results obtained by TEM, Near Edge X-ray Adsorption Fine Structure (NEXAFS) measurements are performed on as-grown TNTs, on as-grown TNT-GOQD composites, and on TNT-GOQD composites annealed at 800°C. The Ti *L* edge of an

anatase TiO_2 (001) single crystal is measured as reference for anatase.[51] The results are depicted in Figure 7a.

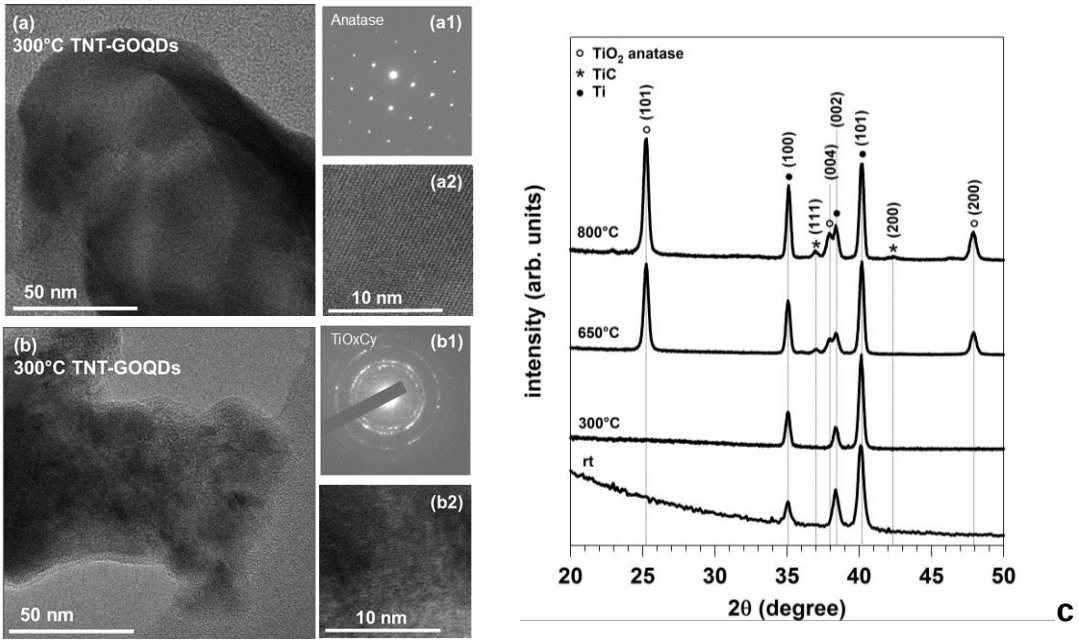

Figure 6. TEM BF images of TNT-GOQD composites after anodization for 3 hours at 20 V in 0.1M PBS / 1 wt% NaF solution containing GOQDs, after annealing at 300° C (a,b). SAED pattern and HRTEM image of (a1,a2) anatase TiO_2 (lattice 0.35 nm and 0.24 nm), and of (b1,b2) TiO_xC_y (lattice 0.25 nm); b: XRD spectra of TNT-GOQD composites after anodization for 3 hours at 20V in 0.1M PBS solution enriched with GOQDs (bottom) and after annealing at 300°C, 650°C and 800°C.

Table 1. d-spacings and corresponding reflection planes for SAEDs obtained by TEM characterization of TNT-GOQD composites, as grown and annealed at 300°C shown in Figures 5 and 6.

d-spacings (nm)		**2θ peaks** (°)		**Reflection planes** (hkl)		**SAEDs**		
Anatase [53]	TiO_xC_y	Anatase [53]	TiO_xC_y	Anatase [53]	TiO_xC_y	**Fig. 5b**	**Fig. 6a1**	**Fig. 6b1**
3.5165		25.33		101		3.52	3.52	
2.4308	2.41(XRD)	36.98	35.95(XRD)	103	111(XRD)		2.42	2.45
2.3786	2.14(XRD)	37.82	41.75(XRD)	004	200(XRD)		2.35	2.16
1.7001		53.93		105			1.77	
1.6663		55.12		211			1.68	
1.4932		62.17		213				1.51
1.2646		75.12		215			1.27	
Phase Identification						**Anatase**	**Anatase**	**TiO_xC_y**

The Ti *L* edge absorption spectra show two major peaks attributed to spin-orbit splitting of the $2p_{3/2}$ (L_3) and the $2p_{1/2}$ (L_2) signals in case of all nanotube arrays. Both L_3 and L_2 peaks are further split into two doublets, being the t_{2g} and e_g sublevels, due to the octahedral crystal field and the strong exchange interaction between the reticular oxygen atoms and the Ti ion in O_h configuration.[40,52-54] The crystal field experienced by the Ti atoms lifts the degeneracy of unfilled Ti 3d orbitals leading to the series of $L_{2,3}$ t_{2g}-e_g electron transitions from the $2p_{3/2}$-$2p_{1/2}$ levels into the $2p_{3/2}{}^{-1}3d\pi$, $2p_{3/2}{}^{-1}3d\sigma$, $2p_{1/2}{}^{-1}3d\pi$ and $2p_{1/2}{}^{-1}3d\sigma$ final states.[54-56] Therefore, the NEXAFS fingerprint can be used as a tool to detect small changes in the local coordination of Ti ions.[40,52,54,55] It is known that for amorphous titania, the lack of long-range order, which suppresses the interaction of Ti with the second-neighbour shells, determines a general broadening of the $L_{2,3}$ peaks and, in particular, the absence of a clear splitting of the e_g subband in the L_3 threshold.[40,54,57] Figure 7a shows that the absorption spectrum of TNT-GOQD composites is characterized by sharper and more intense t_{2g} and e_g subbands, which resemble crystalline anatase, in contrast to the spectral features of the as-grown TNTs that appear less defined. This observation indicates that as grown TNT-GOQD composites consist of an amorphous TiO_2 matrix with embedded crystalline anatase domains, which is in agreement with the TEM data reported above. Thence, the presence of GOQDs in the electrolyte leads to the formation of crystalline domains inside the TNTs and therefore to a decrease of the band gap.[40,58-60] TNT-GOQD composites annealed at 800°C exhibit a Ti *L* edge spectrum characteristic for octahedrally coordinated Ti in a TiC phase.[61] The less intense interaction between Ti and C atoms in TiC leads to broad $L_{2,3}$ peaks weakly split into the t_{2g} and e_g subbands (see Figure 7a).[61]

Valence band (VB) Ultraviolet Photoemission Spectroscopy (UPS) data of TNT-GOQD composites are depicted in Figure 7b. They consist of two main features centred at 5.3 eV (c) and 7.8 eV (d), corresponding to O 2p σ-π states that can be interpreted as bonding states of octahedrally coordinated TiO_2 [40,54], in agreement with the NEXAFS measurements. Two less intense features can be identified at ~1.3 eV (a) and 3.2 eV (b). The signal at 1.3 eV (a) is usually associated with Ti 3d states corresponding to substoichiometric titania (TiO_x) that has already been identified with XPS in the Ti 2p spectra (see Figure 3). The peak at 3.2 eV (b) is mainly present in the VB spectra of the composites produced at temperatures above 300°C, which is the onset temperature for the conversion to TiO_xC_y, as described

above. It can be attributed to the hybridization between C 2p and Ti 3d states,[40,48,62] due to the formation of a TiO_xC_y phase.[40,48] The signal centred at 9.2 eV (e) is associated with 2s states of C atoms involved in a six-fold coordination with Ti atoms.[48,62] The intensity of this feature increases with increasing annealing temperature (i.e. with the conversion degree), similarly to what has been reported in reference.[48] The feature at 10.5 eV (f) is related to 2 s states of C in GOQD fragments, in which the C atoms interact with O atoms of corresponding functional groups. In TNT-GOQD arrays, the intensity of this feature decreases with increasing annealing temperature due to thermal reduction, and disappears after annealing at 400°C which is consistent with the XPS data related to oxygenated carbon components discussed above. Figure 7c depicts the normalized intensities of XPS core level components in comparison with distinctive features identified from VB spectra. The intensities of VB signals (b) and (e), which are associated with Ti–C interaction, increase with increasing annealing temperature, and show a similar trend as the carbide component (C1, T1) derived from XPS spectra. The intensity of feature (f), which is indicative for C–O interaction within GOQD fragments, decreases with increasing annealing temperature. All trends show that, with increasing annealing temperature, the interaction between Ti and ingested carbon from GOQD fragments increases, whereas the interaction within GOQDs decreases, which points to a chemical reaction where the oxygenated carbon species of the GOQDs are progressively eliminated during the annealing forming coordinatively unsaturated carbon species that can react with the reduced titania forming the TiC phase.

The UPS measurements show that, already at 400°C, it is possible to convert TNT-GOQD composites from a semiconductor to a semimetal composite material as demonstrated by the density of states just below the Fermi level, which is in accordance with the literature.[40,48,63]

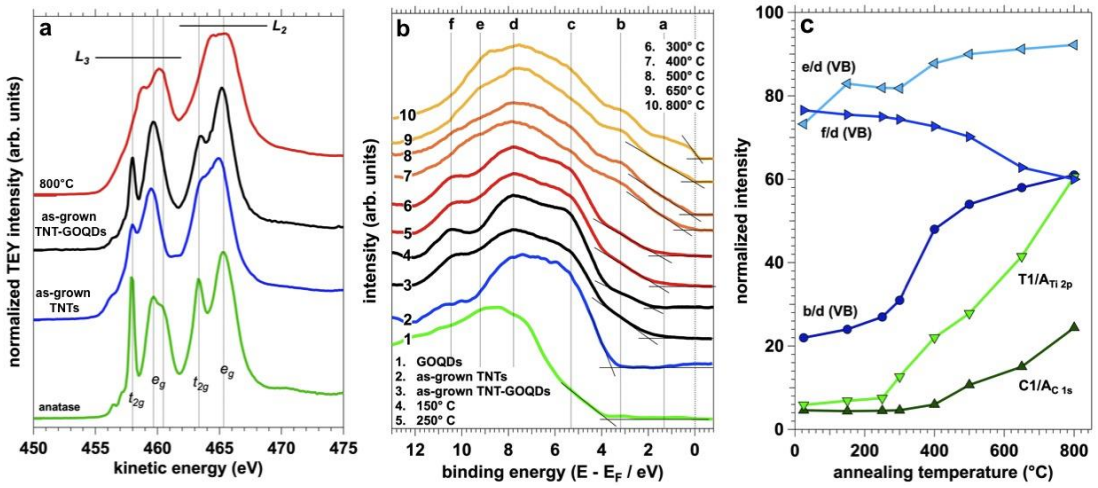

Figure 7. (a) Ti L edge spectra (acquired in TEY mode) for as grown TNTs, as-grown TNT-GOQDs and for TNT-GOQDs annealed at 800°C. The spectrum of anatase TiO_2 is shown as reference; (b) valence band (VB) spectra acquired with 40.8 eV for GOQDs, as grown TNTs/ TNT-GOQD composites, and TNT-GOQD composites annealed between 150 and 800°C annealing temperature. (c) normalized intensities of C1 (C1s) and T1 (Ti2p) components (from XPS), and b/d, e/d and f/d ratios (from UPS).

To confirm the results obtained at the solid/gas interface with surface science tools, we have performed Mott-Schottky measurements at the solid/liquid interface of the TNT-GOQD composites. Electrochemical capacity values are extracted from electrochemical impedance spectroscopy (EIS) data at 1 kHz determined by the imaginary part (Equation 1) for each potential applied to the TNT-GOQD composite working electrodes (WEs). These capacitance values are plotted as a function of the potential applied to the WE (Figure 8a) according to the Mott-Schottky approach,[64] which establishes a relation of the space charge capacitance (C_{SC}) with the applied potential according to Equation 2.

$$C = -\frac{1}{2\pi f Z''} \qquad (1)$$

$$C_{SC}^{-2} = \frac{2}{\varepsilon\varepsilon_0 e N_D}\left(E - E_{FB} - \frac{kT}{e}\right) \qquad (2)$$

In eq. (1), f is the frequency (in Hz), Z'' is the imaginary part extracted from the EIS spectra (in Ω cm^2), C_{SC} is the space charge capacitance of the semiconductor (in mF cm^{-2}), ε the dielectric constant of the semiconductor (60 in the case of TiO_2 [65]), ε_0 the vacuum permittivity (8.85 x 10^{-14} F cm^{-1}), e the elemental charge, N_D the apparent electron donor density (cm^3), E the applied potential (in V), E_{FB} the flat

band potential (in V), *k* the Boltzmann's constant (1.38×10^{-23} J K^{-1}) and *T* the temperature (in K). The capacitance values of the as-grown TNTs and TNT-GOQD composites, show a potential dependence with a positive slope characteristic of an n-type semiconductor in contact with an electrolyte. N_D and E_{FB} are extracted by linear regressions of the curves in the depletion zone (above 0.6 V_{SHE} for TNTs, and above 0.3 V_{SHE} for as-grown TNT-GOQD composites), where capacitances values are characteristic for the space charge layer thickness (E above the E_{FB} in n-type semiconductors).[66] N_D values correspond to 9.9×10^{25} m^{-3} and 5.0×10^{26} m^{-3} for the as-grown TNTs and TNT-GOQD composites, respectively. The incorporation of sp^2 and sp^3 carbon, and the formation of carbide and sub-oxide phases, that already starts upon anodic TNT-GOQD composite growth at RT (see above), can contribute to the increase of the doping concentration N_D. Additionally, the presence of domains of crystalline anatase observed by TEM in the TNT-GOQD composites (see Figure 5b) can explain the different electronic properties.

For as-grown TNT-GOQD composites, a displacement of the E_{FB} towards more cathodic potentials (from 483 mV to -17 mV) is found. This is in agreement with the UPS results (Figure 7b), where a shift of the VB maximum towards lower binding energy is observed. Therefore, as-grown TNT-GOQD composites can be considered carbon doped titania nanotubes. It has to be noted that the values of the flat band potentials are positively shifted with respect to the values reported in literature,[67] which is most likely due to the presence of titanium metal under the nanotube film contributing to a relatively high flatband potential and, correspondingly, low position of band edges in terms of electron energy.[68] Only a weak dependence of the apparent capacitance on the applied potential is observed for the TNT-GOQD composites after the thermal treatment at 300ºC and 400ºC (see inset in Figure 8a). The increasing concentration of coordinatively unsaturated C atoms observed up to 300ºC annealing temperature (see Figure 6a) can explain the observed increase of conductivity of the semiconductor. At 400°C, a further flattening of the Mott-Schottky plot indicates that the formation of TiO_x and TiC phases lead to a further increase of the conductivity. Above 400ºC, no dependence of the capacitance on the applied potential is observed anymore, and apparent capacitances are only determined by the double layer at the solid/liquid interface (Helmholtz layer) so that no reasonable E_{FB} can be extracted, which suggests that the TNT-GOQD composites have semimetallic properties. It is important to note that Mott-Schottky analysis has

been used to extract qualitative information on electron transport properties in the studied system.

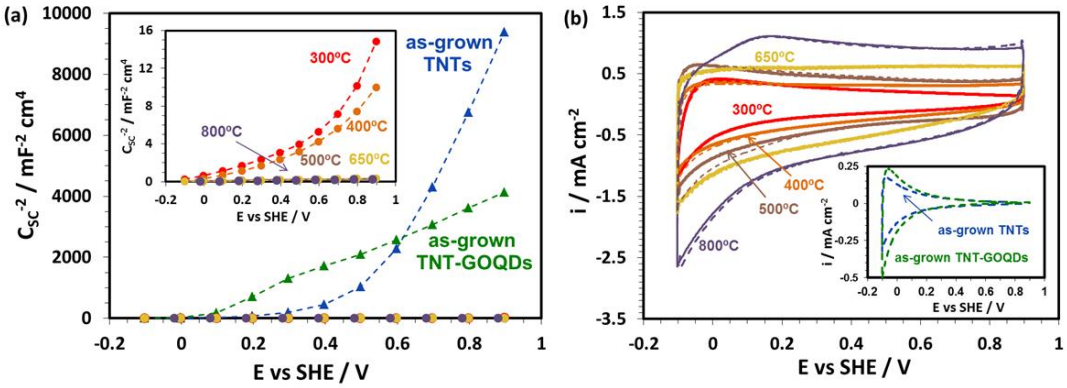

Figure 8. (a) Mott-Schottky plots of as TNTs synthesized in PBS and in PBS with GOQDs, and annealed at different temperatures, in 1M $HClO_4$ solution at 1kHz. Inset: enlargement of plots corresponding to the annealed TNT-GOQD composites. (b) Cyclic voltammograms of TNTs synthesized in PBS and in PBS with GOQDs, and annealed at different temperatures, in 1M $HClO_4$; scan rate: 100mVs^{-1}. First cycles: dotted lines, 20th cycles: continuous lines. Inset: CVs corresponding to the as-grown TNTs and as-grown TNT-GOQDs.

Figure 8b shows cyclic voltammograms (CVs) in 1M $HClO_4$ of pure as-grown TNTs, of as-grown TNT-GOQD composites (inset), and of TNT-GOQD composites annealed at different temperatures. The overlap of the first and the 20th cycle observed for the TNT-GOQD composites, annealed at 300, 400, 500, 650 and 800°C, shows the reversibility of electrochemical processes in the double layer region of the material. Significant differences are visible between as-prepared and annealed nanotube arrays. In case of as-grown TNTs and TNT-GOQD composites (inset of Figure 8b), a considerably low current density is detected, especially in the anodic potential range, and the CV has a shape characteristic for a semiconductor material. A similar shape of the CV is preserved for TNT-GOQD composites annealed at 300ºC, suggesting semiconductive behavior of the material after the annealing treatment at this temperature. However, the increase of the number of charge carriers in the band gap explained above together with the formation of carbide and suboxide phases upon annealing at T ≥ 300ºC lead to an enhancement of current density with increasing annealing temperature in comparison with the non-annealed materials. For nanotube arrays annealed at 400°C and above, a steady and uniform shape of the current density is obtained in the CVs, representing a well-defined electrical double layer capacitance. Values of the specific capacitance are extracted from the CVs

following the procedure described by Yuan et al. [69] and Xie et al. [70] and are summarized in Table 2. Current due to hydrogen desorption in the anodic scan, as a consequence of hydrogen formation in the cathodic scan, has not been taken into consideration.

Table 2. Specific capacitance values extracted from CVs (Figure 8b) for TNT-GOQD composites annealed at different temperatures.

Annealing Temperature	Specific capacitance (mF cm^{-2})
300ºC	-
400ºC	7.88
500ºC	11.43
650ºC	14.86
800ºC	22.90

It is noteworthy that no redox peak appears in the CVs within the selected potential window which indicates that no reactions between the species present in the TNT-GOQD composites (TiO_xC_y, TiC, TiO_x, etc.) and the electrolyte take place. This behavior validates the use of the Mott-Schottky analysis to study transport properties of the nanotube arrays, and demonstrates that the variation of the capacitance with potential (Figure 8a) is exclusively due to the modification of band edges inside the material (variation of the space charge layer thickness with the applied potential).

Factors affecting the increase of specific capacitance with increasing annealing temperature under the studied experimental conditions can be (i) increase of the active surface area and/or (ii) increase of the conductivity. According to the SEM cross sections of the nanotube arrays depicted in the insets of Figure 2, no modification of the active surface area has been introduced through the thermal treatment. To confirm that the modification of the capacitance is due to an increase of electrical conductivity, electrochemical measurements are carried out in an electrolyte containing hexacyanoferrate ions (Figure 9). The qualitative measure of the conductivity is given by the potential difference between anodic and cathodic peak. It shows a clear dependence of the conductivity on the annealing temperature. The minimum potential difference, i.e., the highest conductivity, is found for the

TNT-GOQD composites annealed at 650ºC and 850ºC with peak separation values of 84 and 88 mV, respectively (Table 3).

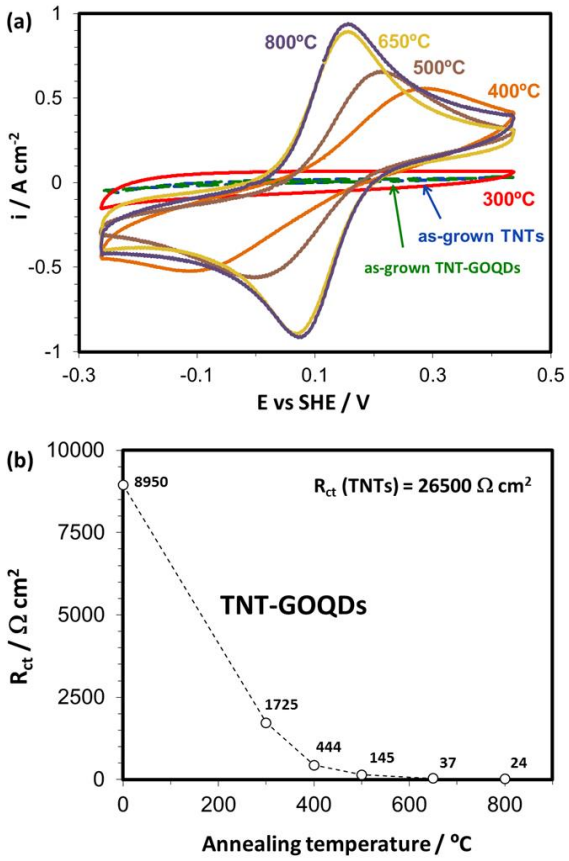

Figure 8. (a) Cyclic voltammograms (CVs) of as-grown TNTs, as–grown TNT-GOQDs and TNT-GOQD composites in 5mM $K_{3,4}[Fe(CN)_6]$ in 0.1M H2SO4 after 20 cycles; scan rate: 50 mV/s. (b) Charge transfer resistance (R_{ct}), extracted from EIS data (frequency range: 100kHz - 0.1Hz) obtained at the redox potential, as a function of the annealing temperature.

Table 3. Potential difference between anodic and cathodic peaks extracted from the CVs shown in Figure 8a.

Annealing Temperature	Peak distance ΔE (mV)
300ºC	-
400ºC	399
500ºC	220
650ºC	88
800ºC	84

This behavior corroborates the enhancement of semimetallic properties observed in the Mott-Schottky plot with increasing annealing temperature (Figure 8a). Thus, the increase of specific capacitance with annealing temperature (Figure 8b) can only be due to an increase of the electronic conductivity in the studied nanotube arrays.

Quantitative values for the TNT conductivity are obtained extracting the charge transfer resistance (R_{ct}) from EIS spectra after fitting them to the same electrical equivalent circuit (EEC) as described in [30,71,72]. A decrease of R_{ct} with increasing annealing temperature from 1725 Ω cm^2 at 300ºC to 24 Ω cm^2 at 800ºC is found. It is important to note that similar values of the electrical conductivity have been measured for flat TiO_xC_y films converted via a carbothermal treatment above 650ºC.[30]

Conclusions

In the present work, we have investigated the anodic growth of in-situ carbon doped self-organized titania nanotubes. Carbon doping, which is known to promote the formation of oxygen vacancies and therefore Ti^{3+} ions in TiO_2, is achieved by anodic polarization in GOQD containing electrolyte, and leads to the formation of anatase TiO_2 domains, as well as to the reduction of TiO_2 to substoichiometric oxide and TiC.

SEM has been used to image the TNT and TNT-composite arrays, revealing that a change of array morphology occurs when the electrolyte is enriched with GOQDs. A more pronounced self-ordering effect is observed for TNT-GOQD composites, which might be caused by a local change in pH induced by the presence of $OH^{\bullet}$ radicals formed by the strong oxidation of water at the oxide/electrolyte interface at high anodic potentials. After annealing, no morphological change of the TNT-GOQD composites is observed.

XPS shows that TNT-GOQD composites are carbon doped directly after anodic production. This is evidenced by the presence of sp^2 and sp^3 carbon components, substoichiometric oxide TiO_x and TiC. Annealing in UHV leads to an increase of TiO_x and TiC component concentrations. With increasing annealing temperature, coordinatively unsaturated C atoms, due to the formation of C vacancies at increasing temperature, are produced in the TNT-GOQD composite material. The vacancy concentration shows a maximum at ~300°C, above this temperature, carbon dangling bonds formed by thermal reduction can interact with Ti suboxide species, leading to the formation of new chemical bonds between carbon and Ti, with the subsequent formation of a TiO_xC_y phase. The observed stabilization of both C vacancy and TiO_x concentration above 500°C might be due to a dynamical equilibrium between TiO_x/C vacancy formation and their reaction to TiO_xC_y.

TEM reveals that as-grown TNT-GOQD composites contain small TiO_2 anatase domains, which is most likely promoted by the presence of GOQDs, whereas as-grown TNTs are completely amorphous. After annealing, the materials crystallinity increases, and a crystalline anatase phase consisting of single-crystalline domains and a TiO_xC_y phase, consisting of smaller domains, are detected. Even after annealing at 800°C, no rutile TiO_2 formation is observed, which must be due to the presence of carbon from GOQDs in the material. NEXAFS confirms the presence of crystalline anatase domains in as-grown TNT-GOQD composites, and the presence of a TiC phase in annealed TNT-GOQD composites.

UPS confirms the presence of substoichiometric titania TiO_x, the formation of TiO_xC_y at temperatures ≥300°C, the decrease of C–O interactions in GOQD fragments, and the increase of Ti–C interactions in the composites with increasing annealing temperature, which correlates well with the XPS results. Already at 400°C, TNT-GOQD composites are converted from a semiconductor to a semimetallic material, which is evidenced by the increased density of states below the Fermi level. Mott-Schottky analysis reveals an increase of the apparent electron donor density from as-grown TNTs to as-grown TNT-GOQD composites, which must be due to the incorporation of graphitic carbon, and the formation of carbides and sub-oxides, that already starts upon anodic TNT-GOQD composite growth at RT. Flattening of the Mott-Schottky plots with increasing annealing temperature, implying an increase in conductivity, can be explained by the increase in carbon vacancy concentration and in crystallinity up to 300°C, and by the formation of TiO_x and TiC that leads to a further conductivity increase at 400°C. Above 400ºC, apparent capacitances are exclusively determined by the Helmholtz layer, showing that TNT-GOQD composites have semimetallic properties after annealing at this temperature. Cyclic voltammetry shows that, at the solid/ liquid interface, TNT-GOQD composites show semiconductive behavior up to an annealing temperature of 300°C, whereas at ≥400°C annealing temperature, a well-defined electrical double layer capacitance is measured, where an increase of specific capacitance with increasing annealing temperature is observed due to increasing electronic conductivity.

References

[1] A. Fujishima, K. Honda, *Nature* **1972**, *238*, 37.

[2] A.L. Linsebigler, G. Lu, J.T. Yates, *Chem. Rev.* **1995**, *95*, 735.

[3] R. Wang, K. Hashimoto, A. Fujishima, M. Chikuni, E. Kojima, A. Kitamura, *Nature* **1997**, *388*, 431.

[4] B. O'Regan, M. Grätzel, *Nature* **1991**, *353*, 737.

[5] K. Zhu, N.R. Neale, A. Miedaner, A.J. Frank, *Nano Lett.* **2007**, *7*, 69.

[6] A. Ghicov, J.M. Macak, H. Tsuchiya, J. Kunze, V. Haeublein, L. Frey, P. Schmuki, *Nano Lett.* **2006**, *6*, 1080.

[7] V. Zwilling, E. Darque-Ceretti, A. Boutry-Forveille, D. David, M.Y. Perrin, M. Aucouturier, *Surf. Interface Anal.* **1999**, *27*, 629.

[8] J.M. Macak, H. Tsuchiya, A. Ghicov, K. Yasuda, R. Hahn, S. Bauer, P. Schmuki, *Curr. Opin. Solid State Mater. Sci.* **2007**, *11*, 3.

[9] D.J. LeClere, A. Valota, P. Skeldon, G.E. Thompson, S. Berger, J. Kunze, P. Schmuki, H. Habazaki, S. Nagata, *J. Electrochem. Soc.* **2008**, *155*, C487.

[10] S. Berger, J.M. Macak, J. Kunze, P. Schmuki, *Electrochem Solid-State Lett.* **2008**, *11*, C37.

[11] S. Berger, J. Kunze, P. Schmuki, D.J. LeClere, A. Valota, P. Skeldon, G.E. Thompson, *Electrochim. Acta* **2009**, *54*, 5942.

[12] H. Kisch, M. Macyk, *ChemPhysChem* **2002**, *3*, 399.

[13] R. Asahi, T. Morikawa, T. Ohwaki, K. Aoki, Y. Taga, *Science* **2001**, *293*, 269.

[14] S.U.M. Khan, M. Al-Shahry, W.B. Ingler, *Science* **2002**, *297*, 2243.

[15] D. Dvoranová, V. Brezová, M. Mazúr, M.A. Malati, *Appl. Catal., B* **2002**, *37*, 91.

[16] L. Yong, F. Pingfeng, D. Xuegang, D. Zhuwei, *Prog. Chem.* **2004**, *16*, 738.

[17] C. Di Valentin, G. Pacchioni, A. Selloni, *Chem. Mater.* **2005**, *17*, 6656.

[18] S. Andersson, B. Collén, U. Kuylenstierna, A. Magnéli, *Acta Chem. Scand.* **1957**, *11*, 1641.

[19] Y. Gotoha, K. Fujimura, M. Koike, Y. Ohkoshi, M. Nagura, K. Akamatsu, S. Deki, *Mater. Res. Bull.* **2001**, *36*, 2261.

[20] R. Koc, J.S. Folmer, *J. Mater. Sci.* **1997**, *32*, 3101.

[21] R. Koc, *J. Eur. Ceram. Soc.* **1997**, *17*, 1309.

[22] P. Lefort, A. Maitre, P. Tistant, *J. Alloys Compd.* **2000**, *302*, 287.

[23] M.A.R. Dewan, G. Zhang, O. Ostrovski, *Metall. Mater. Trans. B* **2009**, *40*, 62.

[24] G. Zhang, O. Ostrovski, *Metall. Mater. Trans. B* **2000**, *31*, 129.

[25] D. Bresser, E. Paillard, E. Binetti, S. Krueger, M. Striccoli, M. Winter, S. Passerini, *J. Power Sources* **2012**, *206*, 301.

[26] P. Acevedo-Peña, M. Haro, M.E. Rincón, J. Bisquert, G. Garcia-Belmonte, *J. Power Sources* **2014**, *268*, 397.

[27] H.S. Kim, S.-H. Yu, Y.-E. Sung, S. H. Kang, *J. Alloys Compd.* **2014**, *597*, 275.

[28] D. Liu, Y. Zhang, P. Xiao, B. Batalla Garcia, Q. Zhang, X. Zhou, Y.-H. Jeong, G. Cao, *Electrochim. Acta* **2009**, *54*, 6816.

[29] R. Hahn, F. Schmidt-Stein, J. Salonen, S. Thiemann, Y. Y. Song, J. Kunze, V.-P. Lehto, P. Schmuki, *Angew. Chem. Int. Ed.* **2009**, *48*, 7236.

[30] C. Rüdiger, F. Maglia, S. Leonardi, M. Sachsenhauser, I.D. Sharp, O. Paschos, J. Kunze, *Electrochim. Acta* **2012**, *71*, 1.

[31] C. Rüdiger, J. Brumbarov, F. Wiesinger, S. Leonardi, O. Paschos, C. Valero-Vidal, J. Kunze-Liebhäuser, ChemCatChem **2013**, *5*, 3219.

[32] B.C. Brodie, *Philos. Trans. R. Soc. London* **1959**, *149*, 249.

[33] D.R. Dreyer, S. Park, C.W. Bielawski, R.S. Ruoff, *Chem. Soc. Rev.* **2010**, *39*, 228.

[34] P. Roy, S. Berger, P. Schmuki, *Angew. Chem. Int. Ed.* **2011**, *50*, 2904.

[35] Y.-Y. Song, P. Roy, I. Paramasivam, P. Schmuki, *Angew. Chem.* **2010**, *122*, 361.

[36] A. Valota, D. J. LeClere, P. Skeldon, M. Curioni, T. Hashimoto, S. Berger, J. Kunze, P. Schmuki, G.E. Thompson, *Electrochim. Acta* **2009**, *54*, 4321.

[37] X. Feng, J.M. Macak, P. Schmuki, *Chem. Mater.* **2007**, *19*, 1534.

[38] Y. Li, Y. Hu, Y. Zhao, G. Shi, L. Deng, Y. Hou, L. Qu, *Adv. Mater.* **2011**, *23*, 776.

[39] A. Mukherjee, J. Kang, O. Kuznetsov, Y. Sun, R. Thaner, A.S. Bratt, J.R. Lomeda, K.F. Kelly, W.E. Billups, *Chem. Mater.* **2011**, *23*, 9.

[40] M. Favaro, S. Agnoli, C. Di Valentin, C. Matevi, M. Cattelan, L. Artiglia, E. Magnano, F. Bondino, S. Nappini, G. Granozzi, *Carbon* **2014**, *68*, 319.

[41] Y. Li, D.-S. Hwang, N.H. Lee, S.-J. Kim, *Chem. Phys. Lett.* **2005**, *404*, 25.

[42] C. Mattevi, G. Eda, S. Agnoli, S. Miller, K. A. Mkhoyan, O. Celik, D. Mastrogiovanni, G. Granozzi, E. Garfunkel, M. Chhowalla, *Adv. Funct. Mater.* **2009**, *19*, 2577.

[43] I. Jung, D.A. Field, N.J. Clark, Y. Zhu, D. Yang, R.D. Piner, S. Stankovich, D.A. Dikin, H. Geisler, C.A. Ventrice, R.S. Ruoff, *J. Phys. Chem. C* **2009**, *113*, 18480.

[44] R. Larciprete, S. Fabris, T. Sun, P. Lacovig, A. Baraldi, S. Lizzit, *J. Am. Chem. Soc.* **2011**, *133*, 17315.

[45] R. Larciprete, P. Lacovig, S. Gardonio, A. Baraldi, S. Lizzit, *J. Phys. Chem. C* **2012**, *116*, 9900.

[46] A. Barinov, O. B. Malcioglu, S. Fabris, T. Sun, L. Gregoratti, M. Dalmiglio, M. Kiskinova, *J. Phys. Chem. C Lett.* **2009**, *113*, 9009.

[47] R. Koc, *J. Mat. Sci.* **1998**, *33*, 1049.

[48] L. Calvillo, D. Fittipaldi, C. Rüdiger, S. Agnoli, M. Favaro, C. Valero-Vidal, C. Di Valentin, A. Vittadini, N. Bozzolo, S. Jacomet, L. Gregoratti, J. Kunze-Liebhäuser, G. Pacchioni, G. Granozzi, *J. Phys. Chem. C* **2014**, *118*, 22601.

[49] T.N. Lambert, C.A. Chavez, B. Hernandez-Sanchez, P. Lu, N.S. Bell, A. Ambrosini, T. Friedman, T.J. Boyle, D.R. Wheeler, D.L. Huber, *J. Phys. Chem. C* **2009**, *113*, 19812.

[50] L. Mai, C. Huang, D. Wang, Z. Zhang, Y. Wang, *Appl. Surf. Sci.* **2009**, *255*, 9285.

[51] C.J. Howard, T.M. Sabine, F. Dickson, *Acta Crystallogr.* **1991**, *B47*, 462.

[52] L.E. Walle, S. Agnoli, I.-H. Svenum, A. Borg, L. Artiglia, P. Krüger, A. Sandell, G. Granozzi, *J. Chem. Phys.* **2011**, *135*, 1.

[53] R.S. Liu, Y.C. Cheng, J.M. Chen, R.G. Liu, J.L. Wang, J.C. Tsai, M.Y. Hsu, *Mater. Lett.* **1998**, *37*, 285.

[54] T. Caruso, C. Lenardi, R.G. Agostino, M. Amati, G. Bongiorno, T. Mazza, A. Policicchio, V. Formoso, E. Maccallini, E. Colavita, G. Chiarello, P. Finetti, F. Sutara, T. Skála, P. Piseri, K.C. Prince, P. Milani, *J. Chem. Phys.* **2008**, *128*, 1.

[55] F.M.F. de Groot, J.C. Fuggle, B.T. Thole, G.A. Sawatzky, *Phys. Rev. B* **1990**, *41*, 928.

[56] R.S. Liu, J.B. Wu, C.Y. Chang, J.G. Lin, C.Y. Huang, J.M. Chen, R.G. Liu, *J. Solid State Chem.* **1996**, *125*, 112.

[57] J. Crocombette, F. Jollet, *J. Phys.: Condens. Matter* **1994**, *6*, 10811.

[58] A.C. Fernandes, P. Carvalho, F. Vaz, S. Lanceros-Méndez, A.V. Machado, N.M.G. Parreira, J.F. Pierson, N. Martin, *Thin Solid Films* **2006**, *515*, 866.

[59] B. Prasai, B. Cai, M.K. Underwood, J.P. Lewis, D.A. Drabold, *J. Mater. Sci.* **2012**, *47*, 7515.

[60] H. Zhang, X. Lv, Y. Li, Y. Wang, J. Li, *ACS Nano* **2010**, *4*, 380.

[61] K. Kanda, K. Fukuda, K. Kidena, R. Imai, M. Niibe, S. Fujimoto, K. Yokota, M. Tagawa, *Diamond Relat. Mater.* **2014**, *41*, 49.

[62] A.N. Enyashin, A.L. Ivanovskii, *Chem. Phys.* **2009**, *362*, 58.

[63] F. Dong, H. Wang, Z. Wu, *J. Phys. Chem. C* **2009**, *113*, 16717.

[64] A.J. Bard, L.R. Faulkner, *Electrochemical methods: fundamentals and applications*, John Wiley and Sons, Inc., New York, USA **2001**, p.751.

[65] M. Metikos-Hukovic, M. Ceraj-Ceric, *Surf. Technol.* **1985**, *24*, 273.

[66] A.W. Bott, *Curr. Sep.***1998**, *17*, 87.

[67] G. Cooper, J.A. Turner, A.J. Nozik, *J. Electrochem. Soc.* **1982**, 129, 1973.

[68] A.S. Bondarenko, G.A. Ragoisha, *J. Solid State Electrochem.* **2005**, *9*, 845.

[69] C.-Z. Yuan, B. Gao, X.-G. Zhang, *J. Power Sources* **2007**, *173*, 606.

[70] Y. Xie, Y. Wang, H. Du, *J. Mater. Sci. Eng. B* **2013**, *178*, 1443.

[71] C. Valero Vidal, A. Igual Muñoz, *Electrochim. Acta* **2009**, *54*, 1798.

[72] D. Landolt, *Corrosion and Surface Chemistry of Metals*, EPFL Press (CRC Press), Lausanne, Switzerland **2007**, pp. 206-224.

[73] M. Favaro, S. Agnoli, M. Cattelan, A. Moretto, C. Durante, S. Leonardi, J. Kunze-Liebhäuser, O. Schneider, A. Gennaro, G. Granozzi, *Carbon* **2014**, *77*, 405.

Appendix A4.1: Synthesis and purification of pure and doped-GOQDs

The Working Electrodes (WE) for the electrochemical procedure [22] were made from a GC plate (Tokai GC-20), polished to a mirror finish with silicon carbide papers of decreasing grain size (Struers, grit: 500, 1000, 2400, 4000) followed by diamond paste (3, 1 and 0.25 μm particle size). The samples were cleaned by ultrasonic treatment in a mixture of isopropanol/ethanol (Aldrich, 1:1) for 10 minutes. Finally, 150 μL of a concentrated dispersion of GO in water (15 mg of GO/mL) were drop casted on the GC substrates (GO/GC) and then annealed in a tubular furnace at 150°C for 30 minutes under an overpressure of N_2 (flow rate 500 sccm). A standard three-electrode electrochemical cell, using a Pt ring as Counter (CE) and a saturated $Ag/AgCl/Cl^-$ as Reference Electrode (RE) was employed (standard electrode potential $E^{\Theta}_{Ag/AgCl\ (sat.)} = 0.197$ V with respect to the Standard Hydrogen Electrode, SHE). The electrodes were assembled in an EC cell with a 30° degrees configuration and an inter-electrode gap of 1 cm. The electrolyte solutions (constant volume of 50 mL) were kept at 25 °C by a thermostat-controlled water bath during the both synthesis or characterization. The stirring of the electrolyte during the reactions was carried out by a magnetic stirrer. All the cyclic voltammograms (CVs) were acquired with the same disk area exposed to the electrolyte (2.5 cm^2), by enveloping the samples with Teflon tape and contacting them from the back with a copper plate. The electrochemical measurements were carried out with an EG&G PARC 173 potentiostat/galvanostat.

The electrochemical synthesis of GOQDs was performed in a Phosphate Buffer Solution (NaH_2PO_4, PBS) 0.1M, after the addition of few drops of a NaOH 10M solution in order to reach a pH value of 6.86÷6.88 at 20° C. Then, the potential was cycled between ± 3.0 V (vs. $Ag/AgCl/Cl^-_{(sat)}$) at a scan rate of 500 mV/s. After 2000 CVs the obtained light yellow solutions were filtered twice using cellulose acetate membranes (VWR) with a porosity size of 400 and 200 nm, respectively. Then, the filtered solutions were dialyzed for five days (in MilliQ water) with osmotic membranes (Spectra/Por, Molecular Weight Cut-Off (MWCO) of 1 kD) to remove the electrolyte salt and finally they were freeze-dried under low vacuum conditions (~10-1 mbar). For further characterizations (XPS and Raman, IR and fluorescence spectroscopy) the obtained yellow powder was re-dispersed in MilliQ water.

For the synthesis of doped-GOQDs, a molecular precursor of the target dopant was introduced in the electrolyte. Table A.1 reports the experimental conditions for the different syntheses, while Figure A.1 reports the CVs, the molecular structures and the digital images of the different doped-GOQD solution obtained via electrochemical etching of a GO WE in the molecular precursor-containing electrolyte.

Table A.1. Experimental conditions for the synthesis of doped-GOQDs.

	Electrolytic Solution	**Dopant Molecule** [1]	**Final pH** [2]
GOQDs	PBS 0.1M (pH 6.86)	-	6.86
B-GOQDs	PBS 0.1M (pH 11.20) [3]	**1.** 1,4-phenylenebis(boronic acid) (**1**) (100 mM)	11.20
N-GOQDs	PBS 0.1M (pH 6.86)	**1.** ethylenediamine (**2**) (100 mM)	11.30
	PBS 0.1M (pH 1.85) [4]	**2.** 1,10-phenantroline (**3**) (100 mM)	1.85
S-GOQDs	PBS 0.1M (pH 12.20) [5]	α-lipoic acid (**4**) (100 mM)	12.20
B,N-GOQDs	PBS 0.1M (pH 6.86)	ethylenediamine (100 mM) + 1,4-phenylenebis(boronic acid) (100 mM)	11.30
S,N-GOQDs	PBS 0.1M (pH 6.86)	L-cysteine (**5**) (100 mM)	6.80

[1] The quantity of the dopant was added in order to obtain a dopant volumetric concentration of 100 mM.
[2] The pH was measured after the addition of the dopant to the 0.1 M buffer solution.
[3,5] The pH was increased by adding few drops of a 10 M NaOH solution, in order to allow the solubilisation of the doping molecules.
[4] The pH was decreased by adding a few drops of concentrated H_3PO_4 (85 %), in order to allow the solubilisation of 1,10-phenantroline (by protonation of the pyridinic nitrogens).

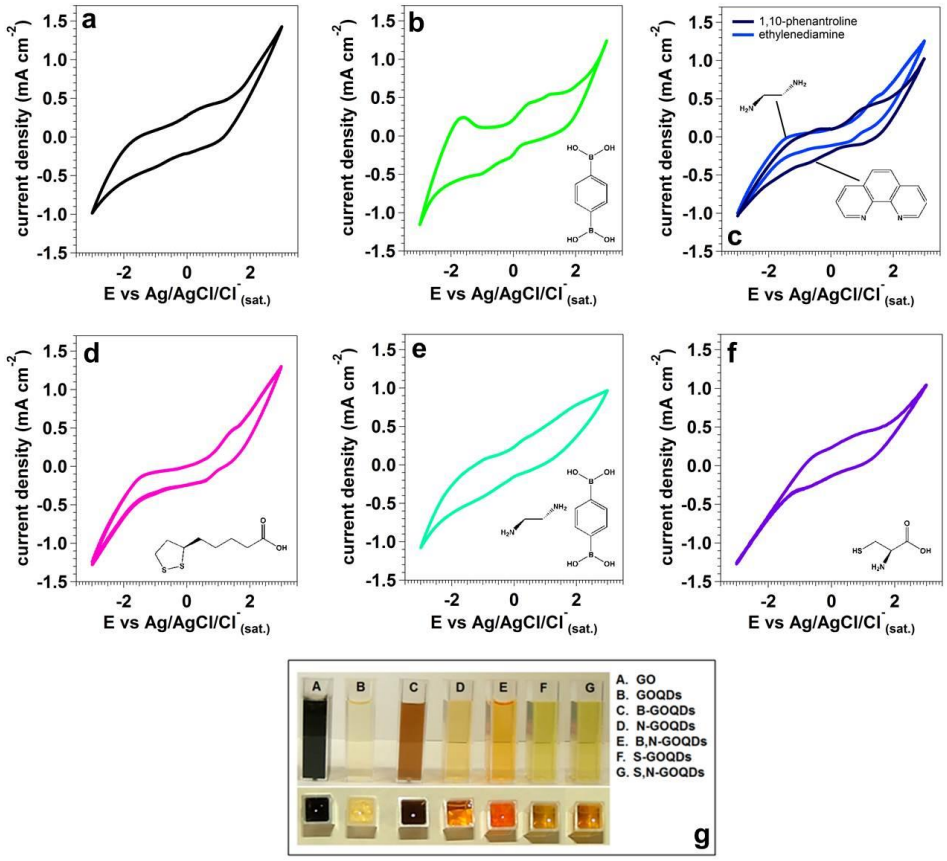

Figure A.1. Cycled polarization curves of a GO WE in pure PBS (a) and in 1,4-phenylenebis(boronic acid)- (b), ethylenediamine- or 1,10-phenantroline- (c), α-dipoic acid- (d), ethylenediamine+1,4-phenylenebis(boronic acid)- (e) and L-cysteine-containing PBS (f); g: digital image, under environmental lighting, of the different doped and co-doped-GOQDs produced via electrochemical etching of a GO WE.

Appendix A4.2: Further characterizations of GOMWs

Figure A.2 reports the ball and stick model [28] of the two inorganic scaffolds used for the preparation of the GOMWs.

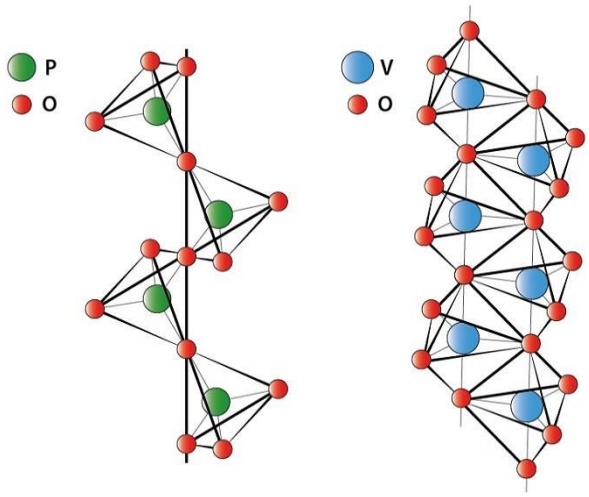

Figure A.2. Ball and stick model for the two inorganic scaffolds used as soft templating agent for the preparation of GOMWs (left: orthophosphates linear chain; right: hydrated metavanadates linear chain).

Figure A4.3 reports the distribution of the diameters of the GOMWs, prepared from orthophosphates (Figure A.3a) and metavanadates (Figure A.3b) scaffolds: the average diameter is equal to 360±49 nm and to 375±64, respectively.

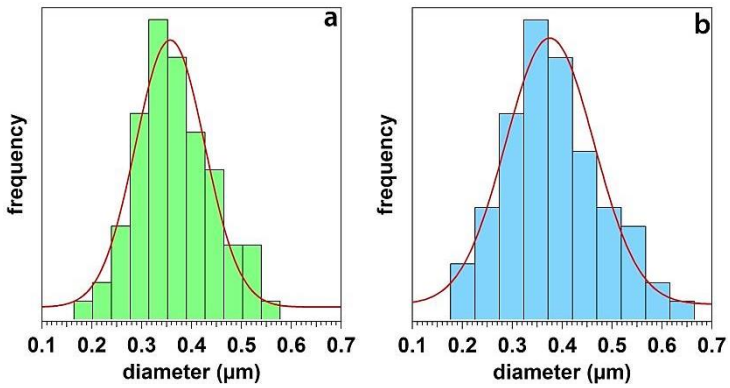

Figure A4.3. Diameter distributions for the GOMWs, prepared from phosphates (a) and metavanadates (b) scaffolds.

Figure A4.4 reports the XPS analysis of the GOMWs, while Figure A4.5 reports the solid state photoluminescence measurements of GOQD-based nanospheres and of GOMWs

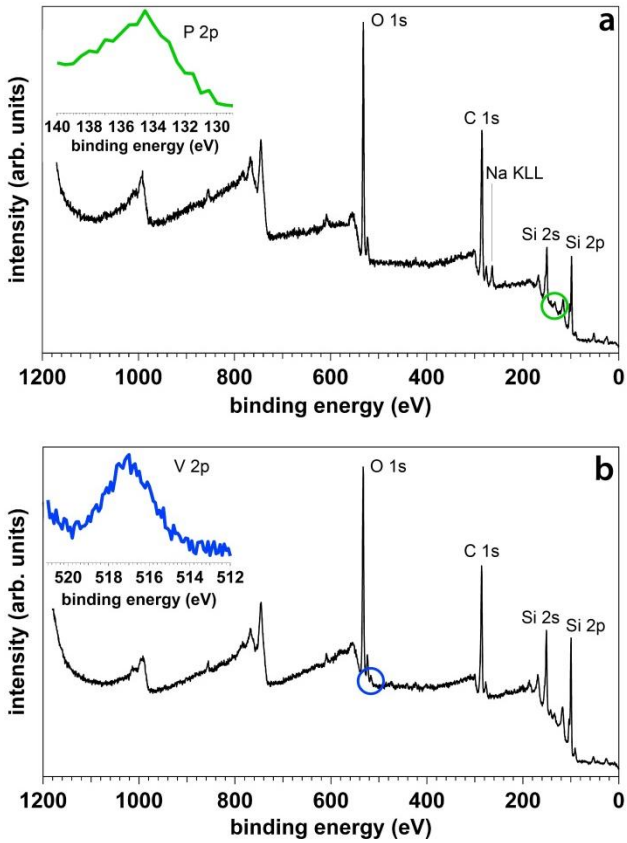

Figure A4.4. XPS survey scans of the GOMWs (deposited by drop casting on a P:Si(100) single crystal) obtained from phosphates (a) and from metavanadates (b).

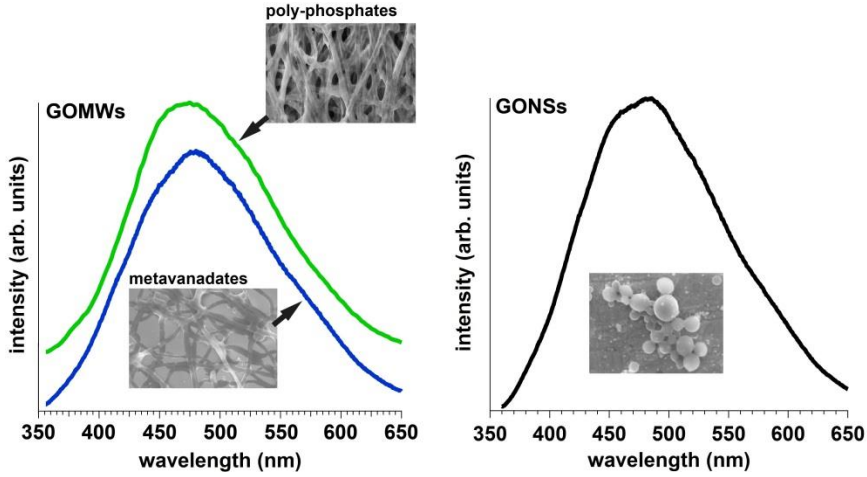

Figure A4.5. Photoluminescence measurements on GOMWs (left) and on GONSs (right), after the deposition on a quartz substrate. The excitation wavelength is 340 nm.

REFERENCES

[1] X. Yan, X. Cui, L.S. Li, Synthesis of Large, Stable Colloidal Graphene Quantum Dots with Tunable Size, *J. Am. Chem. Soc.* **132**, 5944-5945 (2010).

[2] J. Tobik, A. Dal Corso, S. Scandolo, E. Tosatti, Organic molecular crystals in electric fields, *Surf. Sci*. **566-568**, 644-649 (2004).

[3] G. Eda, Y.-Y. Lin, C. Mattevi, H. Yamaguchi, H.-A. Chen, I.-S. Chen, C.-W. Chen, M. Chhowalla, Blue Photoluminescence from Chemically Derived Graphene Oxide, *Adv. Mater.* **22**, 505-509 (2010).

[4] X. Yan, X. Cui, B. Li, L.S. Li, Large, Solution-Processable Graphene Quantum Dots as Light Absorbers for Photovoltaics, *Nano Lett.* **10**, 1869-1873 (2010).

[5] S.N. Baker, G. A. Baker, Luminescent Carbon Nanodots: Emergent Nanolights, *Angew. Chem. Int. Ed.* **49**, 6726-6744 (2010).

[6] H. Sun, L. Wu, W. Wei, X. Qu, J.-J. Zhu, Recent advances in graphene quantum dots for sensing, *Materials Today* **16**, 433-442 (2013).

[7] Z. Zhang, J. Zhang, N. Chen, L. Qu, Graphene quantum dots: an emerging material for energy-related applications and beyond, *Energy Environ. Sci.* **5**, 8869-8890 (2012).

[8] J. Shen, Y. Zhu, X. Yang, J. Zong, J. Zhang, C. Li, One-pot hydrothermal synthesis of graphene quantum dots surface-passivated by polyethylene glycol and their photoelectric conversion under near-infrared light, *New J. Chem.* **36**, 97-101 (2012)

[9] L. A. Ponomarenko, F. Schedin, M. I. Katsnelson, R. Yang, E. W. Hill, K. S. Novoselov, A. K. Geim, Chaotic Dirac Billiard in Graphene Quantum Dots, *Science* **320**, 356-358 (2008).

[10] F. Liu, M.-H. Jang, H. D. Ha, J.-H. Kim, Y.-H. Cho, T. S. Seo, Facile Synthetic Method for Pristine Graphene Quantum Dots and Graphene Oxide Quantum Dots: Origin of Blue and Green Luminescence, *Adv. Mater.* **25**, 3657-3662 (2013).

[11] L. Li, G. Wu, G. Yang, J. Peng, J. Zhao, J.-J. Zhu, Focusing on luminescent graphene quantum dots: current status and future perspectives, *Nanoscale* **5**, 4015-4038 (2013).

[12] Lu, J.; Yang, J.-X.; Wang, J.; Lim, A.; Wang, S.; Loh, K. P. One-Pot Synthesis of Fluorescent Carbon Nanoribbons, Nanoparticles, and Graphene by the Exfoliation of Graphite in Ionic Liquids, *ACS Nano* **3**, 2367-2375 (2009).

[13] Y. Zhu, S. Murali, M. D. Stoller, A. Velamakanni, R. D. Piner, R. S. Ruoff, Microwave assisted exfoliation and reduction of graphite oxide for ultracapacitors, *Carbon* **48**, 2118-2122 (2010).

[14] W. Chen, L. Yana, P. R. Bangalb, Preparation of graphene by the rapid and mild thermal reduction of graphene oxide induced by microwaves, *Carbon* **48**, 1146–1152 (2010).

[15] D. Li, M. B. Muller, S. Gilje, R. B. Kaner, G. G. Wallace, Processable aqueous dispersions of graphene nanosheets, *Nat. Nanotech.* **3**, 101-105 (2008).

[16] S. Kim, S. W. Hwang, M.-K. Kim, D. Y. Shin, D. H. Shin, C. O. Kim, S. B. Yang, J. H. Park, E. Hwang, S. H. Choi, G. Ko, S. Sim, C. Sone, H. J. Choi, S. Bae, B. H. Hong, Anomalous Behaviors of Visible Luminescence from Graphene Quantum Dots: Interplay between Size and Shape, *ACS Nano* **6**, 8203-8208 (2012).

[17] G. S. Kumar, R. Roi, D. Sen, U. K. Ghorai, R. Thapa, N. Mazumder, S. Saha, K. K. Chattopadhyay, Amino-functionalized graphene quantum dots: origin of tunable heterogeneous photoluminescence, *Nanoscale* **6**, 3384-3391 (2014).

[18] Z. Zhang, J. Zhang, N. Chen, L. Qu, Graphene quantum dots: an emerging material for energy-related applications and beyond, *Energy Environ. Sci.* **5**, 8869-8890 (2012).

[19] K. P. Loh, Q. Bao, G. Eda, M. Chhowalla, Graphene oxide as a chemically tunable platform for optical applications, *Nat. Chem.* **2**, 1015-1024 (2010).

[20] L. Tang, R. Ji, X. Cao, J. Lin, H. Jiang, X. Li, K. S. Teng, C. M. Luk, S. Zeng, J. Hao, S. P. Lau, Deep Ultraviolet Photoluminescence of Water-Soluble Self-Passivated Graphene Quantum Dots, *ACS Nano* **6**, 5102-5110 (2012).

[21] J. Shang, L. Ma, J. Li, W. Ai, T. Yu, G. G. Gurzadyan, The Origin of Fluorescence from Graphene Oxide, *Sci. Rep.* **2**, 792, 2012.

[22] Y. Li, Y. Hu, Y. Zhao, G. Shi, L. Deng, Y. Hou, L. Qu, An Electrochemical Avenue to Green-Luminescent Graphene Quantum Dots as Potential Electron-Acceptors for Photovoltaics, *Adv. Mater.* **23**, 776-780 (2011).

[23] a: J. Hou, Y. Shao, M. W. Ellis, R. B. Moore, B. Yi, Graphene-based electrochemical energy conversion and storage: fuel cells, supercapacitors and lithium ion batteries, *Phys. Chem. Chem. Phys.* **13**, 15384–15402 (2011); b: H.-J. Choi, S.-M. Jung, J.-M. Seo, D.-W. Chang, L. Dai, J.-B. Baek, Graphene for energy conversion and storage in fuel cells and supercapacitors, *Nano Energy* **1**, 534-551 (2012); c: D.-W. Wang, D. Su, Heterogeneous nanocarbon materials for oxygen reduction reaction, *Energy Environ. Sci.* **7**, 576-591 (2014); d: Y. Zheng, Y. Jiao, L. Ge, M. Jaroniec, S. Z. Qiao, Two-step boron and nitrogen doping in graphene for enhanced synergistic catalysis, *Angew. Chem. Int. Ed.* **52**, 1-7 (2013); e: Y. Li, Y. Zhou, H. Cheng, Y. Hu, G. Shi, L. Dai, L. Qu, Nitrogen-doped graphene quantum dots with oxygen-rich functional groups, *J. Am. Chem. Soc.* **134**, 15-18 (2012); f: Y. Jiao, Y. Zheng, M. Jaroniec, S. Z. Qiao, Origin of the electrocatalytic oxygen reduction activity of graphene-based catalysts: a roadmap to achieve the best performance, *J. Am. Chem. Soc.* **136**, 4394-4403 (2014).

[24] a: E. Yaeger, Electrocatalysts for O_2 reduction, *Electrochim. Acta* **29**, 1527-1537 (1984); b: K. Tammeveski, K. Kontturi, R. J. Nichols, R. J. Potter, D. J. Schiffrin, Surface redox catalysis for O_2 reduction on quinone-modified glassy carbon electrodes, *J. Electroanal. Chem.* **515**, 101-112 (2001); c: A. Sarapuu, K. Helstein, D. J. Schiffrin, K. Tammeveski, Kinetics of oxygen reduction on quinone-modified HOPG and K BDD

electrodes in alkaline solution, *Electrochem. Solid-State Lett.* **8**, E30-E33 (2005); d: G. Jürmann, D. J. Schiffrin, K. Tammeveski, The pH-dependence of oxygen reduction on quinone-modified glassy carbon electrodes, *Electrochim. Acta* **53**, 390-399 (2007); e: R. L. McCreery, Advanced carbon electrode materials for molecular electrochemistry, *Chem. Rev.* **108**, 2646-2687 (2008); f: A. Sarapuu, K. Helstein, K. Vaik, D. J. Schiffrin, K. Tammeveski, Electrocatalysis of oxygen reduction by quinones adsorbed on highly oriented pyrolytic graphite electrodes, *Electrochim. Acta* **55**, 6376-6382 (2010); g: I. Kocak, M. A. Ghanem, A. Al-Mayouf, M. Alhoshan, P. N. Bartlett, A study of the modification of glassy carbon and edge and basal plane highly oriented pyrolytic graphite electrodes modified with anthraquinone using diazonium coupling and solid phase synthesis and their use for oxygen reduction, *J. Electroanal. Chem.* **706**, 25-32 (2013); h: M. Mooste, E. Kibena, A. Sarapuu, U. Mäeorg, G. Maia, K. Tammeveski, Electrocatalysis of oxygen reduction on glassy carbon electrodes modified with anthraquinone moieties, *J. Solid State Electrochem.* **18**, 1725-1733 (2014).

[25] Y. Zhou, T. Holme, J. Berry, T. R. Ohno, D. Ginley, R. O'Hayre, Dopant-Induced Electronic Structure Modification of HOPG Surfaces: Implications for High Activity Fuel Cell Catalysts, *J. Phys. Chem. C* **114**, 506-515 (2010).

[26] a: J. Cao, Y. Wang, P. Xiao, Y. Chen, Y. Zhou, J.-H. Ouyang, D. Jia, Hollow graphene spheres self-assembled from graphene oxide sheets by a one-step hydrothermal process, *Carbon* **56**, 383-391 (2013); b: N. Brun, K. Sakaushi, L. Yu, L. Giebeler, J. Eckert, M. M. Titirici, Hydrothermal carbon-based nanostructured hollow spheres as electrode materials for high-power lithium–sulfur batteries, *Phys. Chem. Chem. Phys.* **15**, 6080-6087 (2013).

[27] M. Favaro, S. Agnoli, *unpublished work*.

[28] N. N. Greenwood, A. Earnshaw, *Chemistry of the elements*, Butterworth/Heinemann, 1995.

[29] F. A. Cotton, G. Wilkinson, C. A. Murillo, M. Bochmann, *Advanced Inorganic Chemistry*, Wiley Interscience Pubblication, 1999.

[30] G. Hautier, A. Jain, H. Chen, C. Moore, P. S. Ong, G. Ceder, Novel mixed polyanions lithium-ion battery cathode materials predicted by high-throughput ab initio computations, *J. Mater. Chem.* **21**, 17147-17153 (2011).

[31] H. Kim, Y. Kim, K. S. Kim, H. Y. Jeong, A.-R. Jang, S. H. Han, D. H. Yoon, K. S. Suh, H. S. Shin, T. Y. Kim, W. S. Yang, Flexible thermochromic window based on hybridized VO_2/Graphene, *ACS Nano* **7**, 5769-5776 (2013).

[32] Y. Sun, X. Hu, W. Luo, Y. Huang, Self-assembled hierarchical MoO_2/Graphene nanoarchitectures and their application as a high-performance anode material for lithium-ion batteries, *ACS Nano* **5**, 7100-7107 (2011).

[33] J. Jin, X. Fu, Q. Liu, Y. Liu, Z. Wei, K. Niu, J. Zhang, Identifying the active site in nitrogen-doped graphene for the VO^{2+}/VO_2^+ redox reaction, *ACS Nano* **7**, 4764-4773 (2013).

[34] S. Z. Butler, S. M. Hollen, L. Cao, Y. Cui, J. A. Gupta, H. R. Gutierrez, T. F. Heinz, S. S. Hong, J. Huang, A. F. Ismach, E. Johnston-Halperin, M. Kuno, M. et al., Progress,

challenges, and opportunities in two-dimensional materials beyond graphene, *ACS Nano* **7**, 2898-2926 (2013).

[35] S. Yang, Y. Gong, Z. Liu, L. Zhan, D. P. Hashim, L. Ma, R. Vajtai, P. M. Ajayan, Bottom-up approach toward single-crystalline VO_2-Graphene ribbons as cathodes for ultrafast lithium storage, *Nano Lett.* **13**, 1596-1601 (2013).

[36] D. F. Shriver, P. W. Atkins, C. H. Langford, *Inorganic Chemistry*, Oxford University Press, **2006**.

[37] H. Kisch, M. Macyk, Visible-light photocatalysis by modified titania, *Chem. Phys. Chem*. **3**, 399-400 (2002).

[38] P. Roy, S. Berger, P. Schmuki, TiO_2 nanotubes: synthesis and applications, *Angew. Chem. Int. Ed.* **50**, 2904-2939 (2011).

[39] J. Xu, G. Dong, C. Jin, M. Huang, L.Guan, Sulfur and Nitrogen Co-Doped, Few-Layered Graphene Oxide as a Highly Efficient Electrocatalyst for the Oxygen-Reduction Reaction, *Chem. Sus. Chem.* **6**, 493-499 (2013).

[40] S.-A. Wohlgemuth, F. Vilela, M.-M. Titirici, M. Antonietti, A one-pot hydrothermal synthesis of tunable dual heteroatom-doped carbon microspheres, *Green Chem.* **14**, 741-749 (2012).

[41] S.-A. Wohlgemuth, R. J. White, M.-G. Willinger, M.-M. Titirici, M. Antonietti, A one-pot hydrothermal synthesis of sulfur and nitrogen doped carbon aerogels with enhanced electrocatalytic activity in the oxygen reduction reaction, *Green Chem.* **14**, 1515-1523 (2012).

[42] Z. Yang, Z. Yao, G. Li, G. Fang, H. Nie, Z. Liu, X. Zhou, X. Chen, S. Huang, Sulfur-Doped Graphene as an Efficient Metal-free Cathode Catalyst for Oxygen Reduction, *ACS Nano* **6**, 205-211 (2012).

[43] a: V. Lee, L. Whittaker, C. Jaye, K. M. Baroudi, D. A. Fischer, S. Banerjee, Large-Area Chemically Modified Graphene Films: Electrophoretic Deposition and Characterization by Soft X-ray Absorption Spectroscopy, *Chem. Mater*. (21) 3905-3916 (2009); b: S. Saxena, T. A. Tyson, E. Negusse, J. Phys. Chem. Lett. 2010, 1, 3433–3437; A. Hunt, D. A. Dikin, E. Z. Zurmaev, T. D. Boyko, P. Bazylewski, G. S. Chang, A. Moewes, Epoxide Speciation and Functional Group Distribution in Graphene Oxide Paper-Like Materials, *Adv. Funct. Mater.* **22**, 3950-3957 (2012).

[44] D. Brete, D. Przyrembel, C. Eickhoff, R.Carley, W. Freyer, K. Reuter, C. Gahl, M. Weinelt, Mixed self-assembled monolayers of azobenzene photoswitches with trifluoromethyl and cyano end groups, *J. Phys.: Condens. Matter* **24**, 394015 (2012).

[45] D. Usachov, O. Vilkov, A. Grüneis, D. Haberer, A. Fedorov, V. K. Adamchuk, A. B. Preobrajenski, P. Dudin, A. Barinov, M. Oehzelt, C. Laubschat, D. V. Vyalikh, Nitrogen doped graphene: efficient growth, structure, and electronic properties, *Nano Lett.* **11**, 5401-5407 (2011).

[46] M. S. Dresselhaus, M.S.; Jorio, A.; Saito, R. Characterizing Graphene, Graphite, and Carbon Nanotubes by Raman Spectroscopy, *Annu. Rev. Condens. Matter Phys.* **1,** 89-108 (2010).

[47] S. Kim, S. W. Hwang, M.-K. Kim, D. Y. Shin, D. H. Shin, C. O. Kim, S. B. Yang, J. H. Park, E. Hwang, S.-H. Choi et al., Graphene quantum dots: an emerging material for energy-related applications and beyond, *ACS Nano* **6**, 8203-8208 (2012).

[48] V. Gupta, N. Chaudhary, R. Srivastava, G. D. Sharma, R. Bhardwaj, S. Chand, Luminscent Graphene Quantum Dots for Organic Photovoltaic Devices, *J. Am. Chem. Soc.* **133**, 9960-9963 (2011).

[49] W. Kwon, S. Do, J. Lee, S. Hwang, J. K. Kim, S.-W- Rhee, Freestanding Luminescent Films of Nitrogen-Rich Carbon Nanodots toward Large-Scale Phosphor-Based White-Light-Emitting Devices, *Chem. Mater.* **25**, 1893-1899 (2013).

[50] Gong, K. P.; Du, F.; Xia, Z. H.; Durstock, M.; Dai, L. M. Nitrogen-Doped Carbon Nanotube Arrays with High Electrocatalytic Activity for Oxygen Reduction, *Science* **323**, 760-764 (2009).

[51] Wang, S. Y.; Yu, D. S.; Dai, L. M. Polyelectrolyte Functionalized Carbon Nanotubes as Efficient Metal-free Electrocatalysts for Oxygen Reduction, *J. Am. Chem. Soc.* **133**, 5182-5185 (2011).

[52] W. A. Saidi, Oxygen Reduction Electrocatalysis Using N-Doped Graphene Quantum-Dots, *J. Phys. Chem. Lett.* **4**, 4160-4165 (2013).

[53] Y. Dong, W. Tian, S. Ren, R. Dai, Y. Chi, G. Chen, Graphene quantum dots/L-cysteine coreactant electrochemiluminescence system and its application in sensing lead(II) ions, *ACS Appl. Mater. Interfaces* **6**, 1646-1651 (2014).

[54] D. Qu, M. Zheng, P. Du, Y. Zhou, L. Zhang, D. Li, H. Tan, Z. Zhao, Z. Xie, Z. Sun, Highly luminescent S, N co-doped graphene quantum dots with broad visible absorption bands for visible light photocatalysts, *Nanoscale* **5**, 12272-12277 (2013).

[55] W. Yuan, Y. Zhou, Y. Li, C. Li, H. Peng, J. Zhang, Z. Liu, L. Dai, G. Shi, The edge- and basal-plane-specific electrochemistry of a single-layer graphene sheet, *Sci. Rep.* **3**:2248 (2013).

[56] J. Guo, M. Al-Dahhan, Catalytic wet oxidation of phenol by hydrogen peroxide over pillared clay catalyst, *Ind. Eng. Chem. Res.* **42**, 2450-2460 (2003).

[57] H. El-Hamshary, M. H. El-Newehy, S. S. Al-Deyab, Oxidation of phenol by hydrogen peroxide catalyzed by metal-containing poly(amidoxime) grafted starch, *Molecules* **16**, 9900-9911 (2011).

[58] A. Alverez-Gallegos, D. Pletcher, The removal of low level organics via hydrogen peroxide formed in a reticulated vitreous carbon cathode cell. Part 2: The removal of phenols and related compounds from aqueous effluents, *Electrochim. Acta* **44**, 2483-2492 (1999).

General Conclusion

During the three years of the PhD, the research efforts have been devoted to the preparation and characterization of graphene-derived materials, for applications in electrocatalysis.

The first part of the PhD, mainly has focused on the study of carbon model systems (within the framework of the CathCat european project) has allowed the development of the necessary knowledge and skills for the study of advanced electrocatalysts combining, in a synergic interlacement, Surface Science with Electrochemistry.

The results obtained from these studies have shed new light on the preparation of doped materials via soft ion implantation and, moreover, on the nature of the interaction between Pd and N-centers in N-containing carbon supports. Regarding the ion implantation, we have demonstrated that it is possible to obtain several types of N related defects, even thermodynamically unstable species which are only kinetically stabilized. Interestingly, in order to partially tune the chemical composition of the surface after ion implantation, it is sufficient to anneal the system, and to exploit the different thermal stabilities of the nitrogen species. This ability to control the surface functionality of the carbon support and to study in detail its atomic structure (also using synchrotron radiation) and electrochemical reactivity, represents a solid methodology in order to establish structure-activity relationships. It has been verified that the introduction of nitrogen functional groups enhances the catalytic activity of a typical inert carbon substrate as HOPG toward ORR, and that the reduction process follows a four electron pathway leading directly to H_2O without side reactions to H_2O_2. These results represent a benchmark for explaining the similar reactivity observed on more complex carbon-based systems. Interestingly, it has been demonstrated that the direct interaction of Pd with N centers leads to a low active catalysts towards the ORR, differently from Pt, which is well known to give excellently performing systems when coupled with N-doped graphenes. On the other hand, it has been

demonstrated that the deposition of Pd NPs on N-doped GC leads to a suitable electrocatalyst for the reduction of halogen-aromatic compounds, which is extremely important for water remediation applications.

The second part of the doctorate work have been focused on the preparation of graphene-based materials via Wet-Chemistry and electrochemical approaches. The surface reactivity of GO, influenced by the epoxy groups present in the pristine material, have been deeply investigated by different experimental techniques, in particular by the use of synchrotron radiation at the BACH (Beamline for Advanced DiChroism) beamline of Elettra synchrotron in Trieste (Italy).

The knowledge of the key role played by the epoxides on the surface reactivity of GO has made possible to rationalize the phenomena observed during the electrochemical selective unzipping of the GO itself. This has led to the consequent process optimization with a parallel enhancement of the materials properties. Using GO as flexible starting material, several structures with energy applications have been prepared, like GO foams (for energy storage) and GOQDs. These new and extremely interesting materials, in their doped form with different heteroatoms, exhibit excellent catalytic activity towards the reduction of oxygen, which was the main scope of this thesis work. Furthermore, a careful experimental study supported by DFT calculations (thanks to the collaboration with the theoretical group coordinated by prof. C. Di Valentin) has allowed shedding light on the role played by the oxygen functional groups on the oxygen reduction mechanism. Since these systems are characterized by a nanometer size (about 2 nm), the close proximity between the oxygen functional groups and the dopant atoms leads to an oxygen reduction occurring via a 2 electron reaction pathway. This reaction is not suitable for a real FC cathode, because i) of the lower reachable current density and ii) of the production of hydrogen peroxide in the cathodic side, that may limit the life on stream of the catalytic active phase (as well as the stability of the polymeric membrane)[1]. On the other hand, as documented by Figure 1, it has been found that the recovering of the targeted 4

[1] L. Carrette, K. A. Friedrich, U, Stimming, *Fuel Cells: Fundamentals and Applications*, *Fuel Cells* **1**, 5- (2001); R. O'Hayre, *Fuel Cell Fundamentals*, Wiley Ed., 2008.

electron reaction mechanism is possible simply by a chemical reduction treatment. Since GOQDs, due to their size, are intrinsically semiconductive, the reduction process does not affect significantly the macroscopic electric properties like in micrometric GO sheets, but just locally the oxidation state of the functional groups. This is a strong indication that a highly conductive 3D structure is not necessary to achieve a high catalytic activity, whereas the pivotal point is to reduce the number of oxygenated carbon species (and the oxidation state of the dopants) in order to suppress the competitive 2 electron reaction path to hydrogen peroxide. On the other hand, the high selectivity of the pristine materials towards the production of H_2O_2 can be efficiently exploited for organic synthesis in confined reactors or for the decomposition of organic pollutants in wastewaters.

This thesis work has demonstrated that GOQDs constitute highly versatile and flexible nanocatalysts with an incredible potential for the realization of very efficient electroactive systems. Actually, they represent the extreme frontier of graphene nanotechnologies being single layer and just a few nanometer wide, and expose a huge fraction of highly active edges whose chemical nature can be easily modified to favor a specific functionality. Moreover, the possibility to combine the chemical activity to the optical properties of the GOQDs and of their self-assembly derived materials (like nanospheres and microfibers obtained during this doctorate work, as described above) further enlarges the impact that these nanosystems can have in different technological fields. The detailed investigation of the properties of the GOQD-derived materials is still in progress, with target applications in photocatalysis and sensing.

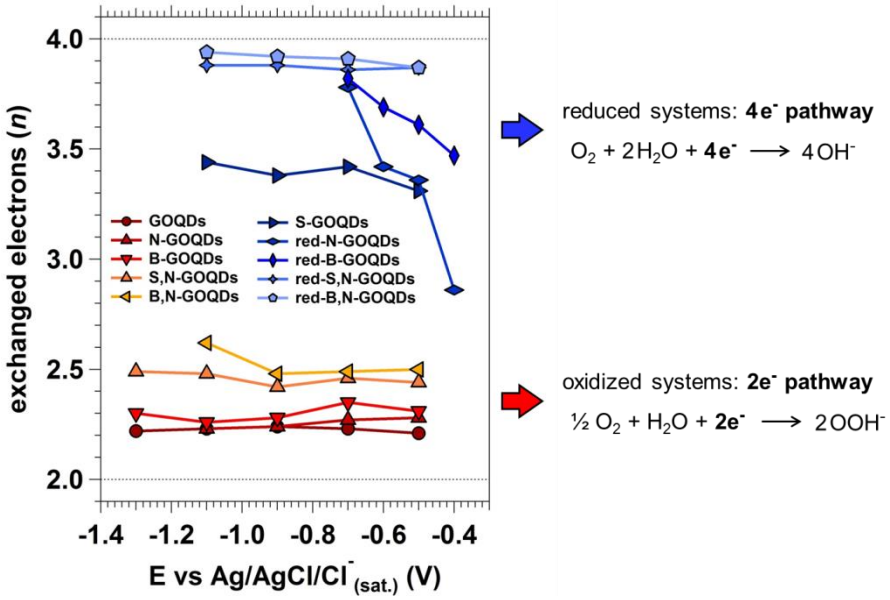

Figure 1. Trend of the number of exchanged electrons as a function of the cathodic potential, for the as-prepared and the chemically-reduced GOQDs.

Acknowledgements

Questo lavoro di tesi è il frutto di quattro anni di ricerca presso il gruppo di Scienza delle Superfici del dipartimento di Scienze Chimiche.
Tutto il lavoro qui presentato non sarebbe stato possibile senza il contributo inestimabile del mio Supervisore, Stefano Agnoli, che ha sempre creduto in me e supportato durante il dottorato. Lo ringrazio sentitamente per tutte le cose che da lui ho potuto imparare; scientificamente parlando, sotto la sua guida sono cresciuto ogni giorno di più, durante questi lunghi quattro anni.
Il mio più sentito ringraziamento va anche al Prof. Granozzi, per la fiducia che ha sempre dimostrato nei miei confronti e per la possibilità di lavorare nel suo gruppo.
Un ringraziamento particolare va anche a Christian Durante e al Prof. Gennaro, per le interessanti (e formanti) discussioni e per avermi permesso di usare i loro laboratori per gli esperimenti di elettrochimica riportati in questo lavoro di tesi.
Vorrei inoltre ringraziare tutti i colleghi ad amici con cui ho avuto il privilegio di lavorare durante questi quattro anni e di passare molti momenti piacevoli in loro compagnia, di cui sempre ne serberò il ricordo: a Lorenzo, Mattia, Jassen, Christoph, Laura, Luca, Marco, Francesco, Jian ed Enrico va tutto il mio più sentito grazie.
Ringrazio Gianandrea per aver colmato le mie lacune di chimica inorganica, il suo aiuto mi è stato e mi sarà sempre prezioso.

Tutto ciò non sarebbe stato possibile se non avessi avuto al mio fianco la mia famiglia, persone speciali come i miei genitori e mia sorella, che mi hanno sempre supportato e spronato a fare del mio meglio. Li porterò sempre nel mio cuore.
A loro va il mio più sincero e profondo ringraziamento.

Infine, desidero ringraziare Celine, una persona straordinaria che ha portato tanta gioia nella mia vita. Da più di due anni lei cammina con me, sempre al mio fianco nelle decisioni importanti, sempre pronta a starmi vicino nei momenti più felici come in quelli di scoramento.
A lei, ed ai suoi genitori Klaus e Karin, va uno speciale ringraziamento.